FERMILAB-THESIS-2024-23

THE UNIVERSITY OF CHICAGO

SEARCH FOR NEW PHYSICS THROUGH A LONG-LIVED DI-MUON RESONANCE IN THE NUMI BEAM WITH THE ICARUS DETECTOR

A DISSERTATION SUBMITTED TO
THE FACULTY OF THE DIVISION OF THE PHYSICAL SCIENCES
IN CANDIDACY FOR THE DEGREE OF
DOCTOR OF PHILOSOPHY

DEPARTMENT OF PHYSICS

BY
GRAY LOUIS CAMPBELL PUTNAM

CHICAGO, ILLINOIS
JUNE 2024

For Joan.

TABLE OF CONTENTS

LIST OF FIGURES

LIST OF TABLES

ACKNOWLEDGMENTS

A friend of mine in neutrino physics is fond of referring to non-physicists (most people, in other words) as "muggles". The joke, framing particle physicists in the role of wizards, I think is speaking to two truths. First, the muggles in *Harry Potter* invite us to wonder whether magic actually exists, and most people are just too unbothered to notice. On days when I'm able to look up from the drudgery of day-to-day research, I think this is exactly what particle physics is. Particle physics lets us peer directly into the fundamental Universe! And when we do, we find a world of magic: phantasmal neutrinos, promiscuous pions, stolid muons, anxious electrons, and the rest of the particle zoo. Of course, there is nothing wrong with being a muggle. And no one's life need be changed by learning about the Standard Model. But personally, I find that mine is fuller for it.

Second, like wizardry, particle physics is both a practice and a community. I'm most grateful for the opportunities during my doctorate that have enabled me to mature as a scientist. I owe those principally to the three overlapping communities I've been a part of: the University of Chicago, Fermilab, and the Short-Baseline Neutrino (SBN) Program.

My time at the University of Chicago has been spent in the neutrino research group. David Schmitz, the head of the group, has been a excellent mentor and advisor to me. I've learned a good deal from the generous way he treats people from a position of leadership. I've also learned a lot from the many people who have passed through the group during my time. First, Johnny, Will, Andy, and Joseph, who welcomed me in when I arrived at Chicago. Then Katrina, who momentarily was my only partner within the group. But then the group grew over the years: Elise, Lynn, Moon, and Yinrui. Then the Yaleies – Avinay, Angela, Matt, and Lee. And then last but not least, Thomas and Nate. Outside the group, there was also Mike, Rob, and Jonah, who I've been fortunate to call friends from the start. Getting to know each of you has made my time here worthwhile.

I spent my first summer of graduate school residing at Fermilab – by day climbing around

a mostly unsuccessful attempt at reanimating the ArgoNeuT detector, and by night cooking ramen in dorm three and drinking at the User's Center. I've met many wonderful people in my time so far at Fermilab, beginning that summer (Ron, Bill, Davio, Minerba, Gustavo, Linda, David) and continuing since then. I've found these people amongst both the backbone of scientists and staff who anchor the community (most especially Tania) and the milieu of students and postdocs plopped into exurban Illinois, looking for something to do. Scientifically, I am most indebted to the patience of the physicists on the twelfth floor of Wilson Hall – fortunately, none of my research output has yet driven any of them to self-harm, despite protestations otherwise. Of all of them, I would especially like to thank Minerba Betancourt, who believed in me earlier than was strictly reasonable, and Joseph Zennamo, who believed in me when I didn't.

Finally, SBN. When I started, SBN materially consisted of two buildings behind Wilson Hall. Now, those buildings house two detectors, one of which already can make measurements. It has been a joy to watch and take part in that transformation. Of the many people who mentored me on SBN, I would especially like to thank Mike Mooney. We spent two years locked together in a Zoom room, trying to figure out how to calibrate the ICARUS detector. After Dave, the work in this dissertation owes the most to Mike. Furthermore, this thesis includes material that will be published under the ICARUS collaboration. This material has already received feedback from members of the collaboration, and has benefited from that editing process.

One aspect of my time during my doctorate that will not be mentioned in this dissertation is SBN Young, which for me has been an attempt to add something to these overlapping communities. I'd like to give my thanks to everyone who created that organization with me – most especially Fernanda Psihas, who provided the spark for it. Putting my time into SBN Young has been worthwhile because of the many friendships I've been able to sustain within this community – in particular with Anna, Jamie, and Chris.

Finally, I'd like to thank all of my people outside work who supported and sustained me through these years. In particular my family, my parents Jon and Christin, my brothers Noah and Gideon, and my cousins, grandparents, aunts and uncles, who all now know that neutrinos are a type of particle, and that I'm not speaking in tongues. And, of course, Joan, my partner through all this time. Following you to Chicago is the best decision I've made. I'm so excited to keep building a life with you.

ABSTRACT

Many of the unexplained phenomena in particle physics and cosmology today, such as the microphysical nature of dark matter, the strong CP problem, and the origin of the neutrino masses, can be resolved by the existence of a light ($\sim$ GeV), weakly-coupled hidden sector of new physics. Such hidden sectors often predict the existence of "long-lived" particles (LLPs) that travel a far distance from production before decaying into Standard Model particles. Neutrino oscillation experiments, which combine intense particle beams with precise imaging detectors, are well equipped to probe LLP models with new sensitivity. This thesis details a search for a long-lived particle decaying to two muons with the ICARUS liquid argon time projection chamber (LArTPC) neutrino detector in the Short-Baseline Neutrino program at Fermilab. The calibration of the ICARUS time projection chamber (TPC) which enables the search is also presented. Notably, the calibration measures an angular dependence in electron-ion recombination in argon, a novel observation relevant for the detector physics of LArTPCs. The search is performed using data taken with the Neutrinos at the Main Injector (NuMI) beam, with an exposure of 2.41×10^{20} protons on target. No significant excess over background is observed, and we set world-leading limits on two new physics models that predict this process: the Higgs portal scalar and a heavy axion model. We also present the sensitivity in a model-independent way applicable to any new physics model predicting the process $K \to \pi + S(\to \mu\mu)$, for a long-lived particle S.

CHAPTER 1

NEUTRINO OSCILLATIONS AND THE INTENSITY FRONTIER

Neutrinos are the particle of big numbers. Amongst the zoo of fundamental particles uncovered in the last century and a quarter since J.J. Thompson's 1897 discovery of the electron, the neutrino stands out for its ubiquity in nature and distance in scale from everyday matter. About 100 trillion neutrinos travel through our bodies each second, originating from a variety of sources natural and man-made. Among these are counted: the sun, nuclear reactors, the earth's crust, bananas, and notably, outside Chicago, from acccelerator beams. These large fluxes pass us by without notice due to the large distances a neutrino will travel before interacting. A neutrino from a nuclear recator would travel through about 200 trillion miles (30 light years) of water, on averge, before interacting. This extremely small interaction strength led the scientist who originally suggested its existence, Wolfgang Pauli, to believe it would never be detected [1].

The neutrino was detected, twenty-six years after its postulation, in 1956 by Clyde Cowan and Fred Reines from a nuclear reactor source [2]. Today, a myriad number of neutrino sources and detectors are paired to perform experiments studying the particle. Many of these are directed towards studying the astounding property of neutrino oscillation: there are three types, or "flavors" of neutrino, and left alone a neutrino particle will swing back and forth between all three. Neutrino oscillation experiments require intense fluxes of neutrinos to impinge on large, sensitive detectors. They therefore offer the opportunity to search for new particles that would be as weakly coupled to normal matter as neutrinos are, or even moreso. Such particles could explain some of the outstanding problems in particle physics today, such as the microphysical nature of dark matter.

1.1 Neutrino Oscillations

Neutrinos oscillate because they have mass, and their mass eigenstates differ from the flavor eigenstates. These two bases can be related by a unitary matrix U

$$|\nu_\alpha\rangle = \sum_i U_{\alpha i} |\nu_i\rangle \ , \tag{1.1}$$

where $\alpha \in e, \mu, \tau$ indexes the flavor states, $i \in 1, 2, 3$ indexes the mass state, and U is the Pontecorvo–Maki–Nakagawa–Sakata (PMNS) matrix [3, 4, 5, 6]. Neutrinos are produced in the weak interaction in a flavor eigenstate $|\nu_\alpha\rangle$, which is a combination of mass eigenstates given by equation 1.1. As the neutrino travels with 4-momentum p_μ a 4-length x^μ, each mass eigenstate picks up a separate phase proportional to: $p_\mu x^\mu = Et - \vec{p}\cdot\vec{x} \approx (p + m^2/2p)L - pL = Lm^2/2p \approx Lm^2/2E$ (in units where $\hbar = c = 1$). The approximation is made that the neutrino is nearly massless and travelling nearly at the speed of light. Thus after travelling a distance L, a neutrino in an initial flavor eigenstate $|\nu_\alpha\rangle$ will have oscillated into a state given by

$$|\nu(L)\rangle = \sum_j e^{-iLm_j^2/2E} U^*_{\alpha j} |\nu_\alpha\rangle \ . \tag{1.2}$$

When it is detected, it is projected into a flavor state β. The oscillation probability from the state $\alpha \to \beta$ is

$$P_{\alpha\to\beta} = \left|\langle\nu(L)|\nu_\beta\rangle\right|^2 = \left|\sum_j U^*_{\alpha j} U_{\beta j} e^{-iLm_j^2/2E}\right|^2 \ . \tag{1.3}$$

In the simple case where there are only two oscillating states with flavors (α, β) and masses m_1, m_2, the neutrino oscillation is described by the disappearance probability $P_{\alpha\to\alpha}$ and the appearance probability $P_{\alpha\to\beta} = 1 - P_{\alpha\to\alpha}$. In this limit, the PMNS matrix is described by

a single mixing angle θ

$$U = \begin{bmatrix} \cos\theta & -\sin\theta \\ \sin\theta & \cos\theta \end{bmatrix} . \tag{1.4}$$

The appearance probability is (adding in numerical factors)

$$P_{\alpha\to\beta} = \sin^2(2\theta)\sin^2\left(1.27\frac{\Delta m^2}{\mathrm{eV}^2}\frac{L}{\mathrm{km}}\frac{\mathrm{GeV}}{E}\right) . \tag{1.5}$$

Thus, in the two neutrino case, there are two measurable parameters: the mass difference $\Delta m^2 (\equiv m_1^2 - m_2^2)$, and the mixing angle θ. The mixing angle controls the amplitude of the oscillation, while the mass difference determines its frequency. In the three neutrino case, there are three mass differences and three mixing angles; one for each pair of neutrinos. Furthermore, when there are three neutrinos the PMNS matrix also has an additional complex phase δ_{CP}. This phase, if non-zero, would violate charge-parity (CP) symmetry: it would cause neutrinos to oscillate in a different pattern than their anti-particle (anti-neutrino) counterparts.

1.2 Neutrino Oscillation Experiments

The imprint of neutrino oscillation was first observed in the Homestake experiment pioneered by Raymond Davis which detected, for the first time, the flux of neutrinos from the sun [7]. Collecting data over many decades, it observed a long running deficit of the expected number of neutrinos by about two thirds. We now know that this is because the flux of solar neutrinos, which when produced is entirely in the electron (e) flavor state, had partially oscillated into the other two flavors muon (μ) and tau (τ). The detector was only sensitive to the electron flavor component of the flux.

In the 1990s, new experiments collected increasingly convincing data supporting the neutrino oscillation picture. The SNO experiment measured separately both the electron

and total component of the solar neutrino flux. The electron component confirmed the results of the Homestake experiment, while the total flux matched the expectation of the rate from the sun [8, 9]. Alongside this evidence, the Super-Kamiokande experiment observed the oscillation of neutrinos produced in the atmosphere as they travelled through the earth [10]. The two experiments were together awarded the 2015 Nobel prize in physics for these discoveries.

Further experiments have solidified this picture using artificial neutrino sources. Neutrinos can be produced in particle accelerators. In the "super-beam" technology, an intense proton beam is directed to a fixed target. In the spray of produced particles, pions and kaons decay to neutrinos which constitute the beam. Experiments using these sources are built with a "near" detector, which is situated close to the source and measures the rate before oscillation, and a "far" detector which measures the oscillated rate. This experimental design has been employed with accelerator neutrino sources (such as by MINOS [11], T2K [12], and NOvA [13]), as well nuclear reactor neutrino sources, to provide precise precise measurements of neutrino oscillations which established the three neutrino, PMNS picture. The mixing angles between the three flavor eigenstates are [14] (rounded to the nearest degree)

$$\begin{aligned} \theta_{12} &\sim 33^\circ \\ \theta_{23} &\sim 49^\circ \\ \theta_{13} &\sim 9^\circ \,. \end{aligned} \tag{1.6}$$

The mixing angles are large and produce significant oscillation effects. They are much larger than the equivalent mixing angles in the quark sector, which could be a clue of the fields which give the neutrinos their mass [15]. The mass differences between the three mass

eigenstates are [14] (rounded to two significant figures)

$$\begin{aligned} \Delta m^2_{21} &\sim 7.4 \times 10^{-5} \text{eV}^2 \\ |\Delta m^2_{31}| \approx |\Delta m^2_{32}| &\sim 2.5 \times 10^{-3} \text{eV}^2 \,. \end{aligned} \tag{1.7}$$

The signs of Δm^2_{31} and Δm^2_{32} are not known. For a 1 GeV neutrino, typical of the energy of neutrinos in accelerator sources, the atmospheric mass splitting ($\Delta m^2_{31}, \Delta m^2_{32}$) drives an oscillation that reaches its maximum (i.e. its quarter cycle) at a baseline of 500 km, while the solar mass splitting (Δm^2_{21}) oscillation does so at a baseline of 16 000 km.

1.3 Experimental Questions in Neutrino Oscillations

There are a couple open questions left to resolve in the neutrino oscillation picture. First, the CP-violating phase of the PMNS matrix has not been measured. The most recent measurements from T2K and NOvA allow any value at the 3σ confidence level [14, 16, 17]. The neutrino mass hierarchy, as determined by the sign of Δm^2_{31} and Δm^2_{32}, is also not known. Finally, the three neutrino oscillation picture does not accommodate the results of all neutrino experiments. A series of "short-baseline anomaly" measurements have found results in tension with the three neutrino picture. These anomalies have found results indicative of neutrino oscillations on a shorter baseline than what the three neutrino picture allows: $\sim 0.1{-}1$ km, for a 1 GeV neutrino. An oscillation explanation for the anomalies therefore would require a new oscillation period from an additional mass difference, and thus a fourth neutrino state. The number of active (weakly-interacting) neutrinos is fixed very precisely to three by the measurements of (e.g.) the Z boson width [18, 19], so this new neutrino state would have to be sterile: not participating in the weak interaction. It would therefore only be observable through its mixing with the active neutrino states.

The state of the short-baseline anomalies presents an evolving and muddled picture.

Significant anomalies have been observed across a variety of neutrino sources such as accelerators [20, 21], radioactive nuclei [22, 23, 24], and nuclear reactors [25]. These anomalies stand alongside other searches for short baseline oscillations that have found null results [26, 27, 28], often in tension with the anomalies [29]. The anomalous results almost all rely on an estimation of the neutrino interaction rate without the presence of a near-er detector to calibrate the unoscillated rate. This estimation is a challenging exercise that is fraught with possibility for experimenter error. Indeed, in the case of the reactor neutrino anomaly, recent results have indicated such a mis-estimation of the expected rate was in fact the cause [30, 31]. However, in the case of the radioactive nuclei sources, the anomaly has persisted and strengthened with the results of the BEST experiment [24]. In the accelerator case, the MicroBooNE experiment has found a null result [32] which is still limited in statistical power compared to the size of the anomalies [33]. In a different vein, IceCube has performed a search with high energy atmospheric neutrinos, which puts limits on some areas of the parameter space but also finds its own (weak) anomaly, at the 90% CL [34].

There is today an ongoing, international program of neutrino experiments dedicated to resolving these open questions. The long-baseline experiments T2HK in Japan [35] and DUNE in the United States [36] will in the coming decades measure δ_{CP} with unprecedented sensitivity and determine the neutrino mass ordering. Operating now, the Short-Baseline Neutrino (SBN) program at Fermilab [37, 38] will probe the short-baseline anomaly with an accelerator source. The program consists of the Short-Baseline Near Detector (SBND) and the ICARUS far detector. The two detectors are placed at baselines necessary to do a near-far oscillation search specifically for a short baseline oscillation. This thesis is the first particle physics result to come out of the SBN program. It, however, does not address the question of the short-baseline anomalies. Instead, it is a search for a different sort of new physics that could also be visible at SBN.

1.4 Searching for a Hidden Sector at the Short-Baseline Neutrino Program

The set of particles we have discovered between the 1897 discovery of the electron and the 2012 discovery of the Higgs boson, as organized into the Standard Model of particle physics, remains incomplete. There are a number of phenomena for which they do not account. One of those is neutrino mass, its existence as indicated by neutrino oscillations. Neutrinos do not necessarily obtain their mass from the Higgs field as do the other Standard Model particles, and so there may be a new field which endows the particles with mass. In addition, the existence of a neutrino mass requires that there be sterile, right-handed neutrino states in addition to the active neutrinos of the Standard Model. The short-baseline anomalies are a hint at a 1 eV sterile neutrino, but the new states could arise at any mass. In particular, the type-I see-saw mechanism indicates the possibility of a sterile neutrino with a mass $\sim$1 GeV and a mixing with active neutrinos $\sim 10^{-10}$ [39] (such a particle would by itself be in tension with cosmological measurements of big bang nucleosynthesis [40]; these can be avoided with the introduction of additional fields [41]). Such a sterile neutrino would be an example of a "hidden sector" of new physics.

Sterile neutrinos are just one example of a possible hidden sector. Many of the unexplained phenomena in particle physics and cosmology today, such as the microphysical nature of dark matter and the strong CP problem, in addition to the origin of the neutrino masses, can be resolved by the existence of a light ($\sim$ GeV), weekly-coupled hidden sector of new physics [42, 43, 44, 45]. Such hidden sectors often predict the existence of "long-lived" particles (LLPs) which can be produced in intense particle beams and travel a far distance before decaying into Standard Model particles. As will be described in detail in chapter 3, the SBN program relies on sensitive liquid argon time projection chamber (LArTPC) detectors placed in intense "super-beams" of neutrinos. This is the same combination of technologies that will be applied in the long-baseline DUNE experiment in the coming decades. This combination

enables sensitivity to a wide variety of LLP models [46, 47, 48, 49, 50, 51].

This thesis presents a search for a physics process that would be induced by LLPs: kaon decay to a scalar LLP which decays to two muons. As is discussed in chapter 2, this process is sensitive to a number of hidden sector models. The search is performed with the ICARUS detector in the SBN program, which is introduced in chapter 3. This thesis also includes the calibration and preparation of the ICARUS dataset necessary to perform the LLP search. First, the application of the main source for these calibrations, cosmic muons, are reviewed in chapter 4. This chapter includes the description of a new effect noted by the author important for calibrating muon energy loss. The calibration of the ICARUS detector is covered in chapters 5 and 6. Novel calibration techniques and a new effect of highly ionizing particles in argon are noted. The results of the calibration are applied in an event selection for di-muon LLPs, which is introduced in chapter 7. This event selection identifies di-muon decays against backgrounds, which originate from neutrino interactions in ICARUS. The event selection is validated in sideband samples, as covered in chapter 8. Systematic uncertainties arise in the event selection from predictions of the neutrino background and scalar signal rates. These are detailed in chapter 9, alongside the statistical procedure used to identify any new physics signal and exclude LLP parameter space. Finally, the result of the analysis is shown in chapter 10. Chapter 11 concludes the thesis.

The headline result of this thesis is the search for new physics in kaon induced LLPs. The studies presented here also reach beyond just this core result. The calibration of the ICARUS data which enables the search will also be used in the broader program of particle physics performed by the detector. In particular, with the start of operation of the Short-Baseline Near Detector (SBND), data from the two detectors can be combined to perform the SBN search for short-baseline oscillations. The calibration of ICARUS includes new techniques and describes novel phenomena in the detector physics of liquid argon time projection chambers. This detector technology will also underlie future neutrino experiments such as

DUNE, and thus the techniques we develop can be applied there. In addition, searching for hidden portals at neutrino experiments is a recent phenomenon. The statistical methods we apply in the LLP search include techniques novel, to our knowledge, in their application at neutrino experiments (though they are well-trodden ideas for collider experiments). Future neutrino experiments, such as DUNE, will be able to probe hidden sector physics with an even greater sensitivity. The techniques that we explore and apply at SBN an be useful for those future searches.

CHAPTER 2

HIDDEN SECTOR MODELS FOR LONG-LIVED DI-MUON RESONANCES IN KAON DECAY

In this chapter, we develop two hidden sector models that contain a new scalar particle that would be produced in kaon decay and decay to two muons: the Higgs Portal Scalar (HPS) [47], and axion-like particle (ALP) decay [48, 52, 53]. These are introduced in sections 2.1 and 2.2 respectively.

The range of new physics models that can be probed at beam dump and neutrino experiments is an active area of research. Accordingly, we orient this search in a model-independent way, sensitive to any new physics model that predicts a rate for the process $K \to \pi + S(\to \mu\mu)$, for some long-lived particle S [54]. Section 2.3 discusses this general scenario.

2.1 Higgs Portal Scalar

In the Higgs Portal Scalar (HPS) model, a new scalar particle is introduced with couplings to the Standard Model through a small mixing with the Standard Model Higgs Boson. This mixing endows the scalar with couplings to all Standard Model particles proportional to their Yukawa coupling. Such a scalar is a candidate for a mediator between the Standard Model and a dark matter particle [55]. The existence of an additional mediator depletes the population of dark matter in the early universe, which avoids the issue of thermal over-production of dark matter in the case that the dark matter particle is light ($\lesssim$2 GeV) [56]. Below, we detail the HPS model and its associated branching ratio and decay widths. These are also plotted in figure 2.1.

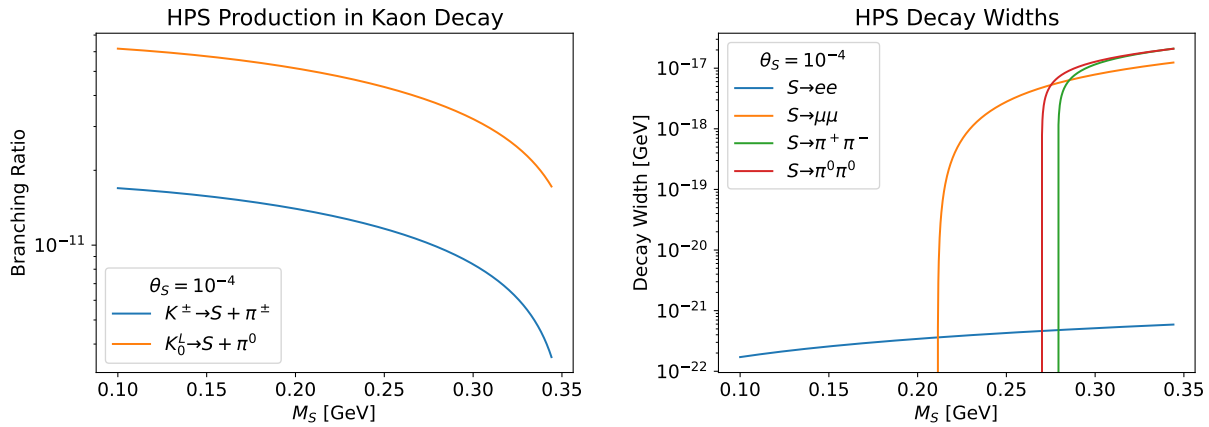

Figure 2.1: (Left) Branching ratio for HPS production in kaon decay. (Right) Widths for HPS decays.

The Lagrangian for this model is [47]

$$\mathcal{L} \supset -\frac{1}{2} m_s^2 S^2 + \sin\theta \; S^2 \left(\frac{2m_W^2}{v} W_\mu^+ W^{\mu\,+} + \frac{m_Z^2}{v} Z_\mu Z^\mu - \sum_f \frac{m_f}{v} \bar{f} f \right) , \tag{2.1}$$

where S is the scalar field with mass m_S and mixing θ, v is the Higgs vacuum expectation value, W_μ^+ is the W boson, Z is the Z boson, and f indexes the Standard Model fermions.

In the NuMI beam, the HPS would be produced in the decays of charged and long kaons. The decay width to the scalar is given by [47]

$$\begin{aligned} \Gamma\left(K^\pm \to S + \pi^\pm\right) &= \frac{\theta^2}{16\pi m_{K^\pm}} \left| \frac{3 V_{td}^* V_{ts} m_t^2 m_{K^\pm}^2}{32\pi^2 v^3} \right|^2 \sqrt{\lambda\left(1, \frac{m_S^2}{m_{K^\pm}^2}, \frac{m_{\pi^\pm}^2}{m_{K^\pm}^2}\right)} \\ \Gamma\left(K^L \to S + \pi^\pm\right) &= \frac{\theta^2}{16\pi m_{K^\pm}} \mathrm{Re}\left(\frac{3 V_{td}^* V_{ts} m_t^2 m_{K^\pm}^2}{32\pi^2 v^3} \right)^2 \sqrt{\lambda\left(1, \frac{m_S^2}{m_{K^\pm}^2}, \frac{m_{\pi^\pm}^2}{m_{K^\pm}^2}\right)} , \end{aligned} \tag{2.2}$$

where V is the CKM matrix and λ is the Kallen function ($\lambda(a,b,c) = (a^2 + b^2 + c^2 - 2ab - 2bc - 2ac)$). The decay proceeds through a penguin diagram, as shown in figure 2.2. The top quark loop dominates the rate due to its large Yukawa coupling to the Higgs. The branching ratio of decay is given by $\mathrm{BR} = \tau_{\mathrm{SM}} \Gamma$, where τ_{SM} is the Standard Model lifetime of the kaon

(either charged or long).

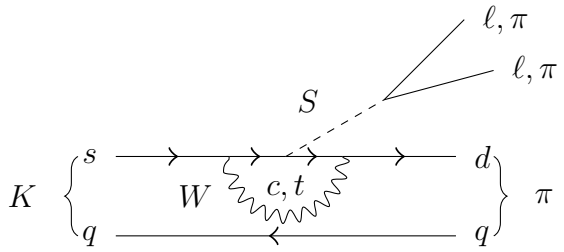

Figure 2.2: Feynman diagram for production of Higgs portal scalar events in kaon decay, from Ref. [47]. The top quark loop dominates the decay amplitude.

Scalars decay predominantly into pairs of electrons, muons, and pions in the mass region relevant at ICARUS. The decay width to leptons is given by ($\ell = e, \mu$)

$$\Gamma(S \to \ell^+\ell^-) = \theta^2 \frac{m_\ell^2 m_S}{8\pi v^2} \left(1 - \frac{4m_\ell^2}{m_S^2}\right)^{3/2} . \tag{2.3}$$

The decay width to pions (either charged, $\pi^+\pi^-$, or neutral, $\pi^0\pi^0$) is given by

$$\Gamma\left(S \to \pi\pi\right) = \theta^2 \frac{3|G_\pi(m_S^2)|^2}{32\pi v^2 m_S} \left(1 - \frac{4m_\pi^2}{m_S^2}\right)^{1/2} , \tag{2.4}$$

where G_π is a form factor. Below the QCD scale (relevant at ICARUS), it is fixed to $G_\pi(s) = \frac{2}{9}s + \frac{11}{9}m_\pi^2$. Above the kaon mass, decays to other hadronic final states, including strange and charm mesons, become available [57, 58]. However, these are not relevant for this analysis.

2.2 Axion-Like Particles and the Strong CP Problem

Axion-like particles (ALPs) arise as Goldstone bosons in any theory with a Peccei-Quinn symmetry, a spontaneously broken global symmetry that is anomalous with respect to the Standard Model gauge interactions [59, 60, 61]. In the case that the axion couples to gluons,

it would resolve the strong CP problem [59, 62]: the observation that the continued non-observation of any neutron electron dipole moment [63, 64] requires that the relevant CP-violating QCD parameter governing its size be un-naturally small [65]. This special case is called the "QCD axion". The minimal realization of this phenomena (by the Peccei-Quinn mechanism) leads to a light axion with a large decay constant, related by $m_a \simeq 5.7\,\text{meV} \times (10^9\text{GeV} \;/\; f_a)$. In such a model, the axion field receives large corrections from gravity, an issue known as the quality problem [66, 67, 68]. Alternative realizations of the axion can resolve the strong CP problem with a heavier axion particle ($M \sim$GeV) and a UV completion that is less susceptible to corrections from gravity [69]. The model we detail in this section is an example of such a "heavy" axion model, or axion-like particle (ALP).

The effective Lagrangian for the ALP, after spontaneous symmetry breaking, is given by [48]

$$\mathcal{L} \supset c_3 \frac{\alpha_S}{8\pi f_a} a G\tilde{G} + c_2 \frac{\alpha_2}{8\pi f_a} a W\tilde{W} + c_1 \frac{\alpha_1}{8\pi f_a} a B\tilde{B} + \sum_f c_f \frac{\partial_\mu a}{2 f_a} \bar{f}\gamma^\mu\gamma_5 f, \tag{2.5}$$

where a is the axion field with mass m_a and decay constant f_a, α_S is the strong coupling, $\alpha_2 = \alpha/\sin^2\theta_W$ the is $SU(2)_L$ coupling (α is the fine structure constant), $\alpha_1 = \alpha/\cos^2\theta_W$ is the $U(1)$ hypercharge coupling, γ^μ and γ_5 are the gamma matrices, G is the gluon field coupled to the axion by c_3, W is the $SU(2)_L$ doublet coupled to the axion by c_2, B is the $SU(1)$ field coupled to the axion by c_1, and f indexes the Standard Model fermions, each with an individual coupling c_f to the axion. We consider a case where only the muon coupling c_μ is non-zero. This generates a decay of axions to two muons. In this chapter, we consider three scenarios for the gauge boson couplings: gluon dominance ($c_3 = 1$, $c_2 = c_1 = 0$), weak dominance ($c_2 = 1$, $c_3 = c_1 = 0$), and co-dominance ($c_3 = c_2 = c_1$).

The coupling of axions to gluons in the mass regime relevant at ICARUS ($m_a \sim$100 MeV) is challenging to compute because it is close to the QCD scale. This is an active area of research with ongoing refinement. We detail below the latest understanding of the gluonic (section 2.2.1) and weak (section 2.2.2) production of axions in kaon decay, as well as the

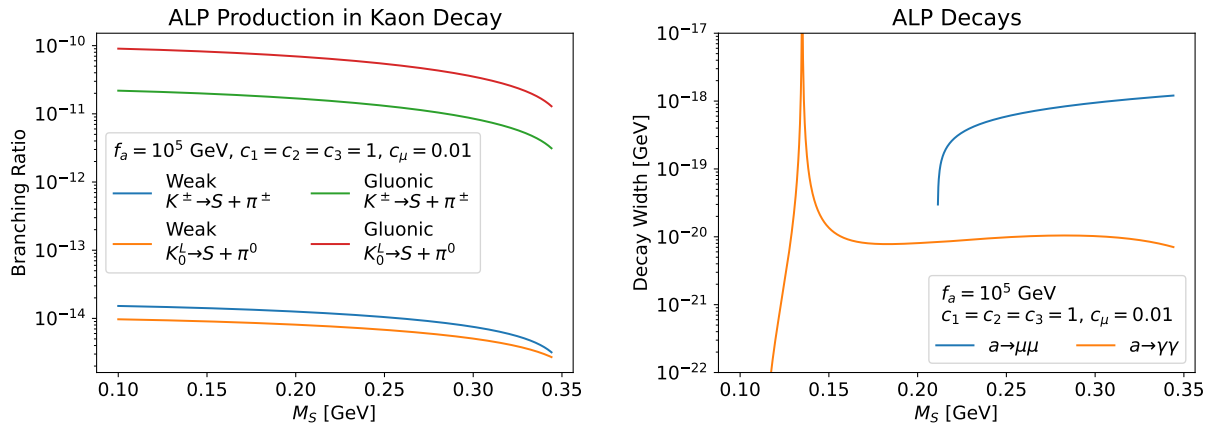

Figure 2.3: (Left) Branching ratio for ALP production in kaon decay. (Right) Widths for ALP decays. The ALP production is shown for the co-dominance case. In the situation of gluonic (weak) dominance, only the gluonic (weak) decay mode is present.

decays of the axion into Standard Model particles (section 2.2.3). The production rates and decay widths are also plotted in figure 2.3.

2.2.1 Gluonic Production in Kaon Decay

Prior studies of the sensitivity of neutrino experiments to gluonic axion like particles have focused on the role of mixing with psuedoscalar mesons (π^0, η, η') [48, 50, 70, 71]. In this case, axions are produced in primary $p - C$ interactions that produce a psuedoscalar meson that transmutes to an outgoing axion through mixing. The rate of this process is proportional to the axion-psudoescalar (P) mixing $|\theta_{aP}|^2$. In the case of the π^0, $\theta_{a\pi} = \frac{1}{6}\frac{f_\pi}{f_a}\frac{m_s^2}{m_a^2 - m_\pi^2}$. The thinking goes that the production of axion production in kaon decay, mixing with the outgoing π^0 also governs the rate. In this case, the production would also be proportional to $|\theta_{a\pi}|^2$. Since there are more pions produced in primary $p - C$ interactions then there are kaons, the psuedoscalar mixing dominates the rate.

However, a recent re-analysis of axion production in kaon decay has demonstrated that this assumption does not hold. Rather, the $K^+ \to a + \pi^+$ decay is dominated by a different set of operators (with a larger coupling) than that of $K^+ \to \pi^0 + \pi^+$ [72], an effect known

as octet enhancement [73]. In particular, this makes kaon decay the dominant production process for axions below the kaon decay mass threshold ($m_a < m_K - m_\pi$). This enhancement is responsible for the significant sensitivity of this search to gluonic coupled axions.

The decay amplitude $\mathcal{A}\left(K^\pm \to a + \pi^\pm\right)$ in chiral perturbation theory is given by [72, 74]

$$\begin{aligned} i\mathcal{A}\left(K^\pm \to a + \pi^\pm\right) =& -2\frac{N_8}{f_a} c_3 \frac{(m_K^2 - m_\pi^2)(m_K^2 - m_a^2)}{4m_K^2 - m_\pi^2 - 3m_a^2} \\ i\mathcal{A}\left(K_0^L \to a + \pi^\pm\right) =& -i\mathcal{A}\left(K^\pm \to a + \pi^\pm\right) , \end{aligned} \tag{2.6}$$

where $N_8 = -\frac{G_F}{\sqrt{2}} V_{ud}^* V_{us} g_8 f_\pi^2$ comes from the weak chiral Lagrangian.[1] It can be related to short kaon decay by [75, 76]

$$\Gamma\left(K_S^0 \to \pi^+\pi^-\right) = \frac{N_8^2}{8\pi f_\pi^2} \frac{\left(m_K^2 - m_\pi^2\right)^2}{m_K^2} \sqrt{m_K^2 - 4m_\pi^2} \, . \tag{2.7}$$

We use the convention that the pion decay constant $f_\pi \approx 130\,\text{MeV}$. The decay width $\Gamma = \frac{|\mathcal{A}|^2}{8\pi} \frac{\sqrt{\lambda(1, m_a^2/m_K^2, m_\pi^2/m_K^2)}}{2m_K}$ is then equal to

$$\begin{aligned} \Gamma\left(K^\pm \to a + \pi^\pm\right) =& \Gamma\left(K_S^0 \to \pi^+\pi^-\right) \frac{2f_\pi^2 c_3^2}{f_a^2} \left(\frac{m_K^2 - m_a^2}{4m_K^2 - 3m_a^2 - m_\pi^2}\right)^2 \sqrt{\frac{\lambda(1, m_\pi^2/m_K^2, m_a^2/m_K^2)}{1 - 4m_\pi^2/m_K^2}} \\ \Gamma\left(K^L \to a + \pi^\pm\right) =& \Gamma\left(K^\pm \to a + \pi^\pm\right) . \end{aligned} \tag{2.8}$$

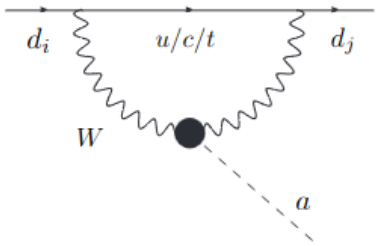

Figure 2.4: Feynman diagram for weak decay of kaons to axions through a penguin, from Ref. [77].

2.2.2 Weak Production in Kaon Decay

The decay proceeds through a penguin diagram, as shown in figure 2.4. The decay widths are [77]

$$\begin{aligned}\Gamma\left(K^{\pm}\to a+\pi^{\pm}\right) =& \frac{m_K^3}{64\pi}\left(1-\frac{m_\pi^2}{m_K^2}\right)^2 |g_{asd}|^2\sqrt{\lambda(1,m_\pi^2/m_K^2,m_a^2/m_K^2)}\\ \Gamma\left(K_0^L\to a+\pi^0\right) =& \frac{m_K^3}{64\pi}\left(1-\frac{m_\pi^2}{m_K^2}\right)^2 \mathrm{Im}(g_{asd})^2\sqrt{\lambda(1,m_\pi^2/m_K^2,m_a^2/m_K^2)}\,,\end{aligned} \tag{2.9}$$

where $g_{asd} = -\frac{3\sqrt{2}G_F M_W^2 c_2\alpha_2}{32\pi^3 f_a}\sum_{\alpha\in c,t} V_{\alpha s}V_{\alpha d}^* f(m_\alpha^2/m_W^2)$ and $f(x)\equiv\frac{x[1+x(\log x-1)]}{(1-x)^2}$[2]. In the co-dominance case, the gluonic decay dominates over the weak decay by many orders of magnitude. However, in the weak-dominance case, the Weak decay would be the only available channel for axion production in kaon decay.

2.2.3 Decays

The decay width to two photons is given by [48, 78]

$$\Gamma_{a\to\gamma\gamma} = \frac{\alpha^2|c_\gamma|^2 m_a^3}{256\pi^3 f_a^2}\,, \tag{2.10}$$

1. There is also a contribution to the amplitude from 27-plet operators in the chiral Lagrangian, which we neglect because it is small.

2. In the notation of Ref. [77], their g_{aW} is equal to our $c_2\alpha_2/2\pi f_a$

where α is the fine structure constant and c_γ is the axion coupling to photons, which gains contributions from all axion couplings once loop diagrams are included:

$$c_\gamma = c_3 \left(-1.93 + \frac{1}{3}\frac{m_a^2}{m_a^2 - m_\pi^2} + \frac{8}{9}\frac{m_a^2 - 4m_\pi^2/9}{m_a^2 - m_\eta^2} + \frac{7}{9}\frac{m_a^2 - 16m_\pi^2/9}{m_a^2 - m_{\eta'}^2} \right) + \frac{5}{3}c_1 + c_2 + c_\mu B(4m_\mu^2/m_a^2)\,, \tag{2.11}$$

where $B(x) = 1 - xf(x)^2$ and

$$f(x) = \begin{cases} \sin^{-1}\left(\frac{1}{\sqrt{x}}\right) & \text{if } x \geq 1 \\ \frac{\pi}{2} + \frac{i}{2}\log\left(\frac{1+\sqrt{1-x}}{1-\sqrt{1-x}}\right) & \text{if } x < 1\,. \end{cases} \tag{2.12}$$

The decay width to two leptons with coupling c_ℓ to first order is given by

$$\Gamma_{a\to\ell\ell} = \frac{c_\ell^2 m_a m_\ell^2}{8\pi f_a^2}\sqrt{1 - \frac{4m_\ell^2}{m_a^2}} \tag{2.13}$$

There is also a $\gamma\gamma\pi$ decay kinematically available to the axion in the mass regime [78]. However, it is not significant for $m_a \lesssim 0.4\,\text{GeV}$.

2.3 General Case

The two models we have enumerated, Higgs Portal Scalars and Axion-Like Particles, are two cases of the general process we are sensitive to: $K \to \pi + S(\to \mu\mu)$. This process is specified by three numbers: the (psuedo-)scalar mass M_S, the branching ratio ($\text{BR}(K \to \pi + S) \times \text{BR}(S \to \mu\mu)$), and the (psuedo-)scalar lifetime τ_S. Physics models for this process (such as HPS and ALP) specify the branching ratio and the lifetime given some coupling(s). This picture is complicated somewhat by the fact that these new particles are produced in both $K^\pm$ and K_L decays, at different relative rates depending on the model. This is studied in appendix B, which demonstrates that we can set the sensitivity on a suitable linear combination of the branching ratio of the two kaon decays.

CHAPTER 3

THE ICARUS DETECTOR IN THE SHORT-BASELINE NEUTRINO PROGRAM

ICARUS is a liquid argon time production chamber (LArTPC) neutrino detector currently taking data as part of the Short-Baseline Neutrino Program [37, 38]. The detector was installed at Fermilab in 2020 after a previous run at Gran Sasso [79] and subsequent refurbishment [80]. Images of the installation of the ICARUS detector are shown in figure 3.1. ICARUS sits at the intersection of two neutrino beams: it is on-axis to the Booster Neutrino Beam (BNB) [81] and is 5.7° off-axis to the Neutrinos at the Main Injector (NuMI) beam [82]. This thesis uses data from ICARUS physics data taking runs 1 and 2, which spanned from June 2022 to July 2023.

Neutrinos are detected in ICARUS through their interactions with argon nuclei in the detector bulk. Charged particles produced in these neutrino interactions propogate through the detector and ionize electrons from argon atoms. The ionization electrons are used to image the charged particle trajectories with high spatial resolution and precise calorimetry. The electrons are drifted by a large electric field to to multiple planes of readout wires which detect the charge. A diagram of this detection scheme for neutrino interactions is shown in figure 3.2. Example images of two candidate neutrino events in ICARUS are shown in figure 3.3.

The same production and detection scheme for neutrinos also enables the detection of possible long-lived particles (LLPs). In the NuMI beam, LLPs can be produced in kaon decay [47, 52, 53]. The produced particles would travel a distance from the NuMI beam to the ICARUS detector, where they would decay into Standard Model particles. These particles would be imaged by the ICARUS LArTPC as in the case of neutrino interactions. Figure 3.4 displays a schematic of the detection scheme. An event display of a simulated di-muon decay from an LLP in ICARUS is shown in figure 3.5.

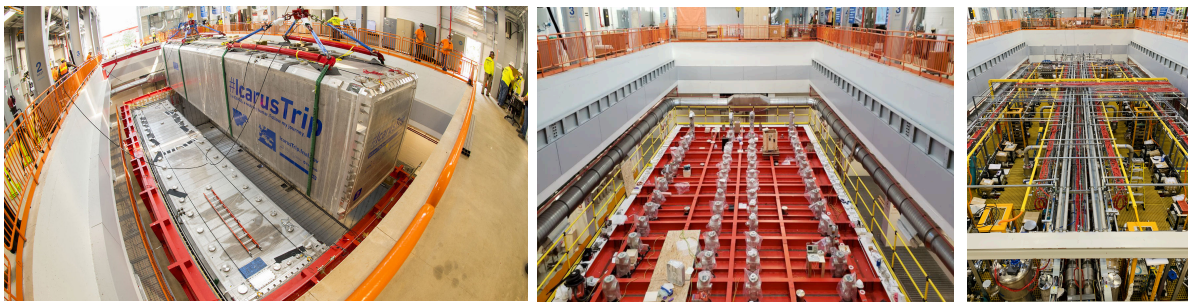

Figure 3.1: Images of the installation of the ICARUS detector. Taken from Ref. [83].

ICARUS consists of 760 t of liquid argon in two modules. Both modules are a cryostat with dimensions $3.6 \times 3.9 \times 19.6\,\mathrm{m}^3$. Both cryostats contain two TPCs divided by a central cathode plane. The TPCs are all operated at a drift voltage of about $500\,\mathrm{V\,cm}^{-1}$. They all have three planes of charge sensing wires: an unshielded front induction plane, a middle induction plane, and a collection plane. The wires on the front induction plane are oriented along the horizontal (beam) direction, and the wires on the middle induction and collection plane are oriented at $\pm 60^\circ$ to the horizontal direction, depending on the TPC. The wires on each plane are each spaced 3 mm apart and the wire planes are spaced 3 mm from each other. In the nominal configuration, the wire bias is $-250\,\mathrm{V}$ on the front induction plane, $-30\,\mathrm{V}$ on the middle induction plane, and $250\,\mathrm{V}$ on the collection plane. A diagram of the layout of the four ICARUS TPCs is shown in figure 3.6.

Each TPC wire is instrumented to digitize the collected and induced charge signals with minimal noise [85]. Signals are run through an offline signal processing chain which subtracts noise that is coherent across wires in the same readout board and deconvolves the signal to provide a Gaussian shape with further reduced noise [83]. These signals provide the input to reconstruction algorithms which group together hits into tracks (from muons, protons, or other charged hadrons) and electromagnetic showers (from electrons or photons) and form three-dimensional particle trajectories. The reconstruction applied for this thesis is supplied by the Pandora framework [86, 87], optimized for the ICARUS detector. The charge loss per length (dQ/dx) along 3D trajectories can be computed after calibrating the detector response

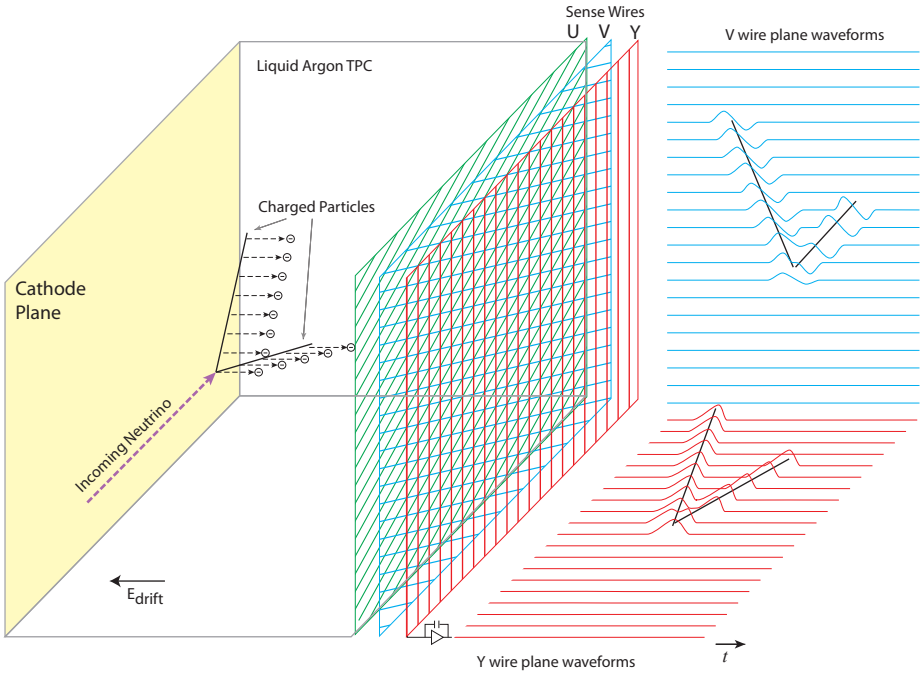

Figure 3.2: Diagram of the liquid argon time projection chamber (LArTPC) concept for neutrino detection, from Ref. [84]. Neutrinos interact in the bulk argon and produce charged particles. These charged particles traverse the argon and ionize electrons from argon atoms. The ionization electrons are drifted by a large electric field to a set of multiple charge sensing wire planes. The wire planes measure multiple two-dimensional views of the charge, which can be combined to reconstruct the three-dimensional trajectory of each charged particle.

to charge (see chapter 5). The charge loss is turned into an energy loss (dE/dx) using a measurement of recombination (see chapter 6). The energy loss, along with topological features of the particle trajectory, are used to determine the particle type and energy for phyics analysis.

In addition to the TPC, ICARUS is also augmented by two other detection subsystems: an array of photo-multiplier tubes (PMTs) inside the argon and a set of scintillator pads forming a cosmic ray tracker (CRT) outside the cryostat. Inside each ICARUS TPC, there are 90 8" Hamamatsu P5912-MOD PMTs arrayed behind the wire planes. The PMTs detect scintillation photons produced by charged particles as they traverse the bulk argon. The

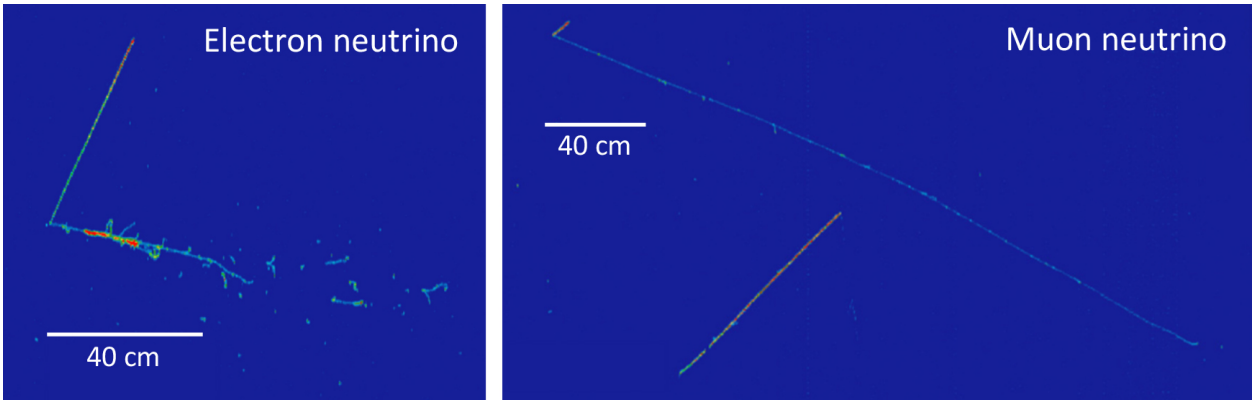

Figure 3.3: Candidate neutrino events in the ICARUS liquid argon time projection chamber. The event displays show the two-dimmensional projection of particle trajectories as observed by one plane (the collection plane) of charge-sensing wires. The horizontal direction shows the axis perpindicular to the wire plane direction, while the vertical direction shows the drift (time) direction. The magnitude of collected charge is shown in a color scale from blue (no charge), to green, yellow, and red (more charge). In the electron neutrino interaction on the left, two particles are detected: an electron which produces a diffuse shower of ionization charge (bottom), and a proton which leaves a straight, highly-ionized track of ionization (top). In the muon neutino interation on the right, a muon and proton are detected. The muon track leaves a long, windy, minimum-ionizing track. The proton produces a short, straight, highly-ionized track. From https://news.fnal.gov/2021/05/icarus-gets-ready-to-fly/.

PMT glass is not transparent to the scintillation photon wavelength (128 nm), so each PMT is coated with Tetra-Phenyl Butadiene (TPB) to shift the scintillation photons to visible light [88]. An image of the PMT system inside one ICARUS TPC is shown in figure 3.7.

Operating nearly at the surface, ICARUS observes a ∼11 kHz rate of cosmogenic muons. This corresponds to about 11 muon tracks observed in a 1 ms TPC readout. The ICARUS cosmic ray tagger (CRT) provides $\sim 4\pi$ tagging of cosmic muon tracks that impinge the detector. Other cosmogenic activity, such as hadrons and high energy photons, are almost completely stopped by a 3 m concrete overburden. The CRT is split into separate top, side and bottom systems. The top CRT consists of 123 modules covering a total surface of about 426 m^2. It catches more than 80% of the cosmic muon flux. Each module is a $1.86 \times 1.86\,m^2$ box with two perpindicular layers of eight scintillator bars. The coincident observation of

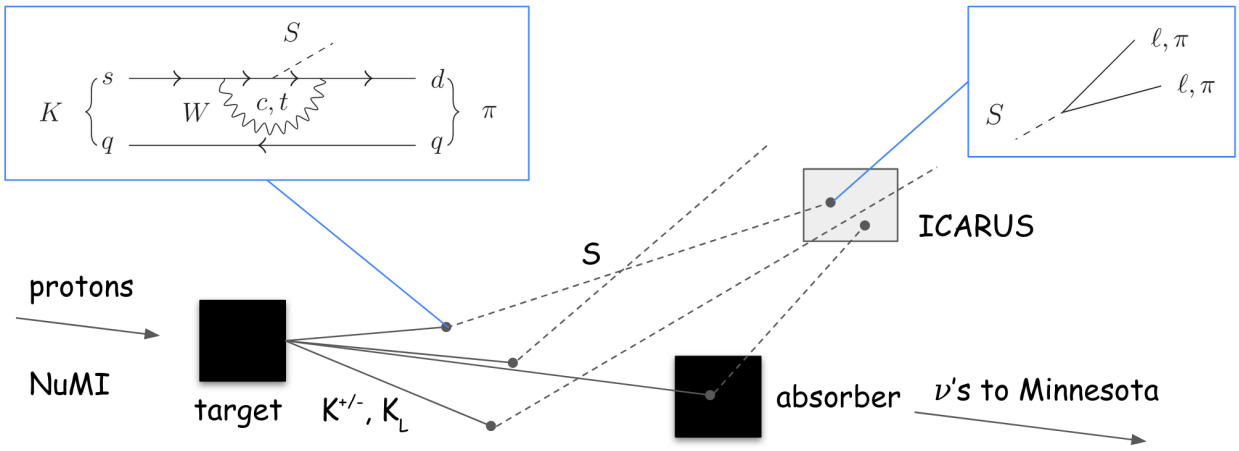

Figure 3.4: Diagram of the phenomenology of the Higgs portal scalar (see section 2.1) in the NuMI beam (see section 3.1) at ICARUS. Scalars are produced in the NuMI beam in kaon decay, travel to the ICARUS detector, and decay into standard model particles: electrons, muons, or pions.

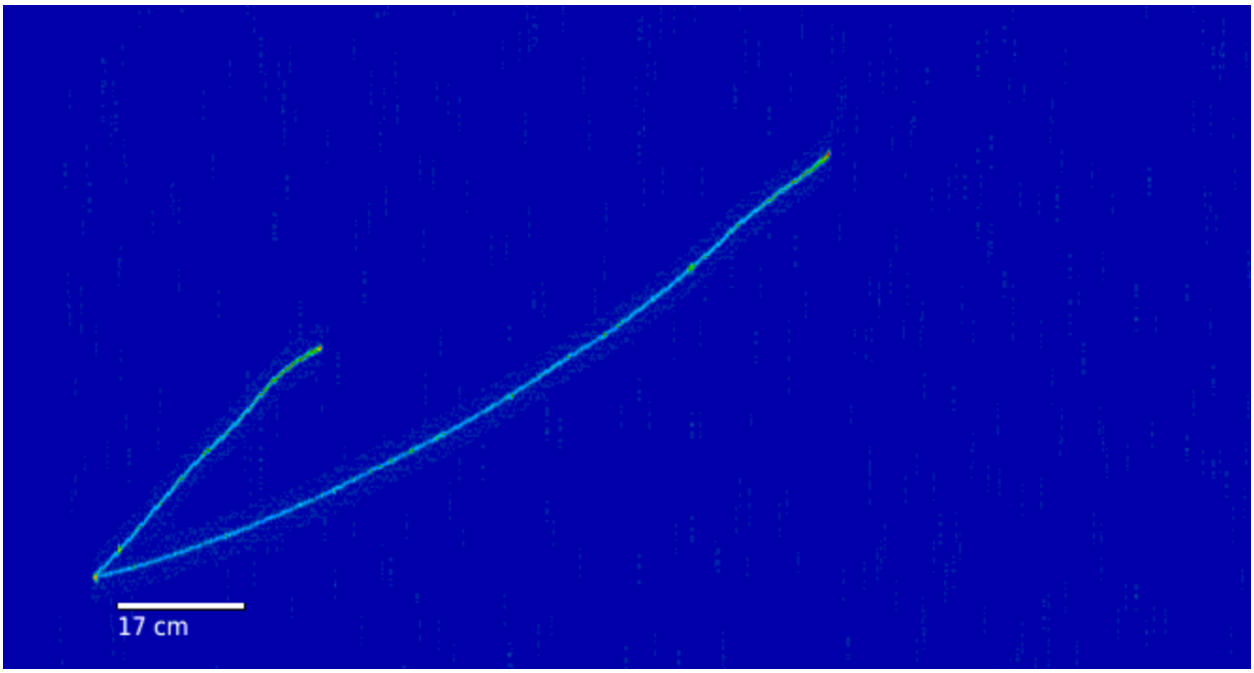

Figure 3.5: Example ICARUS Monte Carlo simulation event display of a Higgs Portal scalar decaying to two muons. The mass of the simulated scalar is 260 MeV.

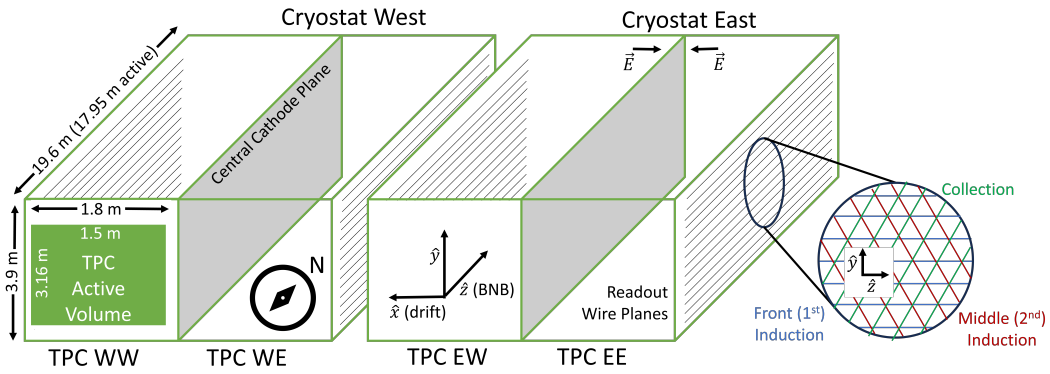

Figure 3.6: Diagram of the layout and enumeration of the ICARUS TPCs. Not to scale. The wire plane orientations are mirrored in opposite TPCs. The East and West cryostats have the same layout.

scintillation light in both layers allows the position to be reconstructed. The side CRT uses scintillator modules from the MINOS experiment [11]. Each module contains twenty adjacent strips of $800 \times 4 \times 1\,\mathrm{cm}^3$ scintillator. On the South side of the detector (upstream to the beam), two layers of modules are arrayed orthogonally to improve the spatial resolution. On the East, West, and North sides, only one layer is installed. The bottom CRT consists of 14 scintillator modules, refurbished from the Double Chooz experiment [89] Each module consists of 64 scintillator strips running in parallel.

The calibration and analysis work discussed in this thesis all exclusivly use measurements made with the ICARUS time projection chamber. However, the PMT and CRT systems will be applied in future results in ICARUS.

3.1 The Neutrinos at the Main Injector Beam

ICARUS receives neutrinos at a far-off-axis location from the Neutrinos at the Main Injector (NuMI) beam [82]. The NuMI beam produces neutrinos from the interaction of 120 GeV protons with a graphite target. A spray of mesons produced in these interactions decay to neutrinos and source the beam.

The proton beam is accelerated to 120 GeV through the Fermilab accelerator complex

Figure 3.7: Image of the PMT system inside one of the ICARUS TPCs. Taken from Ref. [83].

(see figure 3.8). A linear accelerator (Linac) accelerates H^- ions to 400 MeV. The ions are converted into protons in the Booster, which accelerates them to 8 GeV. Protons are bunched into 1.6 µs long batches, each consisting of a number of constituent 2 ns long bunches, each spaced 18.9 ns apart. The batches are then fed into the Main Injector, a synchroton that accelerates the beam to 120 GeV. The Main Injector can accelerate 6 batches from the Booster at a time, which corresponds to a 9.6 µs total spill length.

A method called slip-stacking doubles the intensity of the NuMI beam. In this process, a first set of six bunches are fed into the Main Injector. These are decelerated by one batch length, and then another six batches are fed in. Slip-stacked batches thus have double the protons of nominal batches. This version of the slip-stacking process has been in place at NuMI since 2017 [90]. All ICARUS NuMI data is collected in this configuration.

The batches of 120 GeV protons in the Main Injector are directed at a graphite target. Beam proton interactions in the target produce mesons that decay to neutrinos. The most important meson decays for producing neutrions are:

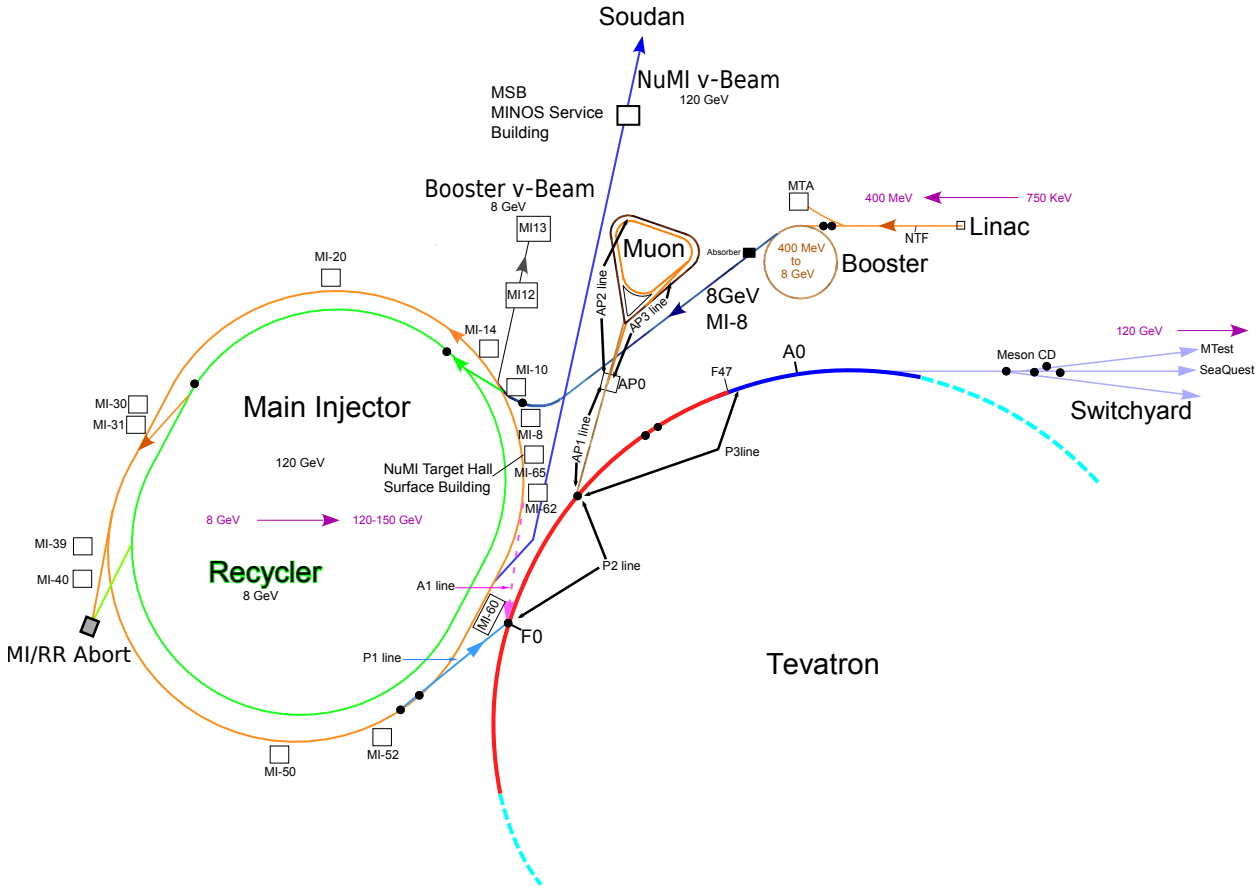

Figure 3.8: From Ref. [82]: diagram of the Fermilab accelerator campus.

$$\pi^+ \to \mu^+ + \nu_\mu \qquad (99.99\%)$$

$$\pi^- \to \mu^- + \bar{\nu}_\mu \qquad (99.99\%)$$

$$
\begin{aligned}
K^+ &\to \mu^+ + \nu_\mu \qquad (64\%) \\
K^+ &\to \pi^0 + e^+ + \nu_e \qquad (5\%) \\
K^+ &\to \pi^0 + \mu^+ + \nu_\mu \qquad (4\%) \\
K^- &\to \mu^- + \bar{\nu}_\mu \qquad (64\%) \\
K^- &\to \pi^0 + e^- + \bar{\nu}_e \qquad (5\%) \\
K^- &\to \pi^0 + \mu^- + \bar{\nu}_\mu \qquad (4\%) \\
K^0_L &\to \pi^- + e^+ + \nu_e \qquad (20\%) \\
K^0_L &\to \pi^+ + e^- + \bar{\nu}_e \qquad (20\%) \\
K^0_L &\to \pi^- + \mu^+ + \nu_\mu \qquad (14\%) \\
K^0_L &\to \pi^+ + \mu^- + \bar{\nu}_\mu \qquad (14\%)\,.
\end{aligned}
$$

Each decay is shown with the corresponding branching ratio on the right hand side. The beam is predominantly ν_μ, with an important but sub-dominant component of ν_e from kaon decays. A pair of magnetic focusing horns steer charged pions and kaons in the forward direction to focus the neutrino beam. The horns can be run in forward horn current mode, where positively charged mesons which source neutrinos are focused, or reverse horn current mode, where negatively charged mesons which source anti-neutrinos are focused. The NuMI beam and horn system is depicted diagramatically in figure 3.9. All of the NuMI beam data for this result were take in forward horn current mode.

As is diagrammed in figure 3.10, ICARUS is situated far-off-axis to the NuMI beam direction: 5.75°. At this off-axis angle, the flux has very different characteristics to the on-axis or near-off-axis case. The energy falls off quickly, so that at ICARUS $\langle E_\nu \rangle$ ~1.5 GeV. The source of the flux mostly comes from pions and kaons that are directly oriented at ICARUS, as well as large-angle 3-body kaon decays. As a result, the focusing system does not have much impact: nearly all of the relevant mesons decay before reaching the second focusing horn. Thus, there is a significant component of anti-neutrino flux, even for the

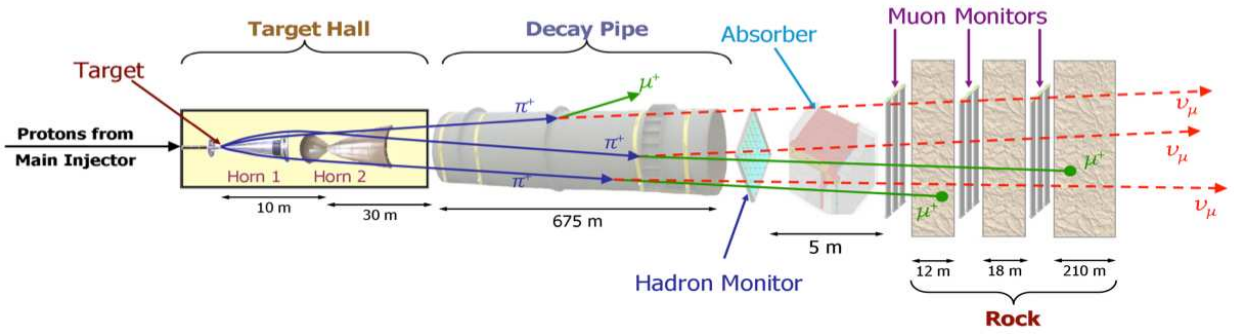

Figure 3.9: From Ref. [82]: diagram of the NuMI neutrino beam.

forward horn current data used in this thesis.

3.2 ICARUS Monte Carlo Simulation

ICARUS detector Monte Carlo simulation enables the generation of neutrino and scalar decay signal events. This simulation emulates the full detection process: the production of mesons in the NuMI beam, the production of neutrinos and LLPs in meson decay and their interaction or decay in the argon, the propogation of particles produced in the interaction, and the full detector response to these particles. Simulated cosmogenic activity (mostly cosmic-ray muons) is also overlaid.

Meson decays in the NuMI beam source both neutrino and scalar events. The NuMI flux is generated by the `GEANT4`-based package `g4numi` [91, 92, 93]. The `g4numi` package simulates the interaction of 120 GeV protons on the graphite target, the production of mesons, and the re-interaction and focusing of those mesons in the magnetic horns, as well as re-interactions in other materials in the target hall. The flux is modified by the `PPFX` package [92, 93], which corrects the flux and determines its systematic uncertainty, taking into account world data on proton-Carbon and other relevant cross sections. ICARUS sits 5.75° off-axis to NuMI, and so has a different flux from on or slightly off-axis detectors. The constraints have been tuned for the ICARUS off-axis location which determines which on-axis constraints are and are not applicable [94]. Unlike the on-axis case, neutrinos at ICARUS are mostly generated

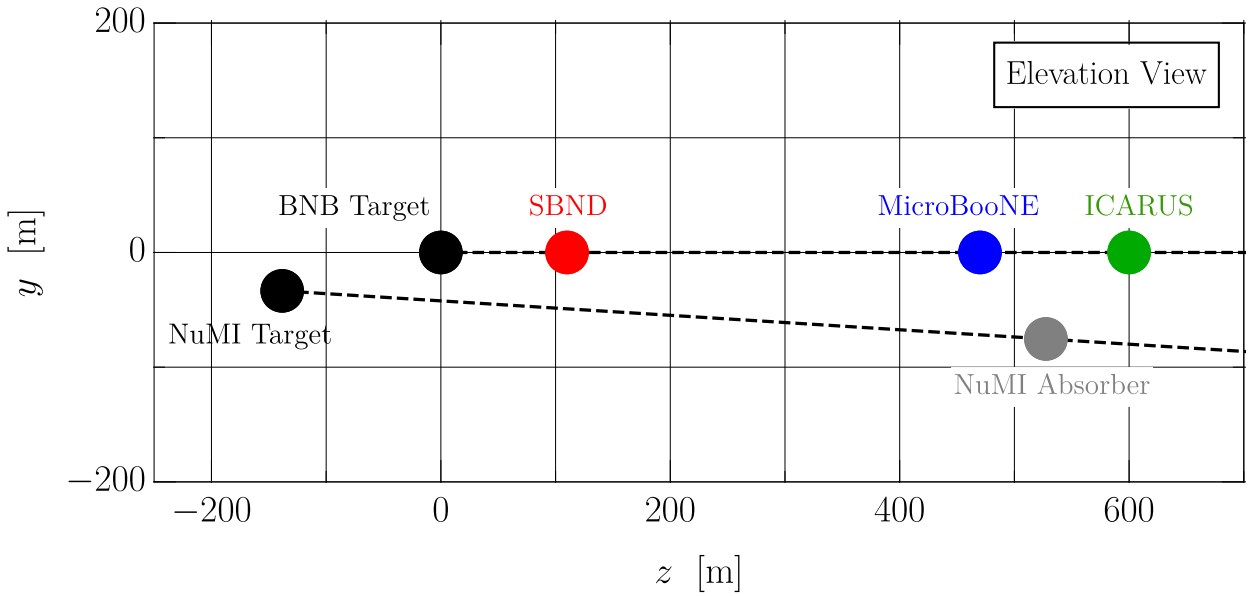

Figure 3.10: From Ref. [47]: elevation view of the relative locations of ICARUS and the NuMI beam direction. Nearly all of the off-axis angle of ICARUS to NuMI is in the vertical direction, as is shown in this figure.

by unfocused pions and large-angle kaon decays.

Neutrino interactions form a background to di-muon decays, so simulating their rate is important to developing the analysis. The intrinsic $\mu\mu$ neutrino background to this signature, from neutrino tridents [95] and charm production [96], is negligible. However, there is a non-intrinsic background from $\mu\pi$ production in muon neutrino charged current interactions (mostly through resonant, deep inelastic, and coherent scattering). Pions cannot be calorimetrically separated from muons in LArTPCs, although they can be identified in cases where they inelastically scatter with an argon nucleus before stopping or exiting the detector. Neutrino interactions are generated by `GENIE` [97]. The study done here uses the SBN tune developed for SBN and DUNE oscillation analyses[1].

As is shown in chapter 7, after event selection cuts the dominant residual neutrino background comes from muon-neutrino charged current coherent pion production (ν_μCC-Coh-π

1. Technical documentation for this tune does not exist, but is being developed.

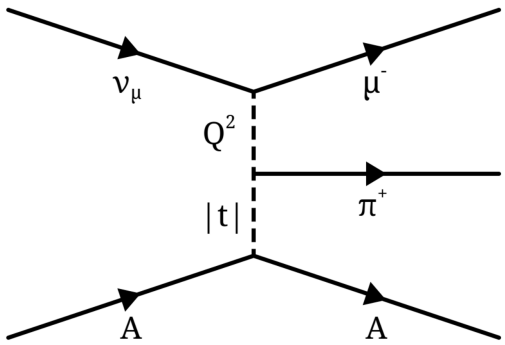

Figure 3.11: Feynman diagram of the ν_μCC-Coh-π interaction, from Ref. [98]. In this process, a muon neutrino coherently upscatters off a nucleus (A) into a $\mu\pi$ final state. The nucleus is left in its ground state. The diagram identifies two relevant momentum transfer variables: t (see equation 3.1) and $Q^2 = -(\boldsymbol{p_\nu} - \boldsymbol{p_\mu})^2$.

) [99, 100]. A diagram of this process is shown in figure 3.11. The interaction comprises a small fraction of the total neutrino rate in ICARUS ($\sim 0.2\%$). However, it has characteristics that make it hard to distinguish from di-muon decays. In this process, a muon neutrino interacts coherently with an argon nucleus, up-scattering to a $\mu - \pi$ final state. It leaves the argon nucleus in its ground state, not producing any other activity that can be used to veto the interaction. Because the process is coherent, it occurs at small energy transfer to the nucleus, as defined by

$$t = |\boldsymbol{p_\nu} - \boldsymbol{p_\mu} - \boldsymbol{p_\pi}|^2 , \tag{3.1}$$

where $\boldsymbol{p_\nu}, \boldsymbol{p_\mu}$, and $\boldsymbol{p_\pi}$ are the neutrino, muon, and pion 4-momenta, respectively. Di-muon decays do not involve a nucleus, so they all occur at $t = 0$.

No data exists on argon to meaningfully constrain the process. The interaction has been observed on argon by the ArgoNeuT experiment [101]. However, the measurement has limited statistical power and was made at a different neutrino beam energy than is relevant for ICARUS. GENIE applies the Berger-Sehgal model [100] for this process, and assigns a 100% uncertainty on the rate. To assess a more realistic central value and uncertainty for this

process, its rate was tuned to a measurement made by the MINERvA experiment on carbon and iron [102]. Figure 3.12 shows spectra of the ν_μCC-Coh-π process for the GENIE nominal value compared to the result of the MINERvA tune. There is about a 60% uncertainty on the interaction rate of this process after the tune. The uncertainty depends most strongly on the pion energy, and gets much larger at low pion energies. The MINERvA measurement has a much larger uncertainty in this area of phase space. In addition, there is a large theoretical uncertainty on the interaction rate at this energy due to the uncertain impact of the Δ resonance on the cross section. Theoretical models that predict the ν_μCC-Coh-π rate from pion-nucleus scattering differ when interpolating from deuterium [99] or carbon [100]. Microphysical models of the process also provide different predictions [103, 104, 105]. The tune uncertainty does not explicitly account for this theoretical uncertainty, although in effect it does reflect it.

Higgs portal scalar decays are generated with the `MeVPrtl` event generator[2]. This tool generates decays of BSM particles such as the Higgs portal scalar [47], heavy neutral lepton [46], and heavy axion [48] models. The `MeVPrtl` generator operates on beam mesons as input. It simulates the meson decay to the BSM particle, which is propagated to the detector volume and decayed into standard model particles. The `MeVPrtl` generator has also been validated by verifying it against an independent, standalone simulation of the scalar decay process.

Cosmic muons are generated on top of scalar and neutrino events by the CORSIKA generator [106]. No sample of cosmic-only simulation is used; off-beam data is instead used to estimate the component of on-beam data where cosmic activity triggers the detector.

Generated particles are turned into simulated events using a robust simulation of the ICARUS detector. Particles are propagated through the detector with a Geant4 simulation configured for liquid argon [91]. Geant4 simulates the deposition of energy in the detector by charged particles, which is recorded as ionization charge applying the ArgoNeuT mea-

2. Internal documentation on this tool exists inside the ICARUS collaboration. Work is ongoing to make this public.

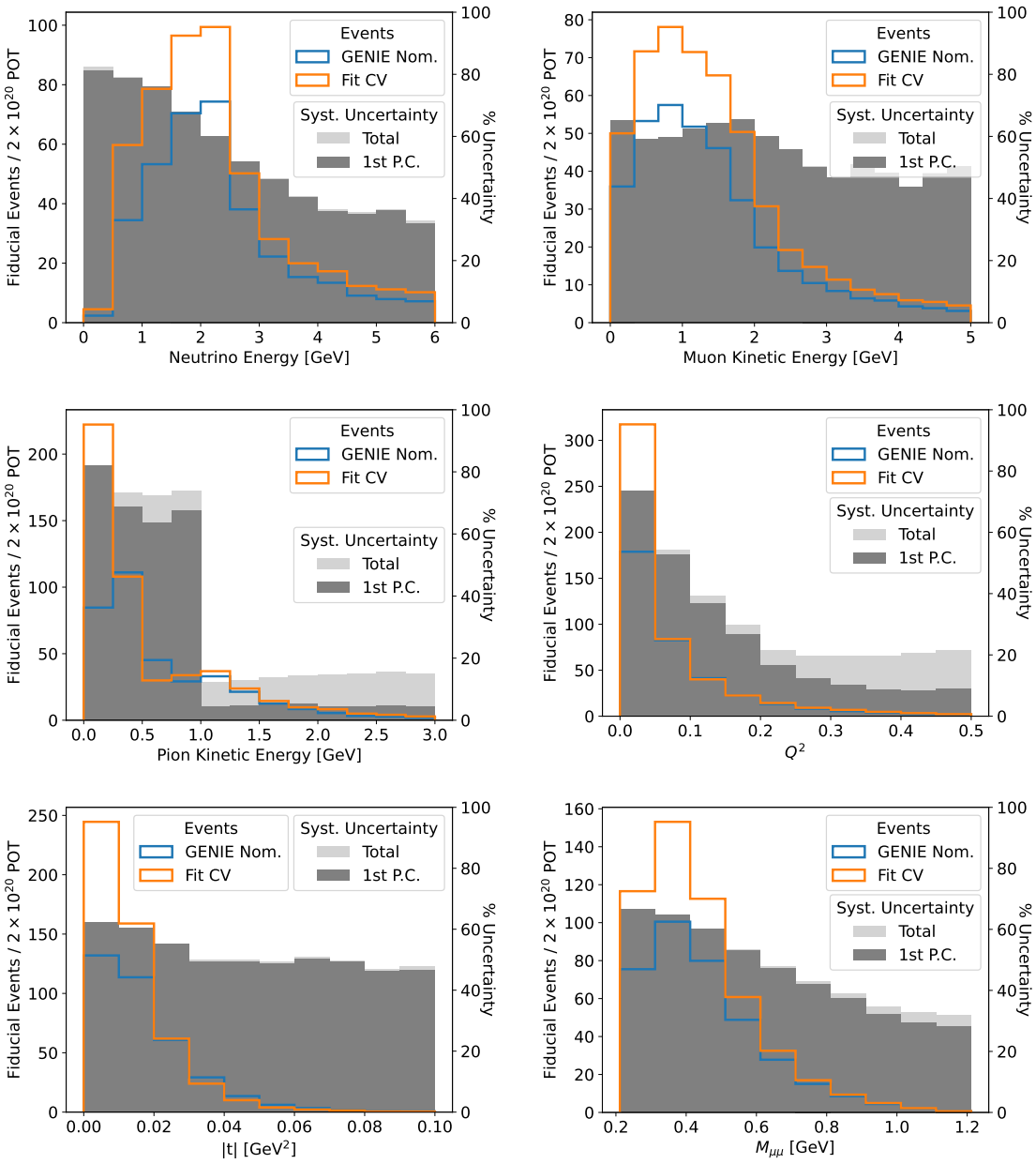

Figure 3.12: Distributions of truth kinematic variables for ν_μCC-Coh-π interactions. The variables are: neutrino energy, muon kinetic energy, pion kinetic energy, energy transfer to the hadronic state ($Q^2 = -(\boldsymbol{p_\nu} - \boldsymbol{p_\mu})^2$), energy transfter to nucleus (equation 3.1), and the invariant mass reconstructed with the di-muon hypothesis ($M_{\mu\mu} = |\boldsymbol{p_\mu} + \frac{m_\mu}{m_\pi}\boldsymbol{p_\pi}|$). $\boldsymbol{p_\nu}, \boldsymbol{p_\mu}$, and $\boldsymbol{p_\pi}$ are the neutrino, muon, and pion 4-momenta, respectively. Each plot compares the nominal GENIE prediction and the result of the tune to MINERvA data. The percent uncertainty in the MINERvA fit is also shown in the gray histograms using the right vertical axis. The plot displays both the total uncertainty and the uncertainty in the first principal component (P.C.) of the covariance matrix. This component represents the dominant systematic fluctuation encoded in the covariance.

surement of electron-ion recombination [107]. Ionization charge is drifted to the wire plane readout by the Wire-Cell simulation [108], which applies ionization field responses computed by GARFIELD [109]. This simulation includes the effect of diffusion, and accounts for long-range induction effects on wire signal shapes (charge induces a signal as far away as 3 cm, or 10 wires). These simulated signal shapes are tuned to match the observed shapes in data (see chapter 5).

3.2.1 Simulated Datasets

Monte Carlo simulation datasets are generated for NuMI neutrino and Higgs portal scalar events. There are two datasets of neutrino interactions:

- The inclusive sample consists of NuMI neutrino interactions with CORSIKA cosmics. Its statistics are $3-4\times$ the data POT.
- The `Coh-Like` sample consists of NuMI neutrino interactions enhanced in the type of neutrino interactions that generate backgrounds in the signal region of the analysis. The sample was generated by filtering events that had at least one neutrino interaction with the following characteristics:
  - At least two generated particles of $\mu, \pi^{\pm}, \Sigma^{\pm}$ [3]
  - No proton generated with a kinetic energy greater than 50 MeV

  The sample was generated with $\sim 150\times$ expected data statistics.

The inclusive and Coh-like samples are combined into a single sample after removing events from the inclusive sample that overlap with the Coh-like definition.

Higgs portal scalar interactions are generated at a number of mass points (M_S) and mixing angles (θ_S) The events can be re-weighted from the nominal mixing (θ_S) to another

3. The Σ baryons predominantly decay to charged pions.

mixing angle (θ'_S) by applying a weight

$$\frac{{\theta'_S}^2}{\theta_S^2} \times \frac{\exp(-\ell_{\text{enter}}/d) - \exp(-\ell_{\text{exit}}/d)}{\exp(-\ell_{\text{enter}}/d \times \theta_S^2/{\theta'_S}^2) - \exp(-\ell_{\text{exit}}/d \times \theta_S^2/{\theta'_S}^2)}, \tag{3.2}$$

where ℓ_{enter} is the distance along the scalar ray to the front of the detector, ℓ_{exit} is the distance along the scalar ray to the back of the detector, and d is the mean decay length of the scalar.

CHAPTER 4

COSMIC MUONS AS A CALIBRATION SOURCE

The calibration of the ICARUS TPC (as will be detailed in chapters 5 and 6) relies on the copious number of cosmic ray muons available at the surface. Muon energy loss deposits ionization charge in the detector which can be used to diagnose any non-uniformities in the TPC, as well as to measure the channel gain. In the kinematic regime relevant at ICARUS, the probability distribution governing particle energy loss observed by a readout wire channel is the Landau-Vavilov distribution [110]. In the limit that the charged particle is relativistic and the slice of the particle track that the channel is sensitive to is small (as is often the case in a LArTPC), this distribution is well-approximated by the Landau distribution [111]. For both distributions, the mean energy loss per length (given by the Bethe-Bloch theory [112]) is independent of the length of the charged particle trajectory observed by the channel. However, the shape of the distribution depends strongly on this length.

The Landau and Landau-Vavilov distributions are governed by the cross-section of charged particles incident on atomic electrons, which has a power law dependency on the energy transfer. This behavior means that the mean energy loss is influenced by a small number of large energy transfers to electrons well above the atomic excitation energy (δ-rays). When the channel is only sensitive to a short enough length of the charged particle trajectory such that it will not observe a δ-ray most of the time, the bulk of the distribution is below the mean value of energy loss with a long tail extending out to high energy losses. The Landau distribution is an appropriate approximation in this case. As the channel-sensitive length increases, more of the delta rays get absorbed into the bulk of the distribution and the location of the peak shifts up as the variance drops, until the distribution is better modeled by a Landau-Vavilov distribution.

Due to the large fluctuations in particle energy loss as described by Landau-Vavilov theory, the mean energy loss is challenging to measure. In ICARUS, we calibrate to the most-

probable-value (MPV) of energy loss, which only depends on the peak of the distribution. In this chapter, we review the derivation of the Landau distribution of particle energy loss and the calculation of the MPV. This derivation reveals a new effect described by the author [113], that diffusion of the ionization electrons perturbs the MPV of the Landau distribution in a LArTPC. This derivation is covered in section 4.1, and the imapct on LArTPC calibration is discussed in section 4.2. Following this derivation, in section 4.3 we state the mean energy loss, which completes the specification of muon energy loss. The concepts developed in this chapter underlie the calibrations detailed in chapters 5 and 6.

4.1 Landau Energy Loss in a LArTPC in the Presence of Diffusion

The Landau-Vavilov and Landau distributions are derived assuming that a detector is sensitive to a discrete section of the charged particle trajectory: there is a region where the channel detects all of the deposited energy, and a region where it detects none [111, 110]. In the case of a LArTPC impacted by diffusion, this assumption does not hold. As is illustrated in figure 4.1, a channel in a LArTPC is sensitive to a fractional amount of the particle energy loss, dependent on its position. To parameterize this effect, we define the channel ionization weight function $w(x)$, which gives this fraction as a function of the particle position x. This weight function defines the probability distribution of energy that the channel measures.

To obtain the distribution of energy loss for a general channel ionization weight function, we go through the usual derivation of the Landau-Vavilov distribution, keeping this weight function along the way. Section 4.1.1 introduces the principles in this derivation. Section 4.1.2 gives an analytic formula for the energy loss distribution. Section 4.1.3 discusses the relativistic/thin-film limit for a weight function. Details of the derivation are given in appendix A.

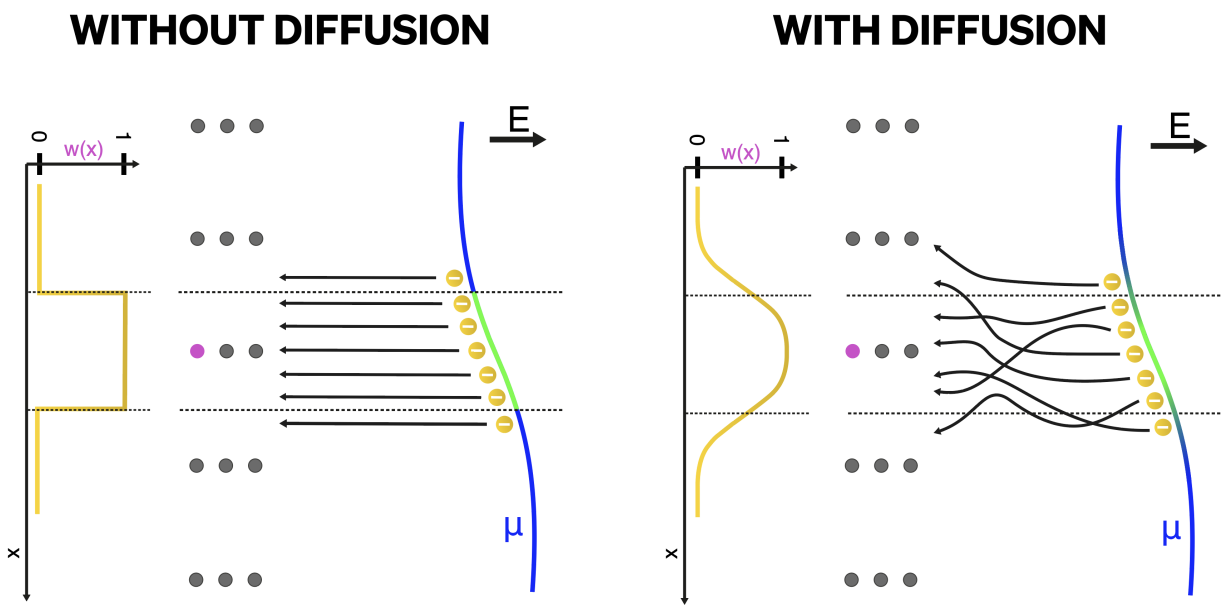

Figure 4.1: Diagrams illustrating the effect of diffusion on the path length of a particle track observed by channels in a LArTPC with a wire plane readout, from Ref. [113]. The graphs on the left of both diagrams plot the weight function, $w(x)$, describing the probability that ionization energy is observed as observed by the central, pink wire as a function of the position of the energy deposition along the particle track (this is also denoted by the color of the particle track). Diffusion in the direction transverse to the wire orientation smears charge in and out of the range each wire is sensitive to.

4.1.1 Principles of the Energy Loss Distribution

We construct the probability distribution of energy loss iteratively. We start from the simple base case of the distribution over an infinitesimal length, and then build it up into the distribution over finite length. Our tool in this construction is the convolution property: given the probability distribution of observing a particle energy loss E over a length ℓ, $p_\ell(E)$, a convolution of $p_\ell(E)$ with itself doubles the length ℓ since a convolution represents all the ways a particle can lose an amount of energy in two steps of ℓ. Thus the convolution property states that

$$p_{2\ell}(E) = \int p_\ell(E - E')p_\ell(E')dE' \,. \tag{4.1}$$

The distribution of energy loss for an infinitesimal length is given by the limit that the

particle travels a short enough distance such that it will scatter off at most one atomic electron. In this case, the probability of energy loss is equal to the probability of colliding with an atomic electron with precisely that amount of energy transfer. The probability of no energy loss is equal to the probability of not interacting with an atomic electron. Thus,

$$\lim_{\ell \to 0} p_\ell(T) = (1 - \rho\sigma\ell)\delta(T) + \rho\ell\frac{d\sigma}{dT}\,, \tag{4.2}$$

where ρ is the number density of electrons, $\frac{d\sigma}{dT}$ is the differential cross section w.r.t. the energy transfer T, $\sigma = \int \frac{d\sigma}{dT} dT$, and δ is the Dirac-Delta function.

In the case of heavy charged particles (such as muons and protons) elastically scattering on bare electrons, the cross section is given by the Rutherford formula [114]

$$\frac{d\sigma}{dT} = \frac{2\pi r_e^2 m_e}{\beta^2}\frac{1 - \beta^2 T/T_{\max}}{T^2}\,, \tag{4.3}$$

where r_e is the classical electron radius, m_e is the electron mass, β is given by the particle velocity, and $T_{\max}$ is the maximum energy transfer in a single collision,

$$T_{\max} = \frac{2m_e\beta^2\gamma^2}{1 + 2\gamma m_e/M + (m_e/M)^2}\,,$$

where M is the mass of the charged particle. The cross section for atomic electrons is modified relative to the bare cross section at low energy transfer by atomic effects. A useful quantity related to the cross section is

$$\zeta = \rho\frac{2\pi r_e^2 m_e}{T_{\max}\beta^2}\,. \tag{4.4}$$

ζ is a quantity with units of inverse length that encodes the rate of scattering.

For the probability distribution of energy loss over an infinitesimal length, the channel ionization weight function can always be assumed to be a constant w. In this case, for a

channel to measure an energy deposition E the particle must deposit an amount E/w. So in the presence of a weight function w, $p_\ell(E)$ transforms to $\frac{1}{w}p_\ell(E/w)$ (the $1/w$ in front fixes the normalization) when the length ℓ is small.

4.1.2 Analytic Form of the Distribution

To build the particle energy loss distribution, we discretize the weight function $w(x)$ into weights w_i over infinitesimal steps dx_i, and build up the probability distribution over the full weight function by performing a product of convolutions:

$$p_w(E) = \int dT_1 \int dT_2 \cdots \int dT_n \frac{p_{dx_0}(\frac{E-T_n-\cdots-T_1}{w_0})}{w_0} \times \frac{p_{dx_1}(\frac{T_n-\cdots-T_1}{w_1})}{w_1} \times \cdots \times \frac{p_{dx_n}(\frac{T_n}{w_n})}{w_n}\,. \tag{4.5}$$

Appendix A.1 goes through the process of simplifying this into an algebraic expression for the case of Rutherford scattering. In the process of this derivation, it is necessary to introduce the mean energy loss $\overline{E}$ as an external input to the distribution. This is because atomic effects modify the bare electron cross section at low energy transfer in a way that can be accounted for through the mean energy loss using Bethe-Bloch theory. We obtain:

$$p_w(E) = \frac{1}{2\pi\zeta T_{\max}} \int_{-\infty}^{\infty} dz\, \exp\left[\frac{iz}{\zeta T_{\max}}(E-\overline{E}) + \int dx\, \zeta(1-e^{-iw(x)z/\zeta}) - izw(x)(1+\beta^2) + \right.$$
$$\left. (\zeta\beta^2 + iw(x)z)(-\mathrm{Ei}[-iw(x)z/\zeta] + \log[iw(x)z/\zeta] + \gamma_{\mathrm{EM}})\right]\,. \tag{4.6}$$

where $\gamma_{\mathrm{EM}} \approx 0.577$ is the Euler-Mascheroni constant and Ei is the exponential integral function, $\mathrm{Ei}(x) = -\int_{-x}^{\infty} dt\; e^{-t}/t$. This is the probability distribution of particle energy loss for a channel with a general ionization weight function $w(x)$ as a function of the charged particle position. Appendix A.3 shows that this distribution reduces to a Landau-Vavilov distribution precisely when the channel ionization weight function is given by a step function.

4.1.3 The Thin-Film/Relativistic Limit

To take the thin-film/relativistic limit, we take the case where the weight function is narrow compared to the size of the scattering length $1/\zeta$ (details in appendix A.2). In this limit, the probability distribution of energy loss converges to

$$p_w(E) = \frac{1}{2\pi i \zeta T_{\max} \not{p}} \int_{-i\infty}^{i\infty} dz' \, \exp\left[z'\left(\lambda + \log|z'|\right)\right] , \tag{4.7}$$

where $\lambda = \frac{E-\overline{E}}{\zeta T_{\max} \not{p}} - \log\zeta \not{p} + \gamma_{\mathrm{EM}} - 1 - \beta^2 + \frac{\int dx \; w(x)\log[w(x)]}{\not{p}}$ and $\not{p}$ is defined as the pitch:

$$\not{p} \equiv \int w(x) dx \, . \tag{4.8}$$

Equation 4.7 can be recognized as the Landau distribution for a parameter λ, which has a maximum at $\lambda_{\mathrm{MPV}} = \gamma_{\mathrm{EM}} - 0.8 \approx -0.22278\ldots$[115]. Therefore:

$$E_{\mathrm{MPV}} = \overline{E} + \zeta T_{\max} \not{p} \left(\log\zeta \not{p} + 0.2 + \beta^2 - \frac{\int dx \; w(x)\log[w(x)]}{\not{p}} \right) .$$

In the case where the weight function $w(x)$ is a step function, E_{MPV} reduces to the usual result [114]. We can recast this result by defining the thickness

$$\not{t} \equiv \not{p} e^{-\int dx \; w(x)\log[w(x)]/\not{p}} \, . \tag{4.9}$$

Then the formula for the MPV energy loss $dE/dx_{\mathrm{MPV}} \equiv E_{\mathrm{MPV}}/\not{p}$ is

$$\frac{dE}{dx}_{\mathrm{MPV}} = \overline{\frac{dE}{dx}} + \zeta T_{\max} \left(\log\zeta \not{t} + 0.2 + \beta^2 \right) . \tag{4.10}$$

This equation, with equation 4.9 as an input, is the main result of this derivation. In this formula, all the dependence on the weight function $w(x)$ is encoded in the $\not{t}$ parameter. This

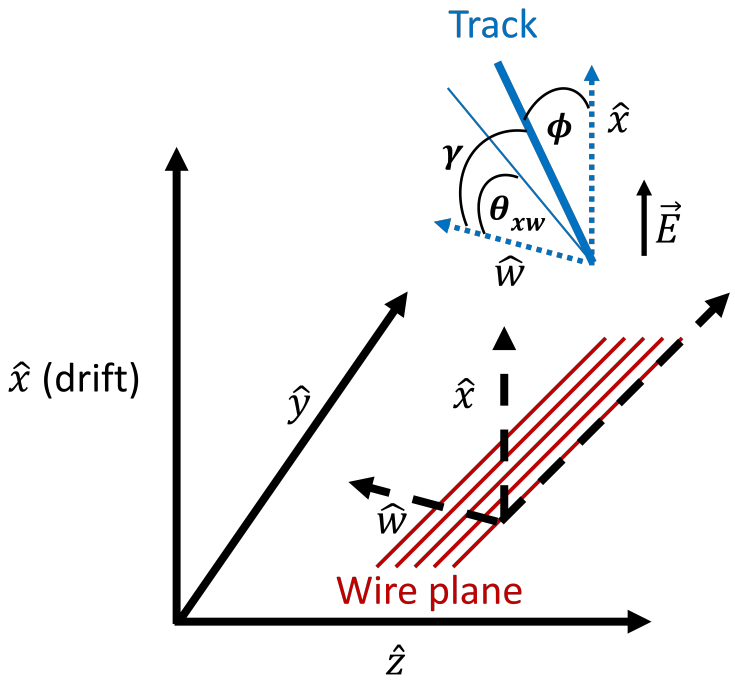

Figure 4.2: Diagram of relevant track angles for tracks in a LArTPC: θ_{xw}, γ, and ϕ.

is precisely the usual formula for the energy loss MPV dE/dx [114], just with the thickness given by equation 4.9. The thickness and pitch transform under scaling and dilation of the weight function as:

$$\begin{array}{rr} \text{Scaling} & \text{Dilation} \\ w(x) \to a \cdot w(x) & w(x) \to w(x/a) \\ \not{p} \to a \cdot \not{p} & \not{p} \to a \cdot \not{p} \\ t \to t & t \to a \cdot t. \end{array} \tag{4.11}$$

4.1.4 The LArTPC Channel Ionization Weight Function

We now apply these results to the case of a LArTPC with a wire plane readout. LArTPC readout wires detect charge from the induced current of ionization electrons either passing through the wire plane (a bipolar, "induction" signal) or collecting on it (a unipolar, "collection" signal). We approximate here that each wire is only sensitive to the ionization electrons directly adjacent to it, motivating the step function response illustrated in the left-hand dia-

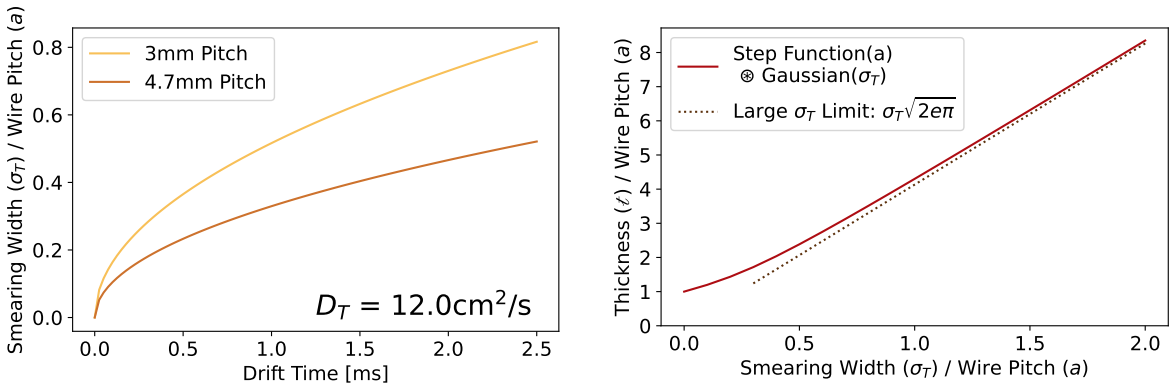

Figure 4.3: (Left) Smearing widths from transverse diffusion (using the Li et al. parameterization for D_T [116]) by drift time for the DUNE (4.7 mm) and SBN (3 mm) wire pitches. (Right) Thickness observed by a channel with a weight function given by a step function of width a convolved with a Gaussian of width σ_{T}, as a function of σ_{T}/a. From Ref. [113].

gram of figure 4.1 (in the absence of diffusion). In reality, electrons can induce a signal as far away as 3 cm (10 wires for a 3 mm spacing) [108]. This effect is subdominant, and any change it makes to the channel thickness will only change the peak energy loss logarithmically (as per equation 4.10). Still, assessing the effect of long-range current induction on the channel ionization weight function merits further study, especially for induction wire planes.

To account for the impact of diffusion, the LArTPC channel weight function is modified to be a convolution of the step function of the wire pitch and a Gaussian smearing induced by transverse diffusion, as illustrated in the right-hand diagram of figure 4.1. In addition, as shown in figure 4.2, a track will in general be at some angle γ to the wire orientation, which dilates the channel weight function w. Putting this together, we obtain

$$w_{\mathrm{LArTPC}}(x) = \int_0^a \frac{dx'}{\sqrt{2\pi}\sigma_{\mathrm{T}}} e^{-(x\cdot\cos\gamma - x')^2/(2\sigma_{\mathrm{T}}^2)} \qquad (4.12)$$
$$\sigma_{\mathrm{T}} = \sqrt{2 \cdot D_{\mathrm{T}} \cdot t_{\mathrm{drift}}}\,,$$

for a wire separation a, drift time t_{drift}, and transverse diffusion constant D_T.

This weight function has a pitch $\not{p} = a/\cos\gamma$ (note that the formula for the pitch $\not{p}$ here

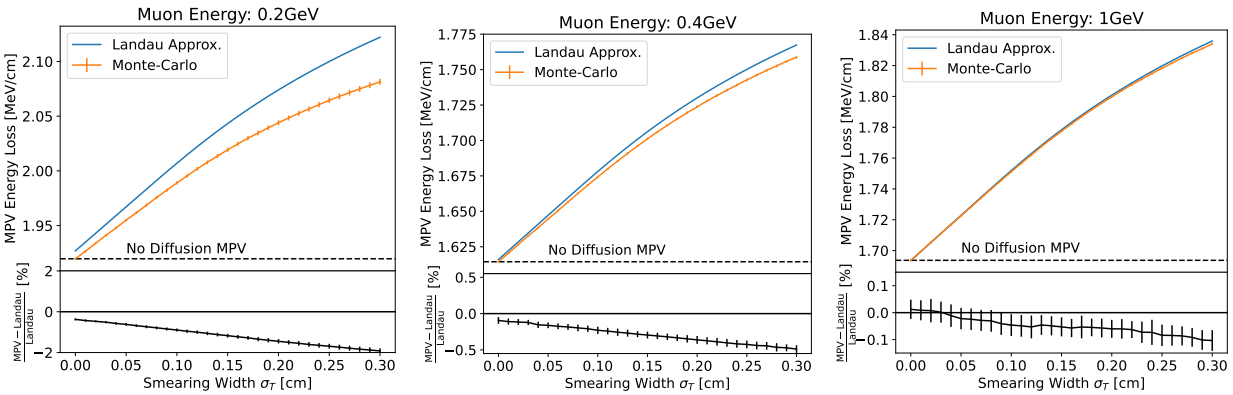

Figure 4.4: Comparison of the MPV energy loss from a Monte-Carlo simulation of the probability distribution in equation 4.6 and the Landau MPV approximation (equation 4.10) for a channel ionization weight function given by a step function of width 3 mm convolved with a Gaussian of varying widths (equation 4.12). The comparison is made at various values of the muon energy. At low muon energy and large channel thickness, the thin-film/relativistic approximation underlying the Landau MPV prediction begins to breakdown, up to the percent level at 0.2 GeV. From Ref. [113].

coincides with the usual definition of the track pitch in a LArTPC). In the limit of a small wire separation relative to the Gaussian width, the thickness converges to $\sigma_{\mathrm{T}}\sqrt{2\pi e}/\cos\gamma$. In general though, we have not found a useful closed form of the thickness for this weight function. A plot of the thickness $\not{t}$ as a function of σ_{T}/a for $\cos\gamma = 1$ is shown in figure 4.3. By the scaling property of the thickness under dilation (equation 4.11), $\not{t}(\cos\gamma) = \not{t}(1)/\cos\gamma$.

Figure 4.4 plots the most-probable-value of energy loss obtained from a Monte-Carlo simulation of muon energy loss observed by a LArTPC-like weight function, as a function of the smearing width σ_T. The value is compared to the energy loss estimate from the thin-film approximation (i.e., using the value of the thickness in the Landau distribution MPV formula, equation 4.10). The Landau approximation works well at small thickness and large muon energy. Outside of this region, numerically obtaining the peak of the general distribution with the weight function (equation 4.6) would be required. Since the LArTPC weight function is not a step function, in this region the distribution is also not a Landau-Vavilov distribution. In the usual Vavilov case, one defines this region of phase space using the parameter $\zeta \cdot \not{p}$, which is a unit-less measure of the "film-thickness" of a channel that

Detector	Wire Pitch [mm]	Drift Time [ms]	Diffusion Const. D_T [cm^2/s]	MPV dE/dx, No Diffusion [MeV/cm]	MPV dE/dx at Cathode (Full Diff.) [MeV/cm]	Difference [%]
MicroBooNE [84]	3.00	2.33	5.85	1.69	1.79	5.9
ArgoNeuT [121]	4.00	0.295	12.0 (9.30)	1.72 (1.72)	1.76 (1.75)	2.3 (1.7)
ICARUS [37]	3.00	0.960	12.0 (9.30)	1.69 (1.69)	1.78 (1.77)	5.3 (4.7)
SBND [37]	3.00	1.28	12.0 (9.30)	1.69 (1.69)	1.79 (1.78)	5.9 (5.3)
DUNE-FD (SP) [36]	4.71	2.2	12.0 (9.30)	1.74 (1.74)	1.82 (1.81)	4.6 (4.0)

Table 4.1: Values of the most-probable-value (MPV) of dE/dx for a muon with 1 GeV of energy with no perturbation from diffusion (this is equivalent to a deposition at the anode) and at the cathode (where the effect of diffusion is largest). The MicroBooNE transverse diffusion constant is taken from the extrapolated measurement in that detector [122], while the others are taken from the Li et al. [116] (Atrazhev-Timoshkin [123]) prediction at an E-field of 500 V/cm. All MPVs neglect the density effect, which would affect the diffusion on and off quantities equally.

is small for large particle energy and small channel thicknesses. Typically, the Landau distribution is taken to be valid for $\zeta \cdot \not{p} < 0.01$ [114]. For our purposes, it is natural to leverage $\zeta \cdot \not{t}$.

4.2 Impact of Diffusion on LArTPC Calibration

In LArTPCs, the peak of the muon energy loss distribution (the most-probable-value, or MPV) is typically used as the observable of the distribution in calibrations (see, e.g.: [117, 118, 119, 120]). The main result of our derivation in section 4.1 is that diffusion changes the MPV across the detector. Table 4.1 lists the MPV dE/dx for energy depositions from a muon with 1 GeV of energy for a few LArTPC detector configurations including that of ICARUS.

The effect of diffusion can bias measurements attempting to equalize the response of the detector as a function of drift time (removing effects such as LAr impurities). Since

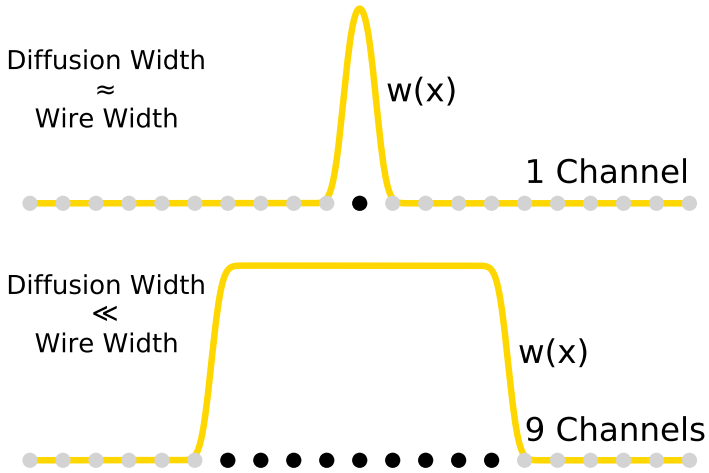

Figure 4.5: Measuring the charge wire-by-wire in a LArTPC (top) means that the thickness of the wire is significantly impacted by diffusion. Summing the charge across a large number of consecutive channels (bottom) diminishes this effect, which can be a useful technique for calibrations. From Ref. [113].

the underlying distribution of energy loss is also drift-dependent in the presence of diffusion, these procedures may be dividing-out a physical effect rather than just the detector response. The effect of smearing induced by transverse diffusion is to push the value of the dQ/dx MPV up along the drift length, as opposed to LAr impurities, which push it down. To combat this effect, one can "coarse-grain" the detector by summing hits across many consecutive channels along the track into each value of dQ/dx. By combining enough channels, the length of the effective channel spacing would dominate over the length of diffusion and thus the drift-dependent effect of diffusion could be made negligible. This process is demonstrated diagrammatically in figure 4.5.

4.3 Cosmic Muon Energy Scale

The derivation of the distribution of muon energy loss takes the mean energy loss as an external input. The mean energy loss must be specified to obtain the overall energy scale for particle energy loss. It is given by Bethe-Block theory [112], with [114]

$$\begin{aligned} \overline{\frac{dE}{dx}} &= \zeta T_{\max} \left[\ln \frac{2m_e c^2 \beta^2 \gamma^2 T_{\max}}{I_0^2} - 2\beta^2 - \delta(\beta\gamma) \right] \\ T_{\max} &= \frac{2m_e c^2 \beta^2 \gamma^2}{1 + 2\gamma m_e/M + (m_e/M)^2} \\ \zeta &= \rho \frac{K}{2} \frac{Z}{A} \frac{1}{T_{\max} \beta^2} \,. \end{aligned} \tag{4.13}$$

The relevant parameters are the particle (muon or proton) mass M, the electron mass m_e, the particle velocity β, the Lorentz factor γ, the mean excitation energy I_0, the argon charge number Z, the argon mass number A, the argon mass density ρ, and the constant K, with units MeV $\times$ cm^2/mol. In these equations, δ is the correction from the density effect [124]. We use the parameterization [125]

$$\delta(\beta\gamma) = \begin{cases} 0 & \log_{10}\beta\gamma < 0.2 \\ 2\ln\beta\gamma - 5.2146 + 0.19559 \times (3 - \log_{10}\beta\gamma)^3 & 0.2 \leq \log_{10}\beta\gamma \leq 3 \\ 2\ln\beta\gamma - 5.2146 & \log_{10}\beta\gamma > 3 \,. \end{cases} \tag{4.14}$$

Together, the mean energy loss in equation 4.13 and the MPV energy loss in equation 4.10 specify the energy scale for cosmic muons.

CHAPTER 5

CALIBRATION AND SIMULATION OF THE ICARUS LIQUID ARGON TIME PROJECTION CHAMBER

The detection of charge in the ICARUS detector is not perfectly uniform in space and time. Effects such as argon impurities [126, 127] and space charge effects [128, 129] can perturb the amount of charge measured across the detector. We have developed a procedure to calibrate these effects so that the non-uniformity they induce can be removed from the data. This procedure relies on the copious number of cosmic ray muons available to ICARUS, which operates under only 10 m.w.e. of concrete overburden. The procedures we have developed leverage many of the ideas first developed by the MicroBooNE surface LArTPC experiment [120], applied to the specific conditions observed in ICARUS.

In addition to calibrating the data, it is necessary to build an accurate simulation of ICARUS detector operation to perf physics analyses. The outline of ICARUS simulation is described in section 3.2. In this chapter we develop ways to tune the Monte Carlo simulation to match what is observed in ICARUS data. In particular, the signal shapes we observe in the detector depart from the nominal prediction made by Wire-Cell and GARFIELD. This departure is significant, although it is not drastically different from the level of disagreement observed by prior experiments applying the same simulation [130]. It is critical to precisely simulate the signal shapes in LArTPCs in order to accurately characterize the performance of signal processing and its impact on physics analysis. The leading systematic uncertainty associated with detector performance in prior LArTPC experiments has been the TPC signal shape (see, e.g., Ref. [131, 132, 133]). We have developed a novel approach to tune the underlying field responses input to Wire-Cell which match the simulated signal shapes precisely to what is measured in the detector.

This chapter is organized as follows. In section 5.1, we describe the procedure used to remove non-uniformities in the ionization charge response of the ICARUS TPCs and

demonstrate its impact on the charge resolution of the detector. In section 5.2, we describe the measurement of TPC signal shapes in ICARUS data, as well as the novel procedure we have developed to tune simulation to match the data. Finally, section 5.3 shows the comparison of charge resolution performance between ICARUS Monte Carlo simulation and data with the calibrations and simulation refinements described here applied.

5.1 Charge Scale Equalization

The goal of the charge scale equalization procedure is to make the TPC response to charge uniform in space and time. This is expressed in terms of the charge per length, or dQ/dx, of hits along particle tracks and showers. This quantity is used to compute energy loss (dE/dx) after correcting for electron-ion recombination (see chapter 6). As is detailed below (section 5.1.1), a number of effects perturb the charge response in ICARUS. To account for these effects, we have elected to equalize the charge response in three steps: an equalization in the drift direction (section 5.1.2), an equalization in the two wire plane directions, $\hat{y}$ and $\hat{z}$ (section 5.1.3), and a final TPC equalization (section 5.1.4). The performance of charge reconstruction in ICARUS after these equalization steps is shown in section 5.1.5.

As a surface detector, ICARUS has access to a copious number of cosmic muon tracks for use in these calibrations. Most muon tracks pass through the detector as nearly minimum-ionizing particles (MIPs). We use a selection of cosmic muons to do these calibrations. The muon tracks are required to cross the cathode. For such tracks, matching the energy depositions in both TPCs on either side of the central cathode enables the identification of the arrival time (t_0) of the track. Knowledge of this time is needed to properly compute and apply the drift time correction.

5.1.1 Effects Leading to Non-Uniformities in Charge Scale

Argon Impurities

As the ionization cloud from a particle deposition drifts to the wire plane, impurities in the argon (primarily O_2 and H_2O [126, 127]) absorb electrons. The attenuation is exponential and can be described by an electron lifetime, which is the mean time an electron will drift in the argon before it is absorbed. The electron lifetime in ICARUS ranged from 3-8 ms over the dataset considered here, which corresponds to a ∼5-15% average attenuation in the charge signal across the ∼1 ms ICARUS drift time.

Drift Field Distortions

The drift electric field in ICARUS is not perfectly uniform. While it is very stable across time, a few effects perturb its value spatially across the detector. The constant rate of cosmic muons ionizing the argon produces a build-up of positive argon ions, or space-charge, that affect the electric field [129, 128]. In addition, the cathode plane in ICARUS is not perfectly flat. This is an effect that was previously observed during the ICARUS run at Gran Sasso [134]. It is still present in the refurbished ICARUS installation at Fermilab at a much reduced magnitude. The biggest deflection is in the East Cryostat, which is bent by as much as 1.5 cm. This perturbs the electric field by a few percent, especially close to the cathode. Finally, there is a failure in the field cage in TPC EE that distorts the drift electric field in that TPC.

The drift field distortions can affect the charge scale in two ways. First, changes to the drift field affect the quantity of electric charge that recombines with argon ions at the point of ionization. Second, distortions to the drift field can deflect ionization tracks and therefore bias the reconstruction of the track pitch – the dx in dQ/dx.

At this time, we have not specifically calibrated the impact of drift field distortions.

We have measured the broad magnitude of the distortions and found them to be small – distortions to the drift field of at most a couple percent which deflect tracks by at most a couple centimeters. The charge scale calibrations here should be understood as folding in the (small) impact of drift field distortions.

Diffusion

As discussed in chapter 4, diffusion in the two directions transverse to the drift field direction impacts the measured charge scale from cosmic muons (see also Ref. [113, 135]). This effect is due to the underlying distribution of energy loss (dE/dx) from muons changing as a function of the magnitude of diffusion. This effect arises from the Landau-Vavilov nature of particle energy loss [111, 110]. The shape of the Landau distribution depends on the length of the muon observed by the readout wire [111]. In particular, the width of the distribution narrows and the location of the peak (which is typically used as the observable of the distribution [114]) shifts upward. Transverse diffusion smears the energy depositions observed by each wire, and thus broadens the length of the muon observed by each wire and impacts the Landau distribution of energy loss.

Therefore, transverse diffusion does not affect the detector response to charge (except perhaps indirectly through any impact on signal processing), but rather makes the "standard-candle" used to equalize the charge scale – cosmic muons – not truly standard in the drift direction. As a result, using cosmic muon depositions to equalize the charge scale produces a biased result, since such a procedure applies a non-uniform dE/dx distribution.

The impact of diffusion is significant because the smearing width of transverse diffusion in ICARUS ($\sim$1 mm for a deposition at the cathode) is on the order of the wire spacing (3 mm). It can therefore be mitigated by summing together adjacent hits on a cosmic muon track into a "coarse-grained" dQ/dx (see section 4.2). For example, summing together 10 hits obtains a dQ/dx with an effective spacing of 10 wires, or 3 cm, much larger than the smearing

width of transverse diffusion. This method also allows us to study the impact of diffusion in data. The drift direction profile of the "coarse-grained" dQ/dx is impacted exactly the same by detector non-uniformities (mostly argon impurities and drift field distortions) as a "wire-by-wire" dQ/dx, but the two observables have different underlying dE/dx distributions which are impacted differently by diffusion.

Figure 5.1 demonstrates this effect. Both the coarse-grained and wire-by-wire dQ/dx attenuate across the drift direction, since the biggest effect is from argon impurities. However, the two values also get closer at larger drift times. The coarse-grained measurement has a longer track sensitive length constant across the detector, and thus a larger dE/dx peak value. The wire-by-wire measurement has a smaller track sensitive length that increases with increasing transverse diffusion across the drift direction. Therefore, the wire-by-wire peak dE/dx is smaller but approaches the coarse-grained dE/dx peak at large drift times. The magnitude of the effect is hard to predict because it depends on the unknown momentum of the through-going muons used in the measurement. Its direction though is consistent with expectation. This is the first confirmation in data of the impact of transverse diffusion on the muon charge scale, which has previously only been predicted from simulation [113, 135]. It validates the approach we have taken in ICARUS towards drift direction charge equalization, as detailed in section 5.1.2.

Induction Wire Plane Intransparency

The induction wire planes in ICARUS (primarily the middle induction plane) absorb charge in a position dependent way across the detector. This effect induces significant variations ($\sim 20\%$) in the charge response on all three readout wire planes. On the collection plane, it directly reduces the amount of visible charge. On the induction planes, the unipolar collection signal from absorbing charge competes with the bipolar induction signal from non-absorbing charge.

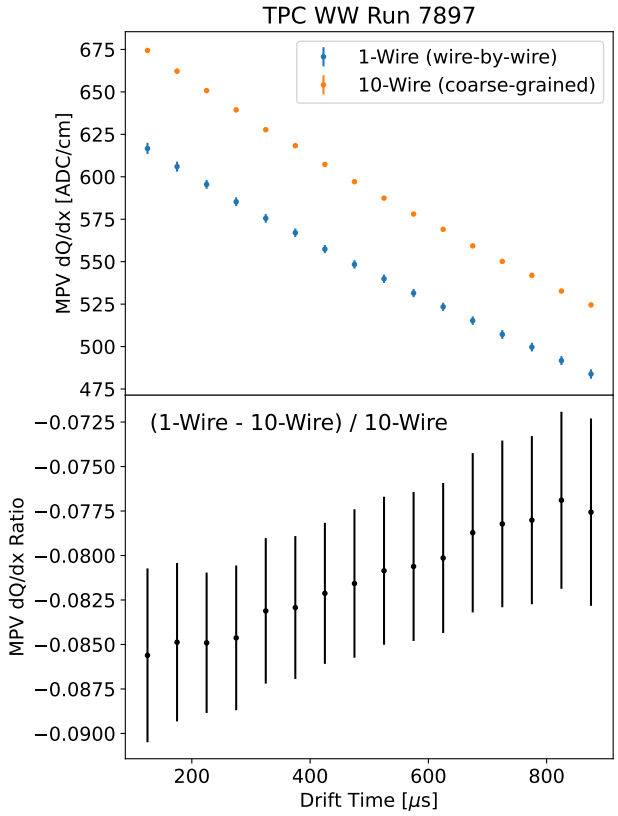

Figure 5.1: Comparison of the 1-Wire (wire-by-wire) and 10-Wire (coarse grained) charge measurements for one ICARUS run in TPC WW. In the top panel, the most-probable-value (MPV) of dQ/dx is plotted as a function of the drift time for both measurements. In the bottom panel, a ratio of the two measurements is shown. The 1-Wire measurement MPV approaches the value of the 10-Wire measurement MPV due to diffusion in the direction transverse to the drift direction.

A GARFIELD simulation [109] of the nominal ICARUS wire plane configuration predicts that the inductions plane absorb 7% of the charge. Thus, to explain the observed variations, the wire plane configuration of ICARUS must depart from the design specification in a position dependent way across the detector. We have checked all components of the wire bias outside of the cryostat and have found only a couple of discrete failures, which have been correlated to features in the non-uniformity but do not explain all of them. Inside the cryostat, some departure of either the wire bias or the inter-plane wire spacing from the nominal configuration must conspire to produce the spatial variations observed in ICARUS.

We have investigated the possibility of changing the ICARUS detector configuration to

mitigate the impact of this effect. The supplied wire bias cannot be turned any higher due to the rating of cables carrying the bias inside the cryostat. We tested operating at a reduced drift electric field (which increases the relative effect of the wire bias) in Summer 2022. We found that the increased effect of recombination and larger attenuation from argon impurities reduced the signal-to-noise in ICARUS by too much to be feasible, especially on the induction planes.

Although significant, the variation in the induction wire plane intransparency has been found to be very stable across time. Thus, we can calibrate out the effect using the very large sample of cosmic muons available to ICARUS.

Channel Gain Variation

The gain of different channels in the ICARUS TPC are not perfectly uniform. This effect has been measured by directly pulsing the electronics with a constant pulse. The measurement found that the variation of gain in different channels is not large, and that it is a smooth effect across the detector. Thus, the spatial resolution of the correction factors computed in section 5.1.3 ($10\times10\,\mathrm{cm}^2$) is adequate to address this effect.

5.1.2 Drift Direction Equalization

The drift direction equalization step corrects charge reconstruction for effects that vary with the ionization drift time. The primary such effect is attenuation from argon impurities. Since the electron lifetime varies across the ICARUS dataset, this equalization is done per-DAQ-run. One DAQ run in ICARUS lasts from a few hours to a few days, and the electron lifetime does not vary significantly over such a period.

The calibration is done with depositions from anode-cathode crossing tracks. The cathode crossing identification is done by matching a pair of aligned tracks in the two TPCs on either side of the central cathode plane. A cut on the drift direction length of the track

in either TPC ensures that it also crosses the anode in that TPC. As described in section 5.1.1, to mitigate the impact of diffusion, the charge is summed in groups of 10 wires into a "coarse-grained" dQ/dx. The coarse-grained depositions are grouped by drift time and are fit with a Landau distribution convolved with a Gaussian distribution to extract the most-probable-value (MPV) of the distribution. The MPV as a function of drift time is fit to an exponential to obtain an effective electron lifetime that parameterizes the non-uniformity. This electron lifetime should be understood to be effective because, while argon impurities have the dominant impact, the measured lifetime also includes effects from field distortions and imperfections in signal processing. We have found that an exponential is able to model the charge non-uniformity in all runs across the ICARUS dataset.

Figure 5.2 shows the electron lifetime across the ICARUS dataset, as well as the corresponding mean signal attenuation in the drift direction. The electron lifetime was maintained at $\sim$3 ms in the West cryostat and at $\sim$5 ms in the East cryostat across Run 1. During Run 2, the lifetime in the West cryostat reached 8-10 ms. There are slight differences between the East and West TPCs in both Cryostats. This is not expected from the argon purity since the same argon circulates in both TPCs in a cryostat. Rather, the differences between the TPCs are an indication of different field distortions in the TPCs which perturb the effective electron lifetime measured here.

5.1.3 Wire Plane Equalization

The wire plane equalization step corrects charge reconstruction for detector effects that vary across the two directions in the plane of the readout wires: $\hat{y}$, the vertical direction, and $\hat{z}$, the (BNB) beamline direction (see figure 3.6). The calibration is done with coarse-grained depositions from through-going cathode-crossing tracks. Depositions are binned in terms of their $\hat{y} - \hat{z}$ location on the wire plane in $10 \times 10\,\mathrm{cm}^2$ bins. This is as small a spatial resolution as is possible given the statistics of cosmic muons ($\sim$ 3 million) available for the calibration.

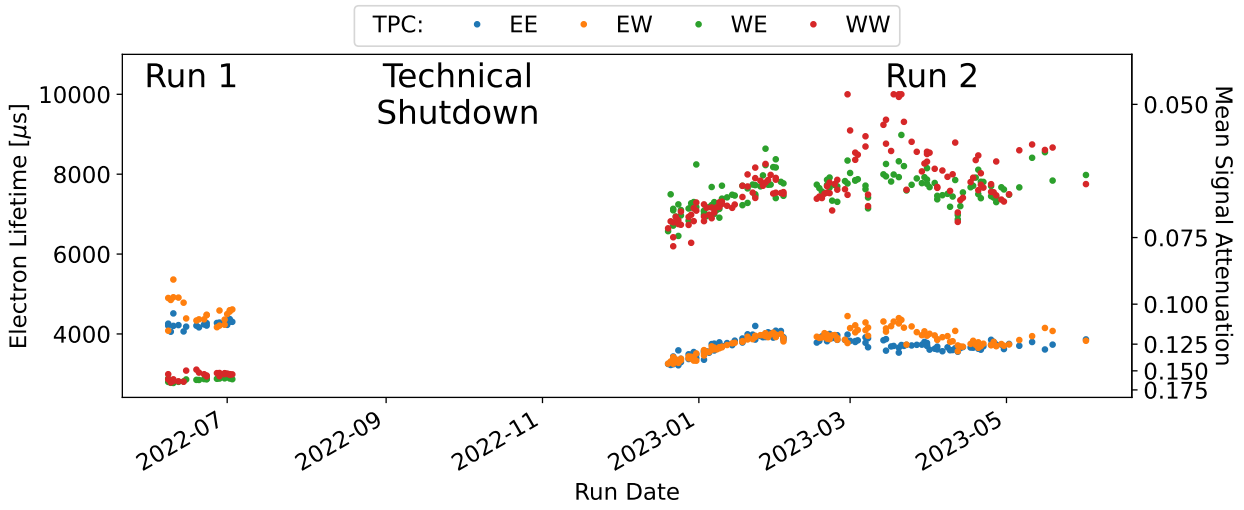

Figure 5.2: Measured effective electron lifetime values measured in each ICARUS TPC across the Run 1 and Run 2 datasets. The right axis shows the corresponding average signal attenuation across the ∼1 ms ICARUS drift period.

As in the drift direction equalization, in each spatial bin the distribution of dQ/dx values is fit with a Landau distribution convolved with a Gaussian distribution to extract the MPV. The MPV in each spatial bin is converted into a scale factor computed to keep the mean MPV across the TPC fixed. The scale factors are computed individually in each TPC in each wire plane. We have also split up the dataset by run to study time dependence of the spatial variations.

The spatial uniformity maps are shown in the Run 1 dataset for the front induction, middle induction, and collection planes in figures 5.3, 5.4, and 5.5, respectively. Some, but not all, of the features in the map have been traced to known faults in the detector. For example, the band of small dQ/dx around $z = 0$ in each TPC is due to perturbations to the applied wire bias field by the presence of a mechanical bar supporting the front induction wires. There are a couple of discrete changes in the uniformity between Runs 1 and 2. The difference in the uniformity between Run 1 and Run 2 is shown for the collection plane in figure 5.6. These changes have been traced to a couple of changes to the detector operation during the 2022 technical shutdown: two additional failures of middle induction plane wire

bias voltage supplies, and a few readout board replacements on the collection plane (which have a slightly different gain). We have not observed any time dependence of the spatial uniformity within either Run 1 or Run 2.

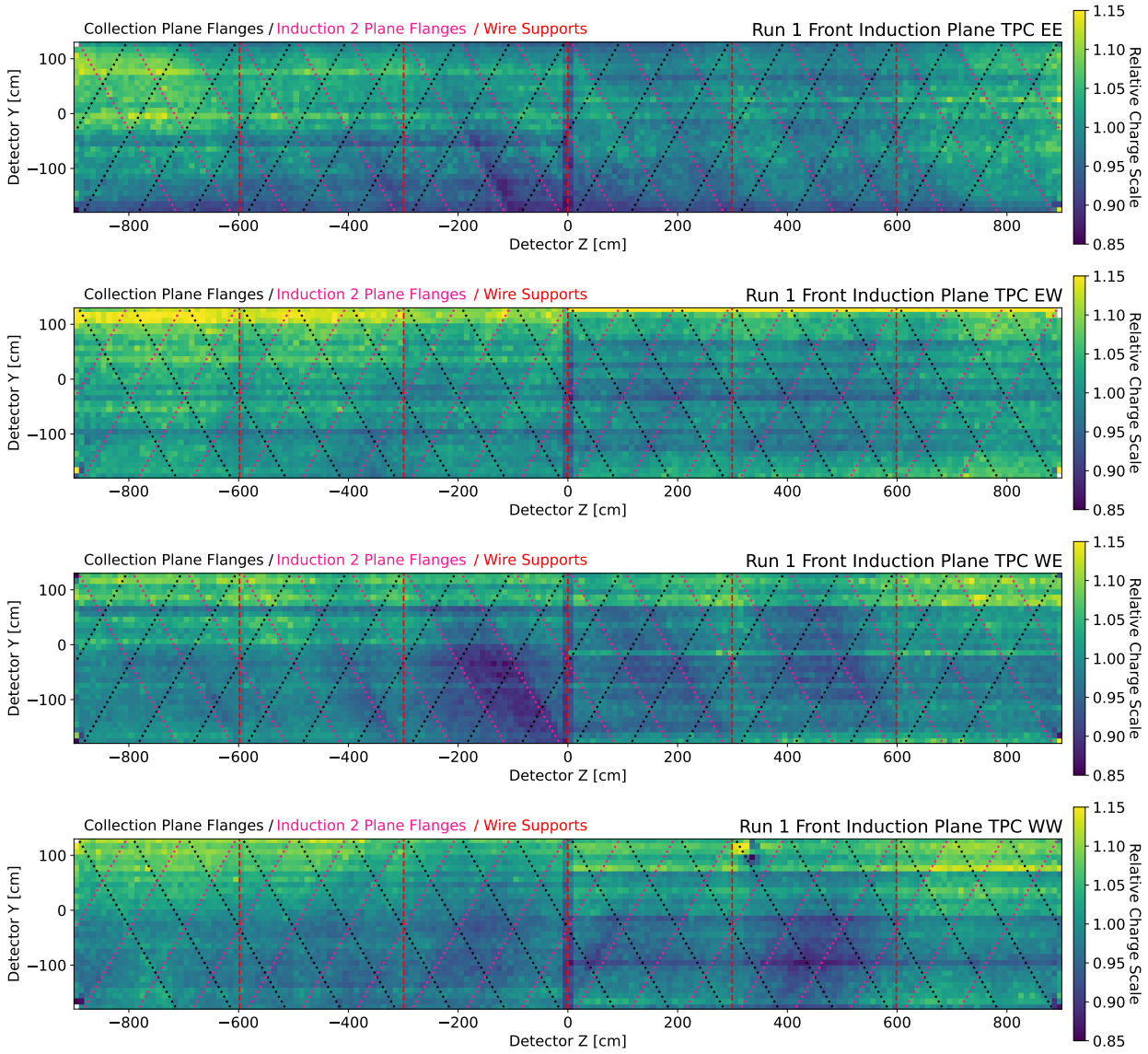

Figure 5.3: Coarse-grained MPV dQ/dx values in $10\times10\,\text{cm}$ bins in each of the ICARUS TPCs on the front induction plane across the Run 1 dataset. The borders between different flanges that supply the wire bias to groups of wires on collection and induction are overlaid, as well as the location of mechanical support structures on the front induction wire plane.

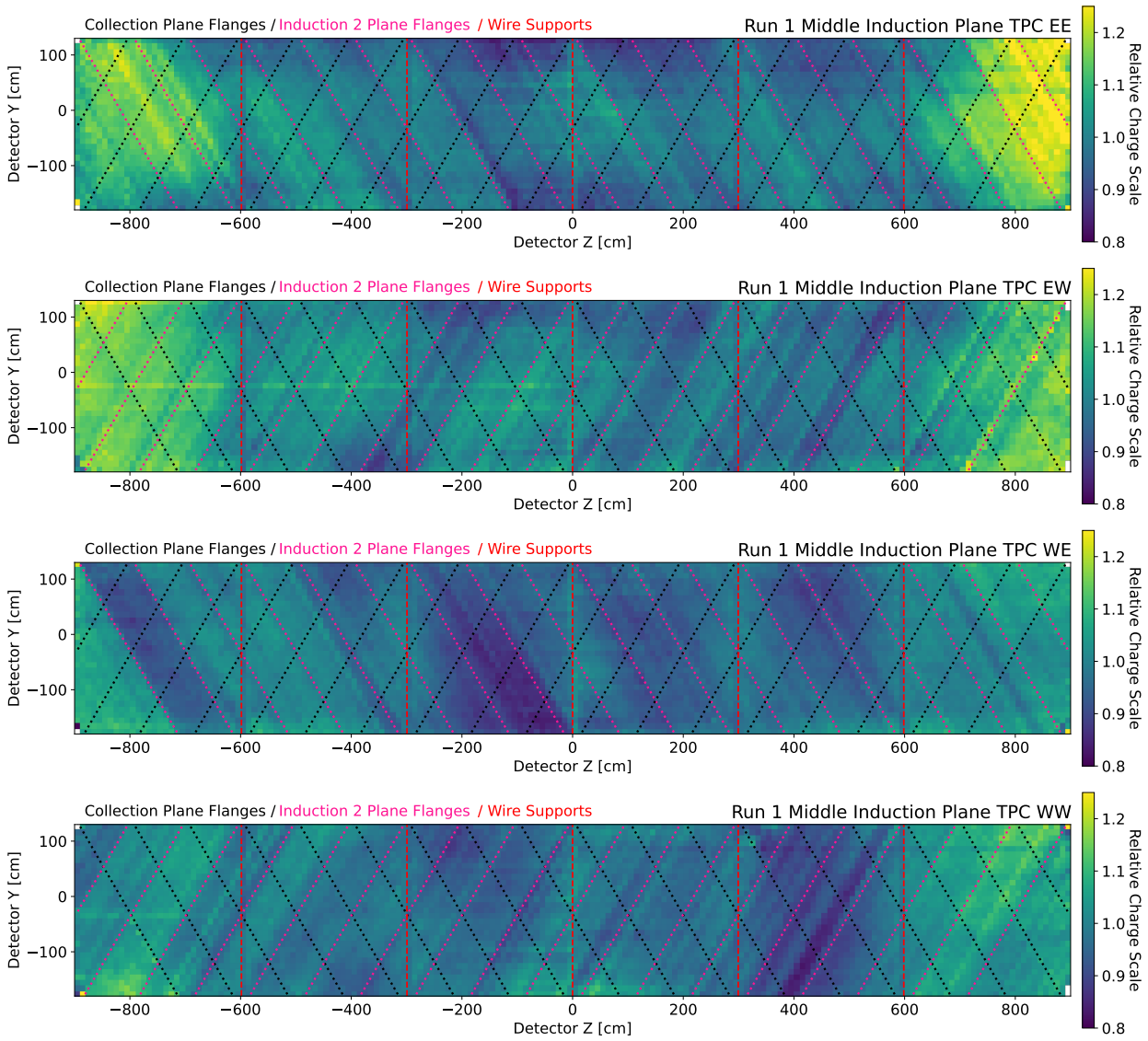

Figure 5.4: Coarse-grained MPV dQ/dx values in $10\times10\,\mathrm{cm}$ bins in each of the ICARUS TPCs on the middle induction plane across the Run 1 dataset. The borders between different flanges that supply the wire bias to groups of wires on collection and induction are overlaid, as well as the location of mechanical support structures on the front induction wire plane.

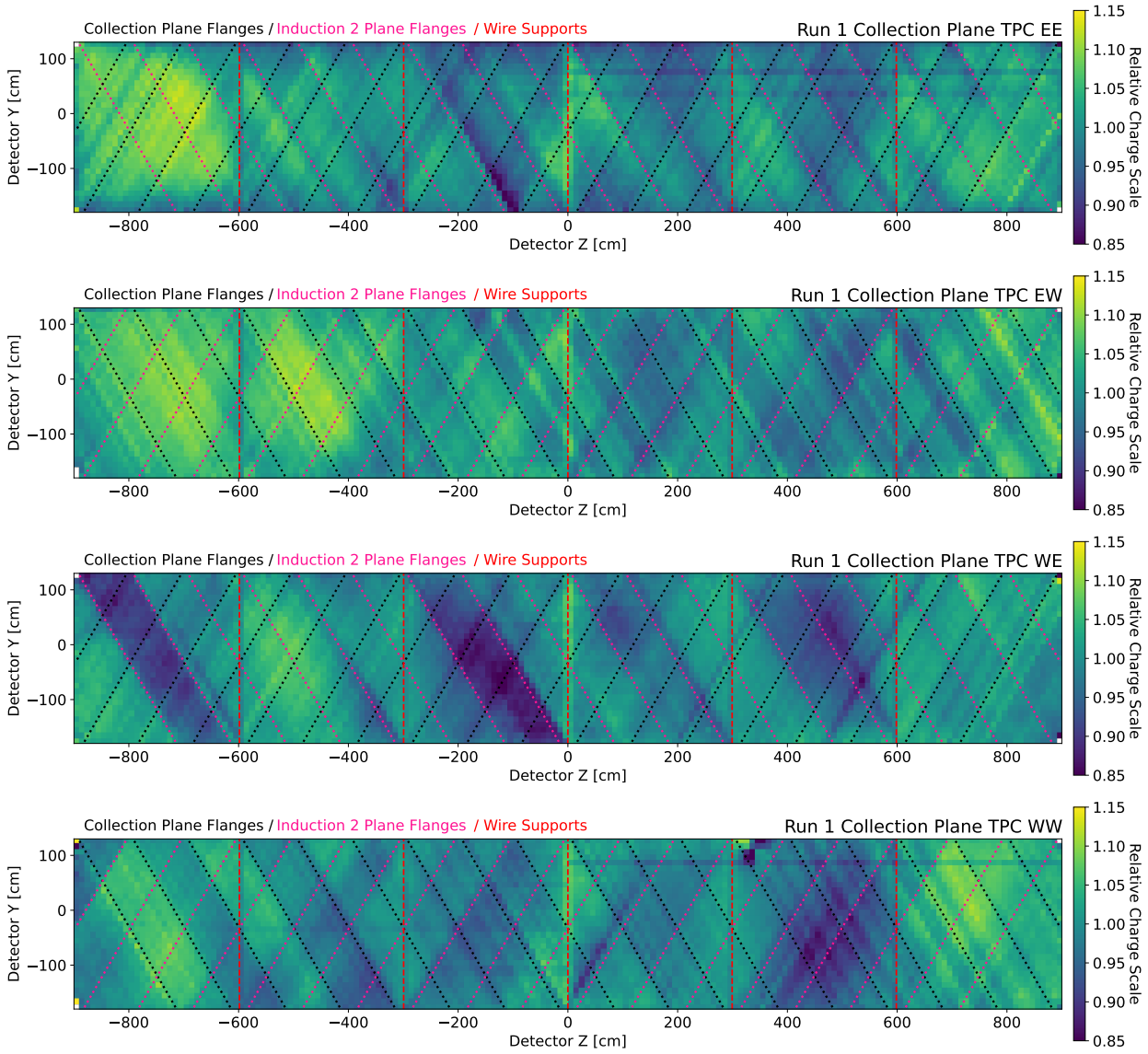

Figure 5.5: Coarse-grained MPV dQ/dx values in $10\times10\,\mathrm{cm}$ bins in each of the ICARUS TPCs on the collection plane across the Run 1 dataset. The borders between different flanges that supply the wire bias to groups of wires on collection and induction are overlaid, as well as the location of mechanical support structures on the front induction wire plane.

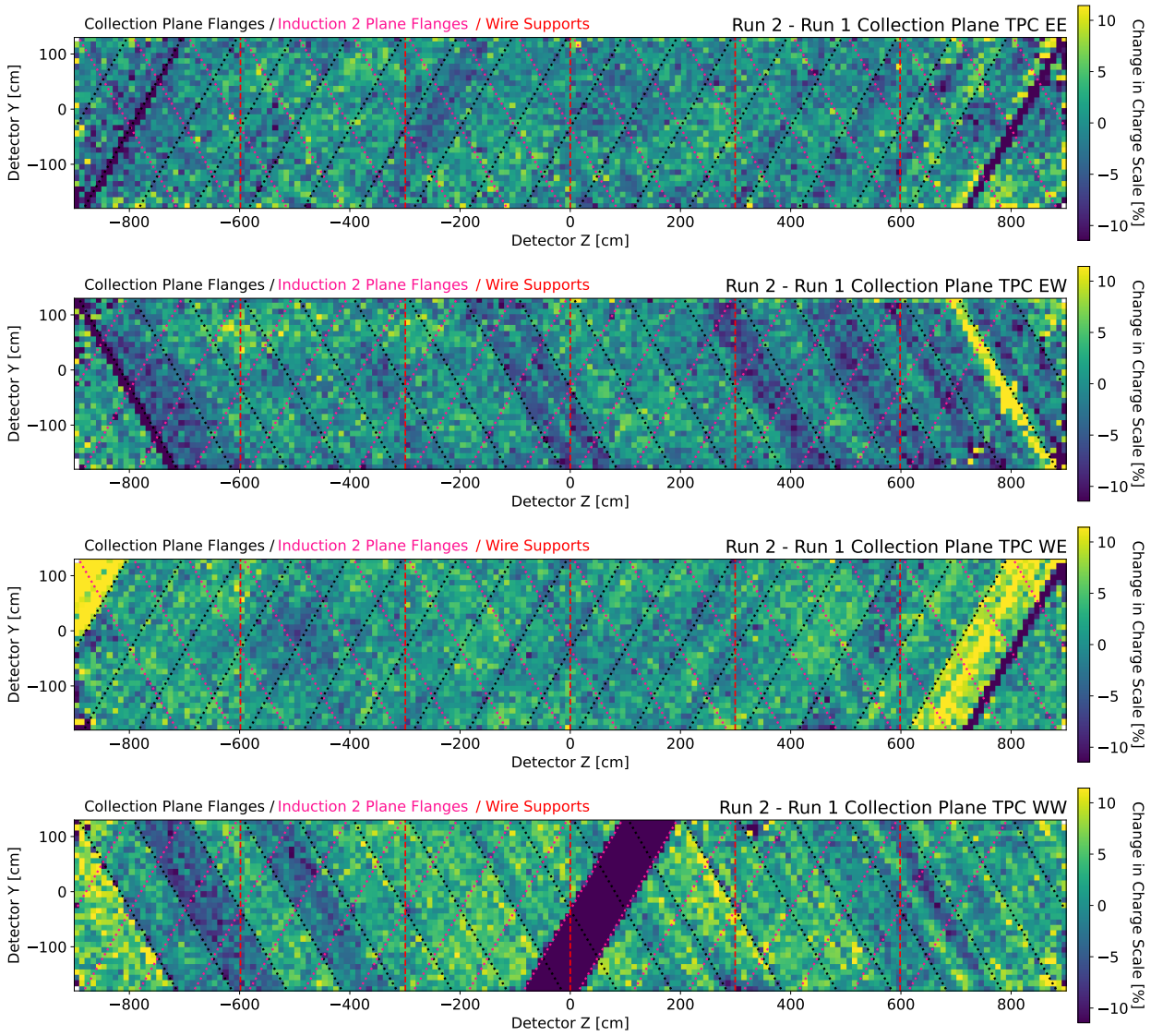

Figure 5.6: Differences between the Run 1 and Run 2 datasets of coarse-grained MPV dQ/dx values in 10×10 cm bins in each of the ICARUS TPCs on the collection plane. The borders between different flanges that supply the wire bias to groups of wires on collection and induction are overlaid, as well as the location of mechanical support structures on the front induction wire plane.

5.1.4 TPC Equalization

As a final step, the gains in the four separate TPCs in ICARUS are equalized. This equalization is done separately for both ICARUS runs. This corrects for any broad differences in the gain between the different TPCs or runs. The charge scale for this equalization is computed using stopping cosmic muons, as opposed to throughgoing muons. This choice is made because stopping cosmic muons are used to measure the absolute gain in ICARUS in the ionization energy scale calibration (chapter 6). Equalizing the TPC gain with the same sample ensures that different TPCs are completely consistent in the gain fit.

The charge scale is computed from distributions of coarse-grained dQ/dx with the drift and wire plane direction equalizations applied. The distributions are split up in terms of the stopping muon track residual range and drift time to select for a single peak dE/dx in each distribution. The residual range is binned in steps of 5 cm from 200-300 cm. The drift time is binned in steps of 100 µs from 500-900 µs. Each histogram of equalized dQ/dx is fit to a Landau distribution convolved with a Gaussian distribution to extract the MPV. The MPVs are averaged over residual range to obtain a single average for each drift time. Then, a scale factor is fit to the mean MPVs per each TPC per each run. This scale factor is normalized so that TPC EW in Run 1 has a scale of 1. The average MPVs and the scale factors are shown in figure 5.7.

5.1.5 Equalization Results

Figure 5.8 plots the distribution of coarse-grained dQ/dx values from throughgoing cathode-crossing cosmic muons before and after the equalization procedure. The width of the dQ/dx distribution noticeably narrows after applying the corrections developed in this section. The narrowing is most significant on the collection plane, where the inherent broadening from readout noise has the smallest effect.

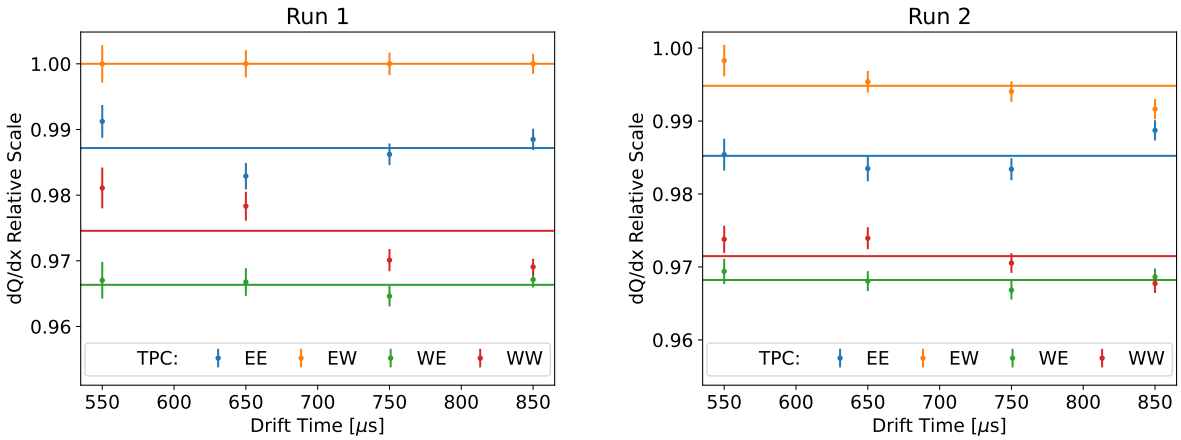

Figure 5.7: Computation of TPC equalization scale factors in each TPC in both runs. The scale factors are computed by equalizing the MPV of stopping cosmic muon depositions across four drift time bins, averaged across a residual range from 200-300 cm. These are shown by the data points per-TPC. The scale factors are given by the horizontal lines. They are normalized so that TPC EW in Run 1 has a scale of 1.

5.2 Signal Shape Measurement and Simulation

Inaccuracies in the simulation of ionization signal shapes in LArTPCs can bias the estimation of the performance of tracking and calorimetry in the detector. In order to minimize these biases, we carry out a data-driven tuning of the ionization signal shape used in ICARUS Monte Carlo simulation. The measurement of the signal shapes in data and Monte Carlo simulation is shown in section 5.2.1. The procedure to tune the simulated signal shape to match the data is described in section 5.2.2.

5.2.1 Signal Shape Measurement

The ionization signal shapes in the ICARUS detector have been measured using a technique first pioneered in the MicroBooNE experiment [130]. The signal shapes of ionizing particle tracks depend on their orientation relative to each wire plane as determined by the θ_{xw} angle (see figure 4.2). The measured signal shapes across three bins of θ_{xw} are compared between data and Monte Carlo simulation in figure 5.9. There is significant disagreement between

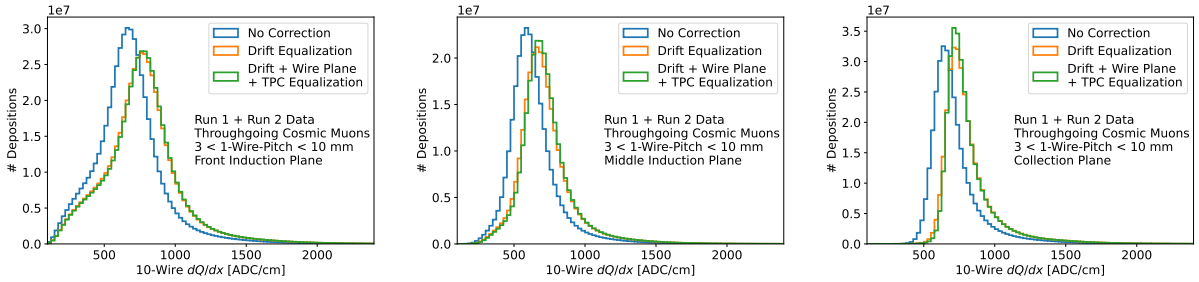

Figure 5.8: Distribution of coarse-grained dQ/dx values for throughgoing cosmic muons in the Run 1 and Run 2 datasets uncorrected, and with the drift and wire plane equalization corrections applied. Shown for the front induction plane (left), the middle induction plane (middle), and the collection plane (right).

the data and the nominal simulation on all three planes. We have identified three main causes for this disagreement: a tail in the channel electronics response not in the nominal shape, distortions in the field response indicated by the intransparency of the induction planes to charge, and differences in the signal-to-noise ratio between the simulation and the data. The first two causes are directly connected to the signal shape. The last is driven by variations in the detector response to charge (such as the varying electron lifetime measured in section 5.1.2, and the varying induction intransparency measured in section 5.1.3) that are not simulated. These variations primarily impact the front induction plane, where the noise is larger and the dependence on the exact signal-to-noise ratio is significant. In the tuning procedure we describe in the next section, we therefore elect to apply the fit only to the measurements on the middle induction and collection planes. The tuning procedure can in principle be applied to the front induction plane once the differences in the variation of signal-to-noise are addressed.

5.2.2 Fit Procedure

We have developed a novel procedure to tune simulated signal shapes to match their measurement in data. This procedure tunes the input single electron field generated by GARFIELD [109] and applied by the Wire-Cell package, which is used in the ICARUS detector signal

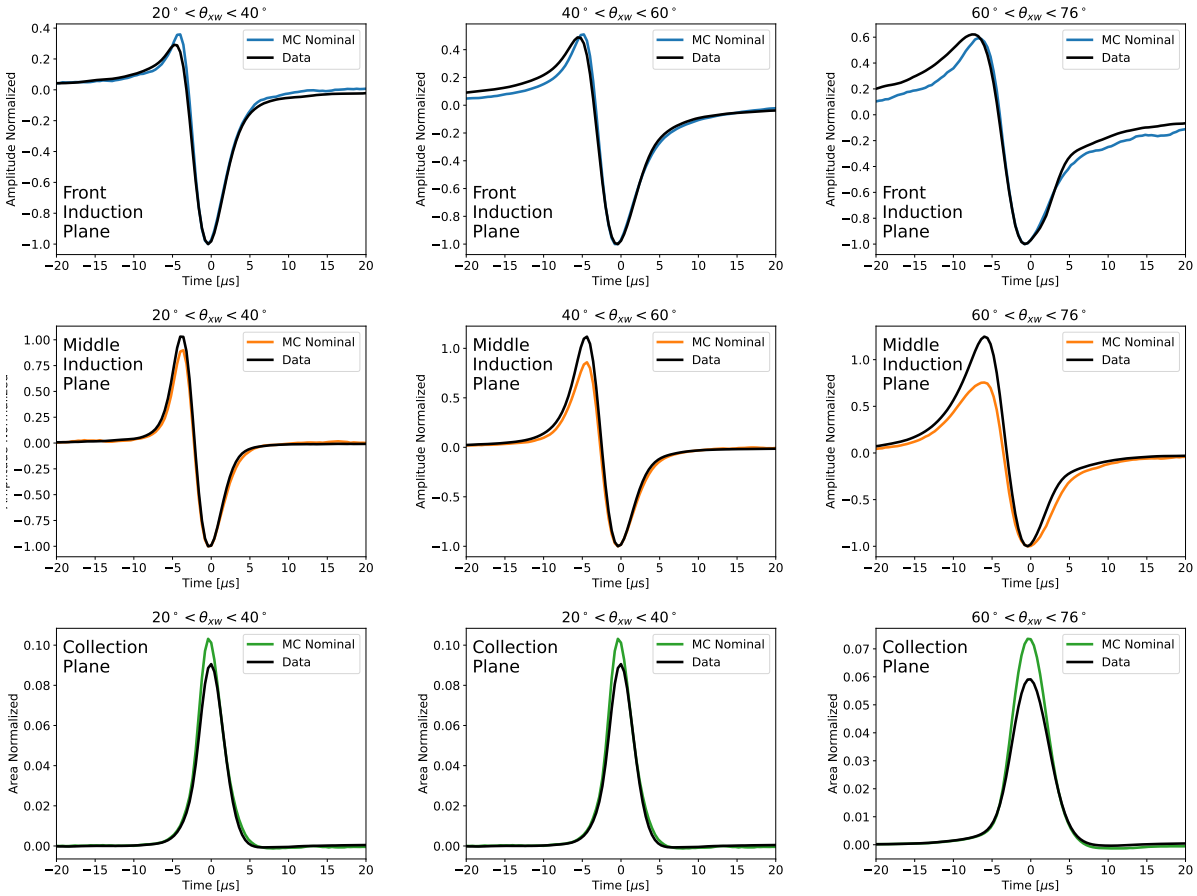

Figure 5.9: Comparison of the signal shape measurement between data and the nominal (untuned) GARFIELD-based Monte Carlo simulation ("MC Nominal") on the front induction plane (top row), middle induction plane (middle row), and collection plane (bottom row). Shown are measured signal waveforms averaged across θ_{xw} ranges of [20°, 40°] (left column), [40°, 60°] (middle column), and [60°, 76°] (right column).

shape simulation. We defer to the initial paper on Wire-Cell for a detailed description of how it works [108]. Here we include an abbreviated discussion necessary to understand the fitting procedure.

Wire-Cell forms signal shapes by summing the single electron field response on each wire from ionization electrons in particle energy depositions. The single electron field response depends on the location of the electron in the direction perpendicular to the wire direction (which we call $\hat{w}$, see figure 4.2). The field response is significant even when the electron is not directly adjacent to the wire. Wire-Cell applies single electron field responses calculated

every 0.3 mm for 3 cm (10 wire-spacings) on either side of each wire. Individual clusters of electrons in the simulation arrive in between the discrete locations where the field responses are calculated, so for a given deposition Wire-Cell linearly interpolates between the two on either side. The combined field response from all ionization electrons in a readout on a given wire is then convolved with the electronics response to create the signal shape for that readout.

The nominal ICARUS single electron field responses are computed by a GARFIELD simulation of the nominal ICARUS wire plane configuration. The nominal electronics response is a Bessel shaping function with a width of 1.3 µs. That the observed signal shapes depart from the nominal simulation indicates that the ICARUS detector departs from this nominal configuration in some way. First, we have observed a tail in the electronics response due to imperfect pole-zero cancellation that we measure separately and include in the tuned electronics response. The remaining differences are harder to attribute and ultimately depend on the inaccessible state of the TPCs inside both cryostats. We have thus taken the perspective that a data driven approach is an apt fix to these discrepancies. We fit the signal shapes in the simulation directly to the measurement. The objects in the fit are the position dependent single electron field responses and the electronics response[1], although we do not claim to be more accurately measuring any of these objects individually after the fit. We only attempt to model their combined impact on the signal shape. Monte Carlo simulation with the signal shapes tuned by this procedure demonstrates a much improved match in the signal shape between data and Monte Carlo simulation, as is shown below.

1. Imperfections in the means to directly pulse the ICARUS TPC readout electronics prevent a precise direct measurement of the electronics response. Instead, the fit described here produces an "effective" electronics response adequate to describe the final signal shape.

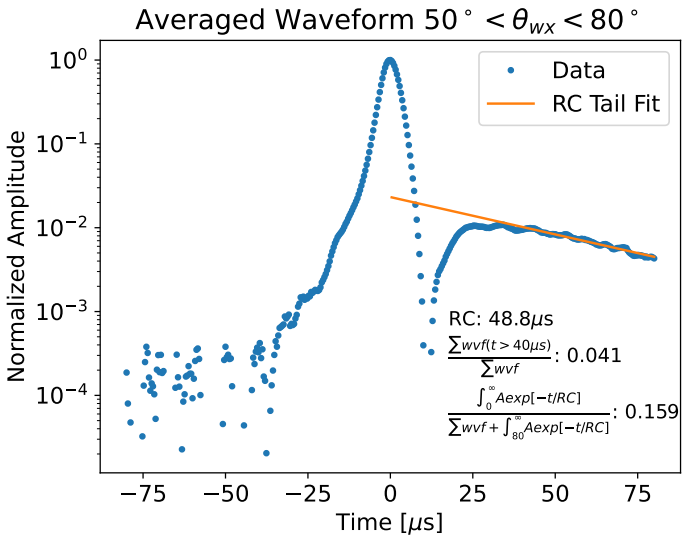

Figure 5.10: Averaged waveform from high angle tracks used to measure the exponential tail in the electronics response.

Electronics Response Tail Measurement

We have observed a long tail, with a time constant of ∼50 µs, in the electronics response of ICARUS. The origin of the effect is imperfect pole-zero cancellation in the transfer function of the electronics. The tail is measured by averaging together waveforms on the collection plane from a large number of high angle muons (large θ_{xw}). High angle muons are used because the coherent noise subtraction can depress the effect of the tail when the track is closer to perpendicular to the drift direction. An exponential ($e^{-t/\tau}$) is fit to the averaged waveform values between 40-80 µs (100-200 ticks), which is far past where the field response impacts the shape. This fit obtains an exponential with a time constant of 48.8 µs that contains 15.9% of the charge from the pulse. The fit exponential is convolved with the nominal electronics response to obtain the effective electronics response. Figure 5.10 displays the data and the fit. The exponential describes the waveform shape well in the fit region.

Signal Shape Model

We have developed a model of the signal shape measurement that takes the single electron field responses and the electronics response as input and produces the expected signal shape as a function of the track angle θ_{xw}. The fit of the field and electronics responses are done by fitting this model to the measured signal shapes.

The model first turns the set of single electron field responses (201 total, each spaced 0.3 mm apart) into an angle dependent "track field response". This is done by sub-sampling the single electron field responses. Each sample linearly interpolates the responses on either side (as is done in Wire-Cell). The samples are shifted in time according to the chosen track angle and summed together. Given the single electron field responses $s_{-30\,\mathrm{mm}}(t), s_{-29.7\,\mathrm{mm}}(t), \ldots, s_{30\,\mathrm{mm}}(t)$ relative to the wire at time t, the track field response $f(\theta_{xw}; t)$ is equal to

$$f(\theta_{xw};t) = \sum_{x_i} \left(1 - \frac{x_i - \lfloor x_i \rfloor}{0.3\,\mathrm{mm}}\right) \cdot s_{\lfloor x_i \rfloor} \left(t - \frac{x_i \tan\theta_{xw}}{v_D}\right) + \left(1 - \frac{\lceil x_i \rceil - x_i}{0.3\,\mathrm{mm}}\right) \cdot s_{\lceil x_i \rceil} \left(t - \frac{x_i \tan\theta_{xw}}{v_D}\right), \tag{5.1}$$

where v_D is the drift velocity, x_i are the sampled locations, $\lfloor x \rfloor$ is the position immediately below x of a sampled single electron field response, and $\lceil x \rceil$ is the position immediately above x of a sampled single electron field response. In our implementation, we sub-sampled the single electron field responses every 0.03 mm for 2001 sub-samples. The sampled nominal field responses shifted by a few example track angles is shown in figure 5.11. The sum of these samples (i.e., the track field response $f(\theta_{xw}; t)$) is shown for a few example track angles in figure 5.12. The un-physical spikes in the field responses are caused by the finite sampling spacing of the single electron field responses and are smoothed out by the electronics response, as specified below.

The track field response is convolved with the electronics response $e(t)$ to obtain the track signal shape. In addition, the measurement of the signal shape will not perfectly reproduce

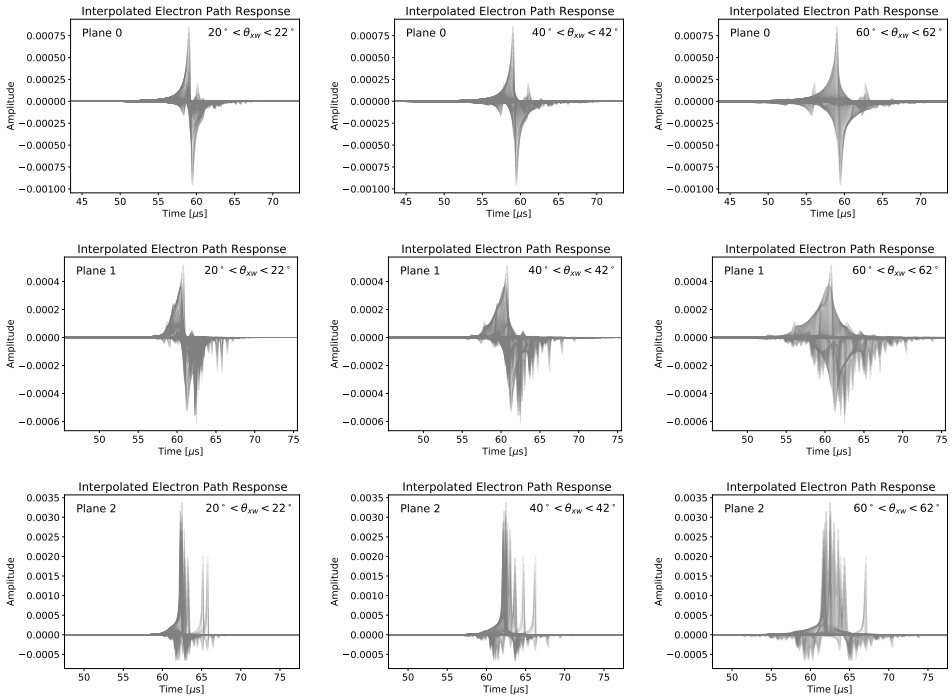

Figure 5.11: Sampled interpolated single electron field responses, shifted by track angle, as defined in equation 5.1. Shown for the front induction plane (top row), middle induction plane (middle row), and the collection plane (bottom row).

the signal. The alignment of signals from different muons in the averaged waveform will not be perfect due to detector noise. The resolution from this misalignment smears the shape. (Other broadening effects, such as diffusion, are insignificant.) To account for this effect, the signal shape is convolved with a "measurement kernel" $m(\theta_{xw}; t)$. The final measured track signal shape $S(\theta_{xw}; t)$ is thus equal to

$$S(\theta_{xw}; t) = \left(f(\theta_{xw}) \circledast e \circledast m(\theta_{xw})\right)(t)\,, \tag{5.2}$$

where $\circledast$ denotes a convolution.

The measurement kernel is determined from a fit on ICARUS simulation where the underlying field and electronics response is known. It is found to be well approximated by a Gaussian with a width σ depending on the track angle by a form $\sigma\left(\theta_{xw}\right) = \sqrt{a^2 + b^2 \tan^2 \theta_{xw}}$,

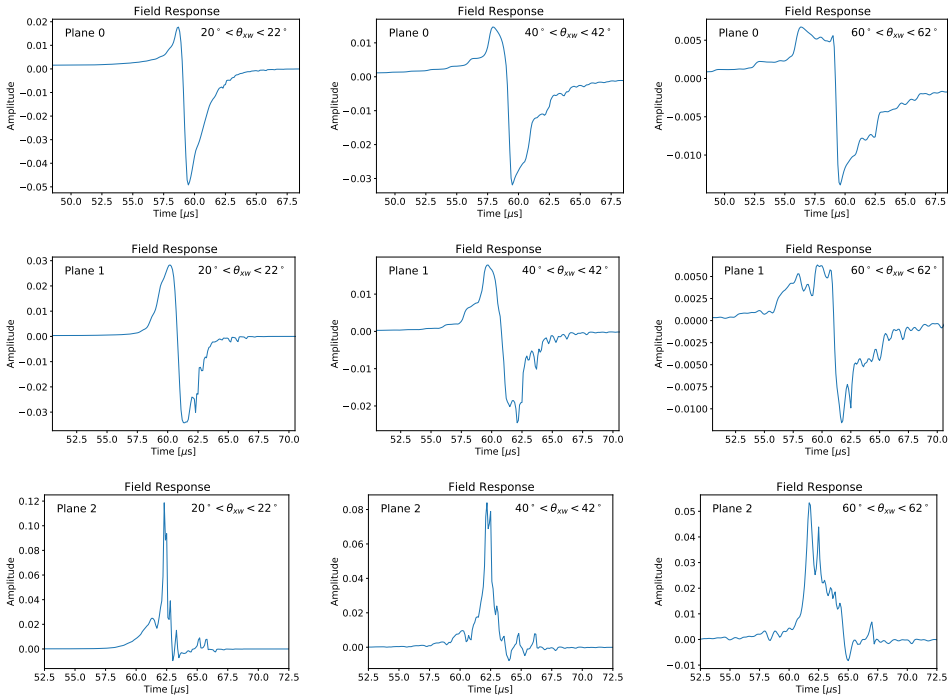

Figure 5.12: Track field response $f(\theta_{xw}; t)$, as defined in equation 5.1. Shown for the front induction plane (top row), middle induction plane (middle row), and the collection plane (bottom row).

where a and b are parameters individual to each wire plane. The measurement kernel width as determined in Monte Carlo simulation on each wire plane is shown in figure 5.13 for the middle induction and collection planes, on which the fit is performed.

The fit to data is done by matching the measured signal shape S to the data by fitting the electronics response e and the single electron field responses s_i (implicit in the track field response f). In this fit, non-linear transformations parameterized by the fit are applied to the nominal field and electronic responses. The details of these transformations are in appendix C. The fit is done on all measured track angles at once.

Fits

The results of the fit are shown in figures 5.14 and 5.15 for the middle induction plane and collection plane respectively. The fit is done in angle bins 2° in width from $\theta_{xw} = 20° - 76°$.

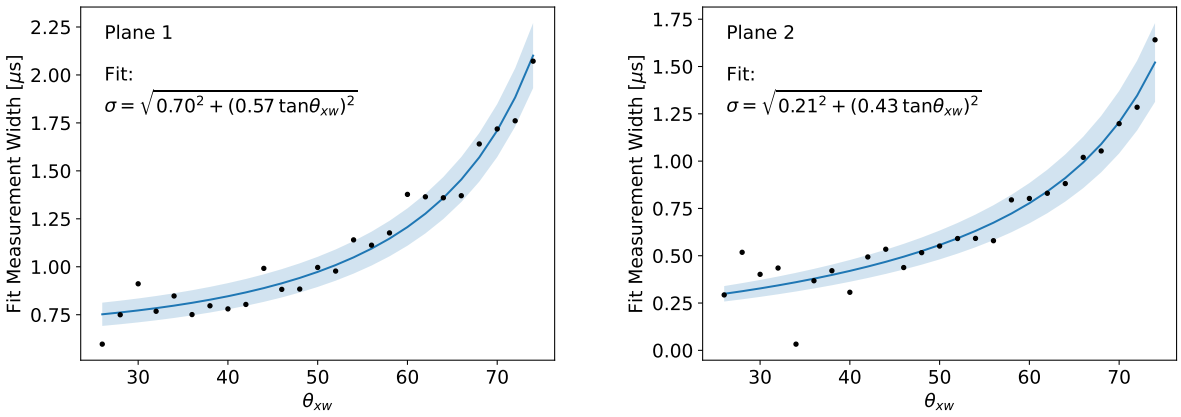

Figure 5.13: Broadening from resolution on track alignment in the signal shape measurement procedure as measured in ICARUS simulation. The width of the broadening is plotted as a function of the track angle which determines the signal shape, θ_{xw}.

The fit improves the signal shape model at all angles on each plane.

5.2.3 Tuned Signal Shape Results

As a validation of the tuned signal shapes, we compare the signal shape measurement from data against Monte Carlo simulation generated with the tuning applied. The comparison is shown above for the nominal signal shapes in figure 5.9. Figure 5.16 shows the comparison on the middle induction and collection planes with the tune applied. The modeling is improved in all angle bins on the both planes.

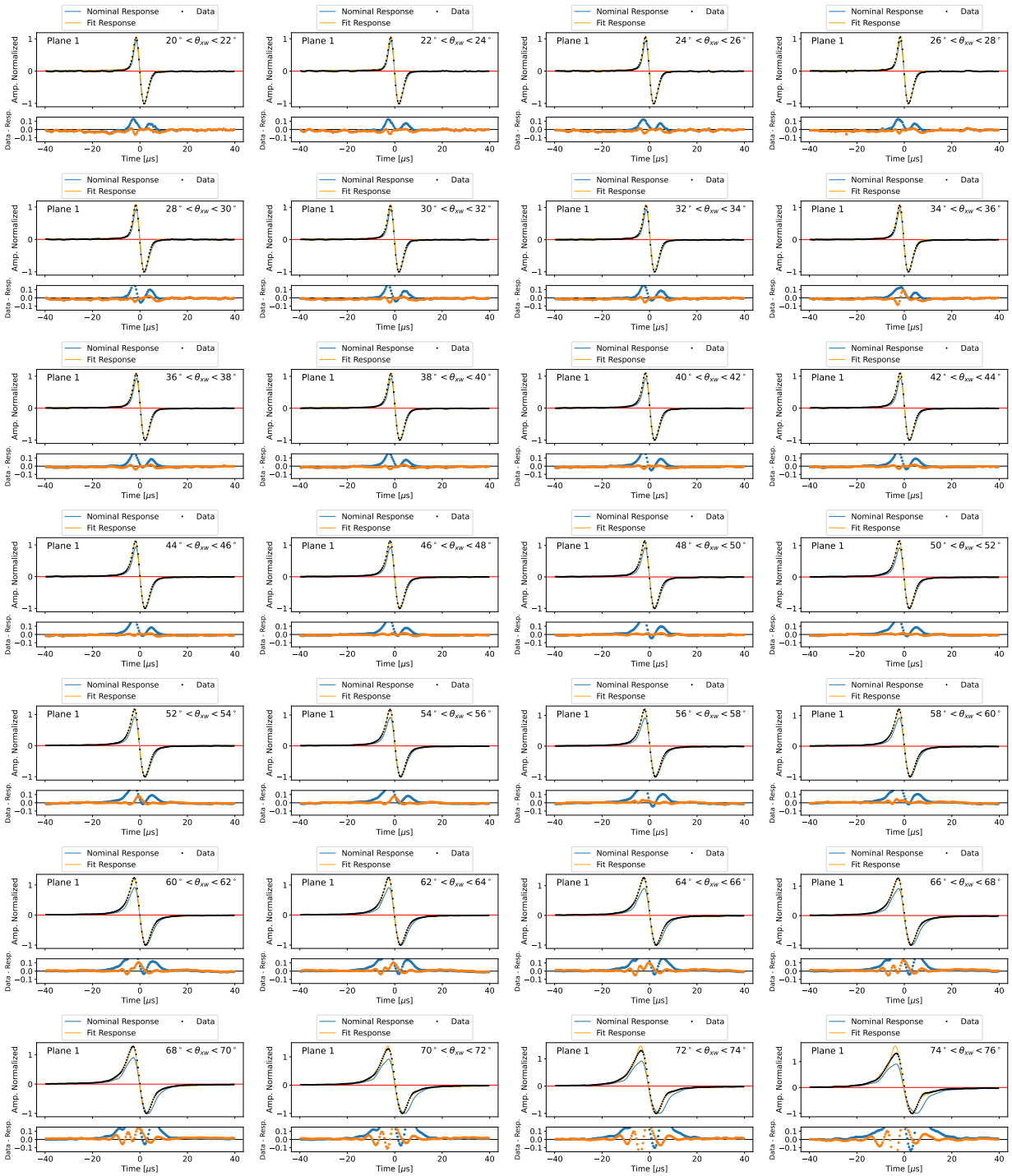

Figure 5.14: Signal shape fits on the middle induction plane. Each plot shows one angle bin between 20° and 76°. The blue curve is the nominal ICARUS signal shape and the orange is the result of the fit.

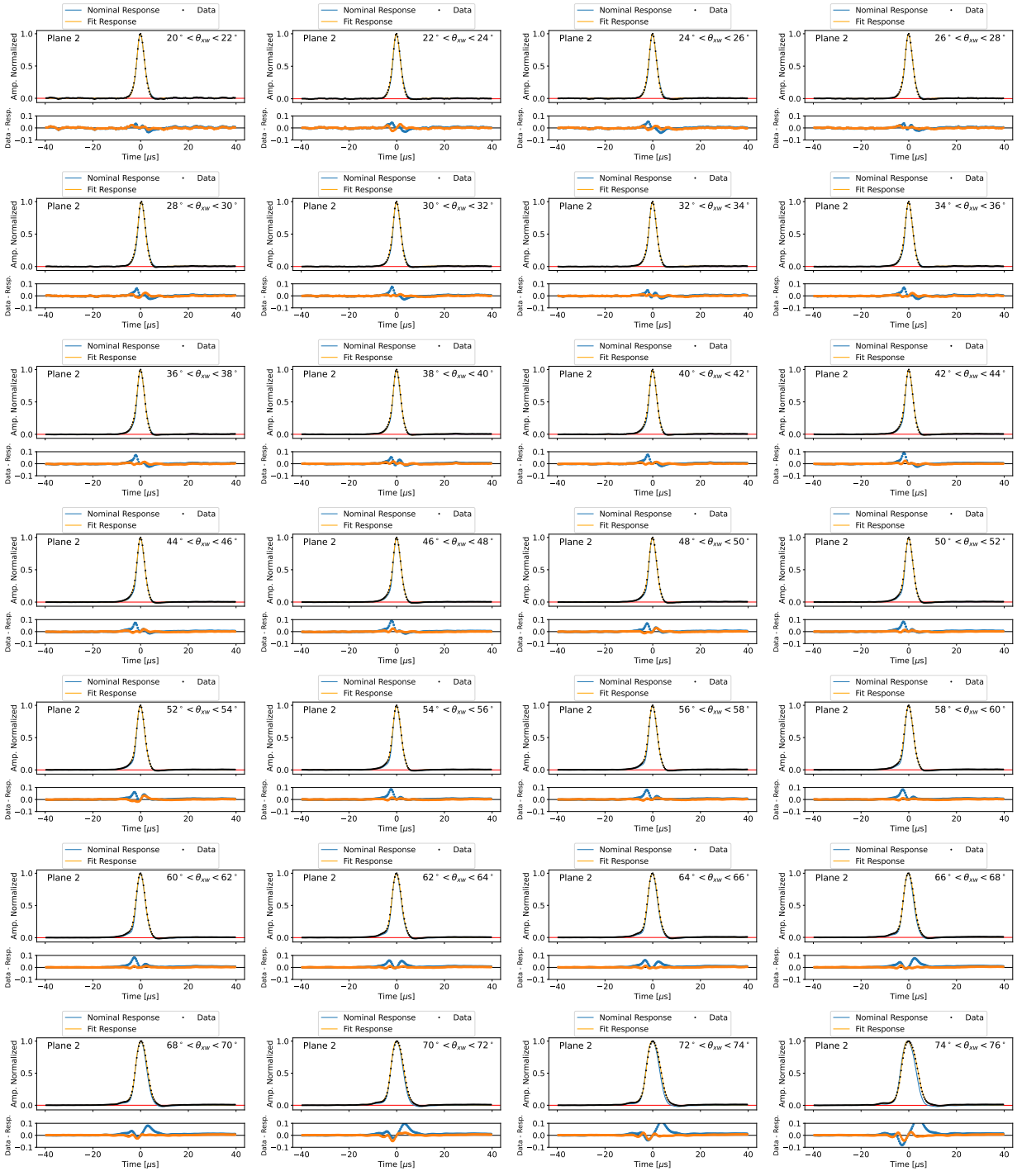

Figure 5.15: Signal shape fits on the collection plane. Each plot shows one angle bin between 20° and 76°. The blue curve is the nominal ICARUS signal shape and the orange is the result of the fit.

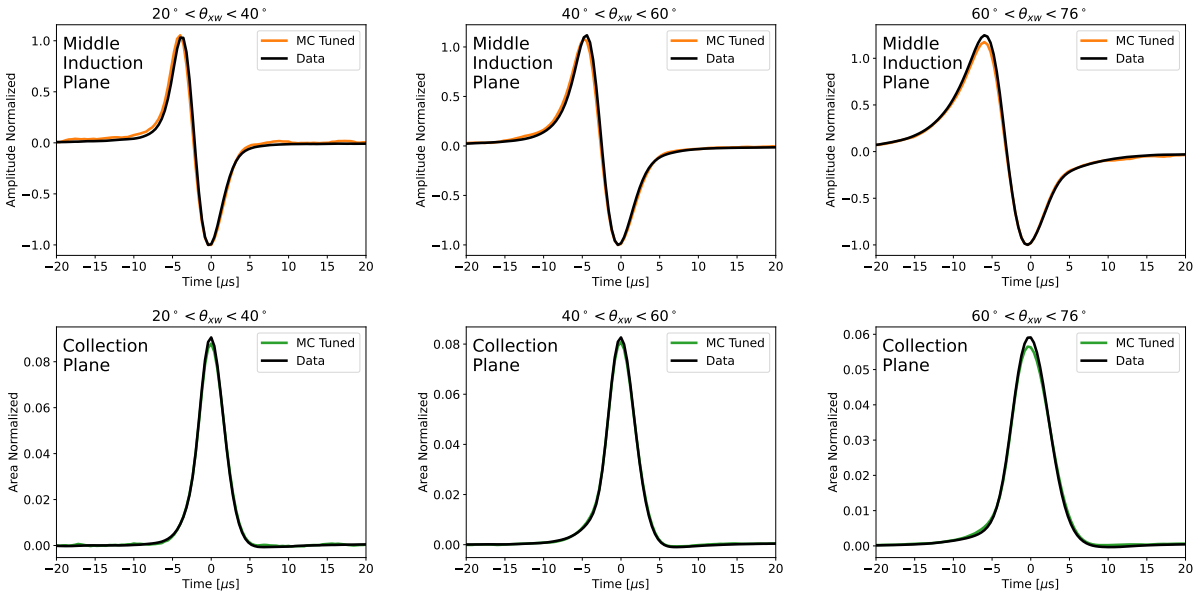

Figure 5.16: Comparison of the signal shape measurement between data and the tuned Monte Carlo simulation ("MC Modified") on the middle induction plane (top row) and collection plane (bottom row). Shown are measured signal waveforms averaged across θ_{xw} ranges of [20°, 40°] (left column), [40°, 60°] (middle column), and [60°, 76°] (right column).

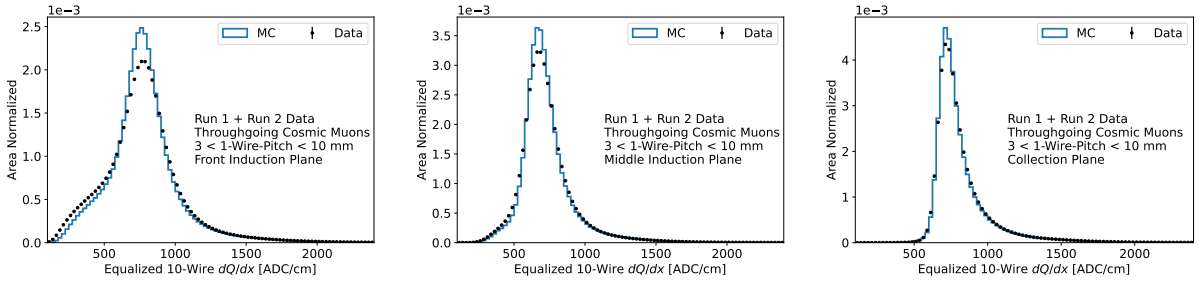

Figure 5.17: Distribution of equalized coarse-grained dQ/dx values for throughgoing cosmic muons, compared between Monte Carlo simulation and data. The simulation uses the nominal GARFIELD signal shape on the front induction plane and the tuned signal shape on the other two planes. The data is taken from the Run 1 and Run 2 datasets. Shown for the front induction plane (left), the middle induction plane (middle), and the collection plane (right).

5.3 Charge Resolution Comparison

To validate the equalization and simulation results of this chapter, we compare the distribution of equalized dQ/dx for throughgoing cosmic muons between data and Monte Carlo simulation. This is shown in figure 5.17. The data is shown after applying the corrections discussed in section 5.1. The signal shape applies the nominal GARFIELD simulation on the front induction plane, and the tuned signal shape (as described in section 5.2) on the middle and collection planes. The Monte Carlo simulation does not include any y-z detector response variations. It is simulated with a uniform 3 ms lifetime, which is corrected for using the same methodology as in the data. The simulated gain was tuned on each plane so that the peaks of the distributions matched.

Taken together, the final comparison shows very good agreement on all planes. There is a small residual underestimation of the charge resolution in simulation. This is observed on all three planes and is biggest on the front induction plane. There are a number of possibilities that could explain this effect: variations in the effective channel gain (from, e.g., the varying electron lifetime) not included in the simulation, deficiencies in the noise model, or differences in the inherent fluctuations from recombination, for example.

CHAPTER 6

ANGLE DEPENDENT ELECTRON-ION RECOMBINATION AND ITS APPLICATION IN THE ICARUS LARTPC

6.1 Introduction

To turn charge measurements (dQ/dx) into measurements of particle energy loss (dE/dx), it is necessarily to correct for the effect of electron-ion recombination. When charged particles deposit energy in the argon, they ionize individual argon ions. Critically, not all of the ionization electrons escape the particle track to be detected. Depending on the charge density, a significant fraction recombines with argon ions at the point of creation [136, 137, 138, 107]. The rate of recombination has a non-linear dependence on the energy per length, or dE/dx, deposited by charged particles. In addition, because the drift electric field points in a specific direction, the recombination process may depend on the angle of the ionizing track to the electric field [139, 140]. Measuring the rate of recombination across relevant variables is necessary for LArTPC detectors to precisely leverage calorimetry for particle identification and energy reconstruction. Any angular dependence in recombination is also of interest for argon-based dark matter detectors, where it could be leveraged to identify weakly interacting massive particle dark matter below the neutrino floor [141].

This chapter reports on a measurement of electron-ion recombination and its dependence on the angle of the ionizing particle direction to the drift electric field with the ICARUS LArTPC. The measurement is applied in the absolute energy scale calibration of the ICARUS TPC. The measurement is performed by fitting for the electronics gain and recombination parameters in a single, self-consistent fit. This fit includes minimum-ionizing depositions from cosmic-ray muons (which are included in the fit to anchor the gain) and highly-ionizing depositions from protons produced in neutrino interactions at ICARUS from the Neutrinos at the Main Injector (NuMI) beam [82] (which provide information on the non-linearity of

recombination).

The recombination measurement observes a clear dependence in recombination on the track angle to the drift electric field. We develop a new model, ellipsoid modified box (EMB) recombination, that is able to fit the data across all measured energies and angles. We further demonstrate that accounting for the angular dependence in EMB recombination improves the accuracy and precision of calorimetric measurements applying dE/dx.

This chapter is organized as follows. Section 6.2 discusses the models used to describe recombination and how to include an angular dependence. Section 6.3 develops how stopping muon and proton tracks are selected. Section 6.4 shows the fit results for the TPC gain and the angular dependent recombination measurement. The fit is applied as the energy scale calibration for ionization calorimetry in ICARUS. Applying this calibration, section 6.5 shows results for particle identification and calorimetric energy measurements and compares data to Monte Carlo simulation. Finally, section 6.6 concludes the chapter.

6.2 Recombination Modeling

Electron-ion recombination in liquid argon is driven by the collective absorption of ionized electrons by the cloud of argon ions along the particle track [136, 107] (the geminate fraction is negligible [142]). Recombination occurs after electrons thermalize and before they diffuse significantly [143]. It happens before the argon ions drift or diffuse significantly. Recombination thus takes place while the ionization electrons are dragged by the drift electric field over a stationary cloud of argon ions. The rate of recombination therefore may depend on the strength of the drift electric field and its orientation to the particle track, as well as the particle stopping power (dE/dx).

We consider two models to parameterize the recombination of ionizing particle tracks in liquid argon. The previous ICARUS measurement of recombination at Gran Sasso applied

the Birks equation [138]

$$\frac{dQ}{dx} = \frac{1}{W_{\text{ion}}} \frac{A\frac{dE}{dx}}{1 + k\frac{dE}{dx}/\mathcal{E}\rho}, \tag{6.1}$$

where W_{ion} is the argon ionization work function, $\mathcal{E}$ is the drift electric field, and A and k are fit parameters. The ArgoNeuT experiment measured recombination in terms of their proposed modified box model [107]

$$\begin{aligned} \frac{dQ}{dx} &= \frac{\log\left(\alpha + \mathcal{B}\frac{dE}{dx}\right)}{\mathcal{B}W_{\text{ion}}} \\ \mathcal{B} &= \frac{\beta}{\mathcal{E}\rho}, \end{aligned} \tag{6.2}$$

where α and β are fit parameters. This equation is a modification of the Thomas-Imel box model [136].

In both of these models one fit parameter (A, α) is uncoupled to the electric field. At the ICARUS drift field, these parameters control the amount of recombination for minimum-ionizing depositions. Both models also include one parameter (k, β) which is coupled to the electric field and determines the non-linearity of recombination with respect to dE/dx.

Neither of these models explicitly include a dependence on the track angle to the drift field, which we refer to as ϕ (see figure 4.2). Different forms of the angular dependence derive from different assumed shapes for the particle track ionization cloud. Two such examples are columnar [139] and ellipsoid [140] shapes. These models give an angular dependence to the drift electric field in the Birks equation. The same angular dependence in the drift electric field can also be applied in the modified box model.

For this measurement, we elect to include an angular dependence with a general form by promoting the parameters coupled to the drift field, k for Birks recombination and β for modified box recombination, to functions of ϕ: $k(\phi)$ and $\beta(\phi)$. These are compared to the columnar and ellipsoid model predictions. Neither phenomenological model assigns any angular dependence to the parameters uncoupled to the electric field (A, α). We do not

include any angular dependence in these parameters in our measurement. We find that our results are well described by including an angular dependence just on the parameters coupled to the electric field (k, β).

Our recombination modeling also assumes that there is no dependence of recombination on the particle type (muon versus proton, e.g.). It is possible that at the same energy loss (dE/dx), muons and protons would deposit different amounts of ionization (dQ/dx) because the two particles produce different energy spectra of ionization electrons. Our results are well described by neglecting any particle type dependence, although they do not include any data where the expected muon and proton energy loss overlaps. The search for such an effect merits further study.

In the fit, we also include the electronics gain $(\mathcal{G})$ as a free parameter. The gain enters the fit equations as $\frac{dQ}{dx}_{\text{ADC}} = \frac{1}{\mathcal{G}} \frac{dQ}{dx}$. The gain for the ICARUS TPC readout electronics has been previously measured [85]. The gain in this fit should be understood as an effective parameter which encodes any perturbations induced by signal processing and charge corrections. In addition, by including the gain directly in the fit, we are able to include the uncertainty that the unknown effective gain induces on the measurement of recombination.

6.3 Track Selection

Particle tracks are identified in ICARUS with the Pandora reconstruction framework [86, 87], run on hits produced by the ICARUS signal processing chain [83]. Separate track selections identify cosmic-ray muon and neutrino-induced protons useful for the energy scale calibration. These are detailed in sections 6.3.1 and 6.3.2, respectively. The charge measured from tracks is equalized across space, time, and track orientation, as described in section 6.3.3. Distributions of dQ/dx are then constructed from hits along tracks, as discussed in section 6.3.4. Table 6.1 outlines the selection for proton and muon hits.

Selection Step	Muons	Protons
Topological Selection	Cathode-crossing (see section 6.3.1)	From neutrino candidate (see section 6.3.2)
Calorimetric Selection	Median dQ/dx in last 5 cm > 75 ke$^-$/cm	μ-like PID > 40, p-like PID < 80 (see figure 6.1)
Fiducial Volume X Inset (drift)	10 cm from anode and 15 cm from cathode	
Fiducial Volume Y Inset (vertical)	20 cm from top and bottom.	
Fiducial Volume Z Inset (BNB)	50 cm from front and back	
Hit Residual Range	33 bins, 80 to 300 cm	16 bins, 2 to 25 cm
Hit Pitch	0.3 to 0.4 cm	0.3 to 1 cm
Hit ϕ	70° to 85°	6 bins, 30° to 85°
Hit θ_{xw}	5° to 20°	5° to 70°
Hit Drift Time	5 bins, 500 to 900 µs	No cut

Table 6.1: Overview of selection to identify hits from muon and proton tracks. The topological section is specified in sections 6.3.1 and 6.3.2 for muon and protons, respectively. The extra fiducial cut in TPC WW removes a problematic detector region. When hits are split into groups by the quantity, the number of bins is specified.

6.3.1 Cosmic-Ray Muon Selection

Cosmic-ray muon tracks are required to cross the central cathode plane in either cryostat. The identification of a track in both TPCs on either side of the cathode allows the arrival time of the muon to be determined. This enables the track charge to be corrected for attenuation due to argon impurities. These "cathode-crossing tracks" are identified by Pandora. The muon is required to stop within a fiducial volume (see table 6.1), and is required to have a median dQ/dx in the last 5 cm along the track greater than ~ 75 ke$^-$/cm [1]. This cut increases the stopping track purity by requiring the measured charge near the endpoint to be consistent with the expectation from the muon Bragg peak. The region of the track where the cut is applied is not included in the calibration, and so the cut should not bias the measurement. This selection identifies 93 thousand muon candidates. A Monte Carlo simulation study (with cosmic-ray muon generation modeled by CORSIKA [106]) of this selection yields a

1. The cut value is expressed directly in terms of analog-digital counts (ADC) per centimeter. The cut is 1000 ADC/cm. The written value is converted to a number of electrons (e^-) applying an approximate gain of 75 e^-/ADC.

93% purity of tracks stopping within 5 cm of the reconstructed endpoint. The remaining 7% consist almost entirely of cosmic-ray muons where the endpoint is mis-reconstructed, either due to track splitting or combining with a Michel electron. The dependence of energy loss on the muon momentum is small for the range of muon momenta used in this measurement, so this impurity has a small impact.

6.3.2 Neutrino-Induced Proton Selection

Neutrino-induced protons are selected by applying topological and loose calorimetric cuts. The tracks are required to originate from a neutrino candidate with a fiducial interaction vertex. The neutrino candidate must have at least two tracks with a length of at least 25 cm each. The cosine of the angle of the longest track in the candidate to the vertical direction must be greater than -0.7. These cuts select for event topologies with multiple tracks and remove events with downward going tracks. They remove the large majority of cosmic-ray muon background events.

After the topological cuts, the proton track candidates are selected by applying a calorimetric particle identification cut. This cut relies on particle identification (PID) variables which compare the reconstructed profile of dE/dx along a track to the theoretical expectation for muon (μ-like) and proton (p-like) hypotheses [121]. Calorimetric cuts are necessary to select proton tracks from muons and pions, and have been used in prior recombination measurements leveraging protons [107, 120]. These variables are computed using a basic energy scale calibration which assumes the ArgoNeuT recombination measurement [107] and fits for the TPC electronics gain using the cosmic muon track sample. Distributions of the PID variables in ICARUS Monte Carlo simulation are shown in figure 6.1. Candidate proton tracks must be contained in a fiducial volume and have p-like PID < 80 and μ-like PID > 40. This selection identifies 4.4 thousand proton candidates. The sample has a 97.5% purity of true protons in a Monte Carlo simulation study. We have performed the recombination

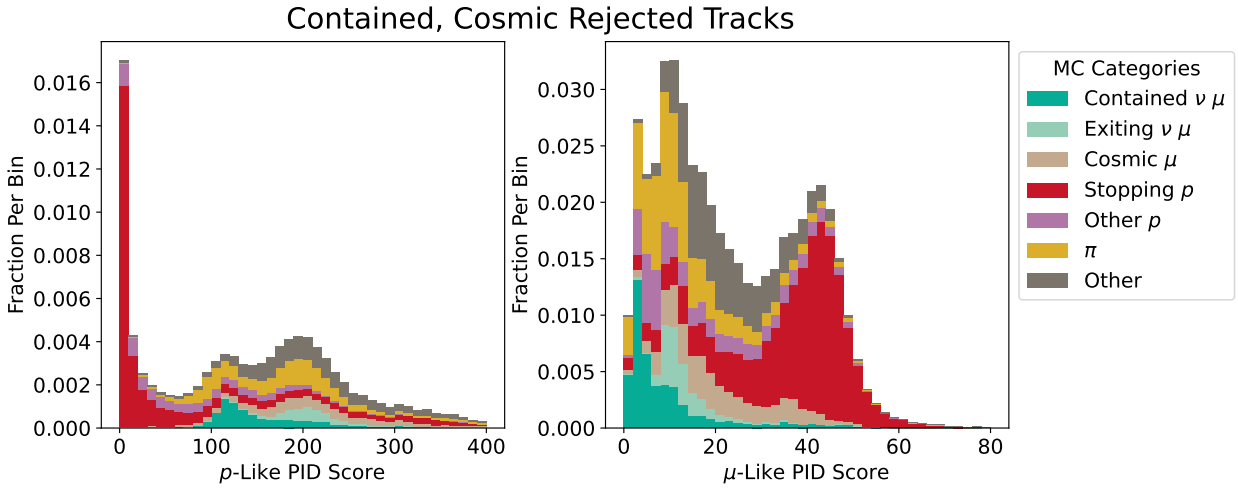

Figure 6.1: Distribution of proton-like (left) and muon-like (right) particle identification (PID) variables in ICARUS NuMI neutrino + CORSIKA cosmic-ray Monte Carlo simulation. Distributions are shown after applying the topological cuts in section 6.3.2. The particle ID variables are computed by comparing the profile of dE/dx along a track to the theoretical expectation for the proton and muon hypotheses.

measurement with variations on the calorimetric cuts and have found that our result is not sensitive to the particular choice of the cut values.

6.3.3 Charge Scale Corrections

Charge signals measured from muon and proton tracks per-wire on the collection plane are equalized per-hit in space and time by applying the charge equalization procedure developed for ICARUS (see chapter 5). This procedure equalizes the detector response by applying corrections obtained from charge depositions by throughgoing cosmic muons.

A small (∼2.5%) angular dependence is also observed in the charge reconstruction for particle tracks as derived by comparing charge reconstruction methods in ICARUS simulation and data. There are two methods for measuring charge in a hit in ICARUS reconstruction. The "Integral" method fits a Gaussian shape to the hit pulse and defines the charge as the area of the fit. The "SummedADC" method sums the ADC values over the range of the hit. The hit range is defined as the region between two local minima below the (baseline

subtracted) zero-point of the waveform on either side of a hit pulse that goes above a set threshold. Monte Carlo simulations in ICARUS indicate that the SummedADC method has a worse charge resolution but no angular dependence, whereas the Integral method has a better resolution and a moderate angular dependence. The TPC signal shapes in ICARUS Monte Carlo simulation have been tuned to directly match the data signal shapes (chapter 5), so we are confident that the Monte Carlo simulation is able to precisely model the amount of angular dependence in the charge reconstruction.

We use the Integral charge method for calibrating the ICARUS TPC energy scale, but use the SummedADC method to diagnose the angular dependence. The ratio of the Integral to SummedADC charge reconstruction is taken as a charge scale correction factor as a function of the track angle ${\theta_{xw}}^2$ (see figure 4.2). Figure 6.2 plots the correction factor in Monte Carlo simulation and data. A systematic uncertainty of 0.2% on the correction is assigned to cover the differences.

Selected protons are required to have $\theta_{xw} < 70^\circ$ so that this correction is applicable. For muons, instead of making a correction, we restrict the θ_{xw} range between $5^\circ < \theta_{xw} < 20^\circ$, over which the angular dependence is not significant ($< 0.2\%$).

6.3.4 dQ/dx Measurements

After selection and charge scale corrections, hits from protons and muons are divided into groups. The MPV dQ/dx is extracted in each group. Both muon and proton hits are required to be contained in a fiducial volume which removes regions where drift electric field distortions are the largest. Muon hits are required to have a reconstructed pitch less than 4 mm and a track angle $\phi > 70^\circ$. They are grouped by TPC, drift time, and residual range (the length of the muon after that hit). The subdivision by residual range and drift time selects for a single expected energy loss MPV in each distribution. The subdivision by

2. This angle determines the shape of the ionization charge signal from a track, and therefore controls any orientation dependence in the charge reconstruction.

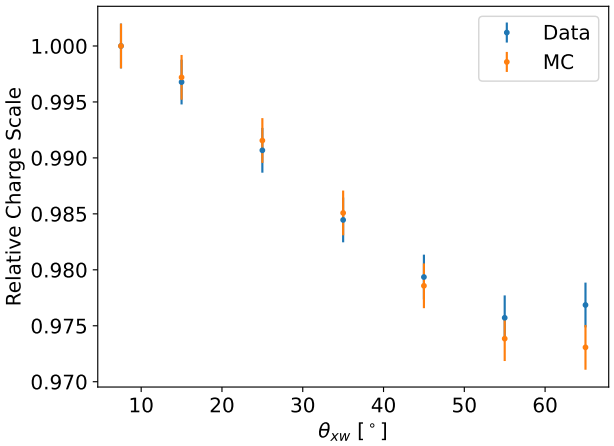

Figure 6.2: Relative scale of charge reconstruction as a function of the track angle θ_{xw} (see figure 4.2), determined in ICARUS data and Monte Carlo simulation. A systematic uncertainty of 0.2% on the correction is assigned to cover the difference between data and Monte Carlo simulation.

TPC checks for any variations in the gain that were not removed by the charge equalization procedure. Proton hits are required to have a pitch less than 1 cm and are grouped by residual range and the track angle ϕ. See table 6.1 for the overview of the cuts applied to muon and proton hits.

The MPV dQ/dx is obtained in each group by fitting the distribution of dQ/dx values to a Landau distribution convolved with a Gaussian distribution. The fit includes a statistical uncertainty on the MPV. Due to the uncertainty in the charge scale corrections to remove angular dependence (section 6.3.3), as well as spatial and temporal variations (chapter 5), we also assign a 1% systematic uncertainty on each proton dQ/dx MPV. The systematic uncertainty is added in quadrature with the uncertainty from the fit. The uncertainty in the muon dQ/dx MPV is separately validated by verifying that the fit uncertainty is consistent with the residuals of the MPVs to a linear fit to the data (since recombination is linear for the minimum-ionizing muon depositions). Thus, no additional systematic uncertainty is added to the muon dQ/dx MPVs.

6.4 Energy Scale Fit

6.4.1 Procedure

The end results of the track and hit selection described in section 6.3 are dQ/dx MPVs for muon and proton tracks as a function of mean pitch, residual range, and (for muons only) drift time. Each dQ/dx MPV is matched to an expected dE/dx MPV by applying the energy scale modeling from chapter 4. Equation 4.10 specifies analytically the MPV energy loss in the Landau limit. The Landau approximation is quantified by the unitless quantity $\zeta \cdot t$ (specified in equations 4.4 and 4.9, respectively), and is typically taken to be valid when $\zeta \cdot t < 0.01$ [114]. When this limit is violated, the distribution of particle energy loss is not well modeled by a Landau distribution and equation 4.10 does not apply. The ζ parameter monotonically decreases with increasing momentum, so the approximation is valid at higher momentum, away from the Bragg peak.

In our calibration procedure, for the muon population we elect to only include depositions where the analytic Landau approximation is valid. This limits us to depositions near the mimumum-ionizing-particle (MIP) region, where recombination is close to linear. To provide information on recombination, we also include highly-ionizing-particle (HIP) depositions from protons near their Bragg peak. In this case, the distribution of energy loss is approximately a Landau-Vavilov distribution [110], although there is a perturbation to the shape from diffusion (see chapter 4). The MPV of the Landau-Vavilov distribution cannot be expressed analytically. We use the numerical computation provided by the ROOT VavilovAccurate routine[3] [144].

The measured dQ/dx MPVs are fit to the expected dE/dx MPVs with either the Birks or modified box recombination model. The electronics gain is included as a free parameter in

3. We have found in our simulation that in this region the MPV of the proton energy loss distribution is modeled well by the ROOT numerical computation, using the track pitch (not the track thickness) as the input to the Landau parameter (λ_L) and κ value used in the VavilovAccurate routine.

both fits. The A parameter in Birks recombination is degenerate with the gain in the fit, so we use the A value from the ICARUS Gran Sasso measurement [138]. The parameters coupled to the electric field, $k(\phi)$ for Birks recombination and $\beta(\phi)$ for modified box recombination, are allowed to be different in each proton angular bin. The muon data bridges two of the proton angular bins, $70^\circ < \phi < 80^\circ$ and $80^\circ < \phi < 85^\circ$. We use the average β and k values from those two bins to calculate the expected amount of recombination. We have verified in a Monte Carlo simulation study that this method is able to reproduce the simulated recombination and electronics gain parameters.

The external values of parameters used in the fit are listed in table 6.2. The largest uncertainty in any parameter relevant to energy loss modeling comes from the mean excitation energy. We do not specifically include an uncertainty from this parameter in the energy scale fit, as other uncertainties in the fit dominate over the impact of the excitation energy on the mean energy loss. There is a 1.7% uncertainty in the electric field which translates directly into an uncertainty in β and k which is fully correlated across angular bins. The uncertainty in the electric field arises from distortions due to space charge and bending of the cathode observed in both cryostats in ICARUS. There is an additional localized drift field distortion in one TPC (the East TPC in the East cryostat, TPC EE) due to a failure in the field cage. We have confirmed that removing data from that TPC does not change the measurement by more than the uncertainty on the drift electric field. We therefore include data from that TPC in the measurement.

6.4.2 Results

The result of the fit comparing measured dQ/dx and expected dE/dx is shown for muons in figure 6.3 and for protons in figure 6.4. The χ^2 values of the modified box and Birks

4. This value is taken from an analysis in ICARUS in preparation to be published. The preliminary value applied here will not change in the final result by an amount significant enough to impact the results of this chapter.

Parameter	Value
Energy loss coefficient K [114]	$0.307\,075\,\mathrm{MeV cm^2/mol}$
Mean excitation energy I_0 [145]	$197(7)\,\mathrm{eV}$
Transverse diffusion constant ${D_T}^4$	$7.5(2)\,\mathrm{cm^2\,s^{-1}}$
Argon ionization work function W_{ion} [146]	$23.6 \pm 0.3\,\mathrm{eV}$
Argon density ρ	$1.393\,\mathrm{g\,mL^{-1}}$
Drift electric field $\mathcal{E}$	$492.6 \pm 8.4\,\mathrm{V\,cm^{-1}}$
Wire pitch $\not{p}$ [79]	$2.991\,\mathrm{mm}$

Table 6.2: Numerical values of parameters that determine the muon and proton charge scale. A reference is included for external measurements. Uncertainties are shown when their size is relevant.

fits are compared for the proton data in table 6.3 (there is no significant difference for the muon data). The modified box fit results in a lower χ^2 across all proton angular bins. This reduction is greater than can be accounted for by the additional degree of freedom from the extra parameter in the modified box fit (α). We use the modified box fit for the energy scale calibration for ICARUS. Figure 6.5 plots all of the modified box fits together, and shows the ϕ dependence in the β parameter in the fit.

We observe a clear difference in the measured MPV dQ/dx between different proton track angle bins. This can be seen both in the proton data in figure 6.4, as well as in the β parameter fit in figure 6.5. At the largest measured dE/dx value (12 MeV/cm), this is a difference of 10% on the measured proton charge between the largest and smallest ϕ bins. We have closely examined any possible angular biases in the charge reconstruction. None were found outside of the 2.5% correction detailed in section 6.3. We attribute the angular dependence observed here to an angular dependence in electron-ion recombination in liquid argon. The success of the modified box fits demonstrates that this can be parameterized by including a dependence on the track angle to the drift electric field (ϕ) in the β parameter.

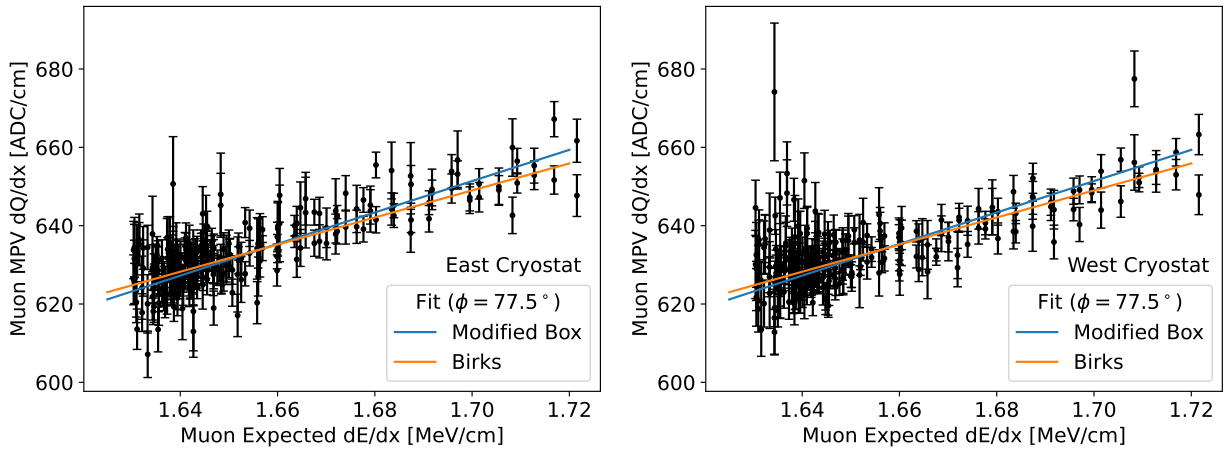

Figure 6.3: Fits of measured MPV dQ/dx to expected MPV dE/dx for muons in the East cryostat (left) and the West cryostat (right). The two lines compare the Birks and modified box fits.

We investigate the ϕ dependence of the β parameter by comparing three models of the angular dependence:

- Constant: $\beta(\phi) = \beta_{90}$
- Columnar [139]: $\beta(\phi) = \beta_{90}/\sin\phi$
- Ellipsoid [140]: $\beta(\phi) = \beta_{90}/\sqrt{\sin^2\phi + \cos^2\phi/R^2}$,

where β_{90} ($\equiv \beta(90°)$) and R are fit parameters. The R parameter of the ellipsoid model interpolates between the constant ($R = 1$) and columnar ($R \to \infty$) models. Figure 6.5

Table 6.3: χ^2 values in the modified box and Birks equation fits to proton data, broken down by the (ϕ) angle bin. There are 16 data points in each angular bin. The Birks fit has 7 free parameters $(k(\phi), \mathcal{G})$, and the modified box fit has 8 $(\beta(\phi), \alpha, \mathcal{G})$.

Proton Angle Bin	Birks Fit χ^2	Modified Box Fit χ^2
$30° < \phi < 40°$	40.6	13.9
$40° < \phi < 50°$	57.7	11.7
$50° < \phi < 60°$	53.2	6.1
$60° < \phi < 70°$	52.3	5.4
$70° < \phi < 80°$	52.3	3.9
$80° < \phi < 85°$	37.7	4.8
Total χ^2/n d.o.f.	293.8/89	45.8/88

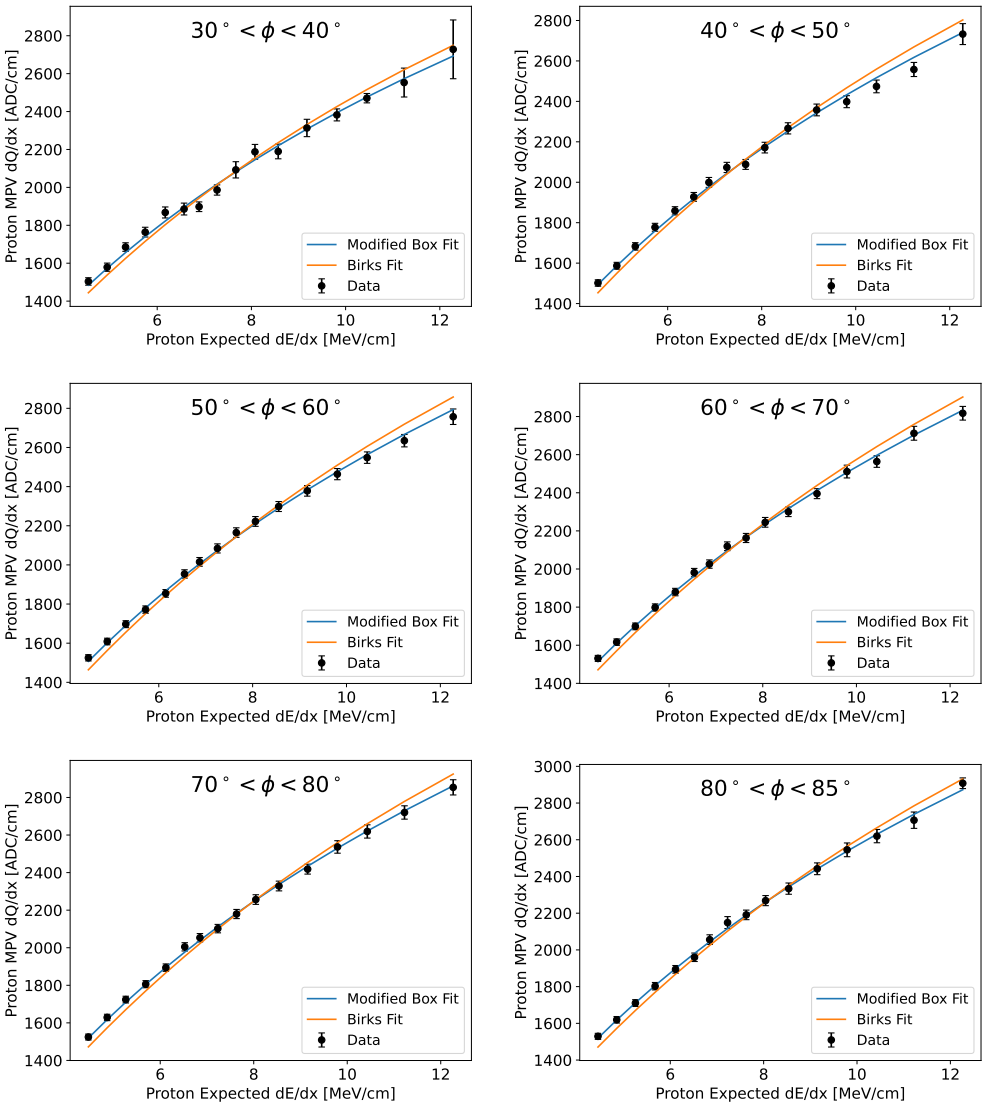

Figure 6.4: Fits of measured MPV dQ/dx to expected MPV dE/dx for protons. The two lines compare the Birks and modified box fits.

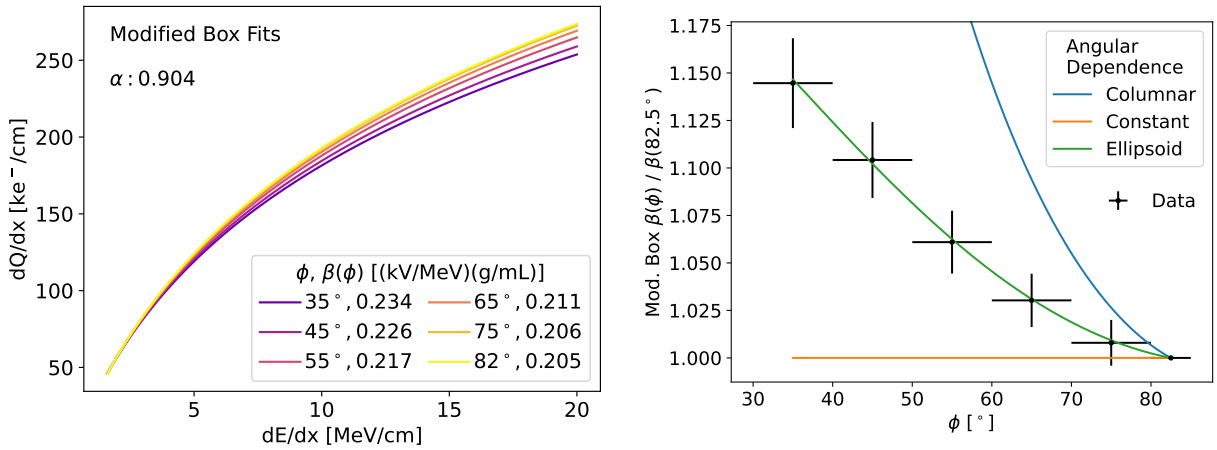

Figure 6.5: (Left) Modified box fit in each proton angle bin. (Right) Ratio of $\beta(\phi)$ measurements in the modified box fit to the value in the $80^\circ < \phi < 85^\circ$ bin. This ratio is compared to three models of the angular dependence, as described in the text. All three models are normalized to match the data in the $80^\circ < \phi < 85^\circ$ bin.

compares the three models to the measured ratio of $\beta(\phi)$ to $\beta(82.5^\circ)$ (the ratio removes the correlated uncertainty due to the drift electric field). Neither the constant nor columnar models match the dependence. However, the ellipsoid model fit is able to describe it well.

Putting this together, we find that the ellipsoid modified box (EMB) model of recombination

$$\begin{aligned} \frac{dQ}{dx} &= \frac{\log\left(\alpha + \mathcal{B}(\phi)\frac{dE}{dx}\right)}{\mathcal{B}(\phi)W_{\text{ion}}} \\ \mathcal{B}(\phi) &= \frac{\beta_{90}}{\mathcal{E}\rho\sqrt{\sin^2\phi + \cos^2\phi/R^2}} \end{aligned} \tag{6.3}$$

is able to describe the muon and proton data across all measured angles. The ICARUS measurement of the EMB model is obtained by re-fitting the dQ/dx data. The result is

$$\begin{aligned} \alpha\text{: } 0.904 \pm 0.008 \qquad R\text{: } 1.25 \pm 0.02 \\ \beta_{90}\text{: } 0.204 \pm 0.008\,(\text{kV/MeV})(\text{g/mL}), \end{aligned}$$

with the ICARUS electronics gain ($\mathcal{G}$) measured as 75.0 ± 1.1 e^-/ADC. Figure 6.6 displays the correlation matrix of the uncertainties in the fit. The measured R parameter is 12.5 stan-

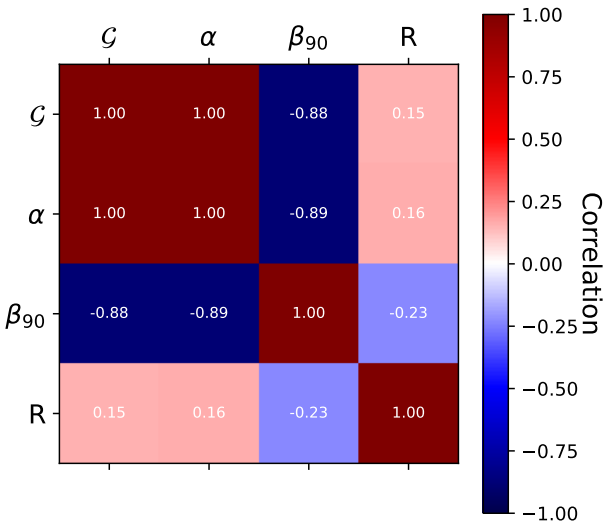

Figure 6.6: Correlation matrix of the uncertainties in the ellipsoid modified box (EMB) recombination measurement.

dard deviations away from a value consistent with no angular dependence in recombination ($R = 1$).

The ArgoNeuT experiment previously measured electron-ion recombination, including its angular dependence, in liquid argon with protons and deuterons at a drift field strength close to the field strength in ICARUS [107]. A comparison is shown in figure 6.7. The two measurements appear consistent. While ArgoNeuT recommended its result be applied in an angular independent way, we have found that the angular dependence in the EMB model is critical to properly calibrate the ICARUS LArTPC. Section 6.5 demonstrates the impact of the angular dependence on particle identification.

6.5 Impact on Particle Identification and Calorimetry

The measurement of ellipsoid modified box (EMB) electron-ion recombination (equation 6.3) and the ICARUS electronics gain presented here provides the TPC energy scale calibration in ICARUS. This calibration enables the use of calorimetric particle identification (PID) and energy reconstruction for ionizing particle tracks. Figure 6.8 shows the distribution of cali-

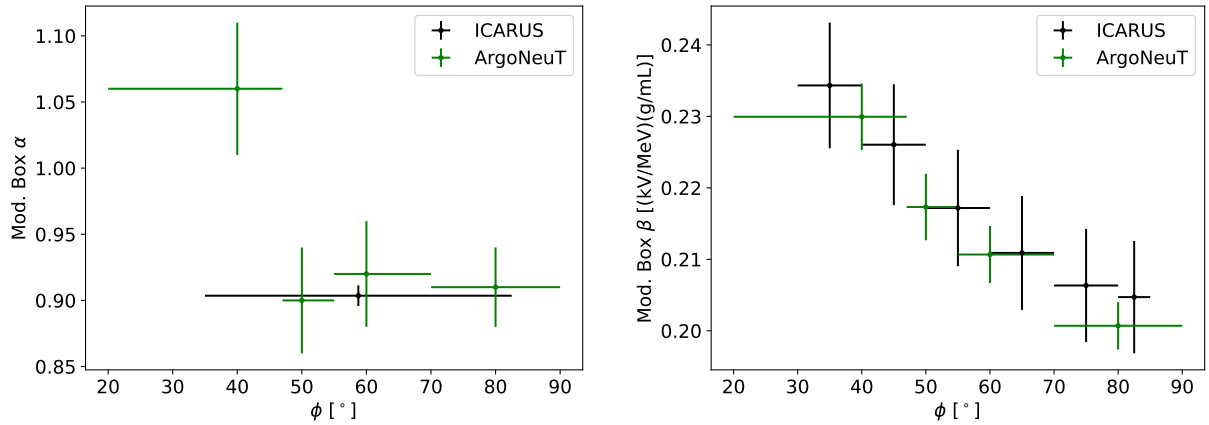

Figure 6.7: Comparison of the modified box recombination model fit between this measurement and the ArgoNeuT result [107]. The two fits are not completely comparable because the ArgoNeuT result allowed the α parameter to be different in the different angular bins. Beyond this limitation, the measurements appear consistent.

brated energy depositions for selected stopping muons and protons. The figure demonstrates both the accuracy of the calibration and the ability of the ICARUS TPC to calorimetrically separate muon and proton tracks.

In this section, the performance of ICARUS calorimetry is compared in detail between data and Monte Carlo simulation. Furthermore, the application in data of the ICARUS EMB-based calibration (equation 6.3) and an ArgoNeuT modified box-based calibration (equation 6.2) are compared. The EMB model values are taken from this chapter. The ArgoNeuT modified box values are taken from ref. [107]. The electronics gain in the ArgoNeuT modified box-based calibration is determined from a fit to muon dQ/dx data.

6.5.1 Particle Identification

Ionization calorimetry can be applied to separate muon and proton tracks with the μ-like PID and p-like PID scores, as is shown for ICARUS Monte Carlo simulation in figure 6.1. Modeling the distribution of these scores precisely is critical for physics analysis. A data to simulation comparison of the μ-like PID score for proton-like tracks is shown in figure

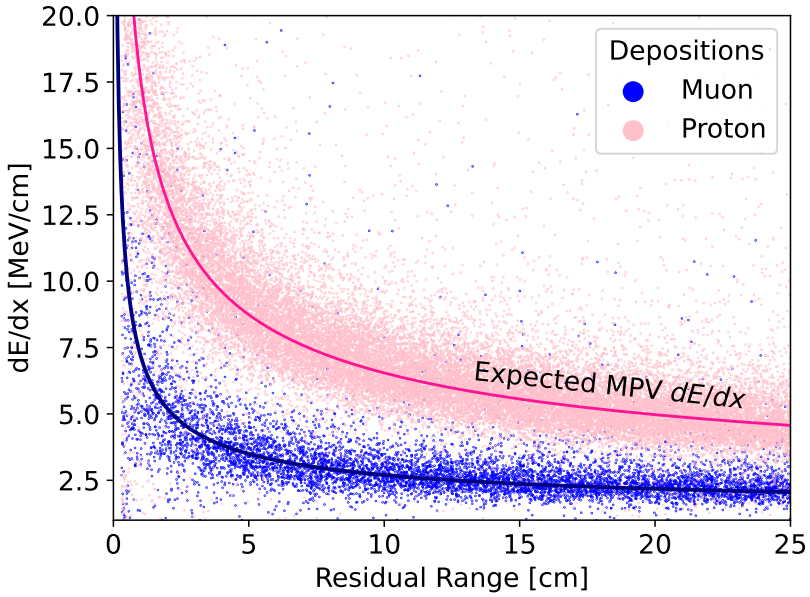

Figure 6.8: Scatter plot of calibrated energy depositions from selected stopping muons and protons in ICARUS data.

6.9. Proton-like tracks are selected with the topological track selection detailed in section 6.3.2. They also must have a p-like PID score less than 80. The comparison is made for energy depositions in data calibrated with the EMB model (equation 6.3) and with the angular-independent ArgoNeuT modified box model.

The data in the comparison is taken with the NuMI beam. The cosmic triggered component is removed by subtracting off-beam data, normalized to the trigger livetime. The Monte Carlo simulation is described in section 3.2. There is a significant uncertainty in the normalization of the Monte Carlo simulation prediction due to neutrino interaction and flux modeling. This uncertainty is mostly removed by the area normalization in the plot. Only statistical uncertainties on the data are shown.

Including the angular dependence in the EMB recombination correction dramatically improves the agreement of the μ-like PID score distributions between data and simulation for stopping protons. There remains some residual disagreement in the broadness of the distribution. A similar effect is also seen in the proton energy reconstruction (see next

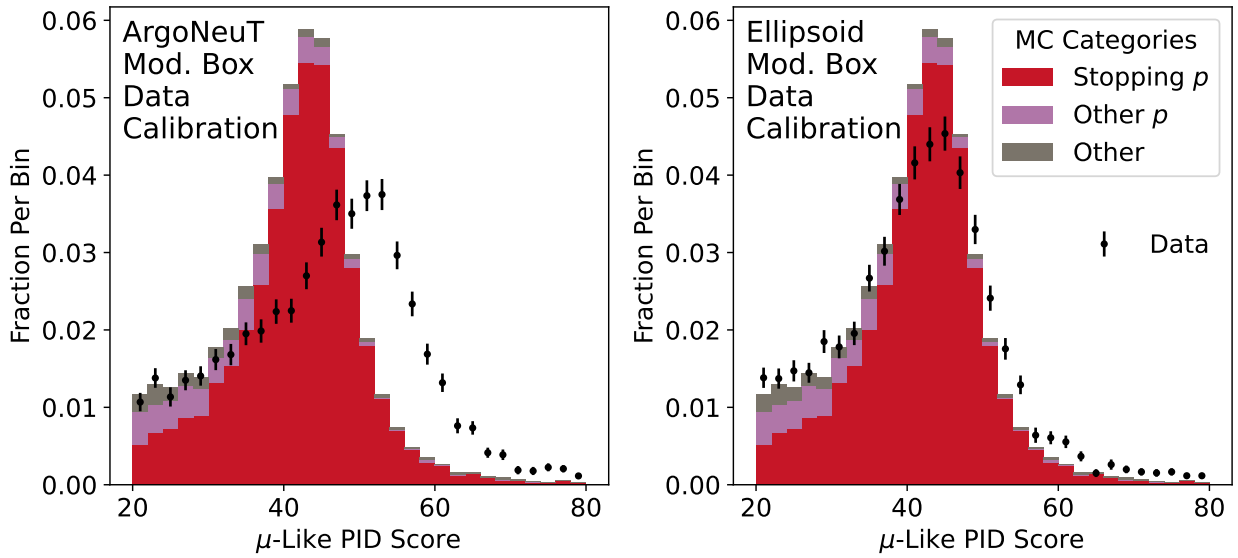

Figure 6.9: Monte Carlo simulation to data comparison of the μ-like PID score applying the angular independent ArgoNeuT modified box-based calibration (left) and with the angular dependent EMB-based calibration (right). Tracks are selected as detailed in section 6.5. The data is taken with the NuMI beam. The cosmic-triggered component of the data is subtracted with off-beam data.

section).

6.5.2 Proton Energy Reconstruction

We further examine the performance of calorimetry in ICARUS by comparing the energy reconstructed by range and by calorimetry for stopping protons. This comparison is made for both data and Monte Carlo simulation. As for particle identification, we also compare the impact of applying either the EMB or ArgoNeuT modified box recombination model to calibrate the calorimetric energy reconstruction in data.

Protons are identified using the selection detailed in section 6.3.2. The energy is measured along the last 25 cm of the track. The range energy is measured with a lookup table mapping proton length to energy. This table applies the continuous-slowing-down-approximation (CSDA) [125], with the mean energy loss taken from equation 4.13.

To precisely reconstruct proton calorimetric energy, a so-called "Q-tip" energy recon-

struction technique has been developed. The charge from the last 3 cm of the proton track is summed into a total charge which is converted to a total tip energy (this is based on the method developed by ArgoNeuT for "blip" energy depositions [147]). Charge in subsequent hits is corrected for recombination hit-by-hit and then summed into a total energy. This method is more precise than correcting for recombination hit-by-hit along the whole track because charge near the proton tip gets smeared out by diffusion and edge effects. The value of energy loss is also changing rapidly near the proton tip due to its Bragg peak, and so this smearing biases the energy reconstruction at the tip if it is applied hit-by-hit.

The comparison of the calorimetric and range based energy reconstruction is shown for ICARUS data and Monte Carlo simulation in figure 6.10. Calorimetric energy calibrations applying the ArgoNeuT modified box model and the EMB model are also compared for the data. The result with the EMB-based calibration is both less biased and has a better resolution than for the ArgoNeuT modified box-based calibration.

The full width at half maximum (FWHM) of the relative difference between the range and (EMB calibrated) calorimetric energy values is 8% in ICARUS data. This resolution is about twice as large in data as in simulation. The resolution of the range-based measurement is likely simulated well by the ICARUS Geant4-based simulation, so the calorimetric energy measurement would be dominating the discrepancy. In principle, this effect could be explained by an underestimation of the inherent charge resolution of the detector in ICARUS simulation. However, as is shown in the next section, for muons (which have mostly minimum ionizing depositions) there is no such disagreement. This points to an effect specific to highly ionizing depositions. In particular, it is possible that fluctuations in ionization recombination are underestimated for highly ionizing depositions in the ICARUS simulation.

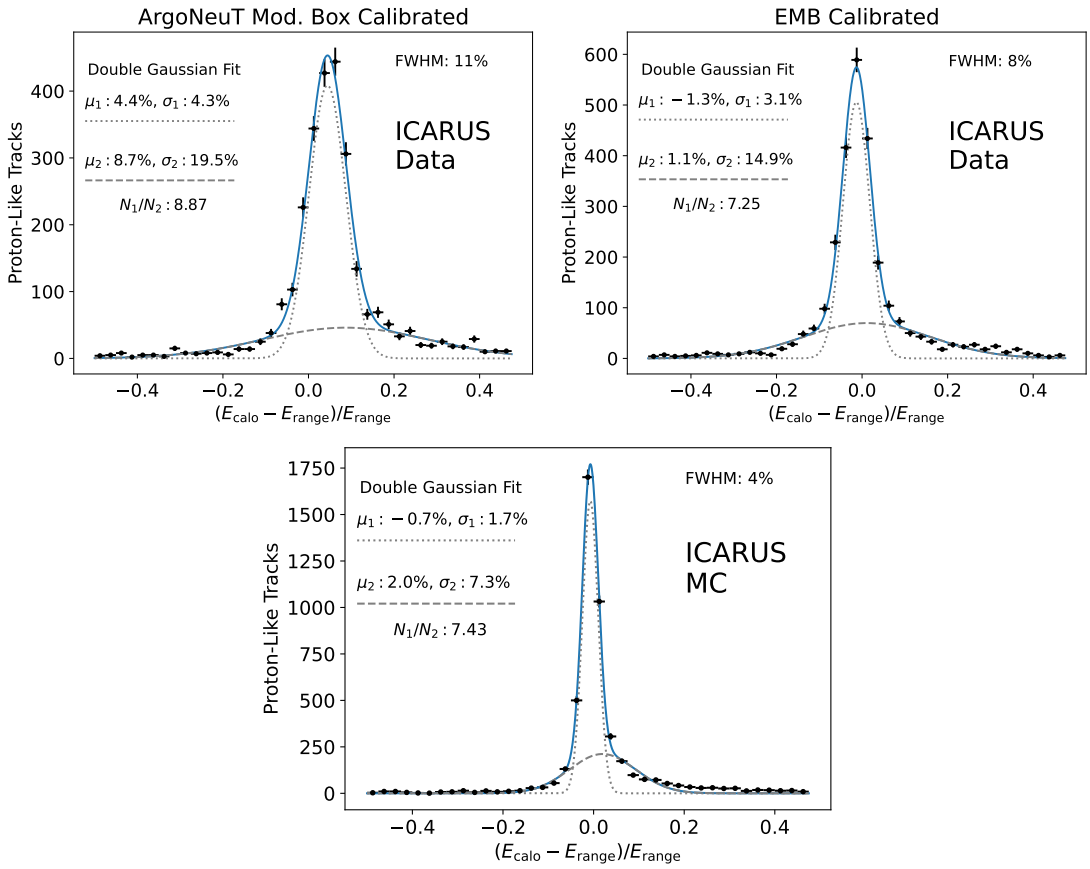

Figure 6.10: Comparison of calorimetric energy (E_{calo}) and range energy (E_{range}) reconstruction (as defined in section 6.5.2) for selected protons in ICARUS data (top) and Monte Carlo simulation (bottom). The comparison is made in data for the ArgoNeuT modified box-based calibration (top-left) and the EMB-based calibration (top-right). The Monte Carlo simulation applies the ArgoNeuT modified box model for both simulating recombination and correcting for it. The data points are fit to a sum of two Gaussian distributions with centers (μ_1, μ_2) and standard deviations (σ_1, σ_2). The ratio of the amplitudes of the Gaussian distributions is quoted as N_1/N_2.

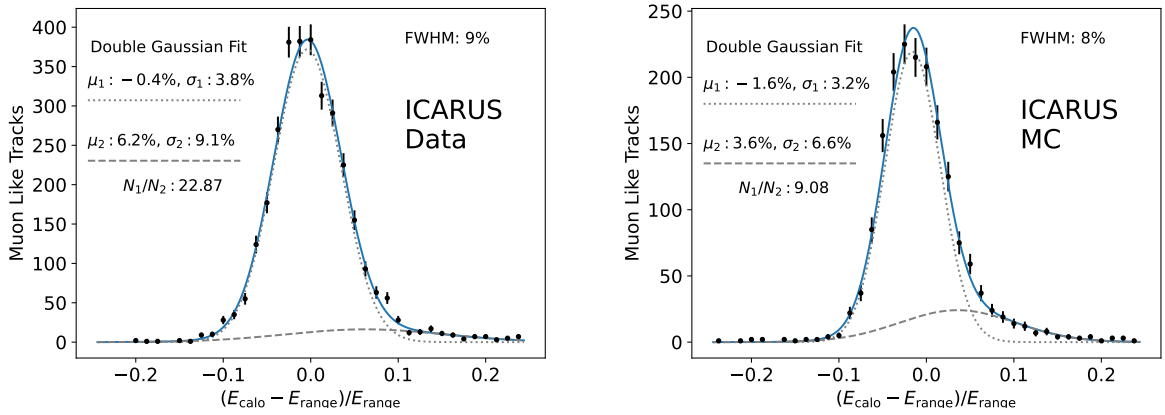

Figure 6.11: Comparison of calorimetric energy (E_{calo}) and range energy (E_{range}) reconstruction for selected muons in ICARUS data (left) and Monte Carlo simulation (right). The EMB-based calibration is applied. The calorimetric energy applies the "Q-tip" energy reconstruction and a correction for missing hits along the track. The data points are fit to a sum of two Gaussian distributions with centers (μ_1, μ_2) and standard deviations (σ_1, σ_2). The ratio of the amplitudes of the Gaussian distributions is quoted as N_1/N_2.

6.5.3 Muon Energy Reconstruction

Stopping muons are identified by the selection from section 6.3.1. The same angular cuts are applied requiring $5^\circ < \theta_{xw} < 20^\circ$ and $70^\circ < \phi < 85^\circ$. The energy is measured along the whole track. The calorimetric energy is computed with the "Q-tip" energy reconstruction. It also includes a correction for missing hits along the track: for any wire along the track without a reconstructed hit, the mean energy loss at the inferred value of residual range is summed into the calorimetric energy. This correction ameliorates cases where charge depositions along the track go below the signal-to-noise threshold to create hits (especially along the minimum-ionizing part of the muon). It is a 5% correction on average.

Figure 6.11 shows the comparison of range and calorimetric energy for stopping cosmic-ray muons in ICARUS data and simulation. The comparison to data is only made for the EMB-based calibration because the difference in recombination modelling is not significant for (mostly minimum-ionizing) muon tracks. Unlike in the proton comparison, the distribution of the relative difference in data is described well by ICARUS Monte Carlo simulation.

6.6 Conclusion

This chapter has detailed a new measurement of electron-ion recombination in liquid argon and its application in the energy scale calibration of the ICARUS time projection chamber. This measurement observes a significant angular dependence in recombination for highly-ionizing particles in liquid argon. The ellipsoid modified box (EMB) model of recombination (equation 6.3) is able to describe the data across all measured angles.

The recombination measurement is used to calibrate calorimetry in the ICARUS TPC for use in particle identification and energy reconstruction. Distributions of particle identification variables match well between ICARUS data and Monte Carlo simulation when the EMB recombination model is used to calibrate the data. The difference between calorimetric energy reconstruction and the estimation of energy by the track length has a resolution of about 5% for both muons and protons in ICARUS data. This matches the expectation for muons from ICARUS simulation but is larger than the expectation for protons. This effect could be the result of larger fluctuations in electron-ion recombination for highly ionizing energy depositions than what is simulated.

CHAPTER 7

EVENT SELECTION FOR DI-MUON DECAYS

At this point, the calibrations necessary to apply measurements in the ICARUS TPC are fully specified. We are thus ready to return to the headline analysis of the thesis: the search for di-muon decays from long-lived particles (LLPs) produced in kaon decay (as introduced in chapter 2).

Di-muon decays from LLPs produce two forward going tracks in the ICARUS detector. Neutrinos, the physics signal for most measurements in ICARUS, for us present a background to this process. The event selection places cuts to select for di-muon decays against neutrino interaction backgrouns. Cuts on particle identification variables identify events with two muon-like (μ or $\pi^{\pm}$) tracks. Cuts on kinematic variables require consistency with a di-muon decay. The most powerful of these is the θ_{NuMI} variable, which is the angle between the direction to the NuMI target and the reconstructed scalar direction (obtained by summing the momenta of the two muon candidates). This angle is diagrammed in figure 7.1. After the cuts, there is a small neutrino background, primarily from muon neutrion charged current coherent pion (ν_{μ}CC-Coh-π) interactions [99, 100].

The event selection for the analysis identifies stopping, muon-like tracks. This selection provides a sample with no cosmic background and a small but non-negligble neutrino background. The momenta of the two stopping muon tracks can be reconstructed with a good resolution. This selection enables a bump-hunt search with the di-muon invariant mass for any new physics signal (see chapter 9).

The event selection relies on Pandora reconstruction [86, 87], applied on hits from ICARUS signal processing. This workflow is described in section 7.1. Event selection cuts leverage a number of tools downstream of Pandora that are used to reconstruct aspects of the tracks such as their calorimetric particle identification and kinematic reconstruction. They are described in section 7.2. The fiducial volume in the selection is defined in section 7.3 and the

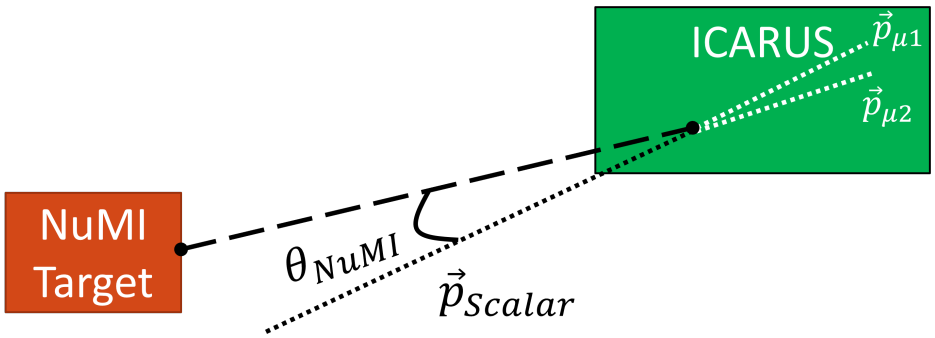

Figure 7.1: Diagram of the θ_{NuMI} angle. Not to scale. The reconstructed 4-momenta of the two muon candidates $\boldsymbol{p_{\mu 1}}$, $\boldsymbol{p_{\mu 2}}$, are summed to obtain the scalar direction. This direction is compared to the angle to the NuMI target.

pre-selection is defined in section 7.4. Distributions of the kinematic variables are shown in section 7.5. A study done to optimize these cuts is developed in section 7.6. Finally, the results of the event selection are shown in section 7.7.

7.1 TPC Signal Processing and Pandora Workflow

Ionization signals on each wire plane are processed to reduce noise and to produce a Gaussian signal shape for hit finding and charge reconstruction. Noise that is coherent across adjacent wires (groups of 64, on each readout board) is subtracted. The resulting wire signals are deconvolved per-wire. The deconvolution forms Gaussian signal shapes and further reduces noise [83].

Hits are identified on deconvolved waveforms by searching for Gaussian pulses above a threshold. Hits are fed into `Cluster3D`, a simple pattern matching algorithm that identifies matched hits across planes to reject noise hits. Matched hits are input to Pandora reconstruction, which reconstructs tracks and showers and places them into neutrino (or di-muon decay) and cosmic-ray candidate events.

Candidate di-muon decay events are identified as Pandora slices of TPC charge with at least two tracks. The two tracks closest to the reconstructed vertex are identified as the two

muon candidate tracks. A pre-selection puts some loose cuts on the muon candidate tracks. The event selection then identifies and cuts any other reconstructed objects in the slice, puts tighter cuts on the muon identification, removes low energy protons / vertex activity, and applies kinematic cuts.

7.2 Reconstruction Tools

7.2.1 Pandora Outputs

Pandora provides the basic objects and a number of reconstructed quantities useful in the analysis. Pandora clusters hits individually on each plane, then matches clusters across planes to perform 3D reconstruction and produce "particles". Multiple particles assumed to have the same origin (either neutrino or cosmic) are part of the same "slice" of charge. Particles in a slice form a "flow": there is a parent vertex (for neutrino slices) or particle (for cosmic slices), and other particles are children, grand-children, etc. of the parent.

Particles are fed to track and shower reconstructions. The track reconstruction creates a track trajectory which is used as the input to downstream algorithms (for particle ID and momentum reconstruction, e.g.).

7.2.2 χ^2 Calorimetric Particle ID

Calorimetric particle identification enables the separation of muon from other particle tracks. Muons and protons deposit very different rates of energy which can be distinguished in most cases. Pions are not calorimetrically distinguishable from muons. However, most pions inelastically scatter in the argon before coming to a stop. The particle ID, which selects specifically for a Bragg peak, rejects the large majority of these pions.

Particle identification is done by comparing the measured dE/dx along the track to its expectation. The dE/dx is reconstructed wire-by-wire along the track. The charge on each

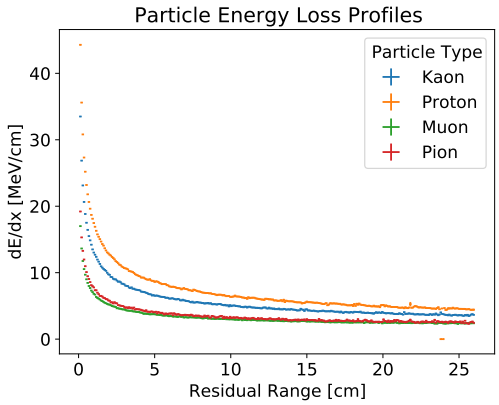

Figure 7.2: Energy loss profiles for particle types leveraged by the χ^2 particle identification algorithm.

wire is reconstructed by extracting the area of a Gaussian fit to signal pulses on the collection plane after the signal processing procedure. Charge is turned into energy loss (dE/dx) by applying the calibrations discussed in chapters 5 and 6.

The reconstructed track dE/dx is compared, as a function of residual range, to an expected profile of energy loss. This technique was originally developed by ArgoNeuT [121]. The profile was built from simulated energy loss of muon, pion, kaon, and proton tracks in Geant4. These profiles are shown in figure 7.2. A χ^2_P score is computed between the reconstructed track and the hypothesized particle P as:

$$\chi^2_P = \sum_{i}^{\text{hits}} \frac{\left(\overline{\frac{dE}{dx}}_P(\text{RR}_i) - \frac{dE}{dx}_i\right)^2}{(\delta\frac{dE}{dx}_P(\text{RR}_i))^2 + (r(\frac{dE}{dx}_i))^2}, \tag{7.1}$$

where $\overline{\frac{dE}{dx}}_P(\text{RR})$ is the expected dE/dx energy loss at the residual range RR, $\delta\frac{dE}{dx}_P(\text{RR})$ is the standard deviation of the energy loss distribution, and $r(dE/dx)$ is the resolution in the measurement of dE/dx. The algorithm applies $r(dE/dx) = (0.04231 + 0.0001783 \times dE/dx^2) \times dE/dx$ (where dE/dx is expressed as MeV/cm). Both of these factors are taken from the profiles in figure 7.2. We apply only the muon and proton χ^2 scores. These variables are good for selecting stopping muons and rejecting protons.

7.2.3 Stub Low Energy Proton ID

At low energies ($\lesssim$ 50 MeV KE), proton tracks do not travel far enough in the detector ($\lesssim$ 3 cm) to create a separate cluster of hits as recognized by Pandora. We have developed a special "stub" reconstruction to identify these low energy protons.

Stubs are recognized by identifying large hits near a reconstructed vertex. For all hits within 5 cm of a reconstructed vertex, a dQ/dx is computed. The dx is computed using an assumed pitch by drawing a track from the vertex to the 3D location of the hit. Hits within 5 cm of the reconstructed vertex and $dQ/dx > 200\text{ke}^-/\text{cm}$, or hits within one 1 wire of the vertex (projected onto the plane) and $dQ/dx > 100\text{ke}^-/\text{cm}$, seed candidate stubs. Hits between the reconstructed vertex and the germinate hit are added to the stub. The hit in the wire immediately preceding the reconstructed vertex and immediately following the germinate hit are also included, if they are present. Stubs are combined if one fully overlaps the other. Stubs can be computed from any wire plane. However, since only the collection plane has been fully calibrated, we only source stubs from that plane.

There are two reconstructed quantities obtained from stubs. The total length of the stub is computed as the distance from the reconstructed vertex to the 3D location of the germinate hit. A total charge is computed as the sum of charge from hits in the stub. If a track overlaps the stub, the expected ionization from a minimum ionizing energy loss (dE/dx =1.6 MeV/cm) is subtracted from the stub. The charge is turned into a kinetic energy by assuming the stub only consists of precisely one proton, and mapping the reconstructed charge to the corresponding proton kinetic energy. This map depends on the track angle to the electric field. This angle is not reconstructed for stubs, which consist of only one or a couple of hits. The map is constructed applying the angle of the NuMI beam (from the target) to the ICARUS drift field, 66.7°. This map is shown in figure 7.3.

The performance of the stub energy reconstruction is shown in figures 7.4 and 7.5. The stub energy reconstructs the true vertex energy well when there is one proton produced in the

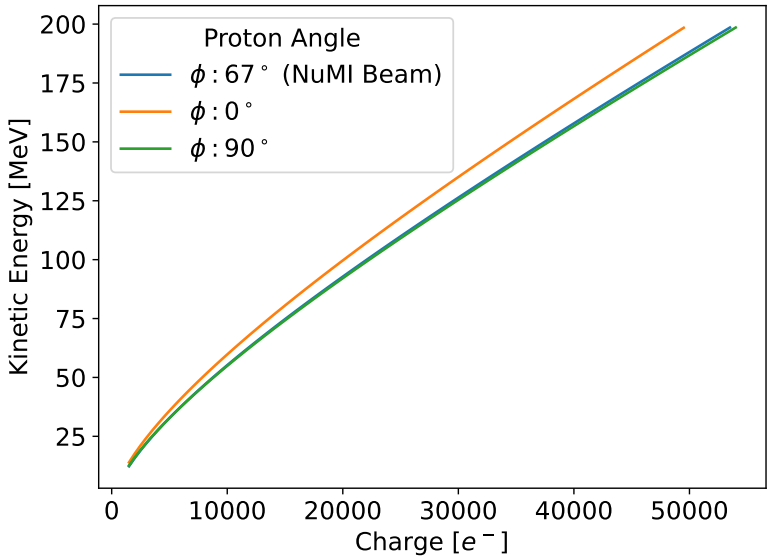

Figure 7.3: Map of charge to kinetic energy for stub low energy proton reconstruction. Due to EMB recombination (equation 6.3), the map depends on the track angle to the drift-electric field, ϕ. This angle is not reconstructed by stubs, so instead the NuMI beam angle to the drift electric field is applied. This is bench-marked by comparing it to angles parallel and perpendicular to the drift field.

neutrino interaction. In general, it underestimates the energy if there are multiple protons at the vertex (which is typically the case). Due to the non-linearity of recombination, to map reconstructed charge to energy it is necessary to make assumptions about the particle content of the vertex. Future work could explore possible improvement from a more sophisticated treatment of the vertex particle content than assuming it consists of one proton. Figure 7.6 demonstrates the improvement in low energy proton identification from stub reconstruction.

7.2.4 Range Momentum Estimation

The range of stopping tracks can be turned into a momentum measurement. This measurement comes from applying the continuous slowing down approximation (CSDA) with the Bethe-Bloch mean energy loss for particle tracks. A power law fit of range to momentum is applied to get the momentum.

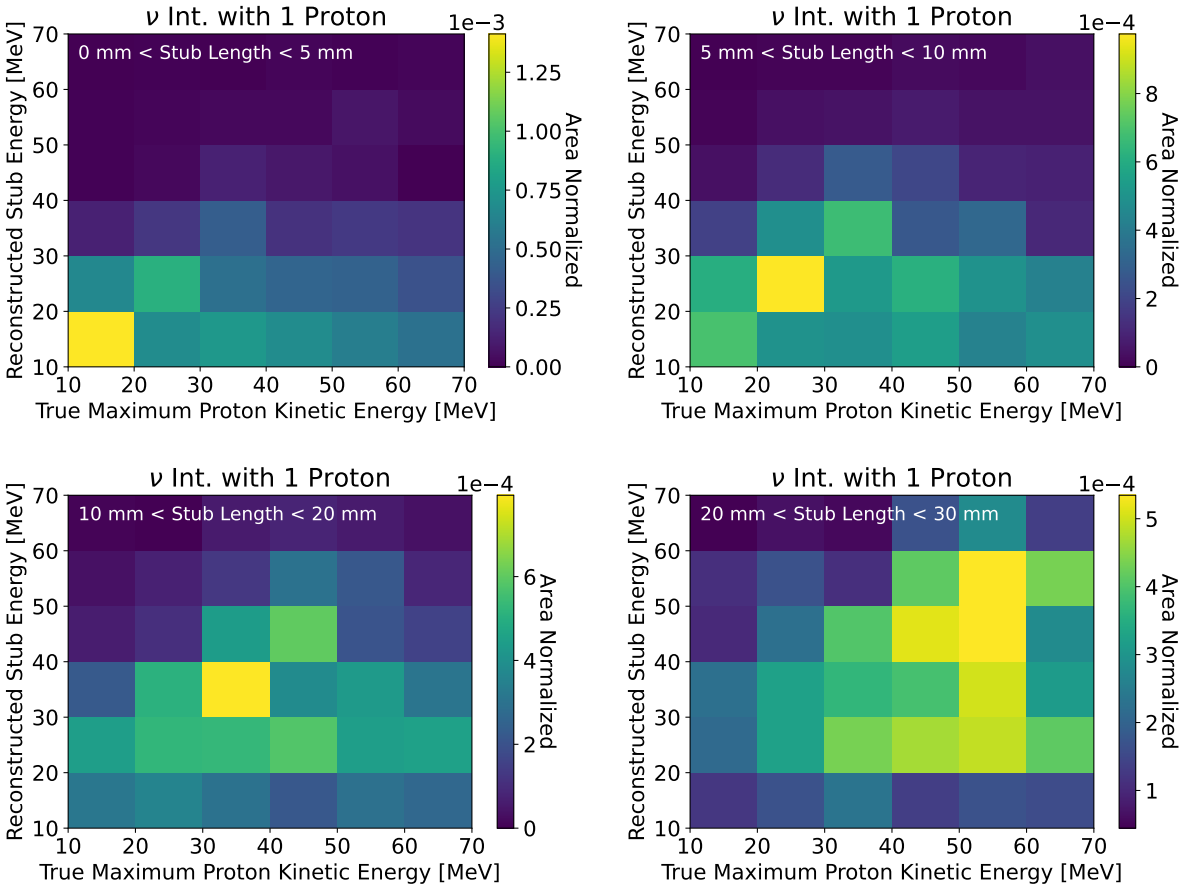

Figure 7.4: Comparison of the reconstructed stub energy to the maximum proton kinetic energy in the interaction. Shown for neutrino interactions that pass the dimuon preselection (section 7.4) that have exactly one proton in the final state.

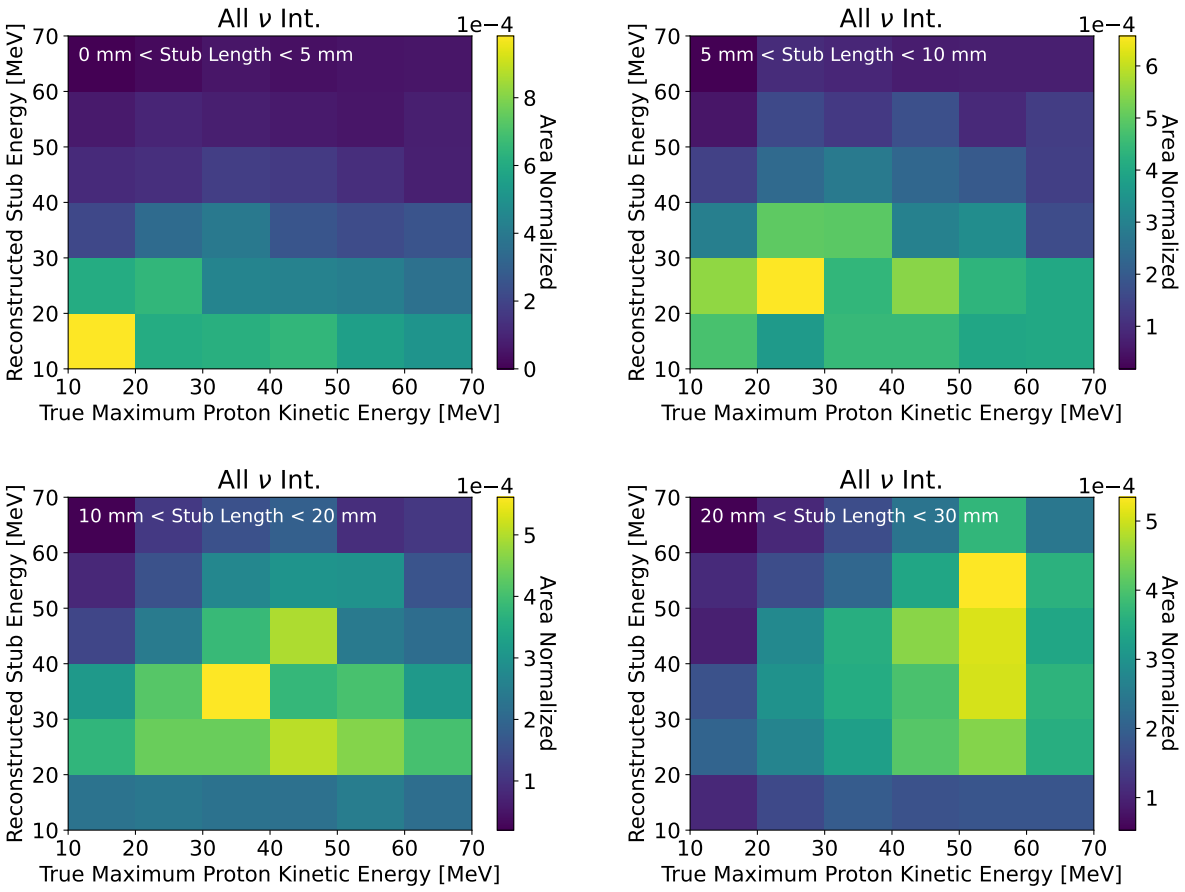

Figure 7.5: Comparison of the reconstructed stub energy to the maximum proton kinetic energy in the interaction. Shown for neutrino interactions that pass the dimuon preselection (section 7.4).

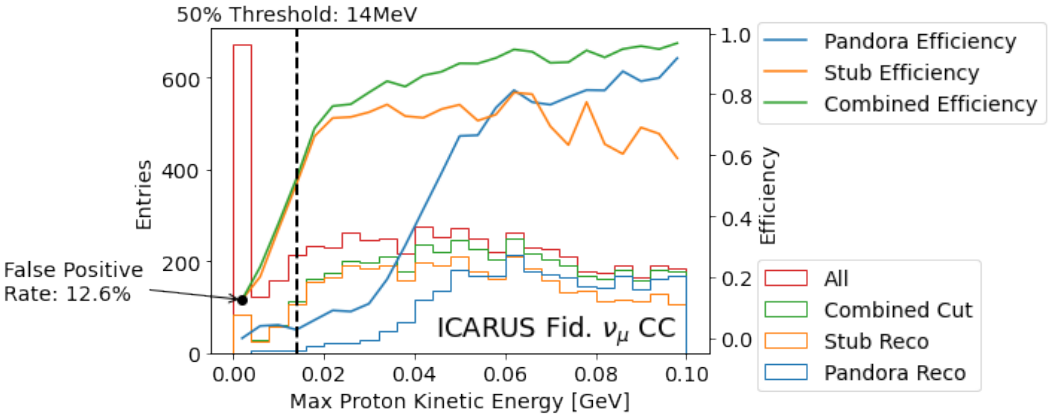

Figure 7.6: Performance of proton identification for low energy "stub" identification, compared with Pandora reconstruction. The spectra of the maximum proton kinetic energy is shown for all fiducial ν_μ CC interactions in ICARUS simulation. Then, the spectra after applying a requirement that Pandora identifies the leading proton (blue), that stub reconstruction identifies the proton (orange), and then either algorithm identifies the proton (green) are all shown. These spectra are used to compute the proton identification efficiency. The plot also shows the 50% identification threshold and the false positive rate (the fraction of interactions without a proton where one is identified).

7.2.5 Multiple Coulomb Scattering Momentum Estimation

The amount of scattering of a muon track can be used to extract the track momentum. This reconstruction can be applied to exiting tracks. In addition, it can be used to verify that stopping tracks are not split. The multiple Coulomb scattering reconstruction implementation is taken from an algorithm developed by MicroBooNE [148]. It has been applied in ICARUS Monte Carlo simulation and calibrated to ICARUS data.

7.3 Fiducial and Containment Volumes

The fiducial volume defines the volume of decay vertices that are considered in the analysis. It is defined as an inset to the detector active volume. This inset is 10 cm in $\hat{x}$ and $\hat{y}$ and 15 cm in the upstream $\hat{z}$. It is 100 cm in the downstream $\hat{z}$.

The containment volume defines the volume of track end points that are considered contained for this analysis. The track containment volume is inset 10 cm in $\hat{x}$ and $\hat{y}$ and

15 cm in $\hat{z}$.

Furthermore, specific bad regions of the detector are excluded from both volumes. In TPC EE, the regions where $Y > 115$ cm and $Y < -161.86$ cm are removed due to the field cage failure (this is an inset of 20 cm from the edges). In TPC WW, the region where $Y > 70$ cm, $Z > 0$ cm is removed due to the dangling cable. The total fiducial volume comprises 308 t of LAr.

7.4 Pre-Selection

The pre-selection identifies slices with a di-muon decay topology and applies a loose muon ID. Candidate slices must have a fiducial vertex with at least two particles that start within 10 cm of the reconstructed vertex and have a length of at least 10 cm. The particle closer to the vertex is labelled the "trunk" and the particle further from the vertex is labelled the "branch". This terminology comes from the way di-muon decays are typically reconstructed. The two muons typically have a region at the start of the particle where they fully overlap (see the event displays in figure 3.5 for an example). Pandora typically reconstructs this topology as one track that starts at the vertex and another particle that "branches" off at the position the tracks split.

The trunk and the branch are both required to stop in the detector in the track fiducial volume. There are also particle ID cuts applied: $\chi^2_\mu < 30$ and $\chi^2_p > 80$. Figure 7.7 shows the fraction of well reconstructed events that pass the pre-selection cuts. In this case, well reconstructed means both muons are associated with two individual particle tracks, both of which start and end within 10 cm of their matched muon. A very high fraction of well reconstructed events pass the pre-selection. However, the fraction of well reconstructed events is itself relatively small ($\sim 50\%$). This is due to Pandora poorly reconstructing muon tracks. Signal-to-noise is relatively small for minimum-ionizing depositions along muon tracks. The reconstruction of these signals can be poor, especially on the induction planes.

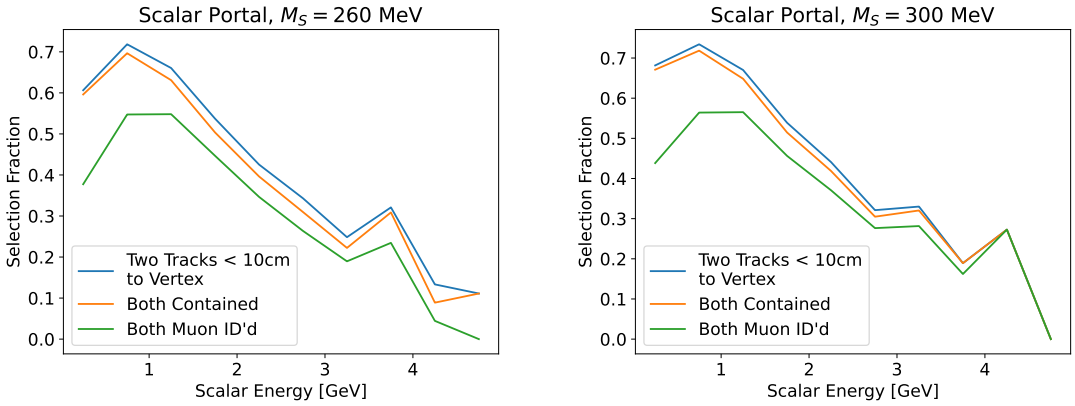

Figure 7.7: Fraction of all fiducial, contained scalar decays that are well-reconstructed and pass pre-selection requirements. First, the blue line shows the fraction of all fiducial, contained scalar decays where Pandora identifies a track for each muon. Both tracks are required to identify the muon start and endpoints to within 10 cm. Further requirements are placed on the two tracks in the next two lines. First, the orange line plots the fraction of events where both tracks are reconstructed as contained. Second, the green line plots the fraction of events where both tracks pass the muon-ID cuts in the pre-selection (see section 7.4).

The poor signal reconstruction can leave gaps on the planes which can lead Pandora to split up tracks. Furthermore, at low scalar mass the two decay muons are very forward and can overlap for a significant length (∼10s of cm). Pandora has trouble reconstructing this topology. Both of these issues would benefit from further optimizations to reconstruction algorithms in future work.

The cut on the distance between the vertex and track start is also studied in figure 7.8. Loosening the cut beyond 10 cm would provide a marginal improvement to the efficiency.

7.5 Cut Variable Distributions

The following figures plot the variables used to select for di-muon decays. Distributions are area normalized comparisons of the scalar signal, as well as neutrino and cosmic backgrounds, for two example scalar model points, at $M_S = 240$ MeV and 320 MeV. The variables are:

1. Object Cuts

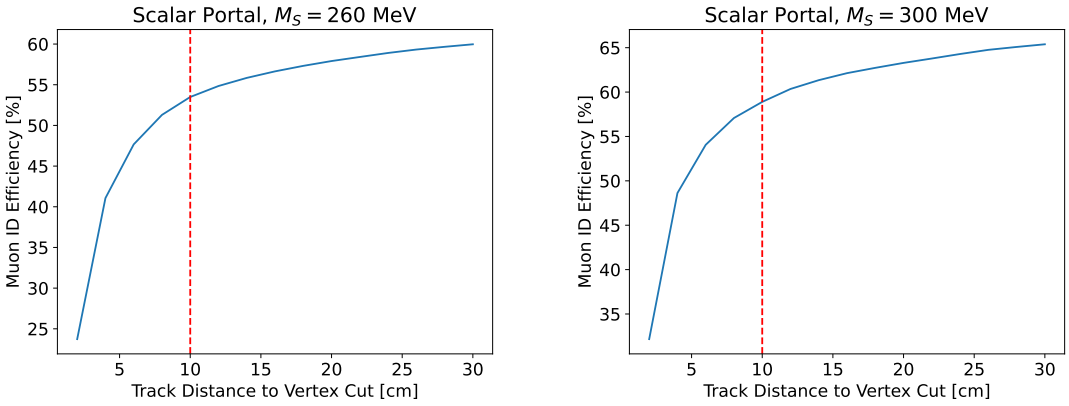

Figure 7.8: Efficiency of the muon ID requirement as a function of the distance between the event vertex and the track start position. In the pre-selection, the cut is placed at 10 cm.

- Maximum shower length: the longest shower that starts within 10 cm of the reconstructed vertex (not applied if there is no such shower). Figure 7.9.
- Maximum other track length: the longest track other than the two muon candidates that starts within 10 cm of the reconstructed vertex (not applied if there is no such track). Figure 7.10.
- Maximum other χ^2_μ: the maximum χ^2_μ value for any particle other than the two muon candidates that starts within 10 cm of the reconstructed vertex. Figure 7.11.
- Minimum other χ^2_p: the minimum χ^2_p value for any particle other than the two muon candidates that starts within 10 cm of the reconstructed vertex. Figure 7.12.

2. Tight muon ID

- Trunk length: the trunk track length. Figure 7.13
- Branch length: the branch track length. Figure 7.14
- Trunk χ^2_μ: the muon χ^2 for the trunk track. Figure 7.15
- Trunk χ^2_p: the proton χ^2 for the trunk track. Figure 7.16.

- Branch χ^2_μ: the muon χ^2 for the branch track. Figure 7.17
- Branch χ^2_p: the proton χ^2 for the branch track. Figure 7.18.
- Trunk MCS P/Range P: the offset between the reconstructed range momentum and the reconstructed multiple-Coulomb-scattering momentum for the trunk track. Figure 7.19.
- Branch MCS P/Range P: the offset between the reconstructed range momentum and the reconstructed multiple-Coulomb-scattering momentum for the branch track. Figure 7.20.

3. Stub ID

- Stub KE, $0 <$ length $< 0.5\,$cm: the maximum kinetic energy for any stub with a length between 0 and 0.5 cm (if at least one exists). Figure 7.21.
- Stub KE, $0.5 <$ length $< 1\,$cm: the maximum kinetic energy for any stub with a length between 0.5 and 1 cm (if at least one exists). Figure 7.22.
- Stub KE, $1 <$ length $< 2\,$cm: the maximum kinetic energy for any stub with a length between 1 and 2 cm (if at least one exists). Figure 7.23.
- Stub KE, $2 <$ length $< 3\,$cm: the maximum kinetic energy for any stub with a length between 2 and 3 cm (if at least one exists). Figure 7.24.

4. Kinematic Cuts

- Track opening angle: the angle between the two candidate muon tracks. Figure 7.25.
- Scalar angle to beam (θ_{NuMI}): the angle of the summed muon momentum vectors to the NuMI beam. Figure 7.26

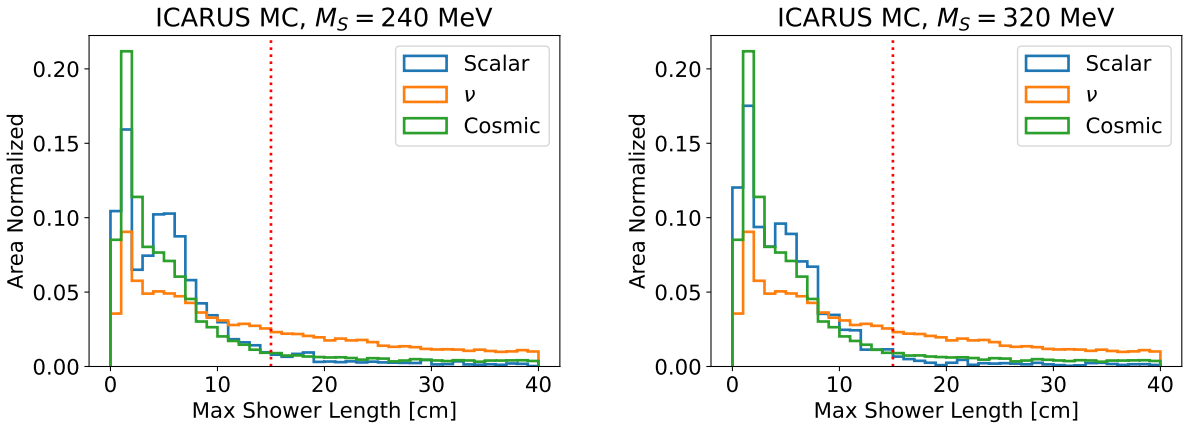

Figure 7.9: Area normalized spectra in ICARUS MC comparing scalar signal and backgrounds. Maximum length of any shower within 10 cm of the reconstructed vertex.

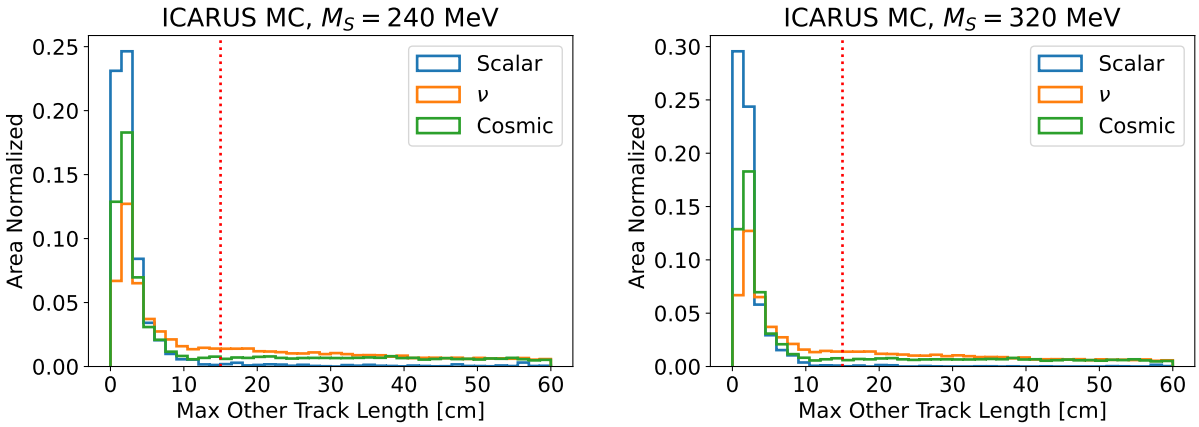

Figure 7.10: Area normalized spectra in ICARUS MC comparing scalar signal and backgrounds. Maximum length of any track other than the two muon candidates within 10 cm of the reconstructed vertex.

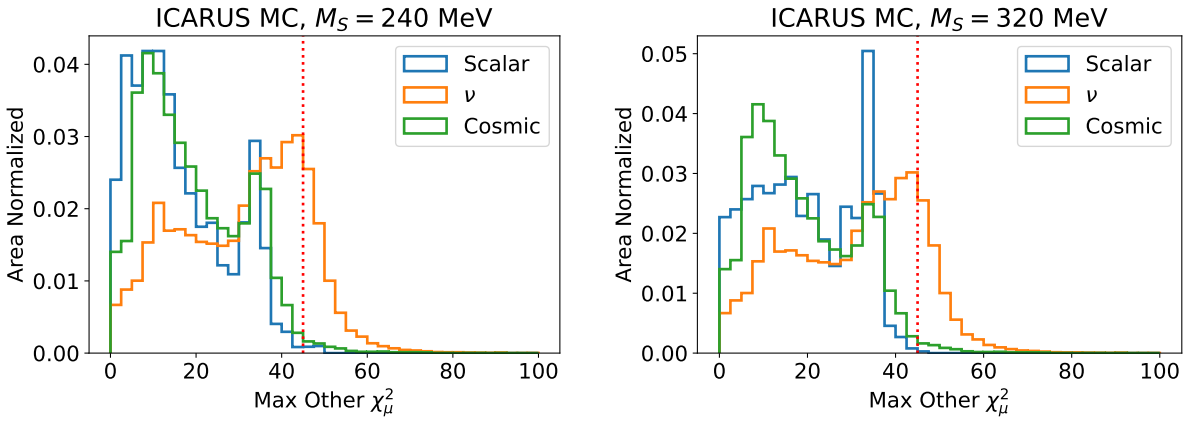

Figure 7.11: Area normalized spectra in ICARUS MC comparing scalar signal and backgrounds. Maximum χ^2_μ value for any particle other than the two muon candidates within 10 cm of the reconstructed vertex.

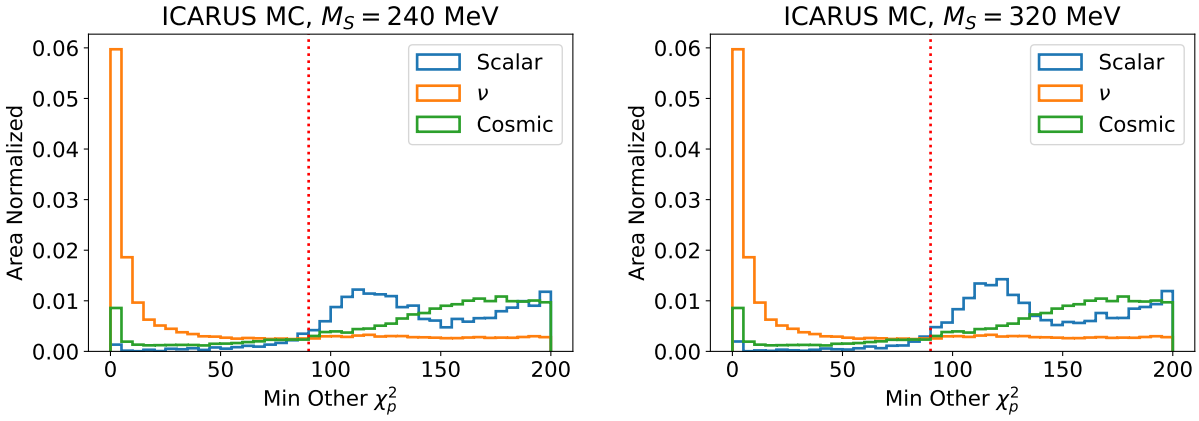

Figure 7.12: Area normalized spectra in ICARUS MC comparing scalar signal and backgrounds. Minimum χ^2_p value for any particle other than the two muon candidates within 10 cm of the reconstructed vertex.

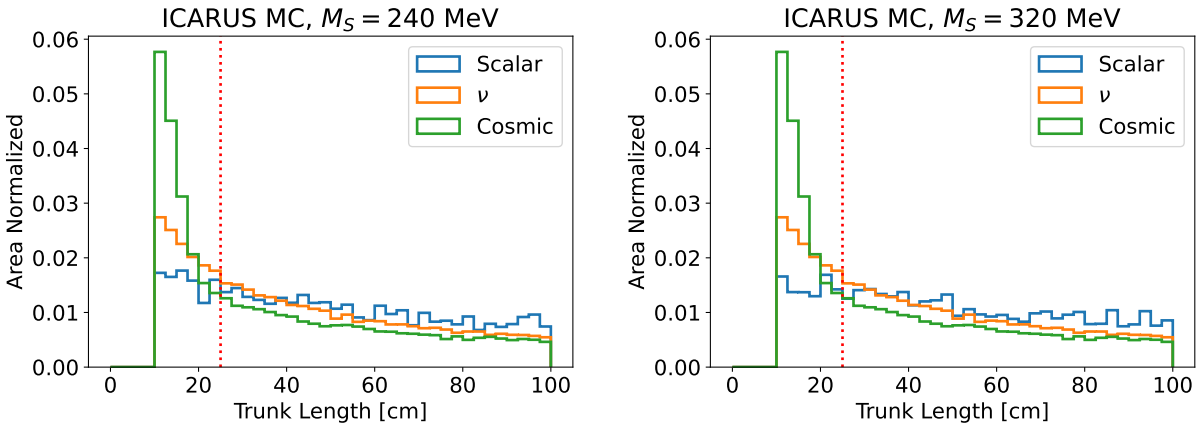

Figure 7.13: Area normalized spectra in ICARUS MC comparing scalar signal and backgrounds. Length of the trunk track.

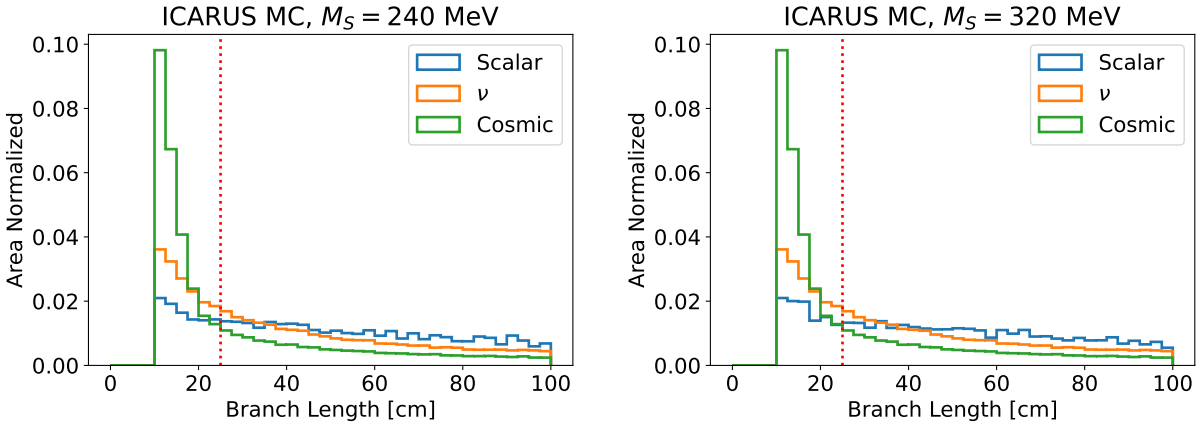

Figure 7.14: Area normalized spectra in ICARUS MC comparing scalar signal and backgrounds. Length of the trunk track.

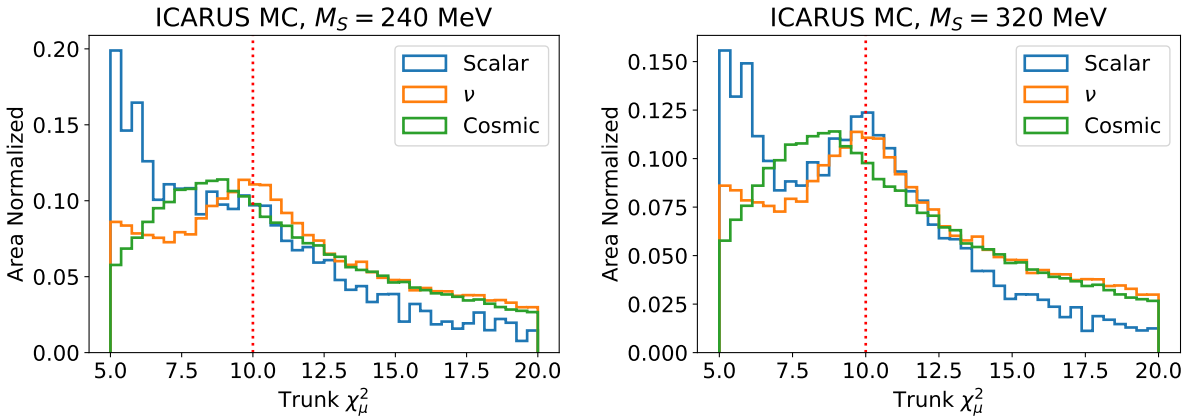

Figure 7.15: Area normalized spectra in ICARUS MC comparing scalar signal and backgrounds. χ^2_μ for the trunk track

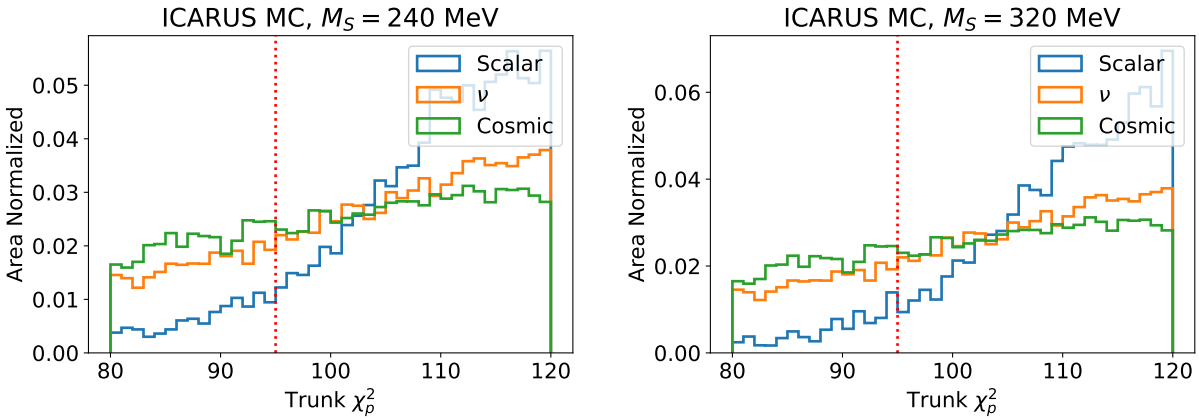

Figure 7.16: Area normalized spectra in ICARUS MC comparing scalar signal and backgrounds. χ^2_p for the trunk track

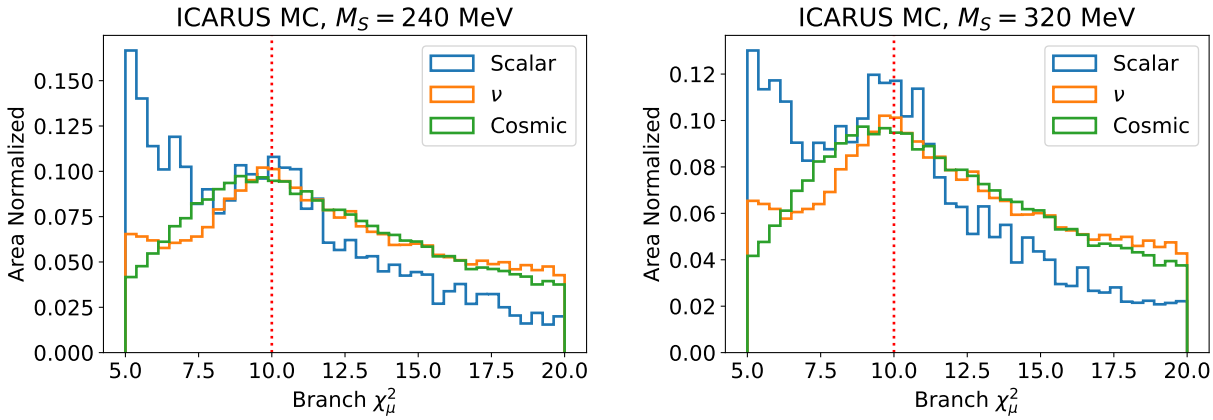

Figure 7.17: Area normalized spectra in ICARUS MC comparing scalar signal and backgrounds. χ^2_μ for the branch track

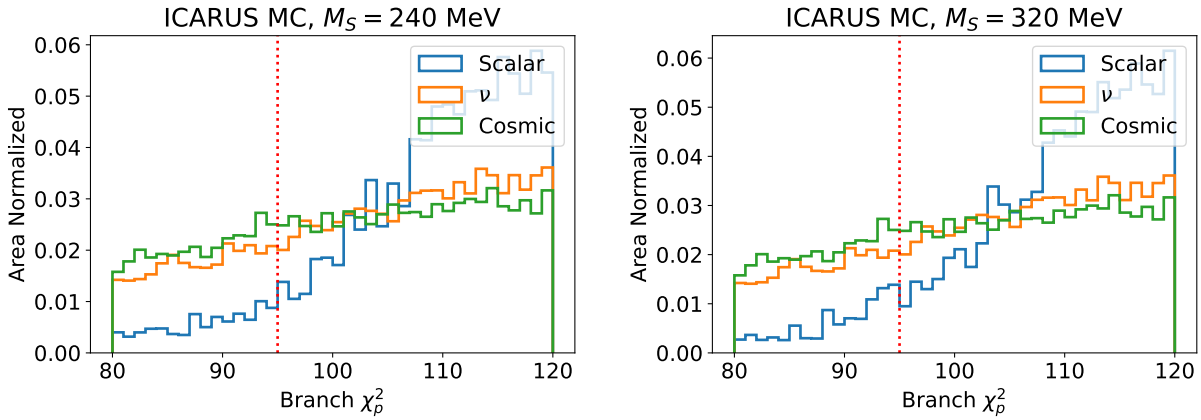

Figure 7.18: Area normalized spectra in ICARUS MC comparing scalar signal and backgrounds. χ^2_p for the branch track

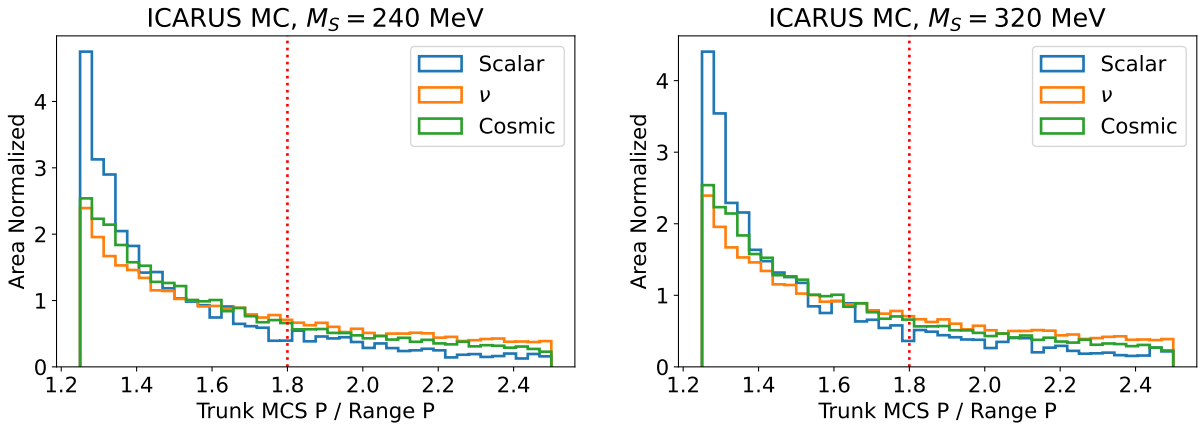

Figure 7.19: Area normalized spectra in ICARUS MC comparing scalar signal and backgrounds. Comparison of the range and multiple-Coulomb-scattering momentum for the trunk track

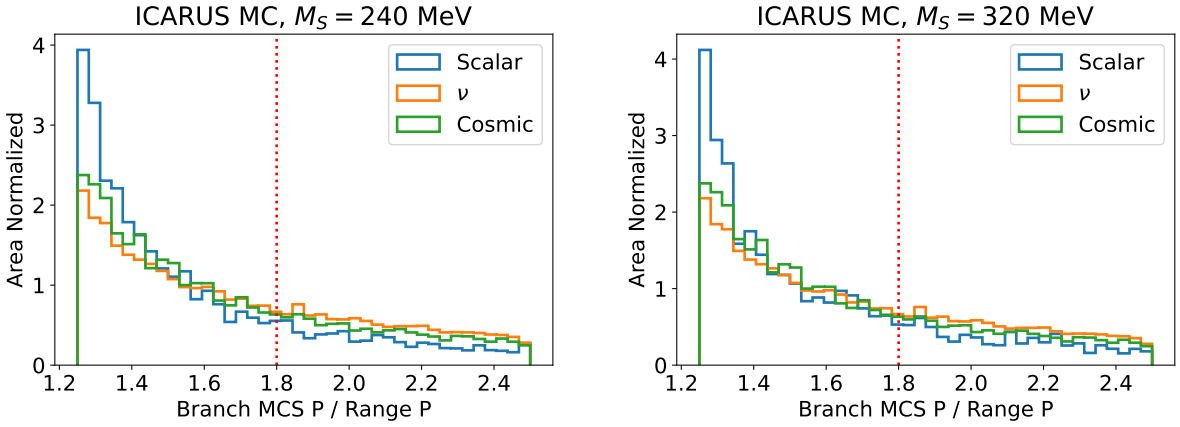

Figure 7.20: Area normalized spectra in ICARUS MC comparing scalar signal and backgrounds. Comparison of the range and multiple-Coulomb-scattering momentum for the branch track

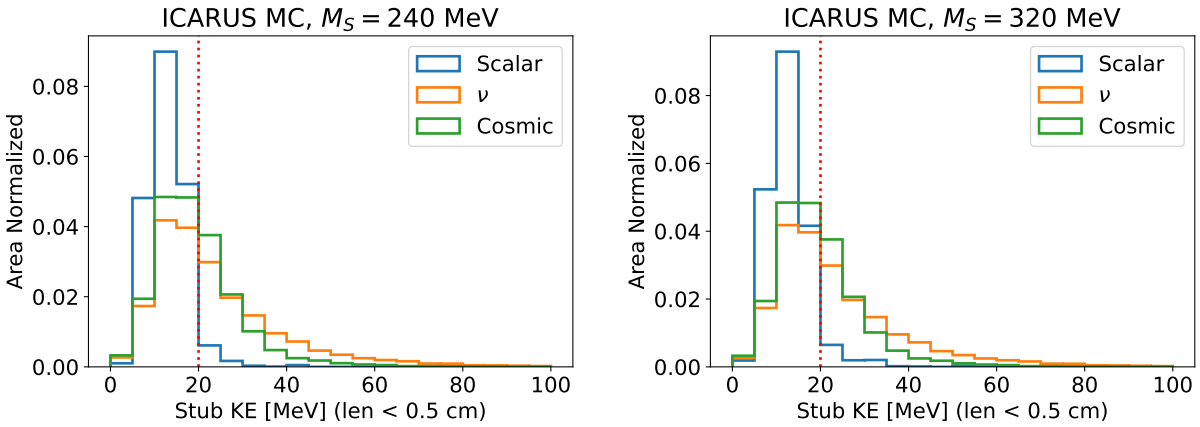

Figure 7.21: Area normalized spectra in ICARUS MC comparing scalar signal and backgrounds. The maximum dQ/dx for any stub with a length between 0 and 0.5 cm (if at least one exists).

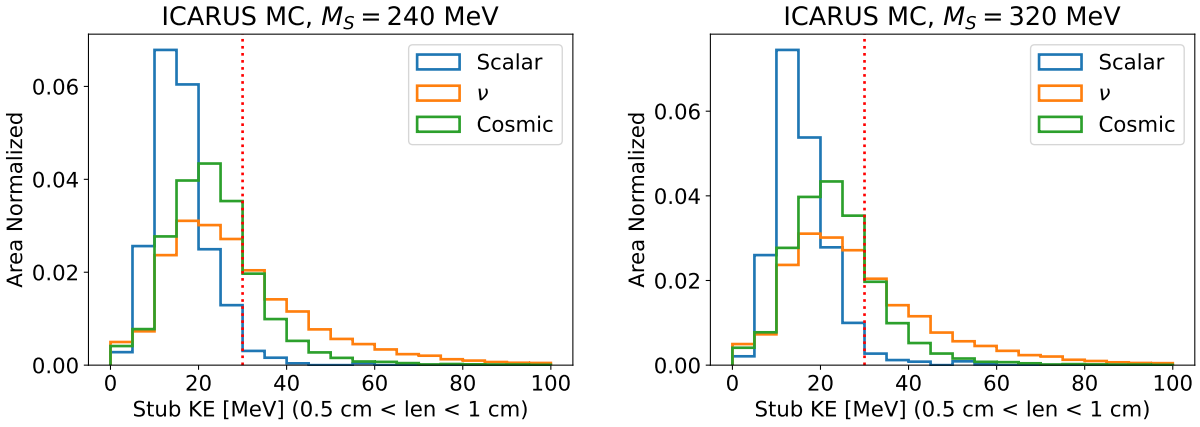

Figure 7.22: Area normalized spectra in ICARUS MC comparing scalar signal and backgrounds. The maximum dQ/dx for any stub with a length between 0.5 and 1 cm (if at least one exists).

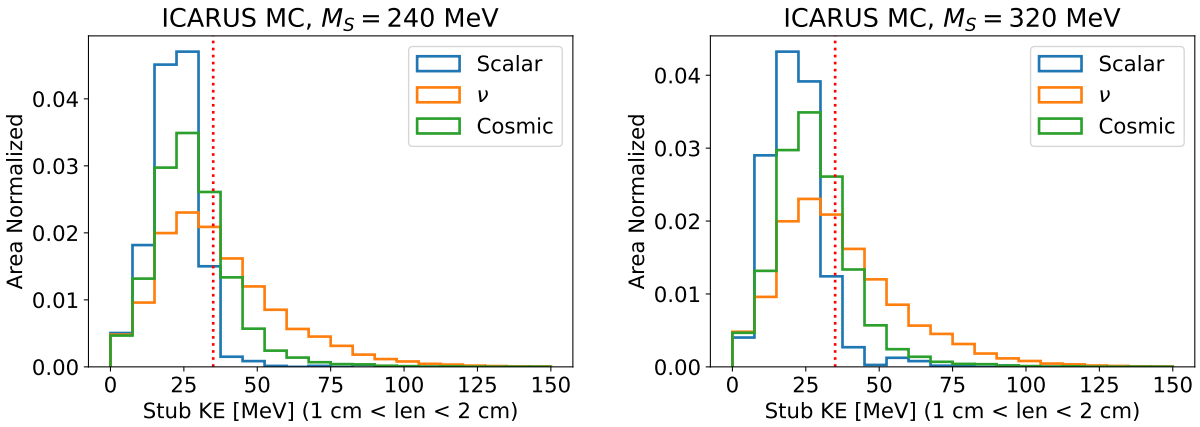

Figure 7.23: Area normalized spectra in ICARUS MC comparing scalar signal and backgrounds. The maximum dQ/dx for any stub with a length between 1 and 2 cm (if at least one exists).

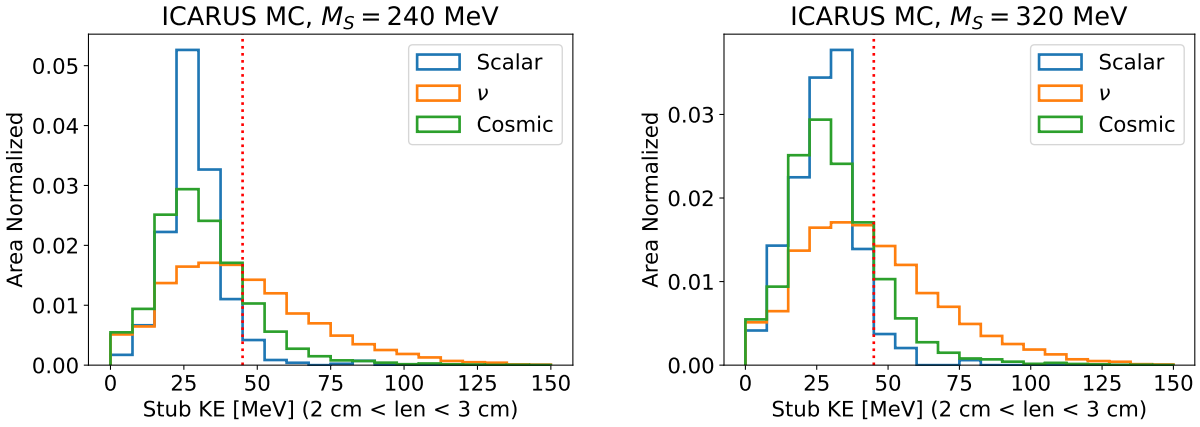

Figure 7.24: Area normalized spectra in ICARUS MC comparing scalar signal and backgrounds. The maximum dQ/dx for any stub with a length between 2 and 3 cm (if at least one exists).

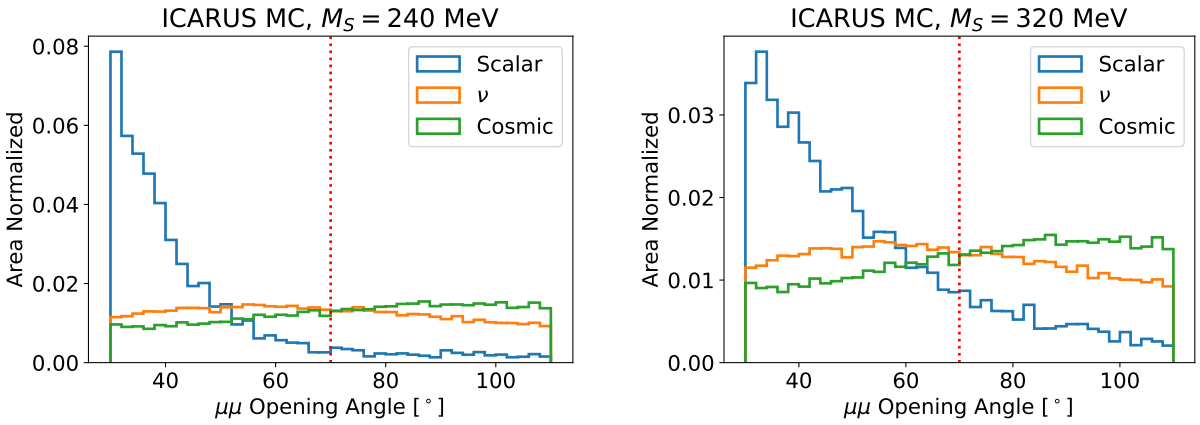

Figure 7.25: Area normalized spectra in ICARUS MC comparing scalar signal and backgrounds. Opening angle between the two muon candidate tracks.

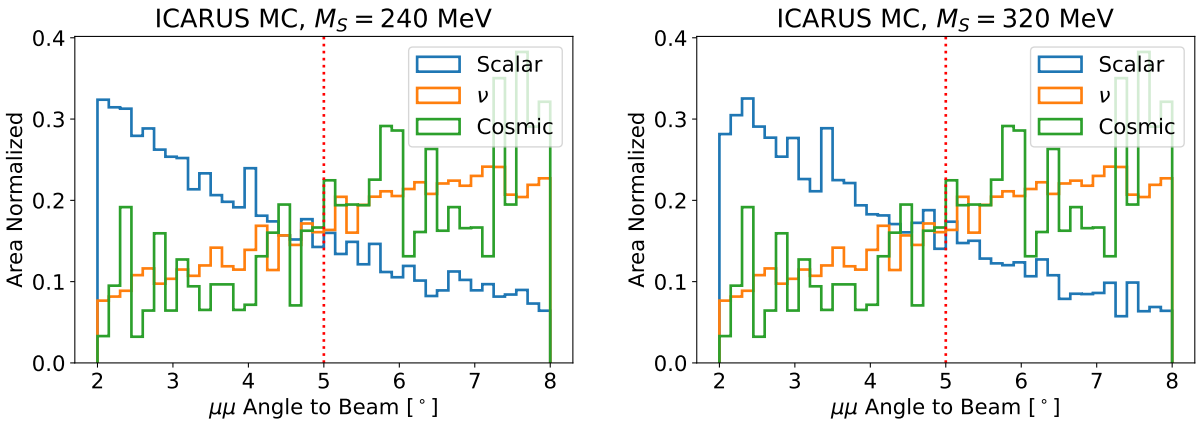

Figure 7.26: Area normalized spectra in ICARUS MC comparing scalar signal and backgrounds. The reconstructed $\mu\mu$ angle to the NuMI beam.

7.6 Cut Optimization

A cut optimization study has been performed using the effective signal significance as the figure of merit. The effective statistical significance is defined for a scalar mass point M as $S/\sqrt{S+B}$ where S and B are the number of signal and background events with a reconstructed scalar mass within 40 MeV of M. The signal model normalization at each mass point is weighted so that 30 events pass the preselection. The signal analysis is oriented as a bump-hunt (see chapter 9), and this range of reconstructed scalar mass defines the statistical significance of the bump.

In this study, for each variable the cut value is varied over its possible range while keeping all other cuts fixed. The effective statistical significance relative to the maximum value for the cut is plotted for each test mass point. This study was done iteratively to find cut values that maximized the effective signal significance across all mass points. It is shown for the object cuts in figure 7.27, for the muon ID cuts in figures 7.28 and 7.29, for the stub ID in figure 7.30, and for the kinematic cuts in figure 7.31.

7.7 Selection Results

The efficiency of the selection at each stage of the cuts is shown in figure 7.32. The efficiency is defined relative to the number of fiducial scalar decays where both tracks stop in the track fiducial region. The di-muon invariant mass distributions with injected scalar model points are shown in figure 7.33. The distributions of selected events before the θ_{NuMI} cut are shown as a function of θ_{NuMI} in figure 7.34. The cuts and their optimized values are summarized in table 7.1.

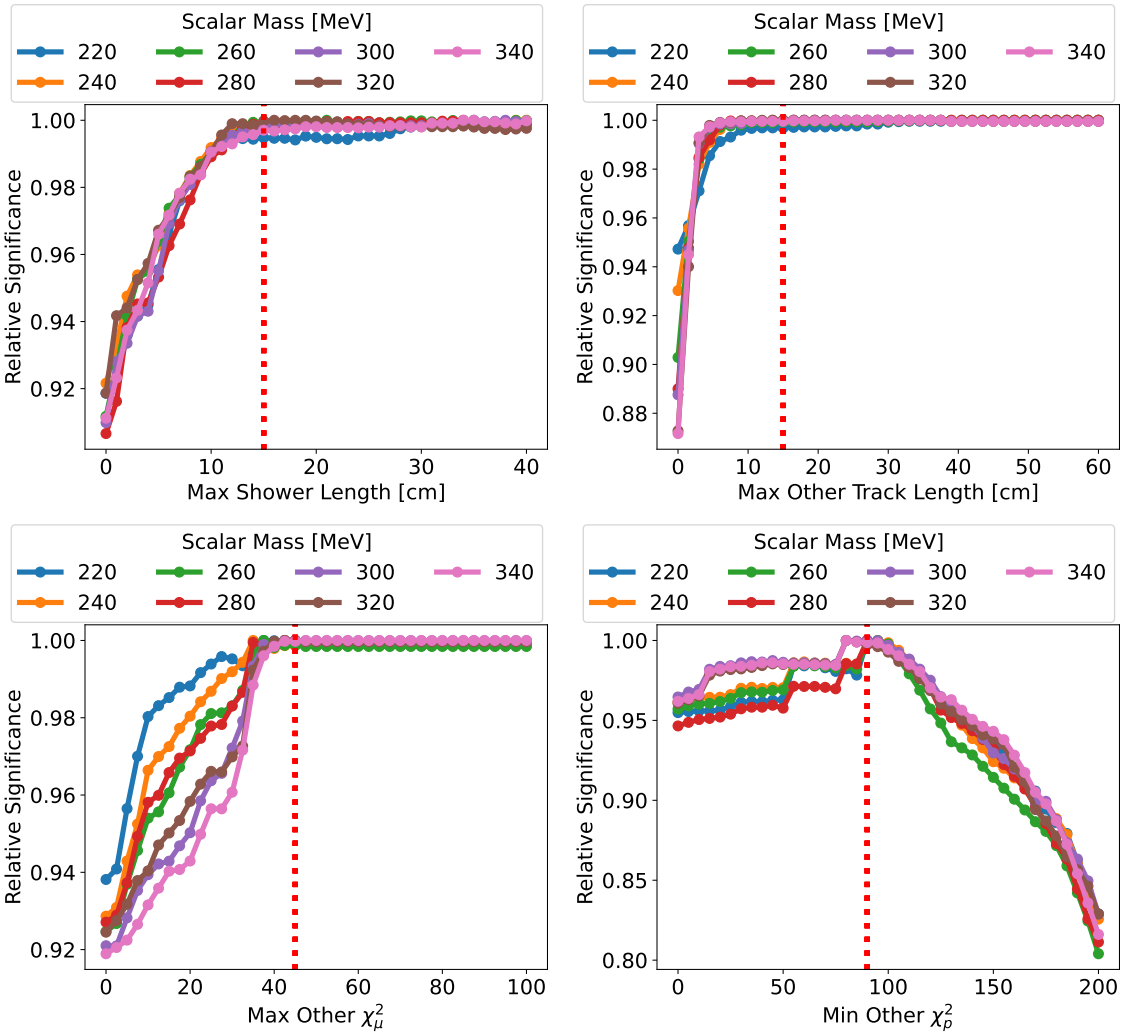

Figure 7.27: Cut optimization study for the object cuts.

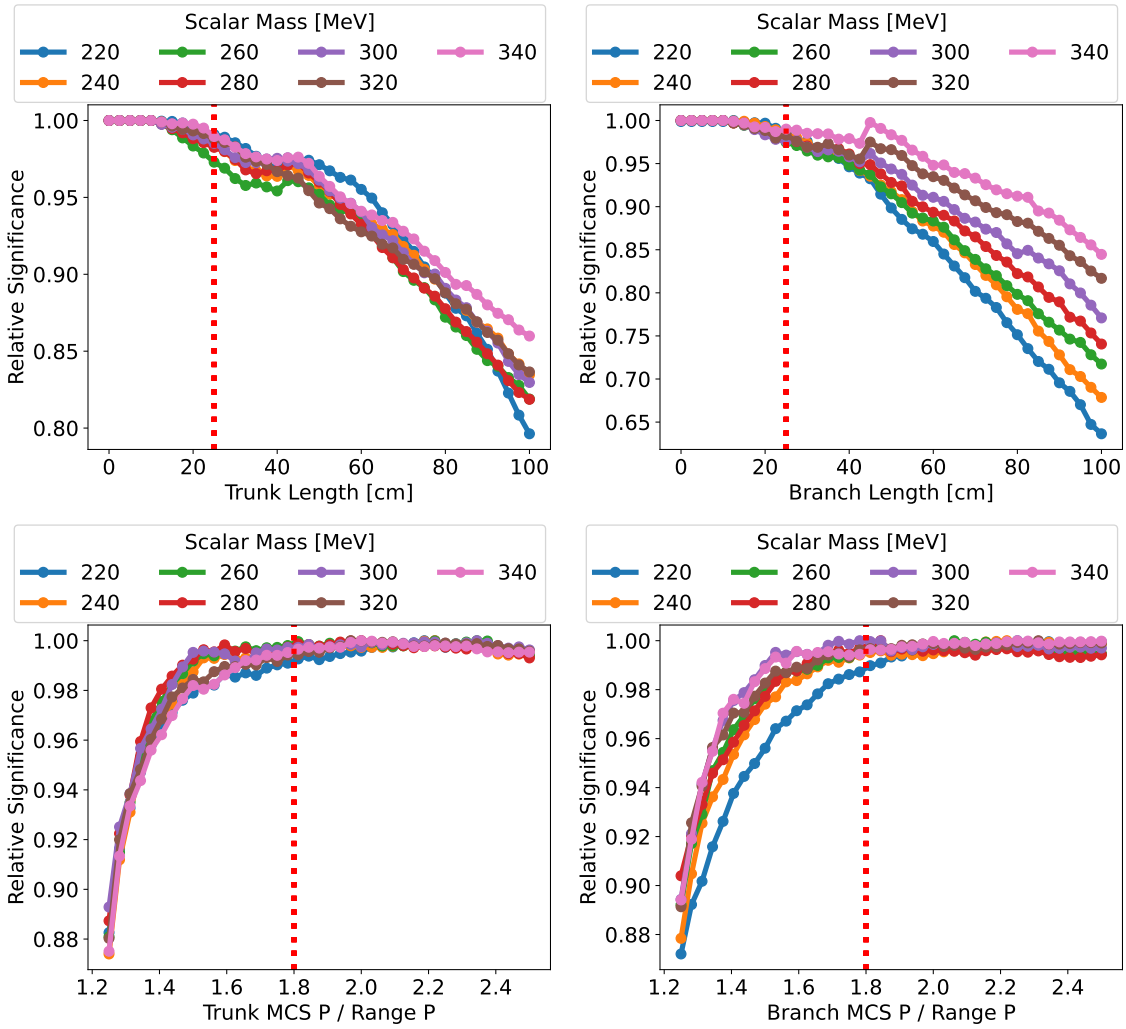

Figure 7.28: Cut optimization study for the muon topological ID cuts.

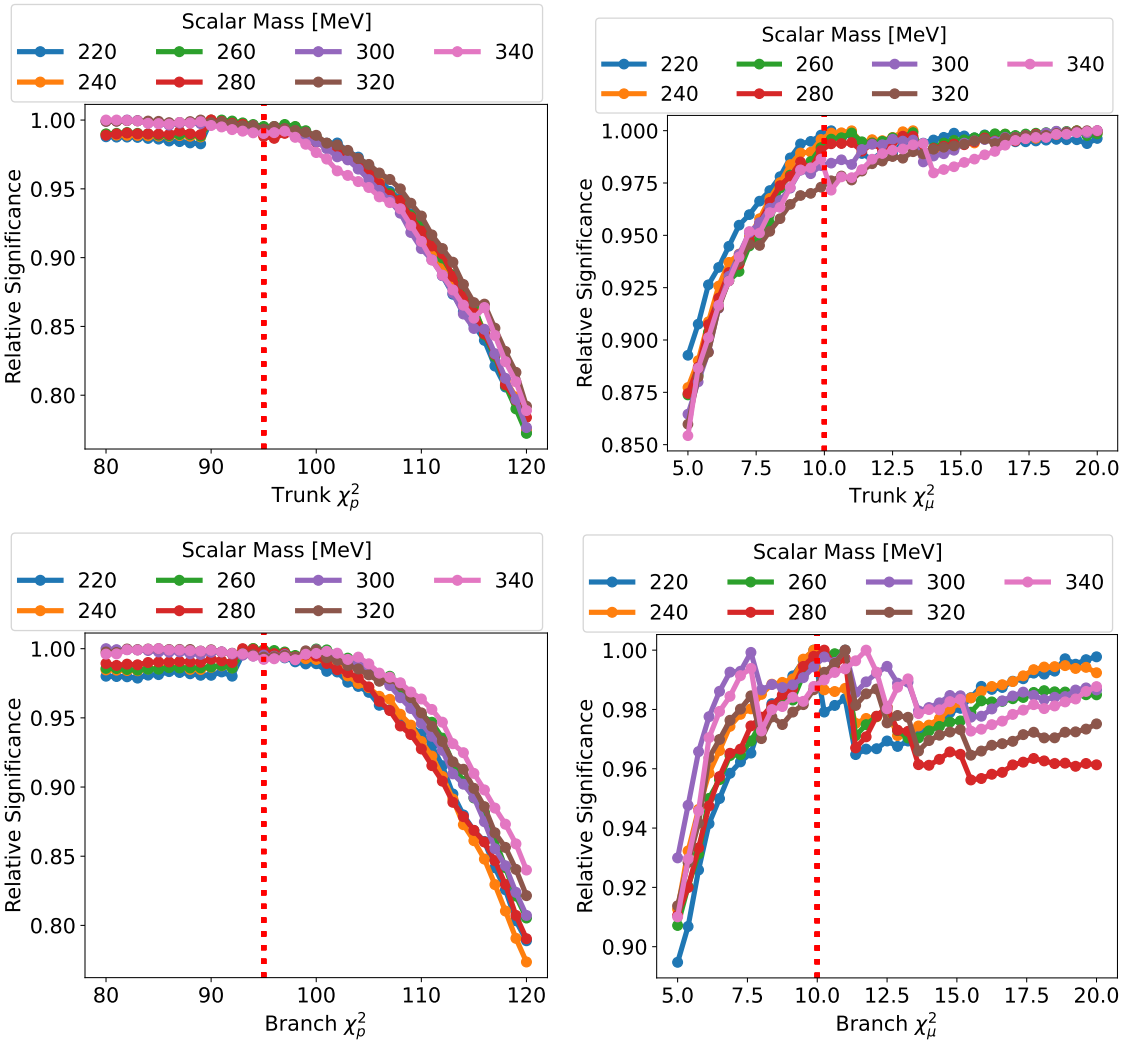

Figure 7.29: Cut optimization study for the muon calorimetric ID cuts.

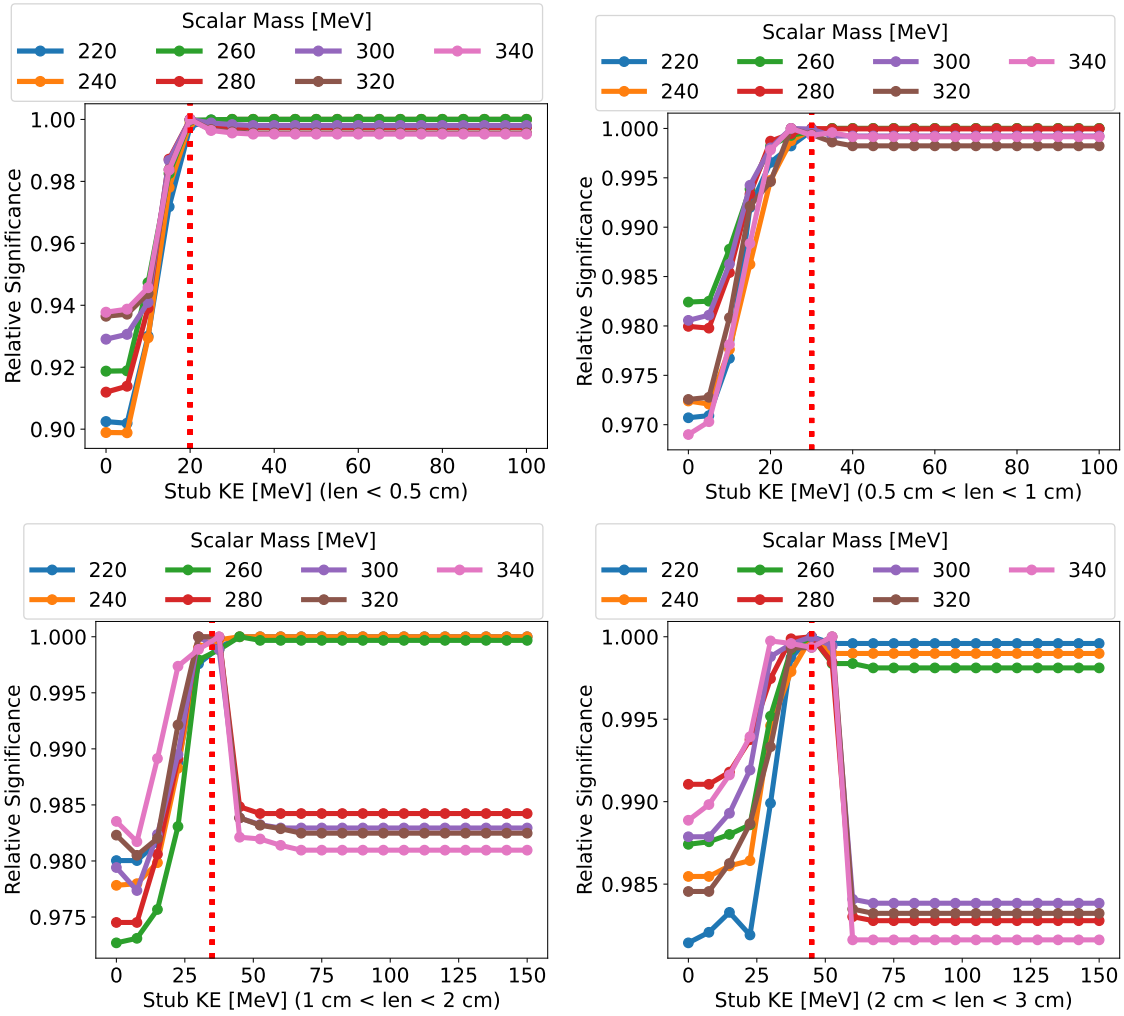

Figure 7.30: Cut optimization study for the stub ID cuts.

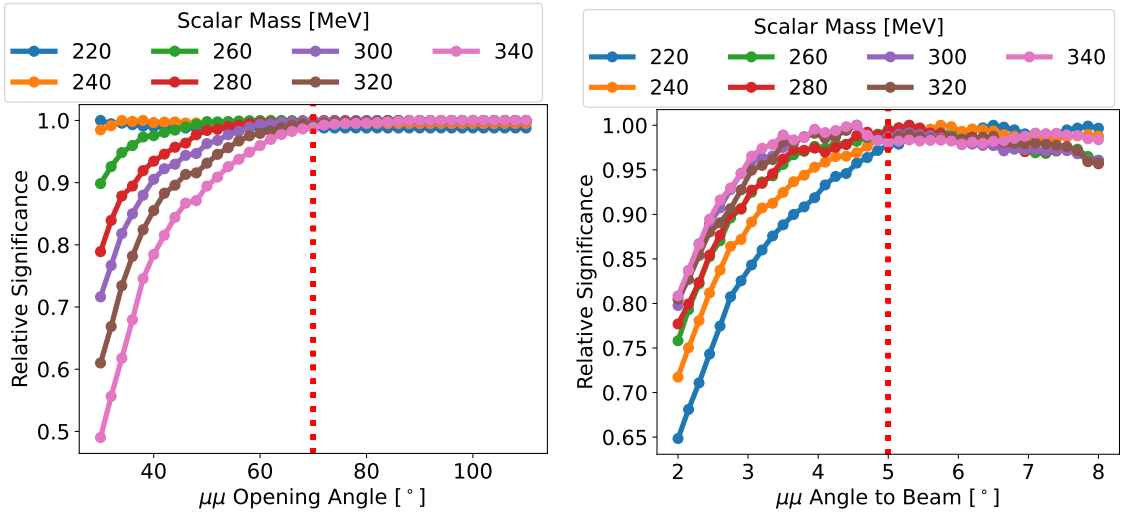

Figure 7.31: Cut optimization study for the kinematic cuts.

Cut	Value
Other Object Cuts	
Maximum shower length in slice	<15 cm
Maximum third track length in slice	<15 cm
Minimum χ^2_p of other particle in slice	>90
Maximum χ^2_μ of other particle in slice	<45
Muon ID Cuts	
Trunk+Branch track length	>25 cm
Trunk+Branch χ^2_μ	<10
Trunk+Branch χ^2_p	>95
Trunk+Branch MCS P/Range P	< 1.8
Stub ID Cuts	
Maximum Stub KE (length 0-5 mm)	<20 MeV
Maximum Stub KE (length 5-10 mm)	<30 MeV
Maximum Stub KE (length 10-20 mm)	<35 MeV
Maximum Stub KE (length 20-30 mm)	<45 MeV
Kinematic Cuts	
Trunk-Branch Opening Angle	$< 70^\circ$
Trunk+Branch (Scalar) angle to beam (θ_{NuMI})	$< 5^\circ$

Table 7.1: Summary of cuts and their optimized values in the event selection.

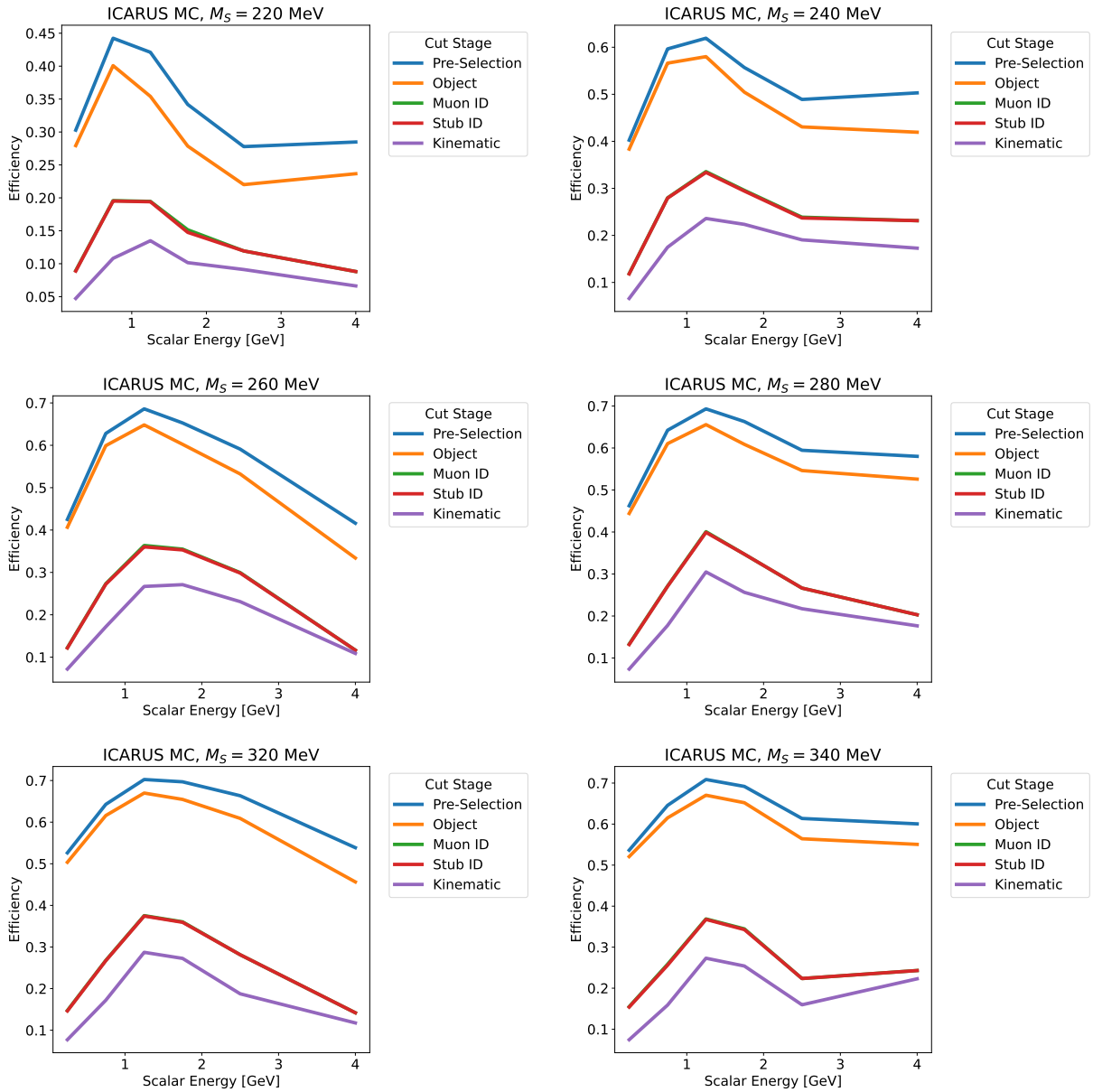

Figure 7.32: Efficiency of the event selection, at each stage in the cuts, for sample model points.

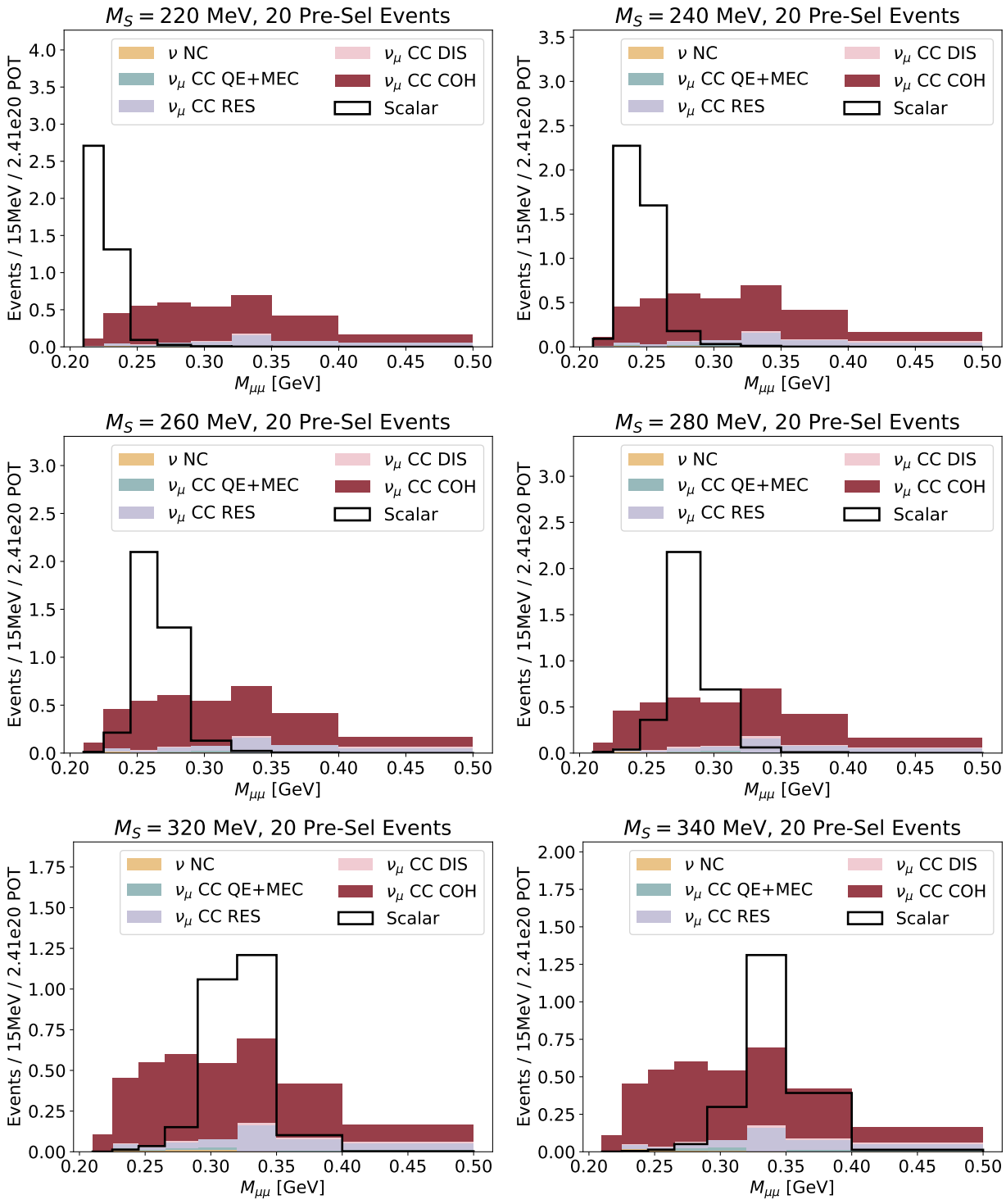

Figure 7.33: Absolutely normalized event spectra after event selection cuts as a function of the reconstructed di-muon invariant mass. The Scalar signal sample is normalized to contain 20 events after applying the pre-selection.

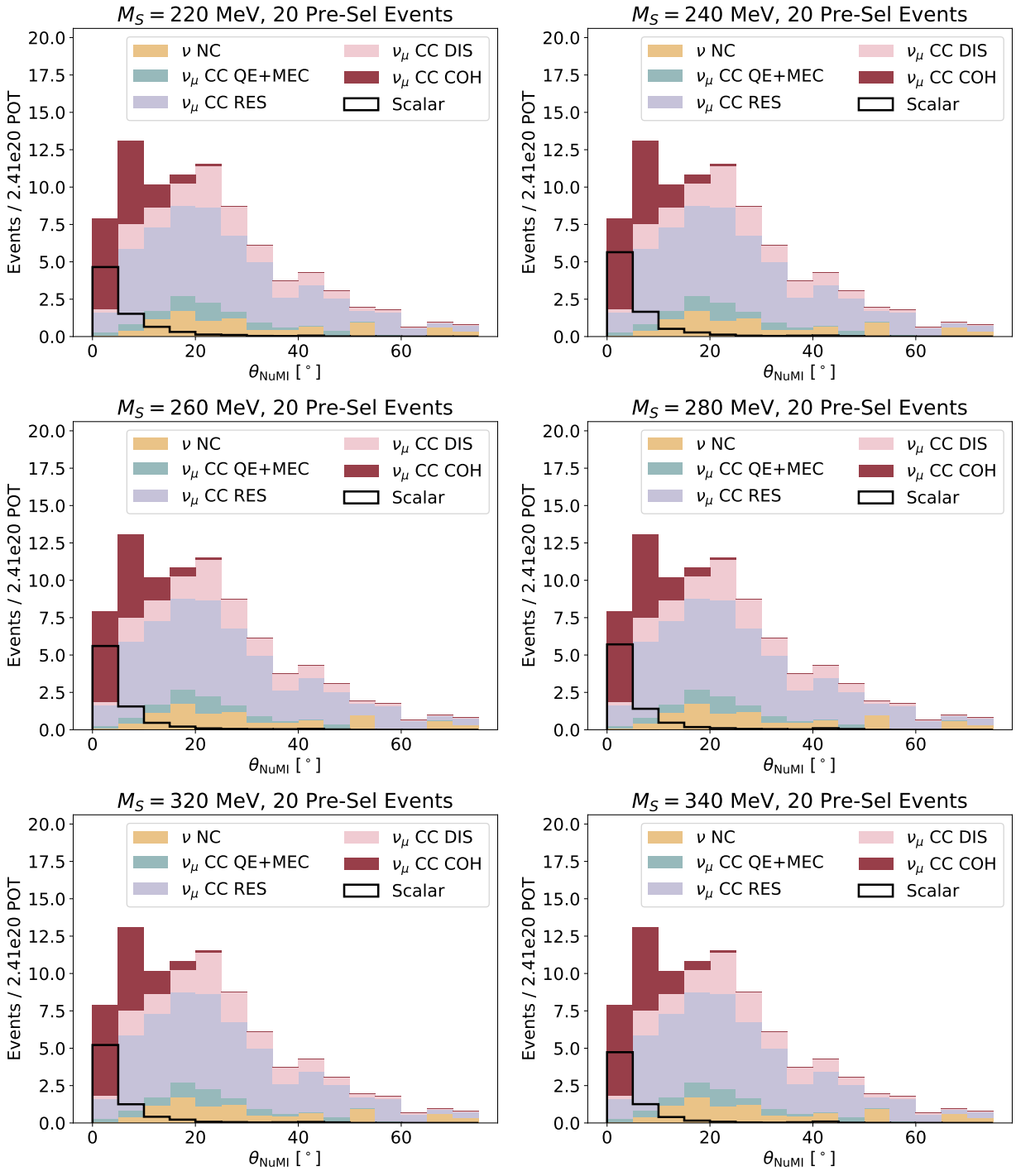

Figure 7.34: Absolutely normalized event spectra after event selection cuts as a function of θ_{NuMI}. The Scalar signal sample is normalized to contain 20 events after applying the pre-selection.

CHAPTER 8

MONTE CARLO SIMULATION TO DATA COMPARISONS

Monte Carlo simulation to data comparisons are made comparing neutrino Monte Carlo simulation to beam off subtracted beam data. These comparisons validate the event selection and our understanding of the neutrino backgrounds in the signal box region, as presented in chapter 7. There are significant systematic uncertainties in the neutrino rate that need to be accounted for in order to make proper comparisons. These are detailed in section 8.1.

Comparisons are first made in a far sideband to the di-muon analysis that is comprised of incoherent neutrino interactions which comprise a sub-dominant background in the signal region of the analysis. The results from this sample validate the modeling of reconstructed variables in the event selection. These are shown in section 8.2.

Comparisons are then are made in a near sideband to allow direct comparisons of the dominant ν_μCC-Coh-π background between data and simulation. These are shown in section 8.3. The observed rate in data matches the expectation from ν_μCC-Coh-π modeling to within uncertainties (which uses the tune detailed in section 3.2 and shown in figure 3.12).

8.1 Systematic Uncertainties

8.1.1 Physics Model

Physics model systematic uncertainties arise from the neutrino flux, the neutrino-argon cross section, the propagation of particles through the argon, and the performance of the ICARUS TPC. Uncertainties in the neutrino flux arise from the mechanical tolerance of the components in the beam target and focusing system, as well as from uncertainties in cross sections in hadron-carbon interactions. They are computed by the `PPFX` package [92, 93]. Uncertainties in neutrino-argon interactions arise from a variety of effects in neutrino-nucleus interaction, such as the axial form factor, the impact of final state interactions in the nucleus, and the

impact of two particle-two hole interactions. They are computed by the `GENIEReweight` package. The GENIE central value and uncertainties used for this result come from GENIE version `3.04.00` configuration `AR23_20i` (the liquid argon tune). Uncertainties in the particle propogation come from proton-argon and pion-argon inelastic collisions, and are computed by the `GEANT4Reweight` package [149].

The systematic uncertainties of all three categories are listed in tables **??**, **??**, **??**, and **??**. All of the physics model systematic uncertainties are implemented as weights on simulated events. There are three types of weight-based implementations of systematic uncertainties. "Multi-sigma" uncertainties are computed with $\pm 1, 2, 3\sigma$ variations as a weight on each neutrino interaction. "Morph" uncertainties are computed with a one-directional uncertainty $+1\sigma$ (representing, e.g., a model change) as a weight on each neutrino interaction. "Multi-sim" uncertainties are computed in many universes, where each universe represents a correlated throw of the relevant parameters.

The systematic uncertainties of various types are combined into systematic universes. Weights of each type (multi-sigma, morph, multi-sim) are turned into universe weights as

- multi-sigma: $u_i^j = 1 + (w_{+1\sigma}^j - 1) \cdot r_i^j$
- morph: $u_i^j = 1 + (w_{+1\sigma}^j - 1) \cdot 2|r_i^j|$
- multi-sim: $u_i^j = w_i^j$,

where i indexes the universe, j indexes the systematic uncertainty, and r_i^j is a random number generated from Gaus($\mu = 0, \sigma = 1$) per universe, per systematic (the same across all events). An event will in general have n neutrino interactions, each with m systematic uncertainties. The total systematic weight (U_i) for the i-th universe is

$$U_i = \prod_{j=1}^{n} \prod_{k=1}^{m} u_{i,k}^j. \tag{8.1}$$

ppfx Neutrino Flux Uncertainties		
Name	Type	Description
Beam div	multi-sigma	Beam divergence
Beam shift x	multi-sigma	Beam shift 1 mm variation in x direction
Beam spot	multi-sigma	Beam spot size variation of -2 mm
Horn 1 x	multi-sigma	3 mm variation of x position of first focusing horn
Horn 1 y	multi-sigma	3 mm variation of y position of first focusing horn
Horn current +	multi-sigma	Horn current variation +2 kA
Water layer	multi-sigma	Horn water layer variation of 1 mm
PCA_i	multi-sigma	i-th Principle component of the meson cross section covariance matrix, $i = 1 \ldots 20$

Table 8.1: Systematic uncertainties on the neutrino flux in ICARUS Monte Carlo simulation. The technical name, type (see text), and a short description are listed.

In other words, the product of the weights across all uncertainties across all neutrinos is the universe weight for that event.

The systematic covariance matrix for a given distribution is then given by:

$$E_{\text{syst}} = \sum_{i=1}^{m} \frac{(\vec{N}^{\text{CV}} - \vec{N}_i^U) \times (\vec{N}^{\text{CV}} - \vec{N}_i^U)}{m}, \tag{8.2}$$

where $i = 1 \ldots m$ indexes the systematic universes, $\vec{N}^{\text{CV}}$ is a vector of entries in each bin for the central-value estimate, and $\vec{N}_i^U$ is the vector in the i-th systematic universe. $\times$ denotes an outer product.

8.1.2 Detector Model

Systematic uncertainties on the neutrino rate also arise from the modeling of the performance of the ICARUS detector. These have been determined and analyzed from the understanding of the operation of the ICARUS detector during physics data taking Runs 1 and 2. This understanding comes directly out of the calibration work for the detector covered by chapters 5 and 6. There are two sources of uncertainty included in the Monte Carlo simulation to

SBN-Tune Genie Neutrino Cross Section Uncertainties		
Name	Type	Description
VecFFCCQEshape	multi-sigma	Shape of vector form factor in charged-current quasi-elastic (CCQE) scattering
RPA CCQE	multi-sigma	Variation on random-phase-approzimation (RPA) in CCQE scattering
Coulomb CCQE	multi-sigma	Varies the strength of Coulomb corrections
ZExpVariationResponse	multi-sim	Variations in z-expansion of axial form factor in CCQE scattering (to 4th order)
Norm CCMEC	multi-sigma	Normalization variation in charged-current meson exchange current (MEC) scattering
Norm NCMEC	multi-sigma	Normalization variation in neutral-current MEC scattering
Decay Angle MEC	morph	Variation of model of decay angle in MEC scattering
CCRESVariationResponse	multi-sim	Normalization uncertainy on charged-current resonant scattering
NCRESVariationResponse	multi-sim	Normalization uncertainy on neutral-current resonant scattering
RDecBR1gamma	multi-sigma	Sale factor for branching fraction of $X + \gamma$
RDecBR1eta	multi-sigma	Sale factor for branching fraction of $X + \eta$
ThetaDelta2Npi	multi-sigma	Reweight from isotropic to Rein-Segall prediction for the π angle dist. in Δ decay
ThetaDelta2NRad	multi-sigma	Reweight from isotropic to $\propto \cos^2\theta$ for the γ angular distribution in Δ decay
NonRESBG-vp[n]CC(NC)1{2}pi	multi-sigma	Non resonant neutrino-proton charged (neutral) current scattering with 1{2}π, one proton [neutron] ($W < 2\,\mathrm{GeV}$)
NonRESBG-vbarp[n]CC(NC)1{2}pi	multi-sigma	Non resonant antineutrino-proton charged (neutral) current scattering with 1{2}π, one proton [neutron] ($W < 2\,\mathrm{GeV}$)
DISBYVariationResponse	multi-sim	Variations in the response of the Bodek-Yang DIS cross section model
FSI pi VariationResponse	mutli-sim	Variations in pion FSI
FSI N VariationResponse	multi-sim	Variations in FSI of nucleons
NCELVariationResponse	multi-sim	Variations in response of neutral-current elastic scattering

Table 8.2: Systematic uncertainties on the neutrino incoherent cross section in ICARUS Monte Carlo simulation. The technical name, type (see text), and a short description are listed.

Tuned ν_μ CC Coherent Pion Uncertainties		
Name	Type	Description
$\pi - C$ A scaling	multi-sigma	Uncertainty on A scaling of $\pi - N$ cross section from C to Ar
$\pi - C$ scale factors	multi-sim	Variations on $\pi - C$ cross section strength as a function of pion kinetic energy
M_A CC COH	multi-sigma	Uncertainty on axial mass in form factor ($\pm 0.3\,\mathrm{GeV}$)

Table 8.3: Systematic uncertainties on coherent neutrino cross section in ICARUS Monte Carlo simulation. The technical name, type (see text), and a short description are listed.

Geant4 Particle Propagation Uncertainties		
Name	Type	Description
piminus	multi-sim	Variations of $\pi^- - Ar$ interactions
piplus	multi-sim	Variations of $\pi^+ - Ar$ interactions
proton	multi-sim	Variations of $p - Ar$ interactions

Table 8.4: Systematic uncertainties on G4 particle propagation ICARUS Monte Carlo simulation. The technical name, type (see text), and a short description are listed.

data comparisons. First, there are uncertainties in the energy scales of the ionization charge (as determined in chapter 6) and multiple-Coulomb-scattering. As an example, the uncertainty in the calibrated dE/dx as a function of reconstructed dE/dx is shown in figure 8.1. This uncertainty is determined directly from the uncertainties in the measurement of ellipsoid modified box recombination (equation 6.3), including the correlations between different parameters in the fit. This uncertainty is propagated to comparisons by "mis-calibrating" the Monte Carlo simulation dE/dx by the uncertainty in dE/dx, and re-computing relevant particle identification variables (see section 7.2.2).

The re-computed variables are treated as 1σ variations on the central value spectra. The alternative spectra is interpreted as a "unisim" implementation of a systematic variation, which is an alternative to the weight-based implementation for the physics model systematic uncertainties (section 8.1.1). The alternative spectra can be turned into a covariance matrix using equation 8.2, where $\vec{N}_i^U$ are the spectra variation(s).

The other source of detector performance systematic uncertainty comes from re-generating

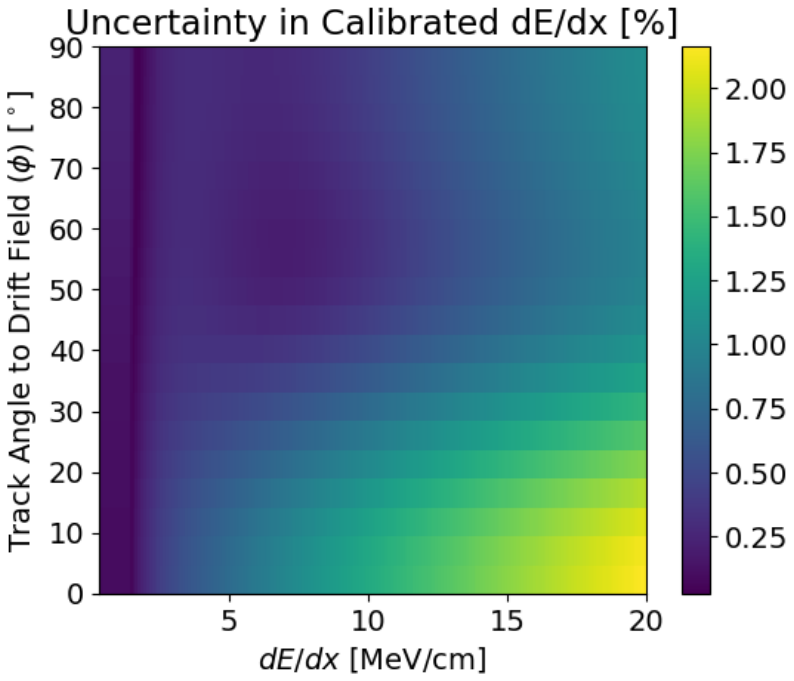

Figure 8.1: Systematic uncertainty in calibrated calorimetric dE/dx as a function of the energy loss and track angle to the drift electric field (ϕ). Obtained from the chapter 6 measurement of the EMB model (equation 6.3).

Monte Carlo simulation with variations in the detector simulation. There are various ways in which the performance of the ICARUS detector varies across the dataset that are simulated. For example, the varying electron lifetime across the dataset (see section 5.1.2) changes the signal-to-noise ratio in the detector over time. This variation is especially impactful on the induction planes, where the average signal-to-noise ratio is small. ICARUS Monte Carlo simulation only applies a single, constant value across all events (3 ms). In addition, the induction plane signal shapes have been observed to vary in a spatially dependant way across the detector. ICARUS simulation only applies a spatially averaged signal shape across the whole detector (see section 5.2). For this analysis, we have elected to vary the detector simulation by the size of these spatial and temporal variations[1]. Alternative simulated datasets are generated with variations on the detector simulation with the "Coh-like" subsample of

1. Future work inside the ICARUS collaboration will include these variations in the simulation, at which point the uncertainties on these variations will be the residual, much reduced, detector systematic uncertainty.

neutrino interactions (see section 3.2.1). The differences in spectra from the detector central value spectra and the varied spectra are treated as unisim 1σ variations. These are scaled up by the fraction of "Coh-Like" sample events in each bin to obtain the complete uncertainty. This approximates that the impact of the detector systematic uncertainties is identical for Coh-like and non-Coh-like neutrino interactions. This is a rough approximation that improves in regions where the Coh-like sample dominates the neutrino rate. In the far sideband plots (section 8.2), about 20% of the neutrino simulation is in the "Coh-Like" sample. In the near sideband plots (section 8.3), the fraction is about 80%.

8.2 Far Sideband

The far sideband is defined as events passing the preselection (section 7.4) that also pass loose particle identification cuts, and have $\theta_{\text{NuMI}} > 10°$. The particle identification cuts require:

- Trunk and Branch MCS P / Range P < 1.8
- Trunk and Branch $\chi^2_\mu < 15$
- Trunk and Branch $\chi^2_p > 80$.

These particle identification cuts select for well reconstructed events with two muon-like particles (typically one muon and one pion). They remove cosmic backgroud events and low energy neutrino interactions, neither of which are well modeled in ICARUS simulation. The θ_{NuMI} cut removes the signal box region ($\theta_{\text{NuMI}} < 5°$), as well as the region where the main background (ν_μCC-Coh-π) arises ($\theta_{\text{NuMI}} < 10°$). The far sideband is thus a sample of incoherent neutrino interactions where data and simulation are on the same footing.

In these distributions, the modeling of kinematic and particle identification variables is valid to within the significant systematic uncertainties assessed on the Monte Carlo simulation prediction, with a few exceptions. None of the exceptions impact the analysis in

the signal box region (chapter 9) in a serious way. First, there is a deficit of events at low transverse momentum, and an enhancement at large transverse momentum. This can be observed most directly in figure 8.9. This is likely due to mis-modeling in the nuclear model for incoherent neutrino interactions. This mis-modeling indirectly impacts the comparisons of other variables in the far sideband (θ_{NuMI}, which is very correlated with p_T, for example). However, incoherent neutrino interactions constitute a subdominant part of the background in the signal region.

Second, in data there is a dearth of events with a low χ^2_μ score (see figure 8.3). This could be caused by a few reasons: underestimation of the charge resolution, the inaccurate mean excitation energy value in MC (188 eV, as opposed to 197 eV [145]), or overestimation of the tracking performance in data relative to the central value. The detector model systematic variations on the signal-to-noise and signal shapes vary the tracking performance in a realistic way. Their inclusion makes the χ^2 of the comparison close to 1, in spite of the deficit compared to the central value. Thus, the discrepancy is covered by the uncertainties developed for the analysis.

Finally, there is also a deficit of events with a small "Minimum Other χ^2_p" score (see, e.g., figure 8.2). This is due to the underestimation of fluctuations in recombination for highly ionizing protons. This effect was also observed in the ionization energy scale calibration (chapter 6, see especially section 6.5). The cut on the χ^2_p in the analysis is very loose (< 90, see table 7.1), and so the resolution effect should not impact the analysis.

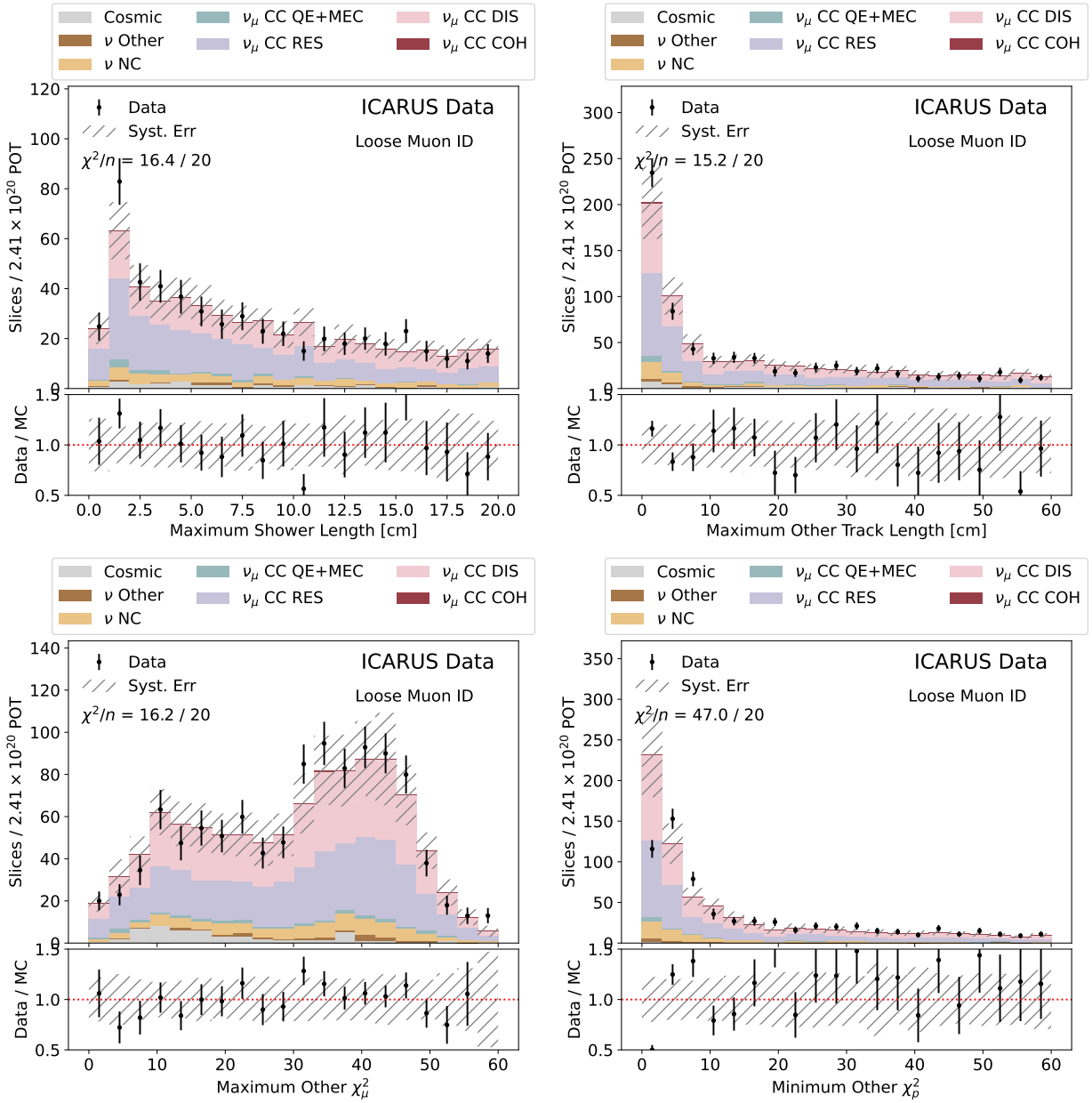

Figure 8.2: Monte Carlo to data comparison of object variable distributions in the Loose Muon ID dataset. Beam-off data is subtracted from the data points. Systematic uncertainties on the flux, interaction, particle propagation, and detector model are included. Detector model variation systematics are only assessed on the "Coh-like" MC subsample and are scaled to the size of the spectrum.

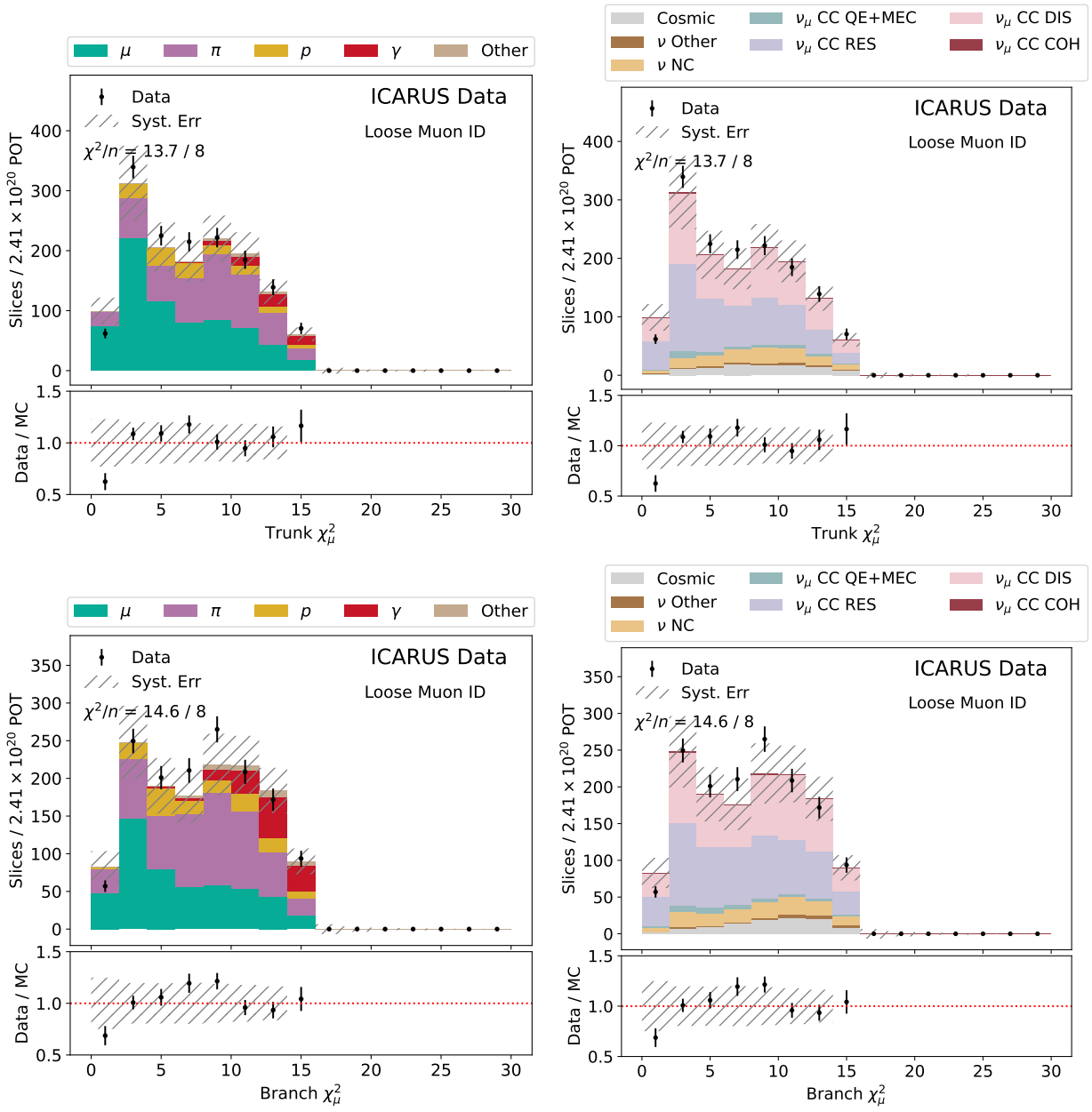

Figure 8.3: Monte carlo to data comparison of muon calorimetric (μ-like) ID distributions in the Loose Muon ID dataset. Beam-off data is subtracted from the data points. Shown by cateogories of the trunk track particle type (left) and the neutrino interaction type (right). Systematic uncertainties on the flux, interaction, particle propogation, and detector model are included. Detector model variation systematics are only assessed on the "Coh-like" MC subsample and are scaled to the size of the spectrum.

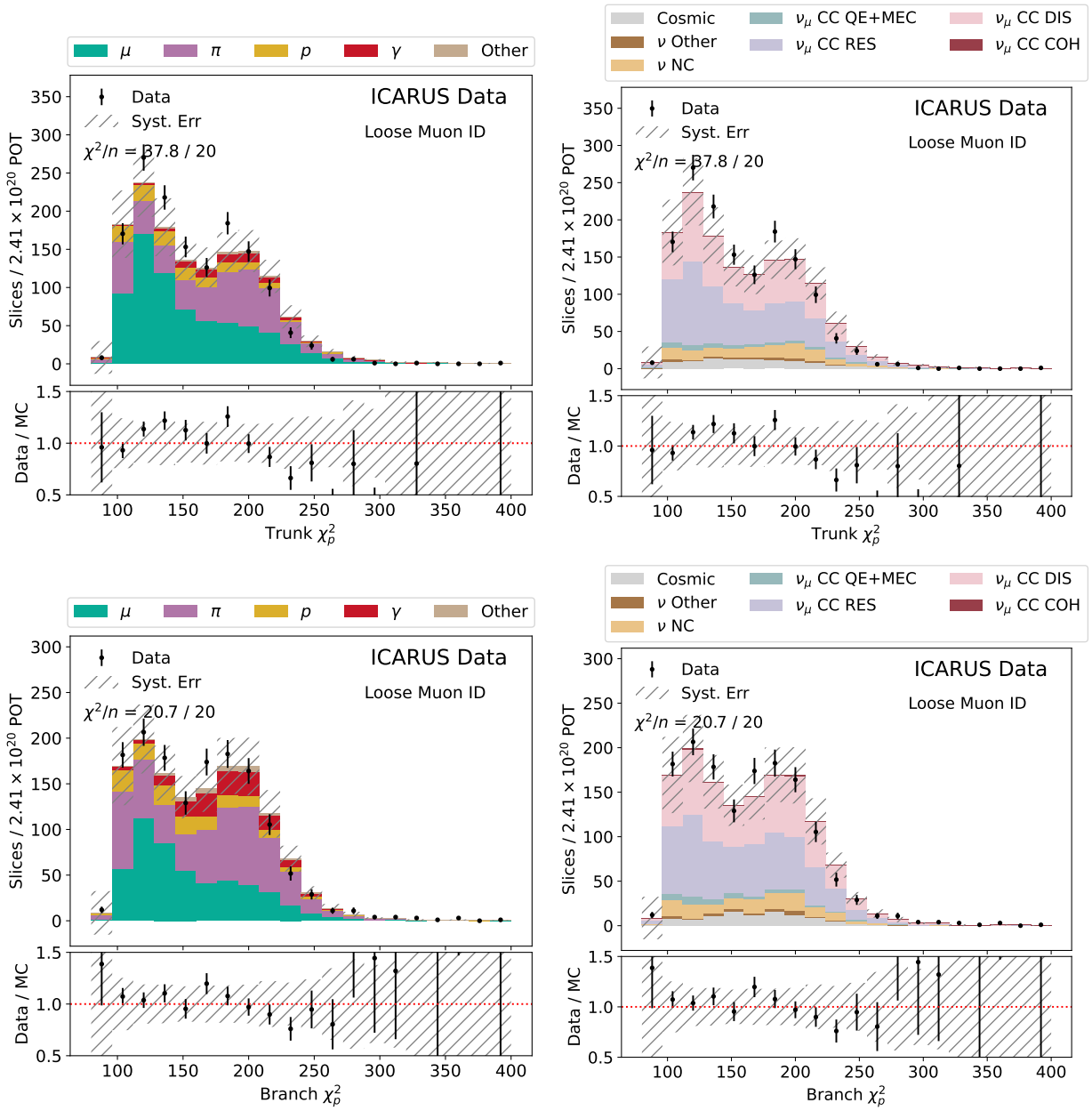

Figure 8.4: Monte carlo to data comparison of muon calorimetric (p-like) ID distributions in the Loose Muon ID dataset. Beam-off data is subtracted from the data points. Shown by cateogories of the track particle type (left) and the neutrino interaction type (right). Systematic uncertainties on the flux, interaction, particle propogation, and detector model are included. Detector model variation systematics are only assessed on the "Coh-like" MC subsample and are scaled to the size of the spectrum.

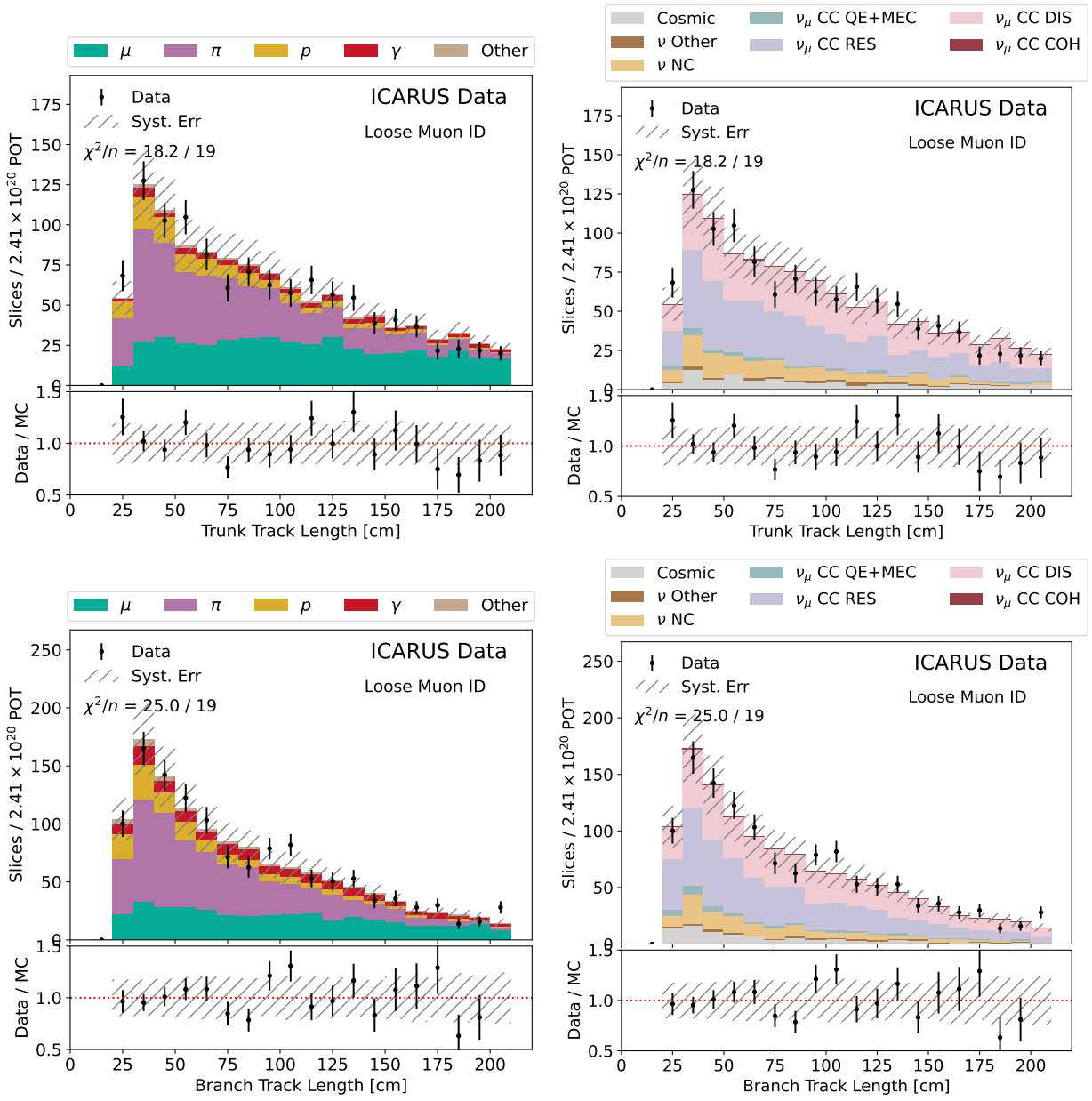

Figure 8.5: Monte carlo to data comparison of track length distributions in the Loose Muon ID dataset. Beam-off data is subtracted from the data points. Shown by cateogories of the track particle type (left) and the neutrino interaction type (right). Systematic uncertainties on the flux, interaction, particle propogation, and detector model are included. Detector model variation systematics are only assessed on the "Coh-like" MC subsample and are scaled to the size of the spectrum.

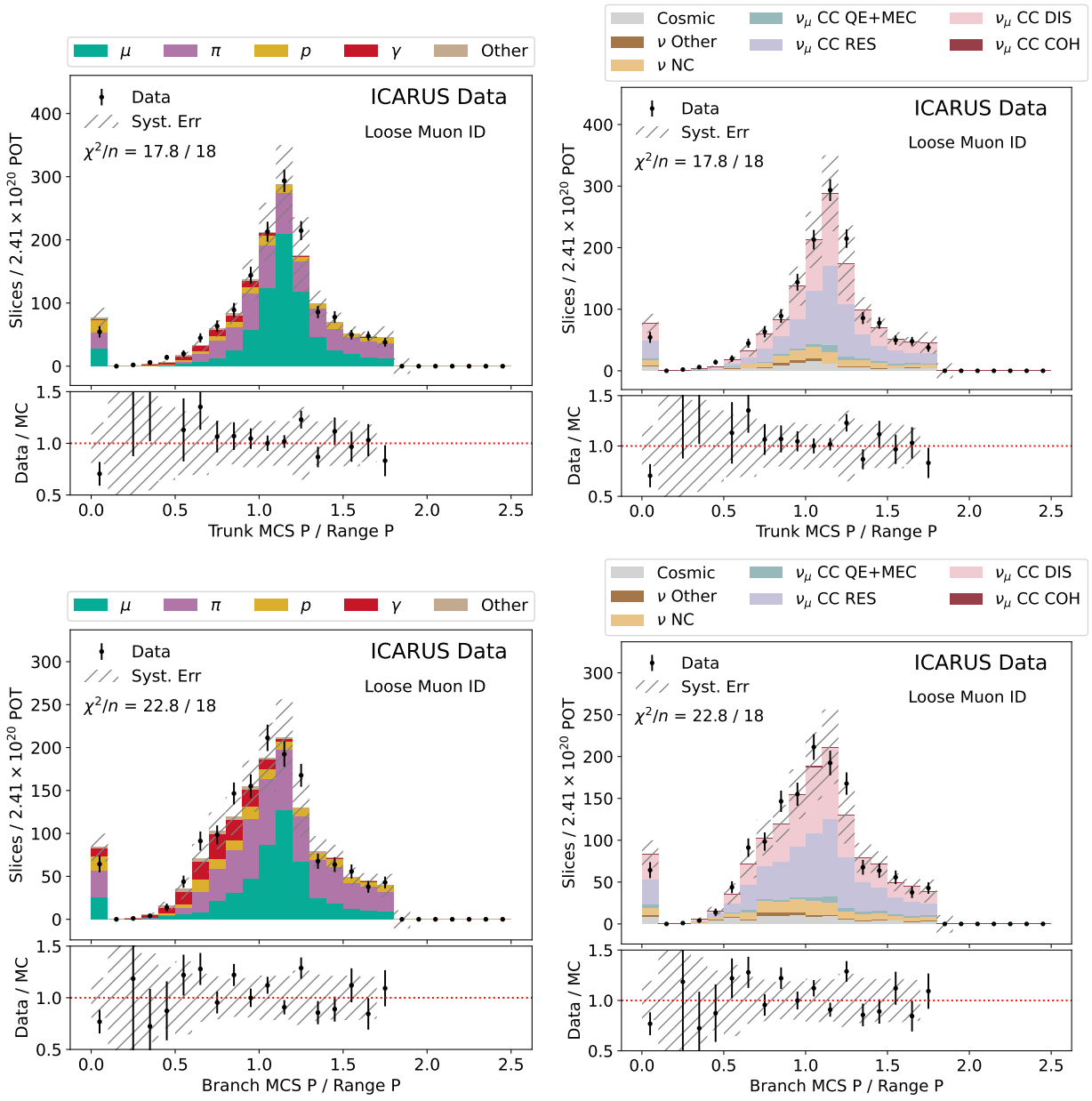

Figure 8.6: Monte carlo to data comparison of muon topological ID distributions in the Loose Muon ID dataset. Beam-off data is subtracted from the data points. Shown by cateogories of the track particle type (left) and the neutrino interaction type (right). Systematic uncertainties on the flux, interaction, particle propogation, and detector model are included. Detector model variation systematics are only assessed on the "Coh-like" MC subsample and are scaled to the size of the spectrum.

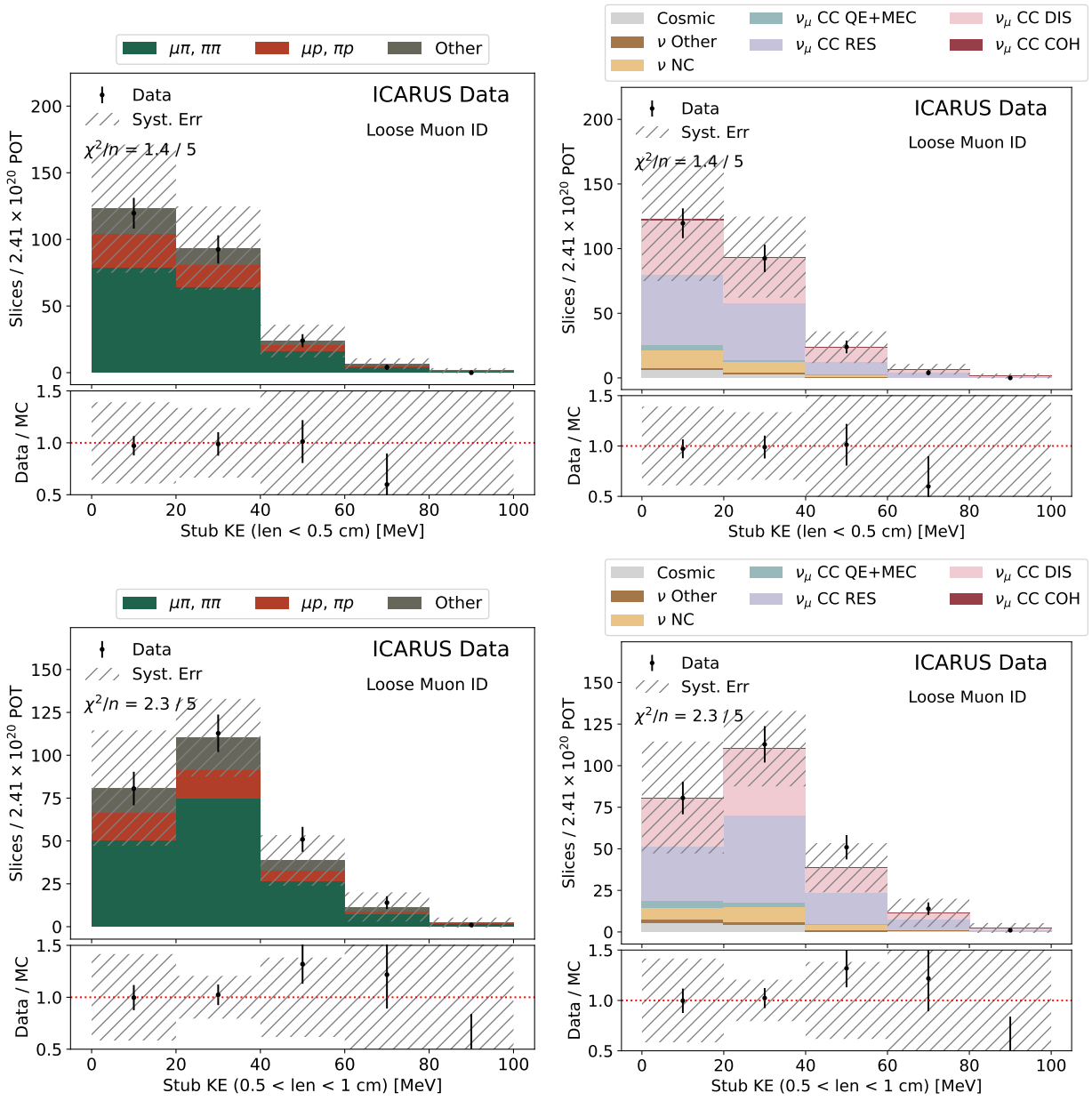

Figure 8.7: Monte carlo to data comparison of stub ID distributions for stub length $< 1\,\text{cm}$ in the Loose Muon ID dataset. Beam-off data is subtracted from the data points. Shown by cateogories of the vertex type (left) and the neutrino interaction type (right). Systematic uncertainties on the flux, interaction, particle propogation, and detector model are included. Detector model variation systematics are only assessed on the "Coh-like" MC subsample and are scaled to the size of the spectrum

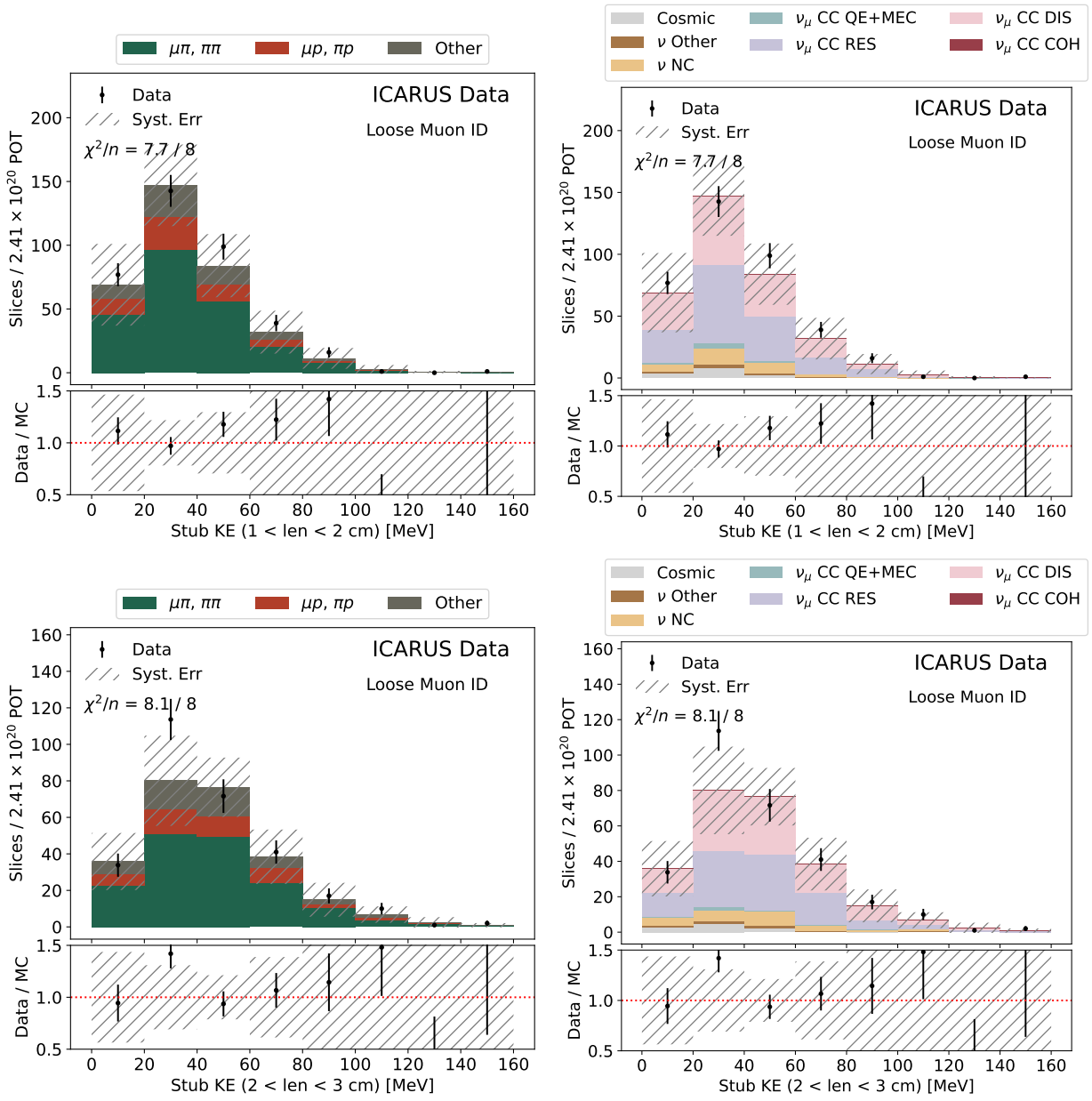

Figure 8.8: Monte carlo to data comparison of stub ID distributions for stub length $> 1\,\text{cm}$ in the Loose Muon ID dataset. Beam-off data is subtracted from the data points. Shown by cateogories of the vertex type (left) and the neutrino interaction type (right). Systematic uncertainties on the flux, interaction, particle propogation, and detector model are included. Detector model variation systematics are only assessed on the "Coh-like" MC subsample and are scaled to the size of the spectrum.

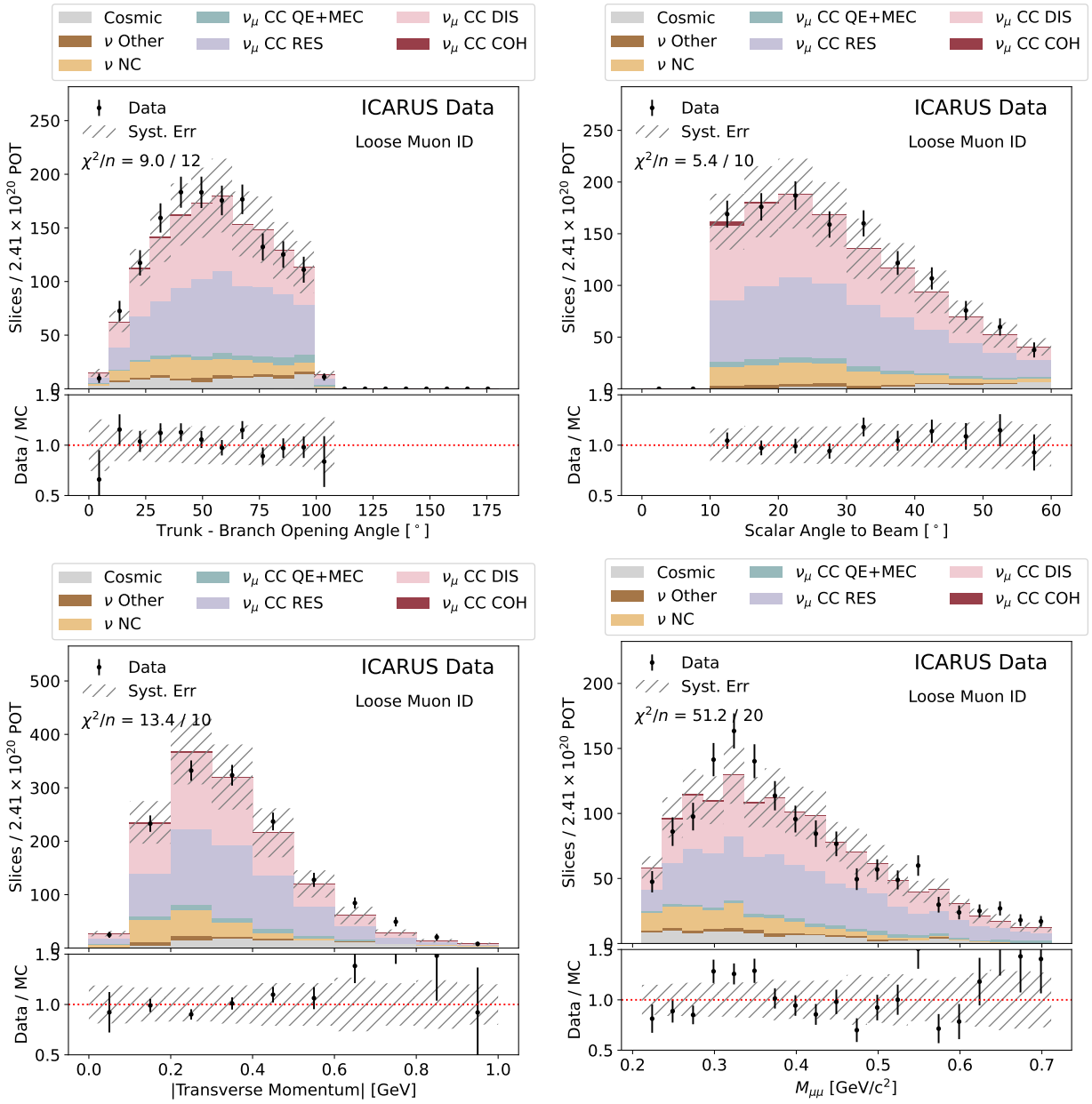

Figure 8.9: Monte carlo to data comparison of kinematic varible distributions in the Loose Muon ID dataset. Beam-off data is subtracted from the data points. Detector model variation systematics are only assessed on the "Coh-like" MC subsample and are scaled to the size of the spectrum.

8.3 Near Sideband

We have also developed a near sideband to examine coherent pion production outside the signal box region. The sideband consists of events where $5^\circ < \theta_{\mathrm{NuMI}} < 10^\circ$. The sideband applies all other cuts in the event selection (see table 7.1). The sideband leverages the kinematic separation between signal scalar and ν_μCC-Coh-π background events. As defined in equation 3.1, ν_μCC-Coh-π events occur at low energy transfer to the nucleus (t). Since decays do not involve a nucleus, they all effectively occur at $t = 0$. The tail in t for ν_μCC-Coh-π interactions induces a broader spread in the θ_{NuMI} variable, which can therefore be used to partially separate signal and background. Applying this sideband therefore necessitates extrapolating the ν_μCC-Coh-π rate from high t (in the sideband) to low t (in the signal region). This extrapolation should be well controlled because the ν_μCC-Coh-π rate, while uncertain, is relatively well constrained as a function of t [102].

A plot of the beam angle variable (θ_{NuMI}) used to define the sideband is shown in figure 8.11 including data both inside and outside the near sideband region. The data distribution displays an overall normalization shift above the simulated background at large θ_{NuMI}. This shift is essentially consistent within the large systematic uncertainties assigned on the neutrino rate (the reduced χ^2 is still about 1). It is also an effect of incoherent neutrino interactions which constitute a sub-dominant background in the signal region. The region of the distribution with the highest sensitivity to ν_μCC-Coh-π interactions is the $5^\circ < \theta_{\mathrm{NuMI}} < 10^\circ$ bin. We observe 14 events with an expectation of $17.8 \pm_{\mathrm{syst}} 6.6 \pm_{\mathrm{stat}} 4.2$. This is consistent with the predicted amount of coherent pion production. A constraint on the amount of coherent pion production from the measurement in this bin is shown in figure 8.10. Due to the limited statistical power of this constraint, we elect to not actually apply it in the systematic analysis in the signal box region. Instead, as will be discussed in chapter 9, the signal identification procedure obtains a constraint on the ν_μCC-Coh-π rate incorporating data from both the near sideband and signal box region.

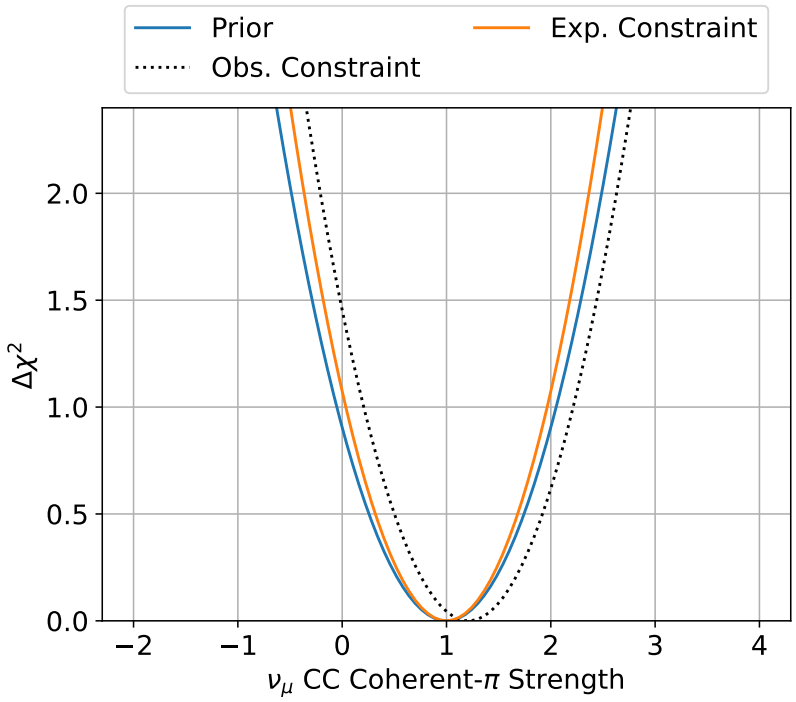

Figure 8.10: Observed and expected constraint on the ν_μCC-Coh-π signal strength in the near sideband.

The events in the lowest angle bin are also shown broken down by relevant kinematic quantities. These are shown in figures 8.12 and 8.13. Event displays of a few of the selected events are shown in figures 8.14 to 8.17. Visually, the background events appear consistent with the expectation from simulation: neutrino interactions with two muon-like tracks. There are no selected events which (e.g.) appear to be cosmogenic.

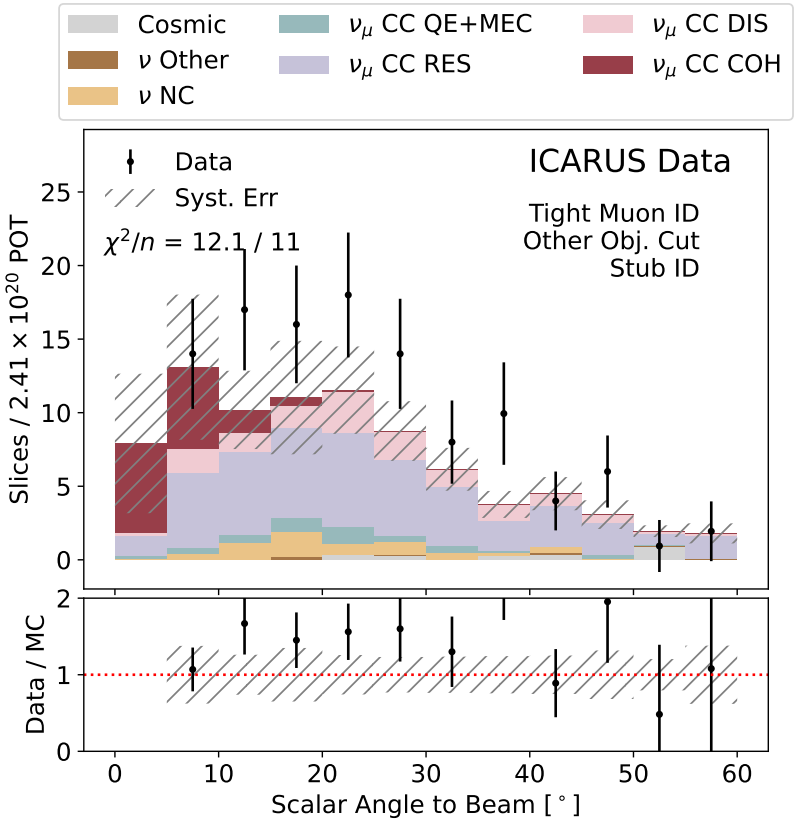

Figure 8.11: Monte Carlo simulation to data comparison for θ_{NuMI} after applying all other event selection cuts. Beam-off data is subtracted from the data points. Systematic uncertainties on the flux, interaction, particle propagation, and detector model are included. Detector model variation systematics are only assessed on the "Coh-like" MC subsample and are scaled to the size of the spectrum.

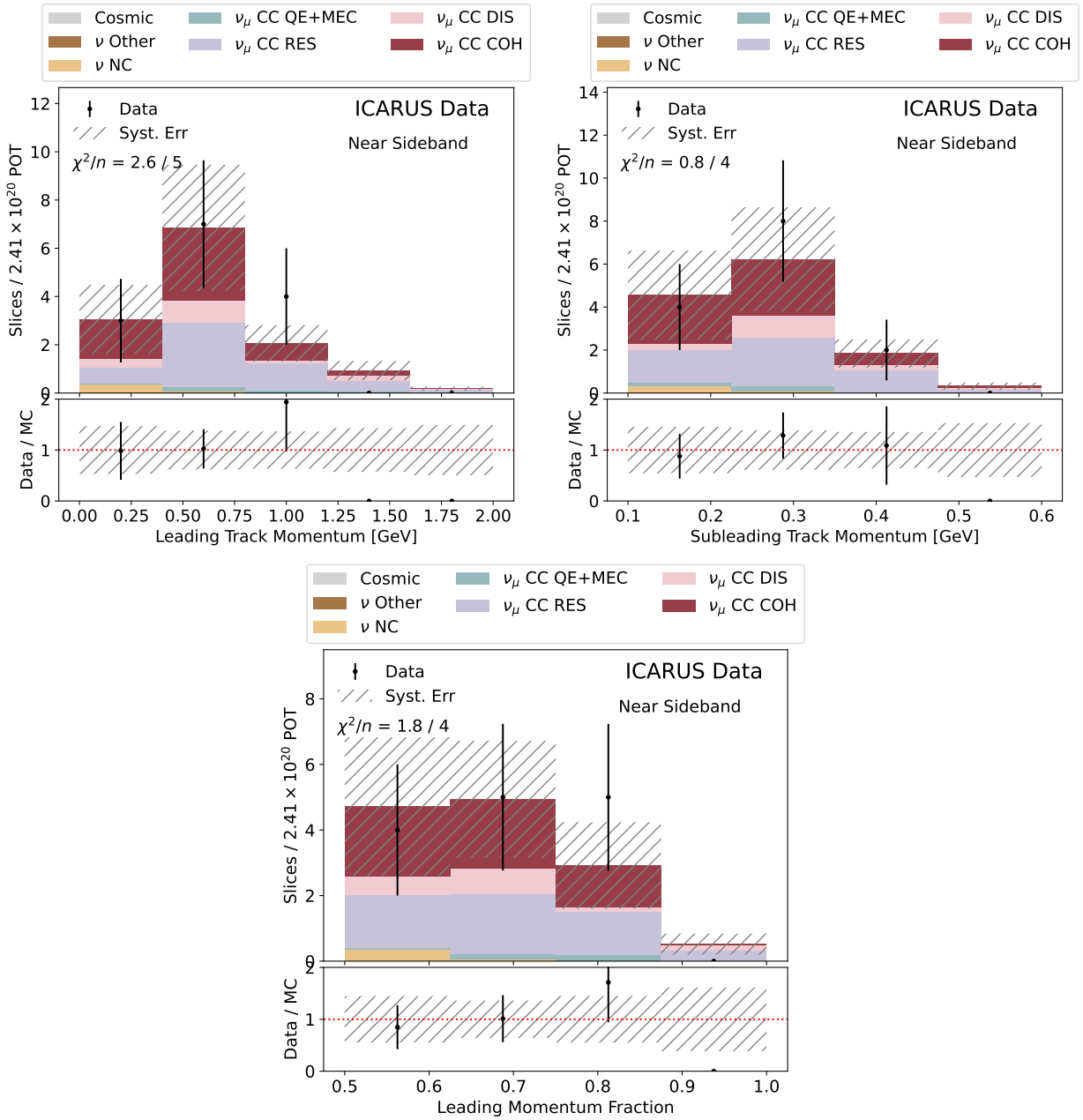

Figure 8.12: Monte Carlo simulation to data comparison for kinematic variables in the near sideband. Beam-off data is subtracted from the data points. Systematic uncertainties on the flux, interaction, particle propagation, and detector model are included. Detector model variation systematics are only assessed on the "Coh-like" MC subsample and are scaled to the size of the spectrum.

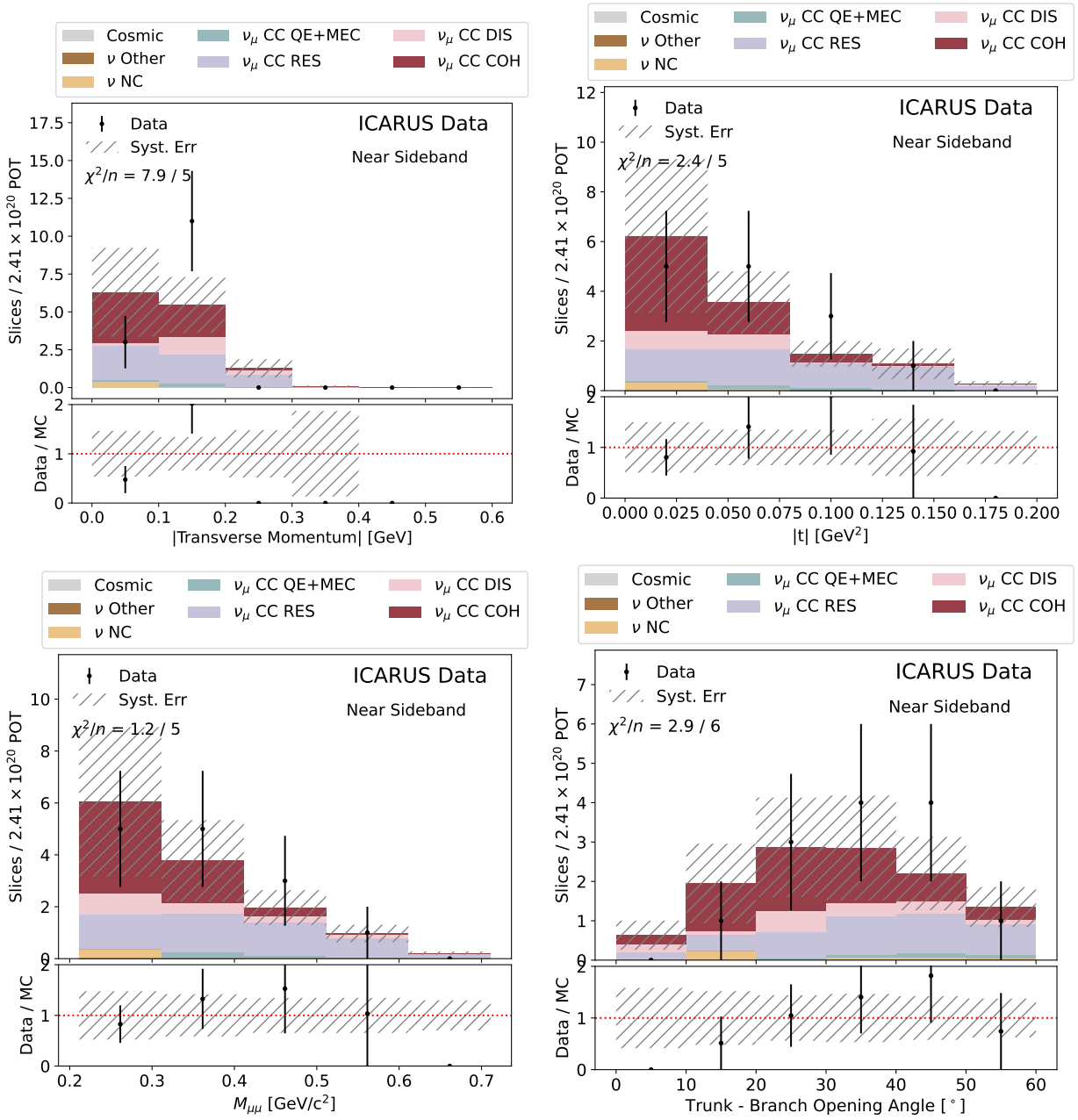

Figure 8.13: Monte Carlo simulation to data comparison for kinematic variables in the near sideband. Beam-off data is subtracted from the data points. Systematic uncertainties on the flux, interaction, particle propagation, and detector model are included. Detector model variation systematics are only assessed on the "Coh-like" MC subsample and are scaled to the size of the spectrum.

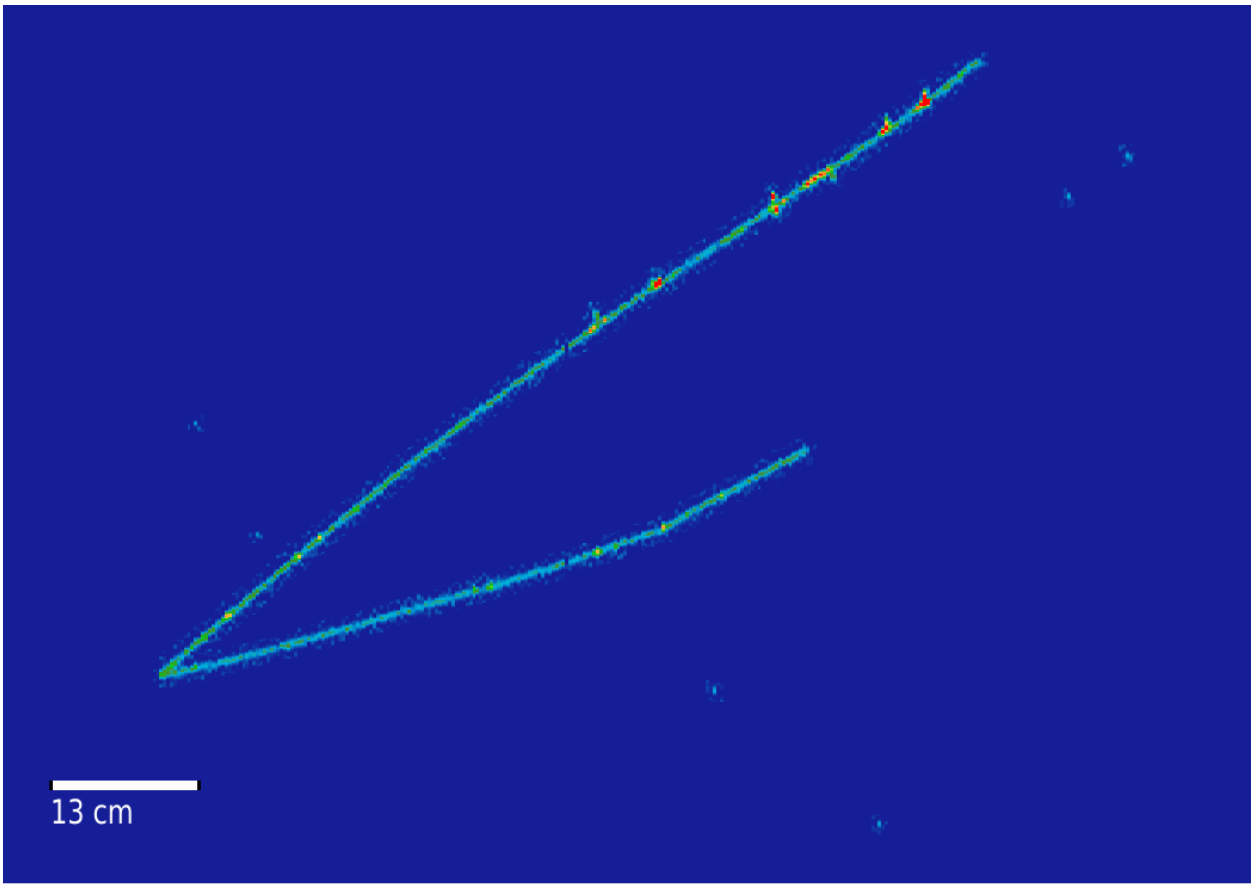

Figure 8.14: Event display of selected event in near side band. Event # 3927 in Run 9750.

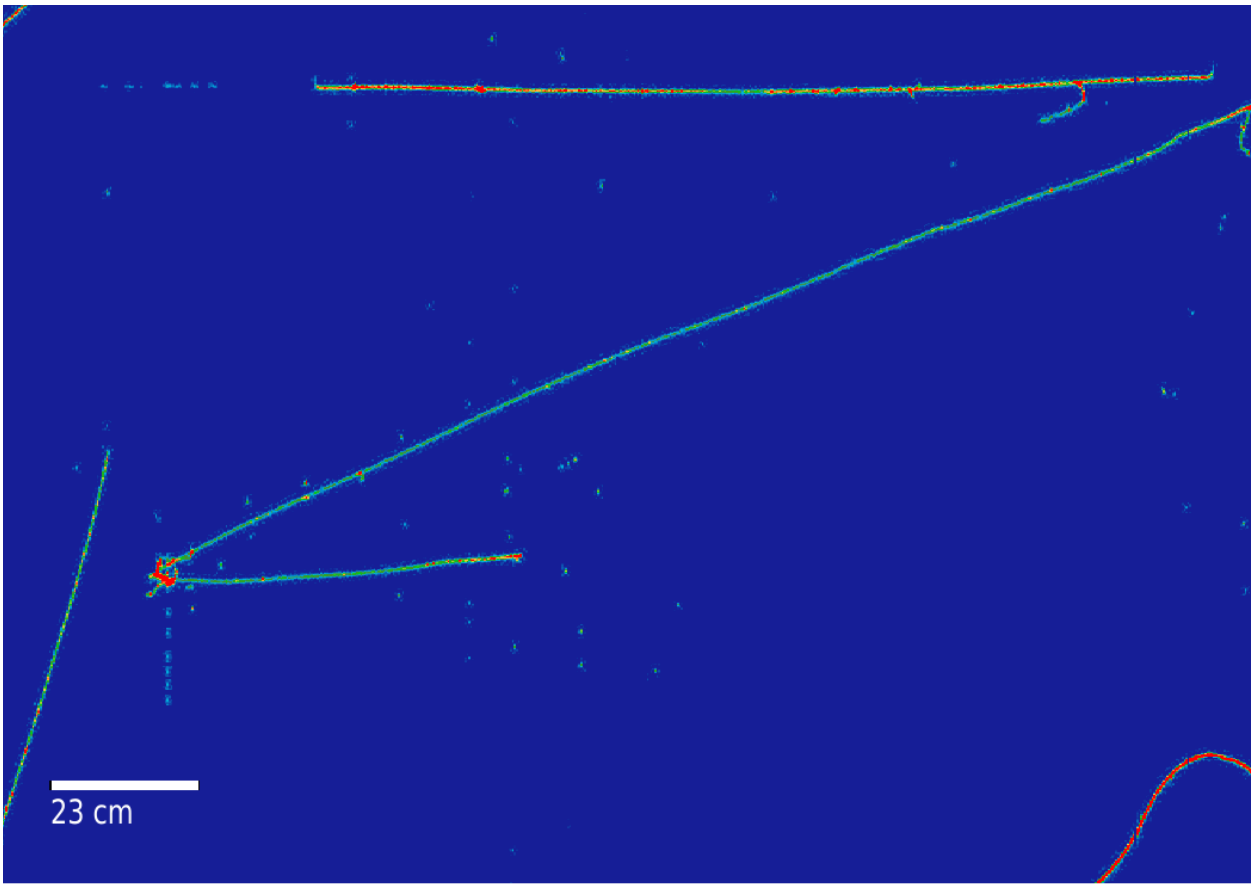

Figure 8.15: Event display of selected event in near side band. Event # 80208 in Run 9807.

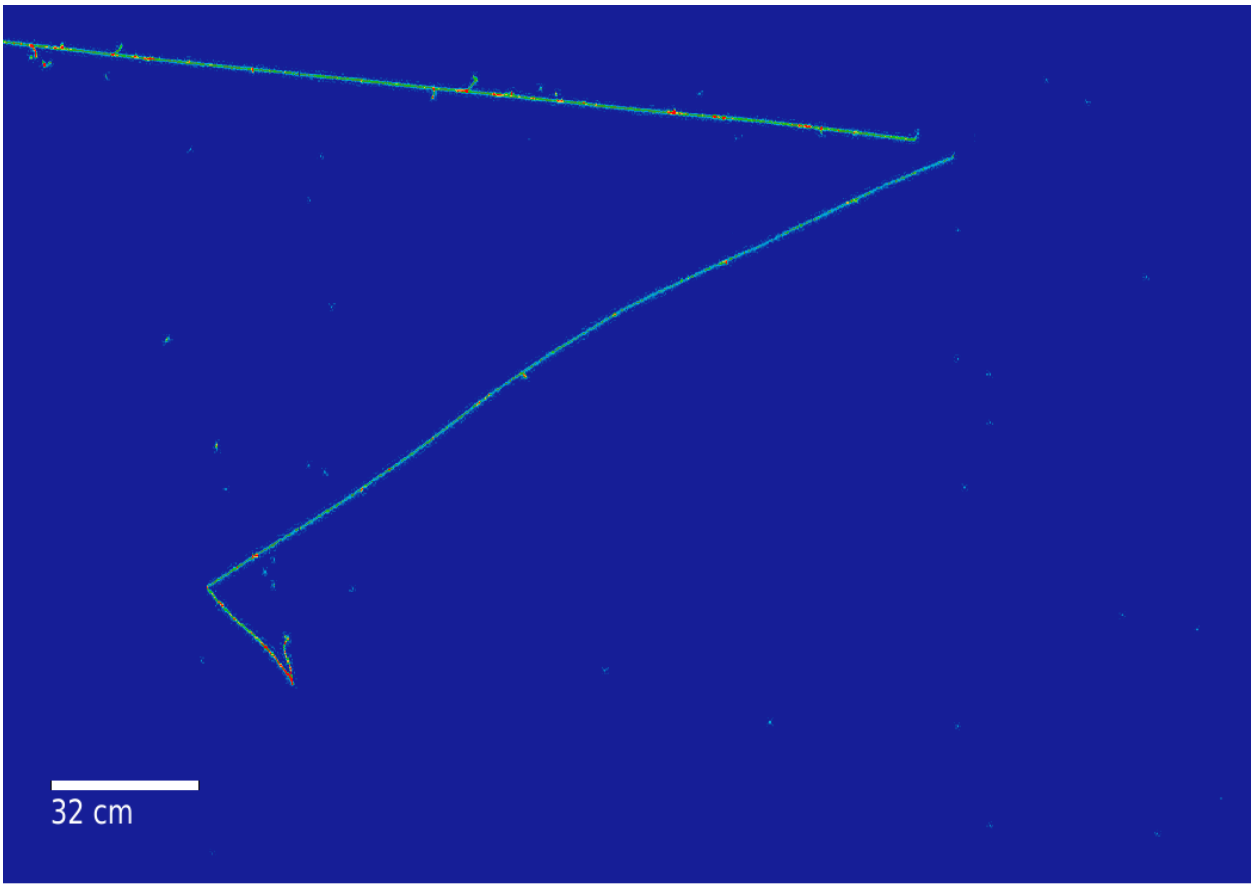

Figure 8.16: Event display of selected event in near side band. Event # 68042 in Run 9838.

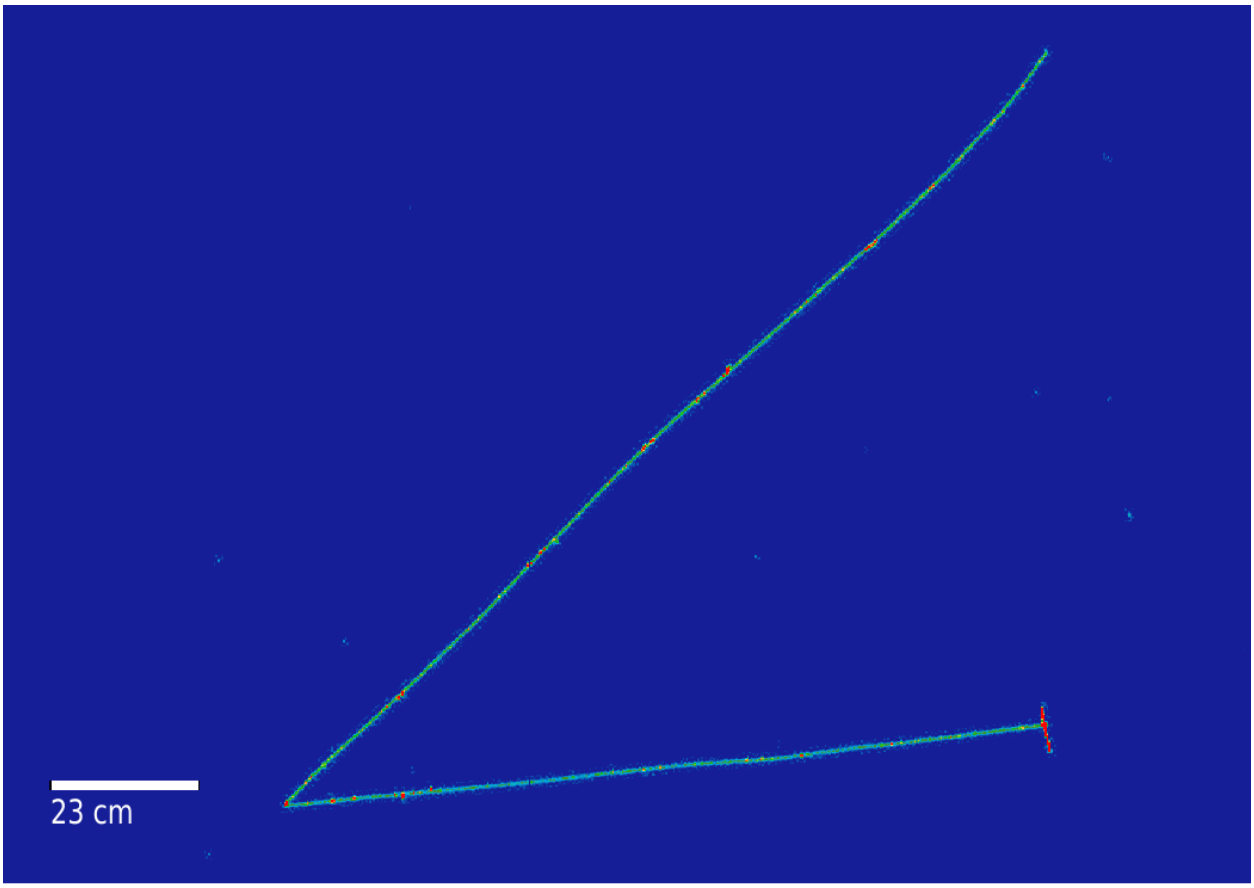

Figure 8.17: Event display of selected event in near side band. Event # 26577 in Run 9945.

CHAPTER 9

SIGNAL IDENTIFICATION PROCEDURE AND SENSITIVITY

The event selection for di-muon decays, as developed in chapter 7 and validated with Monte Carlo simulation to data comparisons in chapter 8, provides an event sample, the signal-box region, with a high sensitivity to new physics models of di-muon decays. This sample is not background-free; there is a small background (~ 8) of neutrino interactions predicted (~ 8), mostly from ν_μCC-Coh-π events. In order to apply this sample in the search, it is necessary to answer two questions. First, is there any new physics in the sample, or is its measured rate consistent with the expectation with neutrino backgrounds? Second, in the event of no new physics, which areas of new physics parameter space can we exclude to some specified confidence level?

This chapter addresses the statistical analysis we have developed to address these two questions. First, there are significant systematic uncertainties on both the neutrino background (mostly from the interaction strength of the ν_μCC-Coh-π process) and the scalar signal (primarily from the flux of the NuMI beam). Section 9.1 addresses the uncertainty analysis for the signal-box sample.

The statistical procedure to identify signal from background leverages the di-muon invaraint mass: $M_{\mu\mu} = |\boldsymbol{p_{\mu 1}} + \boldsymbol{p_{\mu 2}}|$, where $\boldsymbol{p_{\mu 1}}$ and $\boldsymbol{p_{\mu 2}}$ are the reconstructed 4-momenta of the two muon candidates. Scalar signals will produce a resonance in $M_{\mu\mu}$, while neutrinos represent a smooth background. This is a familiar situation in particle physics; it is possible to identify such a new physics signal by looking for the bumps in the $M_{\mu\mu}$ spectrum [150] (see, e.g., Ref. [151, 152, 153]). In the event of no new physics signal, the CLs method is used to put limits on available parameter space [154]. This method is also how previous searches for these new experiments physics models have quoted their sensitivity (e.g., Ref. [155]), and so applying this method enables an apples-to-apples comparison between different experimental limits. The statistical procedure is discussed in depth in section 9.2.

Finally, the sensitivity of the search is shown in section 9.3. The sensitivity is shown both in terms of the expected statistical significance of any new physics model (applying the bump-hunter method) and in terms of the expected excluded parameter space in the case of a null result (applying the CLs method). It is interpreted for both a model-independent scenario of the process $K \to \pi + S(\to \mu\mu)$, as well as the Higgs portal scalar and heavy axion models (as introduced in chapter 2).

9.1 Signal Box Uncertainty Analysis

This section details the uncertainty analysis in the signal box region for scalar signal and neutrino background events. The physics model systematic uncertainties are the same as those introduced for Monte Carlo simulation to data comparisons (see section 8.1, table **??**). They arise from the neutrino flux (computed with `PPFX`), incoherent neutrino-nucleus interactions (computed with `GENIE-Reweight`), ν_μCC-Coh-π interactions (computed with the MINERvA tune, section 3.2), and particle propogation (`GEANT4-Reweight`). Section 9.1.1 details how the detector systematic uncertainties are computed. The combined uncertainty is shown for scalar signals in section 9.1.2 and for neurino backgrounds in section 9.1.3.

9.1.1 Detector Systematic Evaluation

We examine the impact of detector systematic uncertainties in the signal box region for both the neutrino background and signal spectra. As in section 8.1.2, the neutrino background systematic uncertainties are examined with the "Coh-like" sample (see section 3.2.1).

There are three categories of detector systematic uncertainty: detector model variations, energy scale uncertainties, and track splitting. The first two categories were introduced in section 8.1.2. The track splitting uncertainty comes from a study which addressed two regions in ICARUS where un-simulated perturbations to the drift field distort tracks: the bending of the central cathode plane in each cryostat, and a mechanical support on the front

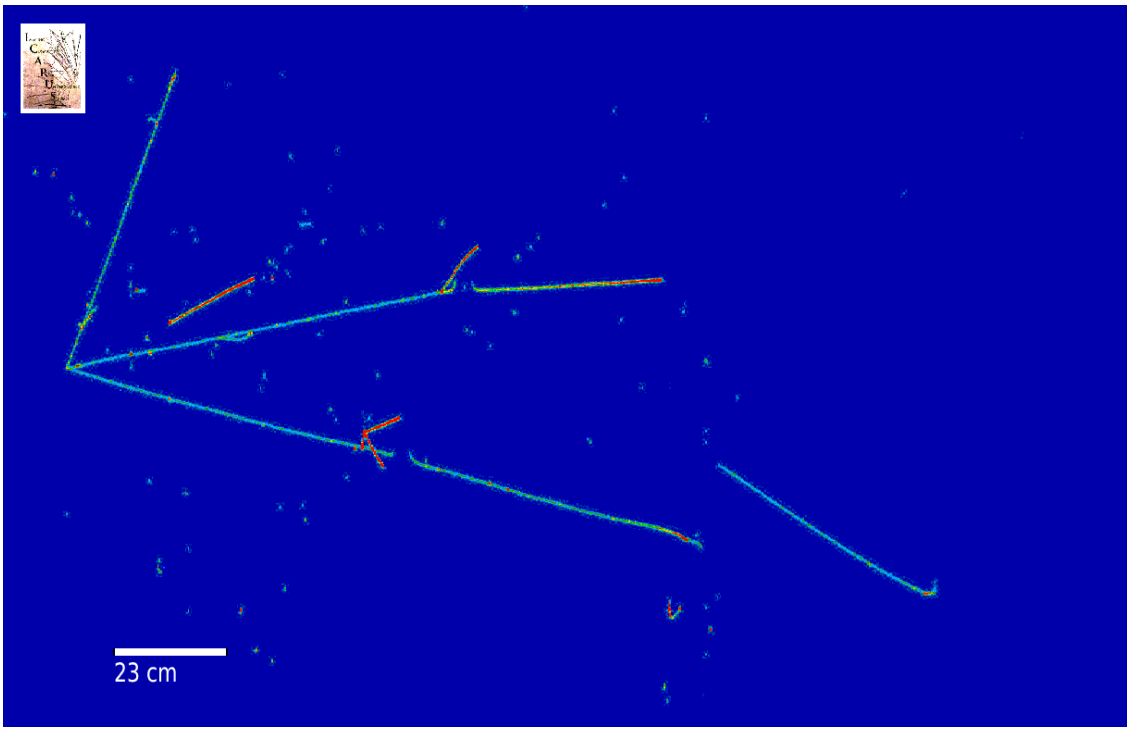

Figure 9.1: Neutrino interaction candidate in ICARUS data with two tracks split by the front induction support.

induction wire plane in each TPC. An event display of a neutrino event in ICARUS data with two tracks that cross the front induction wire support region is shown in figure 9.1. The three subsections below demonstrate the impact of these three uncertainties on scalar signal and neutrino background events in the signal box region. The magnitude of uncertainty from each source in the analysis is summarized in table 9.1.

Detector Model Variations

Figure 9.2 shows the comparison of the number of selected events in each sample under each of the detector model variations detailed in section 8.1.2. For the neutrino "Coh-Like" sample, the full section is shown ("Coh-Like"), as well as an adapted selection where the θ_{NuMI} cut (see figure 7.1) is loosened from 5° to 15° ("Coh-Like Loose"). The expanded definition selects for a larger, more statistically significant Monte Carlo sample, while retaining characteristics

Systematic	Impact on Scalar Signal [%]	Impact on Neutrino Background [%]
Energy Scale		
Calorimetric Gain ± 1%	1.6	2.1
Calorimetric dE/dx	0.4	7.8
Multiple Coulomb Scattering	0.5	1.1
Total Energy Scale	1.8	8.2
Detector Model		
Total Detector Model	9.9	17.6
Track Splitting		
Total Cathode + Wire Gap	5.0	6.4

Table 9.1: Summary of impact of detector systematic uncertainties in the signal box region. The "Energy Scale" and "Detector Model" uncertainties are computed as normalization uncertainties, as detailed in sections 9.1.1 and 9.1.1, respectively. The track splitting uncertainty is computed by weighting individual events (it is not assumed to be a normalization), as discussed in section 9.1.1.

similar to the Coh-Like sample.

The uncertainty in each comparison is estimated as $\sqrt{N}$ of the total number of selected Monte Carlo simulated events N. This is a good estimate of the uncertainty on the difference because different samples have different selected neutrinos. The same underlying neutrino interactions are in each detector model variation. However, the G4 processing is different. The event selection mostly selects stopping pions, and the fraction of pions that stop is small and random between different Geant4 processings. Thus, the G4 step effectively randomizes each detector model variation sample. Empirically, less than 5% of the selected neutrinos are shared between the nominal sample and each variation. The Monte Carlo statistical uncertainty is much smaller for the scalar samples because it is easier to get statistics in the signal box region for the scalar signal. The central value neutrino background sample has 912 selected events, which corresponds to 3.2×10^{22} POT ($\sim 125\times$ data POT). Each model variation neutrino sample has about 130 events, corresponding to $\sim 5 \times 10^{21}$ POT ($\sim 20\times$ data POT). Some scalar variation samples have a larger statistical uncertainty due to fewer events being generated for those samples.

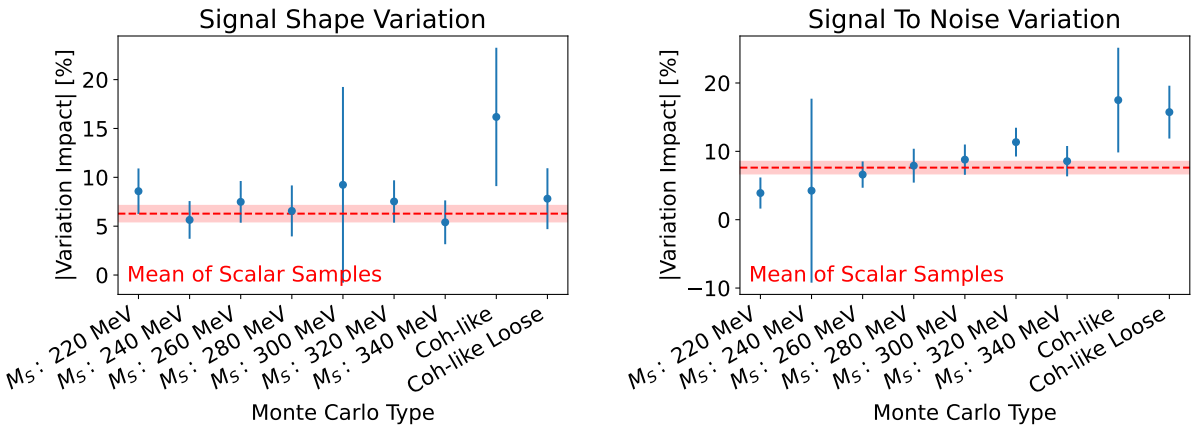

Figure 9.2: Magnitude of the impact on the number of selected events for signal shape detector model variations (left) and signal to noise variations (right). Shown for 7 scalar signal model points (with masses from 220 to 340 MeV) and for the Coh-like subsample of neutrino background (see section 3.2.1). The Coh-like subsample is shown for two definitions of the signal-box region: the nominal definition (plotted first) and a "Loose" version with the θ_{NuMI} cut (see figure 7.1) loosened to 15°.

For each systematic variation, there is no significant difference between any of the scalar model points. There is a somewhat significant variation (up to $\sim 1.5\sigma$) on the impact between the scalar signal and neutrino background samples. This may be a genuine difference of the impact of detector model variations on signal $\mu\mu$ events v. background $\mu\pi$ events, or just a relatively large statistical fluctuation. There is no significant difference between the "Coh-Like" and "Coh-Like Loose" samples for any uncertainty.

We elect to apply a normalization uncertainty on the number of selected events computed separately for scalar signal and neutrino background samples. The scalar signal uncertainty is computed with the fractional difference between the nominal and varied detector simulation, averaged over all of the scalar model points. The neutrino background uncertainty is computed as the fractional difference of the "Coh-Like Loose" sample between the nominal and varied simulations. For scalar samples, there are enough Monte Carlo statistics that this estimate of the uncertainty is precise. This is important because, as is shown in section 9.1.2, the detector has the leading impact on the systematic uncertainty of the scalar rate.

For neutrinos, even the "Loose" sample still has a large Monte Carlo statistical error. The uncertainty reported here should thus be understood as a conservative upper limit, rather than a precise estimate. This choice does not severely impact the analysis because, as shown in section 9.1.3, the background uncertainty is dominated by the ν_μCC-Coh-π rate. The uncertainty is treated as completely correlated between the neutrino background and scalar signal.

Energy Scale

Figure 9.3 shows the comparison of the number of selected events in each sample under the energy scale variations developed in section 8.1.2. There are three energy scale variations: on the EMB recombination measurement (equation 6.3), the channel gain ($\pm 1\%$), and the multiple-Coulomb-scattering momentum ($\pm 3\%$). Each of the three variations are evaluated "up" and "down", which corresponds to a $\pm 1\sigma$ unisim variation. The comparisons are made the same way as for the detector variations (section 9.1.1). The uncertainty in the plot (taken as $\sqrt{N}$) is likely overestimated since the same underlying events are applied with variations on the energy scales.

There is no significant difference on the impact of any energy scale uncertainty on the number of events between the different scalar signal points. There is a clear difference between the scalar signal and neutrino background samples for any uncertainty is the calorimetric dE/dx variation. This is because the neutrino sample includes the variation in low energy proton ("stub") dE/dx due to angular-dependence in recombination (see section 8.1.2), while the scalar signal does not.

As in the case of the detector model variations, we compute a normalization uncertainty separately for neutrino backgrounds and scalar signals. The uncertainty is assumed to be completely correlated between neutrinos and scalars. Each of the three pairs of energy scale variations are treated as $\pm 1\sigma$ variations of the same underlying systematic uncertainty.

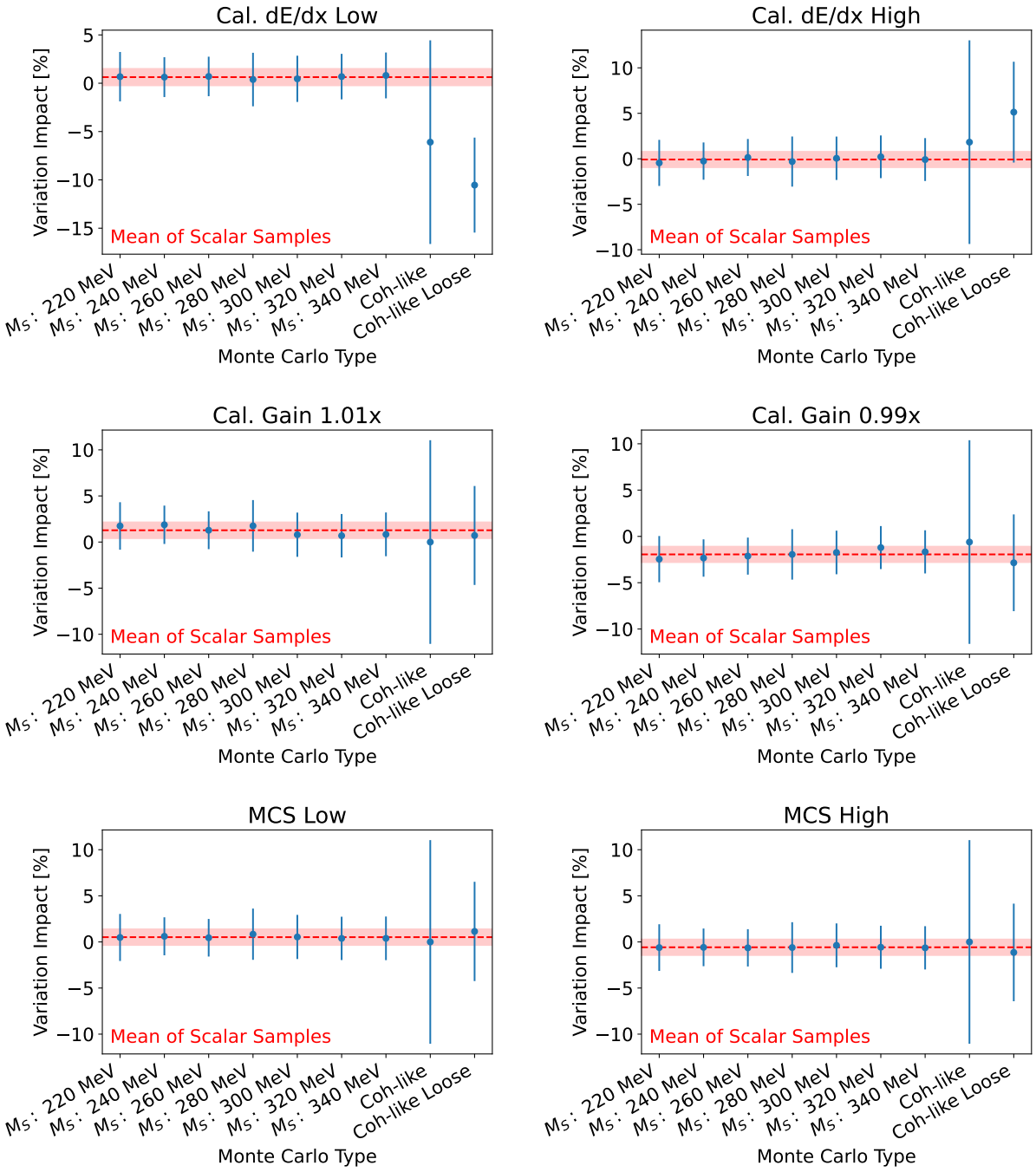

Figure 9.3: Impact on the number of selected events for energy scale uncertainty variations. Shown for 7 scalar signal model points (with masses from 220 to 340 MeV) and for the Coh-like subsample of neutrino background (see section 3.2.1). The Coh-like subsample is shown for two definitions of the signal-box region: the nominal definition (plotted first) and a "Loose" version with the θ_{NuMI} cut (see figure 7.1) loosened to 15°.

For scalar signals, the uncertainty is computed with the difference between the nominal and variation, averaged over the model points. The neutrino background uncertainty is computed with the "Coh-Like Loose" sample.

Track Splitting

There are two regions in ICARUS where un-simulated perturbations to the drift field distort tracks: the bending of the central cathode plane in each cryostat, and a mechanical support on the front induction wire plane in each TPC. An event display of a neutrino event in ICARUS data with two tracks that cross the front induction wire support region is shown in figure 9.1. Since these effects are not directly included in the ICARUS detector simulation, the Monte Carlo simulation is instead re-weighted to correct the amount of track-splitting in these regions, with an associated systematic uncertainty.

Figure 9.4 shows the impact of the reweighting and uncertainty for neutrino events, as a function of the reconstructed dimuon mass. Figure 9.5 shows the impact of the correction and the size of the uncertainty as a function of scalar mass point. The impact of the uncertainty on the normalization of events is shown in table 9.1. However, unlike the other two detector uncertainties, the track splitting uncertainty is not assumed to be a normalization. Rather, the systematic variation on track splitting is computed event-by-event with systematic weights. The weights are correlated between neutrino background and scalar signal.

9.1.2 Scalar Signal

Scalar signal events have uncertainties from the detector and flux. The detector uncertainties are applied as described in section 9.1.1. Flux uncertainties are computed with `ppfx` (see table **??**). There are no Geant4 uncertainties because there is no uncertainty assigned to $\mu - \mathrm{Ar}$ interactions. The uncertainty for each scalar mass point is summarized in figure 9.6.

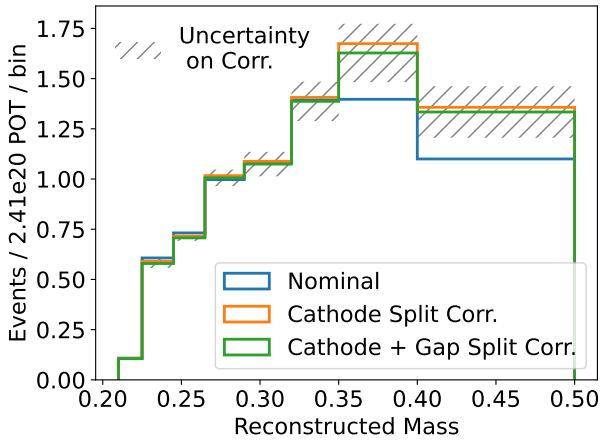

Figure 9.4: Impact of track splitting corrections on neutrino background events, with associated uncertainty. Shown as a function of the reconstructed dimuon mass.

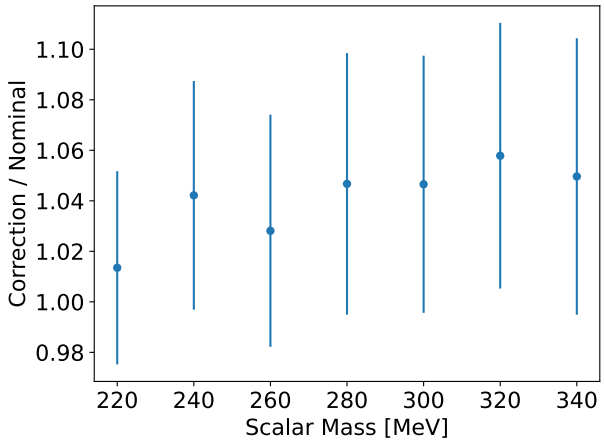

Figure 9.5: Size of track splitting correction on the scalar signal normalization (data point) and systematic uncertainty (error bar) as a function of the scalar mass.

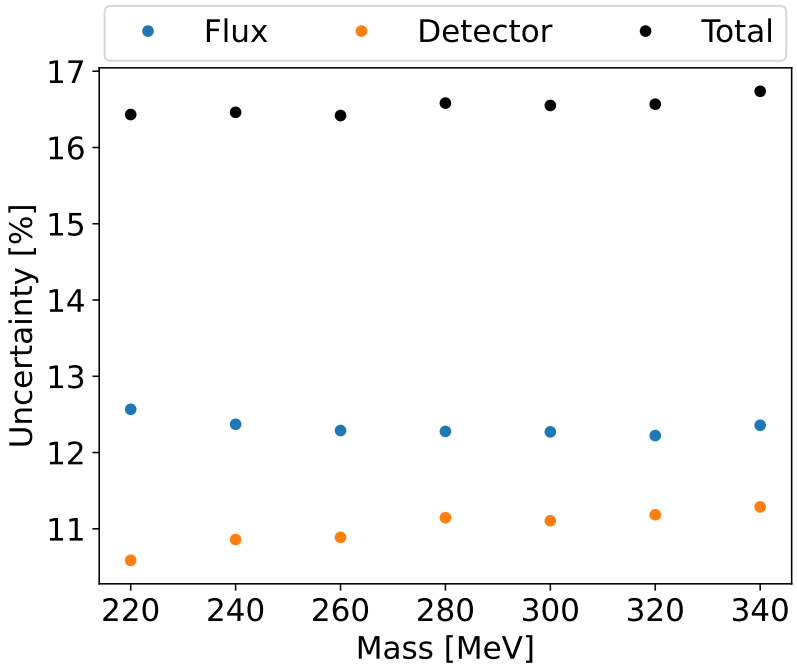

Figure 9.6: Systematic uncertainty by source for scalar events, as a function of the mass.

9.1.3 Neutrino Background

Neutrino background events have uncertainties from the detector, flux, cross-section, and Geant4. The number of simulated events is also relatively small, so there is a significant uncertainty from MC statistics. The detector uncertainties are applied as described in section 9.1.1. The flux, cross-section, and Geant4 uncertainties are applied as described in section 8.1. The systematic uncertainty from each source is shown in figure 9.7, as a function of the reconstructed di-muon invariant mass ($m_{\mu\mu}$).

9.2 Signal Box Statistical Analysis

9.2.1 Identifying a New Physics Signal with the Bump-Hunter Algorithm

The search for new physics in the signal box region is performed as a bump-hunt, using the Bump-Hunter algorithm [150]. We use the `pyBumpHunter` library for the implementation of

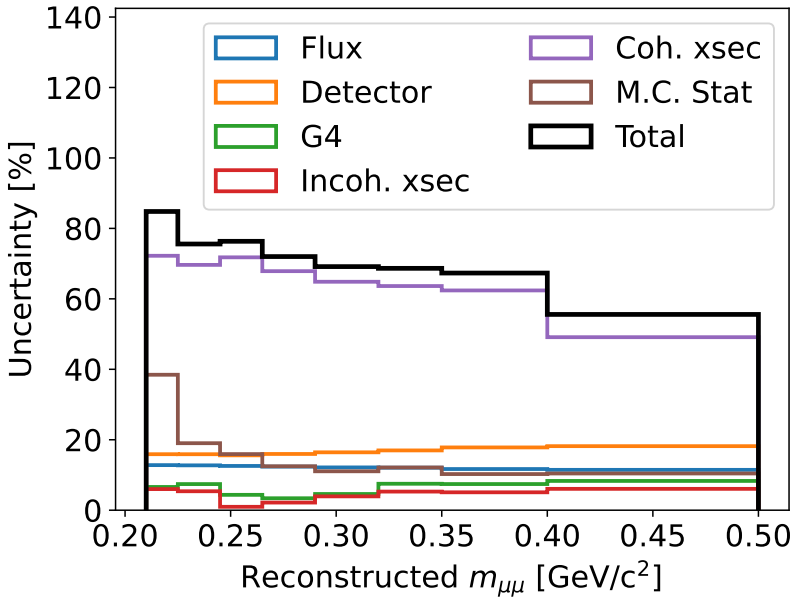

Figure 9.7: Systematic uncertainty by source for neutrino events, as a function of the reconstructed di-muon mass.

the algorithm [156]. This algorithm implements a test statistic which quantifies the level of disagreement between the observed data and the predicted background, depending on the size of the biggest bump. It searches for bumps in all possible windows combining bins in the reconstructed di-muon mass spectrum (see figure 7.33). For our implementation, we allow the window size to be between 1 and 3 bins. The test statistic is defined as the window with the smallest local p-value. The local p-value depends on a local test statistic defined as:

$$t_{\text{window}} = \begin{cases} 0 & \text{if D} < \text{B} \\ f(D-B) & \text{otherwise}\,, \end{cases} \tag{9.1}$$

where D is the observed number of events in the window, B is the predicted background in the window, and f is any positive, monotonically increasing function. For this test statistic,

the local p-value is (in the case of Poisson fluctuations)

$$p_{\text{window}} = \begin{cases} 1 & \text{if D} < \text{B} \\ \Gamma(D, B) & \text{otherwise}\,, \end{cases} \tag{9.2}$$

where

$$\Gamma(D, B) = \frac{\int_0^B t^{D-1} e^{-t} dt}{\int_0^\infty t^{D-1} e^{-t} dt}\,. \tag{9.3}$$

The global, Bump-Hunter test statistic is then defined with the smallest local p-value across all windows ($p^{\text{min}}_{\text{window}}$):

$$t_{BH} = -\log p^{\text{min}}_{\text{window}}\,. \tag{9.4}$$

This test statistic can be computed for the input data. The global p-value is computed from the distribution of t_{BH} generated with psuedo-experiments. Thus, the Bump-Hunter algorithm provides a mechanism to translate a local p-value into a global one. As a result, it correctly penalizes any candidate bump for the "look-elsewhere" effect.

In order to apply the bump-hunter algorithm for the di-muon search, there is one complication that must be accounted for. The rate of the main background, ν_μCC-Coh-π interactions, has a large systematic uncertainty (see figure 9.7). We therefore want our background prediction to be flexible to changes in the data normalization, so that an under-estimation of the overall rate is not mistaken for a bump. We have implemented a three-step procedure that extracts a constraint on the ν_μCC-Coh-π rate and the statistical significance of any bump at the same time. The procedure is as follows:

1. Run the Bump-Hunt algorithm on the signal box region between the data and the nominal background prediction to obtain the mass window with the largest upward fluctuation (if any exist). This window is defined the "mass-exclusion" region.

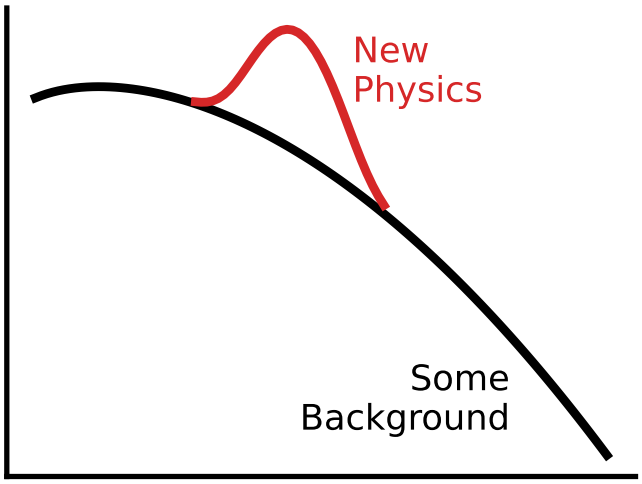

Figure 9.8: Cartoon diagram of a new physics signal on top of a smooth background.

2. Fit an overall scale factor to the ν_μCC-Coh-π rate with a fit region defined as: events passing the signal-box event selection (table 7.1), but with the θ_{NuMI} cut loosened to 10° (to allow more ν_μCC-Coh-π events), and the mass-exclusion region removed.

3. Run the Bump-Hunt algorithm again in the signal box region, to obtain the final test statistic value (t_{BH}).

The global p-value is computed from this test statistic from a distribution of t_{BH} values obtained from running toy experiments. In each toy experiment, a fake data distribution is obtained by throwing all systematic and statistical uncertainties on the neutrino background. This distribution is shown in figure 9.9. The global p-value is treated as a one-tailed p-value to obtain a global significance (σ). This significance is negative when $p > 0.5$. This case corresponds to a bump smaller than the median expectation.

Figures 9.10, 9.11, and 9.12 demonstrate the three steps of this procedure for two fake data studies: one with neutrino background only, and one with Scalar signal injected.

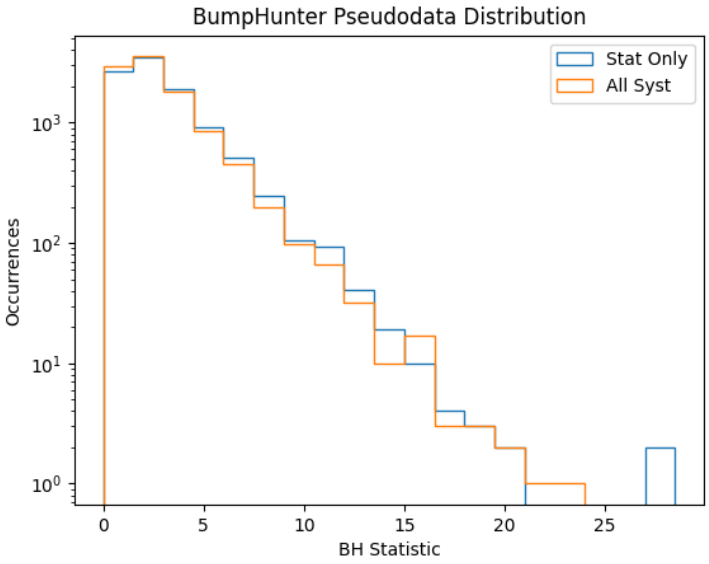

Figure 9.9: Distribution of Bump-Hunter test statistic values (t_{BH}) applying the signal box identification procedure outlined in the text. Shown for statistical variations only, as well as for all statistical and systematic variations.

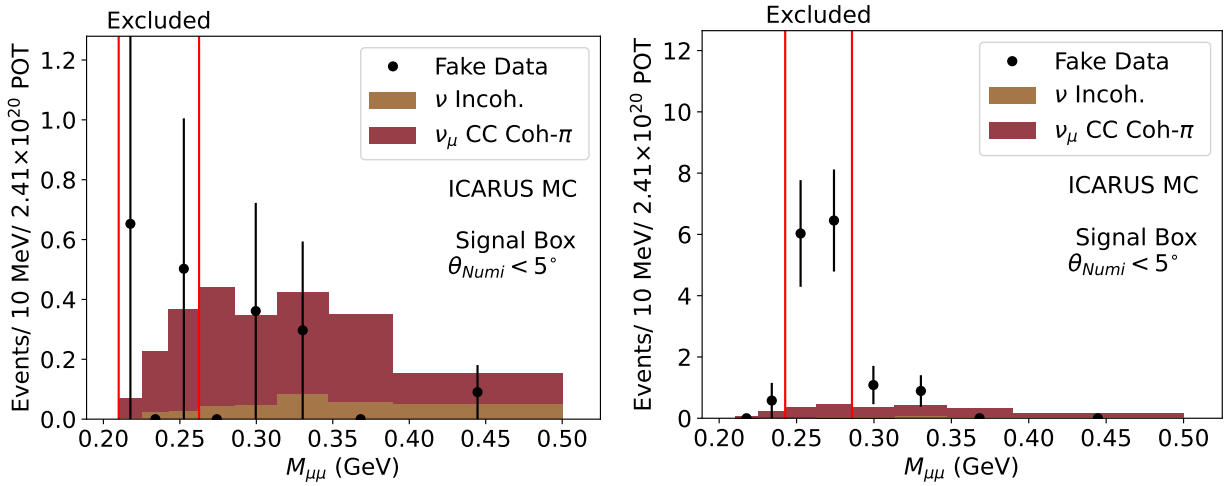

Figure 9.10: Step 1 of the signal identification procedure: The Bump-Hunt algorithm identifies the "mass-exclusion" region as the window with the largest upward fluctuation between the data and the nominal Monte Carlo simulation. Shown for a neutrino-only fake data test (left) and a signal injection test (right).

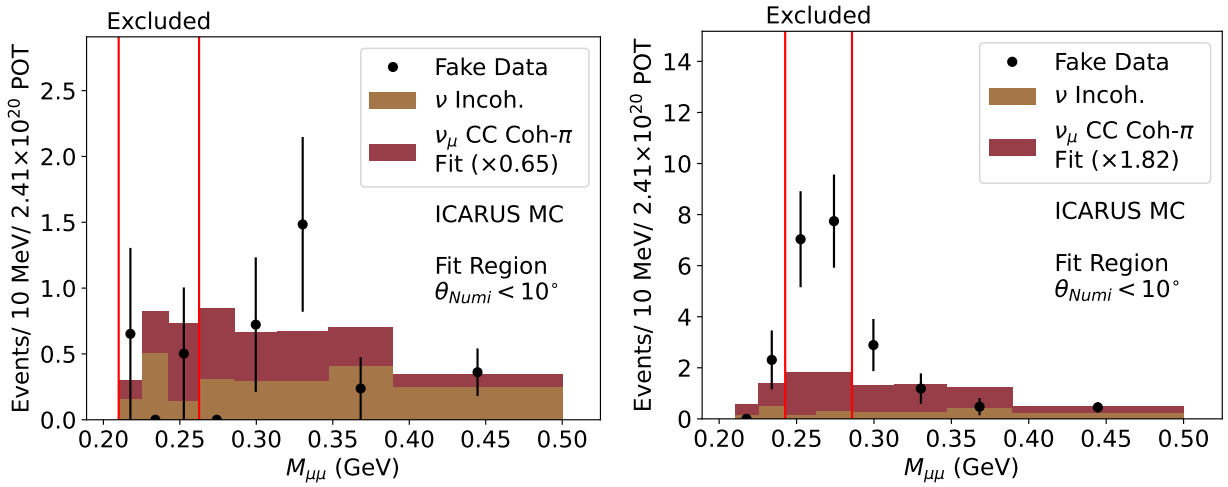

Figure 9.11: Step 2 of the signal identification procedure: a scale factor for the ν_μCC-Coh-π rate is fit with data including $\theta_{\text{NuMI}} < 10^\circ$ and excluding the mass-exclusion region. Shown for a neutrino-only fake data test (left) and a signal injection test (right).

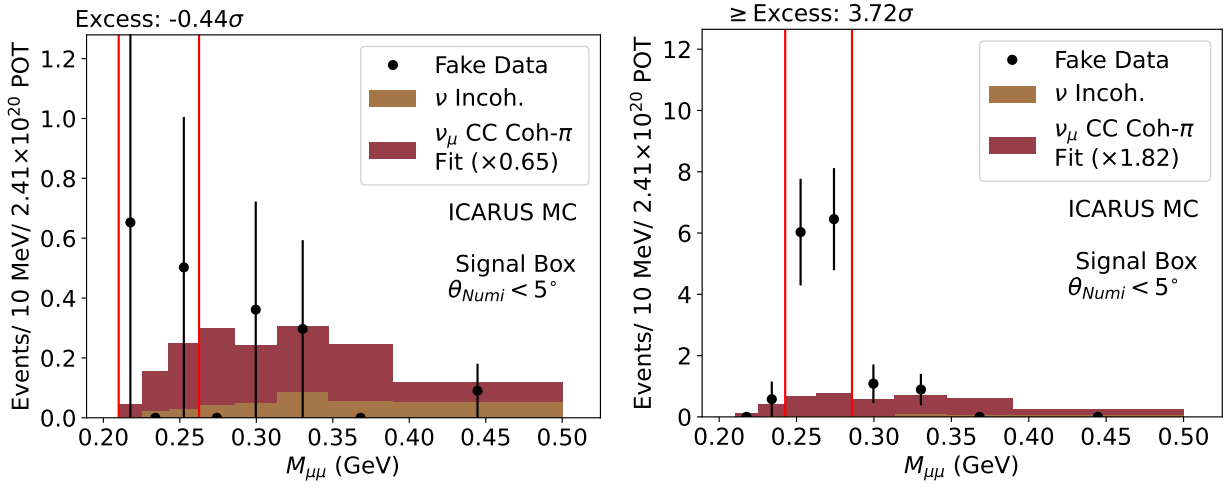

Figure 9.12: Step 3 of the signal identification procedure: the Bump-Hunter algorithm is run comparing the scaled neutrino background prediction to the data. The test-statistic (t_{BH}) is computed, and the distribution of t_{BH} values (figure 9.9) is used to obtain a global p-value. Shown for a neutrino-only fake data test (left) and a signal injection test (right).

9.2.2 Excluding Parameter Space with the CLs Method

In the event of no new physics, the CLs method is used to exclude regions of parameter space at some confidence level [154]. This method applies a new test statistic $-2 \log Q$, where

$$Q = \mathcal{L}(\vec{S} + \vec{B}, \vec{D}) / \mathcal{L}(\vec{B}, \vec{D}) \,, \tag{9.5}$$

where $\vec{D}$ is the spectrum of observed data events (interpreted as a vector), $\vec{B}$ is the expected background spectrum, $\vec{S}$ is the expected signal spectrum, and $\mathcal{L}$ is the Poisson likelihood, defined as

$$\mathcal{L}(\vec{E}, \vec{O}) = \prod_{i=1}^{n} \sum_{j=0}^{\vec{O}_i} \frac{e^{-\vec{E}_i} \left(\vec{E}_i\right)^j}{j!} \,, \tag{9.6}$$

for an expected event spectrum $\vec{E}$ and an observed event spectrum $\vec{O}$, each with n bins.

The value of Q is computed individually for each point in model parameter space (each point gives a different value for $\vec{S}$). The value of $-2 \log Q$ at each point is then compared to a distribution of test statistic values (also computed with toy experiments) to obtain a p-value. In the naive implementation, to exclude a model point at some specified confidence level (say, 95%), one would exclude all model parameter points with $p < 0.05$. However, at such a confidence level one would expect that 5% of the time the background-only hypothesis is rejected. If this happens, then even arbitrarily small signals are rejected at 95% confidence.

The CLs method corrects for this effect. It relies on two distributions of $-2 \log Q$: the background-only distribution, and the signal plus background distribution. These two distributions are used to obtain two confidence levels: CL_b and CL_{s+b}. The confidence level is equal to the fractional area of the distribution that is larger than the observed test statistic value. The CL_s value is then defined as $\mathrm{CL}_{s+b} / \mathrm{CL}_b$. To rule out a point in model parameter space at, say, 95%, one requires that $\mathrm{CL}_s < 0.05$. This treatment ameliorates cases where fluctuations in the data rule out the background hypothesis. In this situation, an arbitrarily

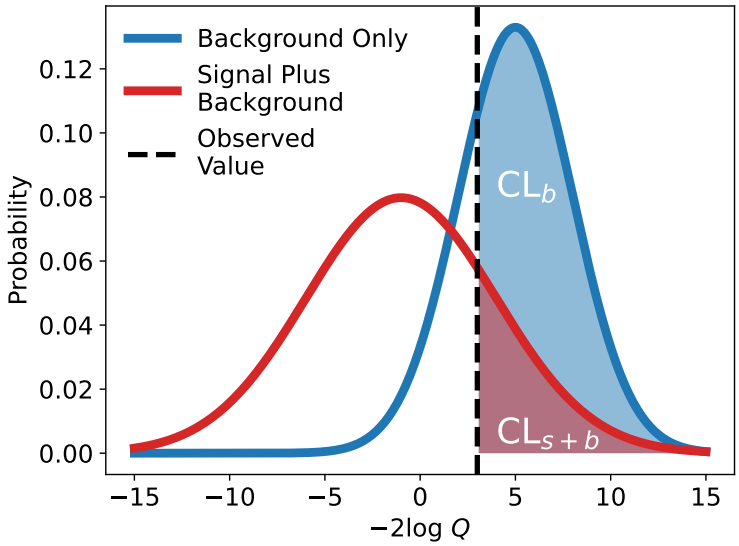

Figure 9.13: Example distributions of the test statistic ($-2 \log Q$) defining the CLs method. The confidence limit CL_s is equal to $\mathrm{CL}_{s+b}/\ \mathrm{CL}_b$.

small signal would have $\mathrm{CL}_{s+b} = \mathrm{CL}_b$, and $\mathrm{CL}_s = 1$, so it could not be ruled out to any confidence level. This procedure is typically described as ad-hoc and conservative. However, it does provide similar results to more principled, Bayesian approaches to limit setting [154]. This procedure is diagrammed in figure 9.13.

To apply the CLs method to the di-muon search, we take the tuned neutrino background prediction (from section 9.2.1) as the value of $\vec{B}$. The signal prediction $\vec{S}$ is computed at each point in model parameter space. Distributions of Q are obtained by varying all statistical and systematic uncertainties on both the neutrino background and the scalar signal. Uncertainties of the scalar signal rate (from the flux and detector modeling) broaden the signal plus background distribution and appropriately penalize our sensitivity to excluding any new physics signal.

9.3 Sensitivity

This section shows the sensitivity result for this analysis. The sensitivity is defined as the expected (median) parameter space that can be excluded by the CLs method in the event of no new-physics signal at 90% confidence (as detailed in section 9.2.2). The sensitivity is first presented in a model independent way (section 9.3.1). Then, it is also shown for two specific models: the Higgs portal scalar (section 9.3.2), and a heavy axion (section 9.3.3). The sensitivity of the two specific models is shown compared to the landscape of previous experimental searches.

9.3.1 Model Independent Sensitivity

As discussed in section 2.3, this analysis is sensitive to any new physics model involving the process $K \to \pi + S(\to \mu\mu)$, for some scalar S. We present our sensitivity to such a general case in a three-dimensional parameter space [54]: the decay length $c\tau$, the scalar mass M_S, and the branching ratio of the process. Scalar production can come from both $K^{\pm}$ and K_L decay in NuMI. As shown in appendix B, we are sensitive to the branching ratio combination

$$\left[\mathrm{BR}\left(K^{\pm} \to \pi^{\pm} + S\right) + 0.12 \cdot \mathrm{BR}\left(K^{L} \to \pi^{0} + S\right)\right] \times \mathrm{BR}\left(S \to \mu\mu\right) . \tag{9.7}$$

The sensitivity is determined for 8 discrete values of scalar mass M_S between 220 and 350 MeV. At each mass point, events are reweighted based on the value of the scalar decay length ($c\tau$) and branching ratio (equation 9.7). The median CLs exclusion at 90% confidence is shown for these model points in figure 9.14. The median and ±50% range of possible exclusion sensitivities are shown for each mass point in figure 9.15.

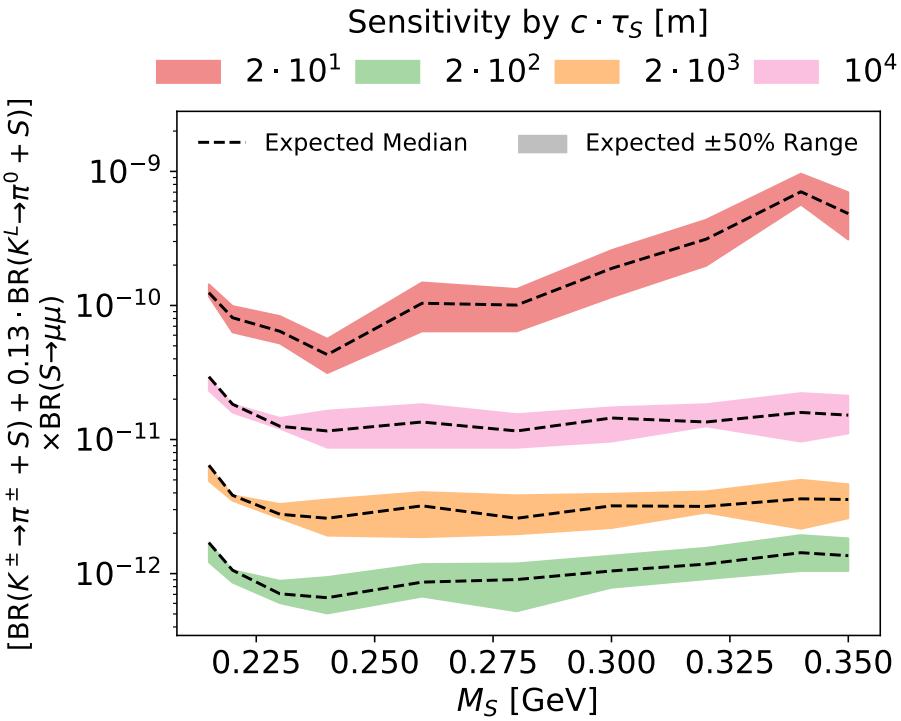

Figure 9.14: CLs exclusion sensitivity to kaon-induced di-muon scalar resonances ($K \to \pi + S(\to \mu\mu)$). Shown as a function of the scalar branching ratio and mass, for a few values of the decay length.

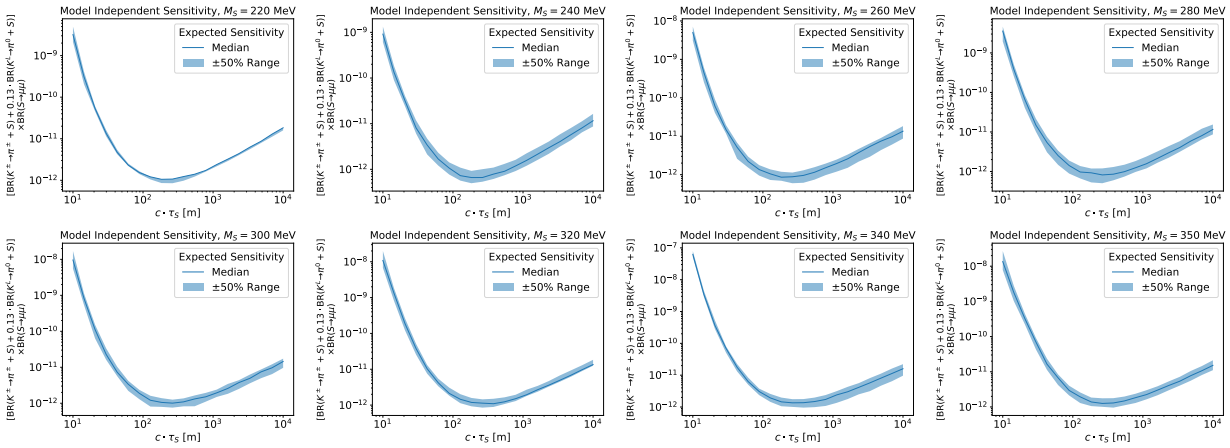

Figure 9.15: The median and expected ±50% CLs exclusion sensitivity to kaon-induced di-muon scalar resonances ($K \to \pi + S(\to \mu\mu)$). Shown in the branching ratio-lifetime space, as a function of M_S.

9.3.2 Higgs Portal Scalar Sensitivity

The first of the two specific models we set limits on is the Higgs Portal scalar. The phenomenology of this model is discussed in section 2.1. Our median sensitivity at 90% confidence is shown in figure 9.16. The limit is compared to other searches for this model. Direct analyses come from rare kaon decay searches (E949 [157] and NA62 [158]), B-meson decay searches (LHCb [159, 160]), and the MicroBooNE neutrino experiment [155]. Also shown are reinterpretations of searches for different models. The CHARM limit [161] comes from a search for axion-like particle production at a beam dump in the $\mu\mu$ final state [162]. The PS191 limit [163] comes from a search for heavy neutral leptons in a beam dump in final states including $\nu\mu\mu$ and $\mu\pi$. The LSND limit [164] is reinterpreted from a search for ν_μ CC interactions at a beam dump [165]. None of these searches were directly for the Higgs Portal scalar or the equivalent physical process it generates. The inferred limits all rely on assumptions about the detector operation made by the authors of the relevant reinterpretation. We therefore elect to show them separately with dashed lines.

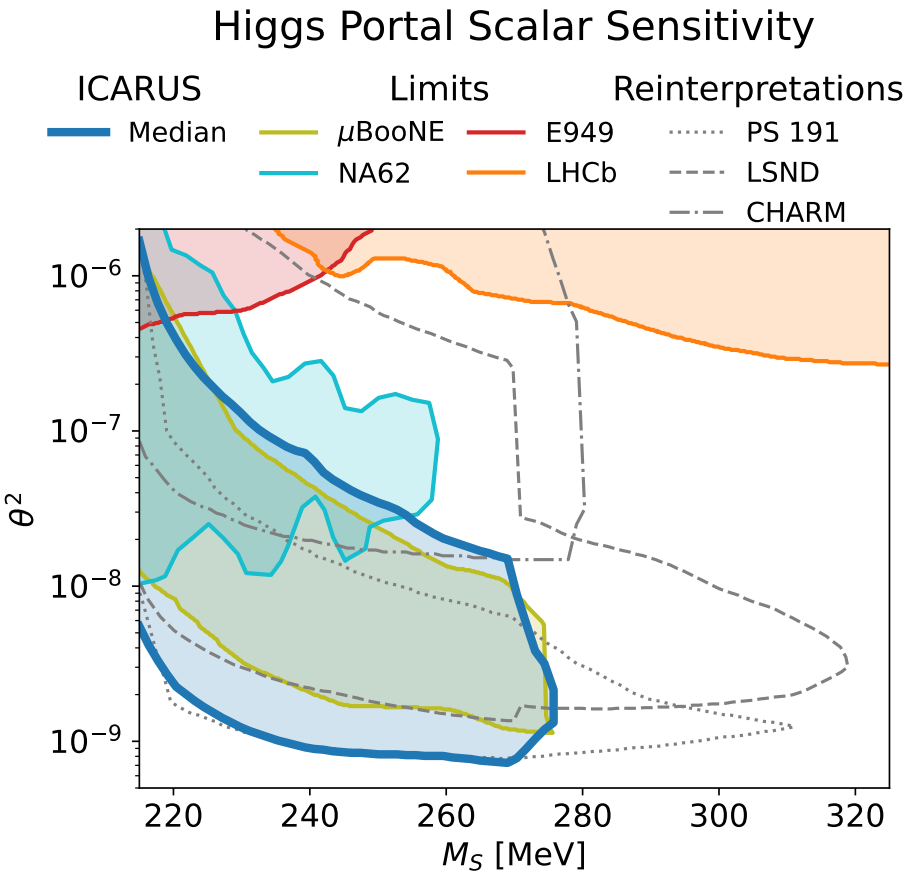

Figure 9.16: Median ICARUS sensitivity to the Higgs Portal Scalar at a 90% confidence level. Shown compared to previous dedicated searches for scalar production in kaon decay (from NA62 [158] and E949 [157]), B-meson decay (from LHCb [159, 160]), and in a neutrino beam (from MicroBooNE [155]). Also shown are reinterpretations of other analyses from PS 191 [163], LSND [164], and CHARM [161].

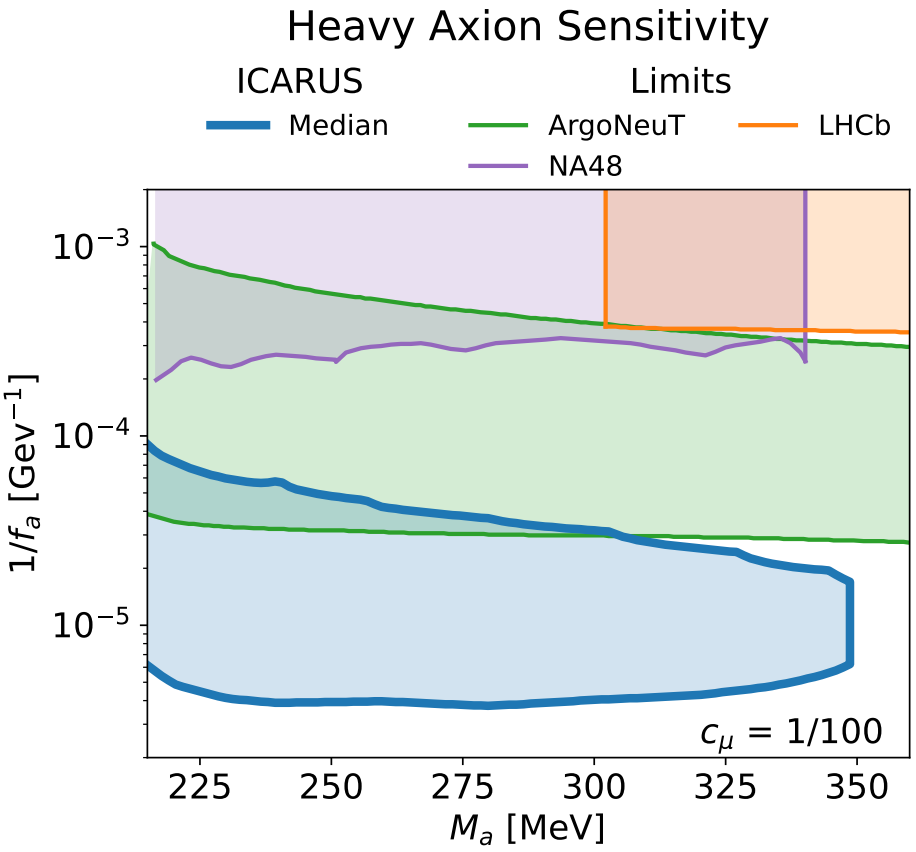

Figure 9.17: Median ICARUS sensitivity to our heavy axion model (with $c_\mu = 1/100$) at a 90% confidence level. Shown compared to previous results from ArgoNeuT [167], NA48 [166], and LHCb [159, 160].

9.3.3 Heavy Axion Sensitivity

Finally, we show our estimated sensitivity for the heavy axion model developed in section 2.2. We interpret our result for the co-dominance scenario ($c_1 = c_2 = c_3 = 1$) for two choices of the axion-muon coupling $(1/36, 1/100)$. Our median limit at 90% confidence is shown in figures 9.17 ($c_{a\mu} = 1/100$) and 9.18 ($c_{a\mu} = 1/36$). Our limit is shown compared to other relevant results from kaon decay searches (NA48 [166]), B-meson decay searches (LHCb [159, 160]), and at the ArgoNeuT neutrino experiment [167].

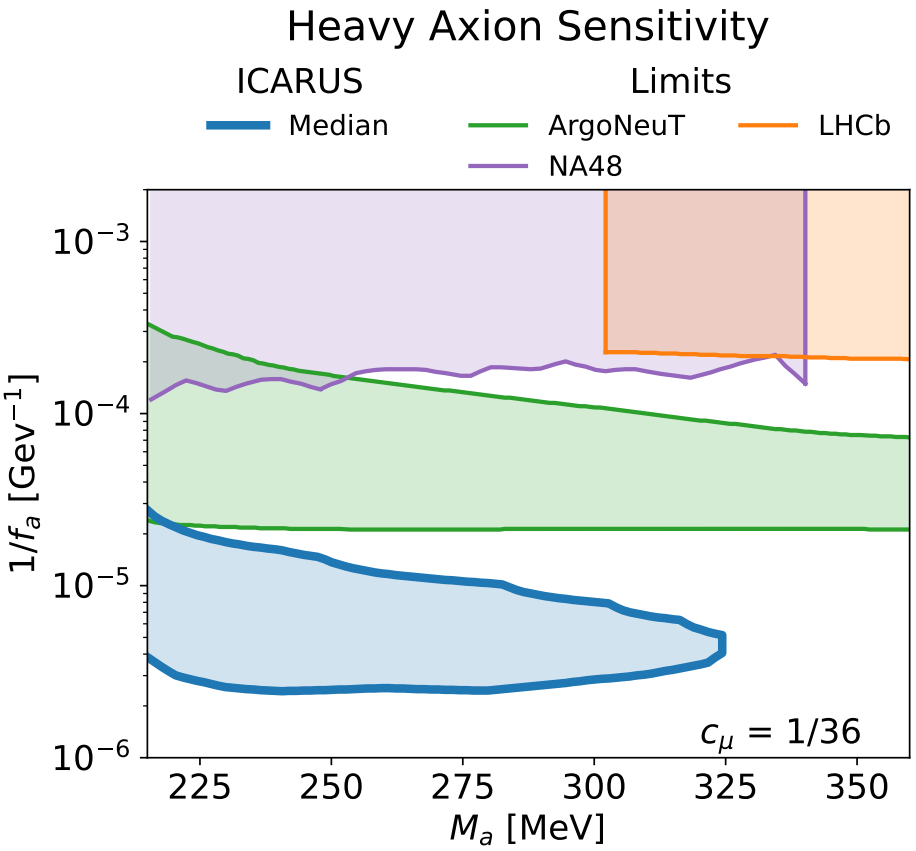

Figure 9.18: Median ICARUS sensitivity to our heavy axion model (with $c_\mu = 1/36$) at a 90% confidence level. Shown compared to previous results from ArgoNeuT [167], NA48 [166], and LHCb [159, 160].

CHAPTER 10

RESULTS

The three steps of the signal identification procedure are shown in figure 10.1. No significant excess over the fit background is observed. As is demarcated on the figure, the largest excess has a 0.19σ global significance.

The null result enables limits to be set on the parameter space of relevant physics models. Limits on the Higgs Portal scalar are shown in figure 10.2 and on the heavy axion model in figures 10.3 ($c_\mu = 1/100$) and 10.4 ($c_\mu = 1/36$). Model independent limits on the new physics process $K \to \pi + S(\to \mu\mu)$ are shown in figures 10.5 (for a few scalar lifetime values) and 10.6 (for a few scalar masses). All limits are at the 90% CL, applying the CLs method. The limit on the branching ratio is determined for scalar decay lengths between 10 m and 10 km. Below a decay length of 10 m, the large majority of scalars decay before reaching ICARUS and the limit on the branching ratio is weak. Above a decay length of 10 km, a negligible number of scalars decay before reaching ICARUS and the limit on the branching ratio scales linearly with the decay length: BR $\propto c\tau_S$

The observed limit is close to the $\pm 50\%$ range for all scalar masses. The limit is a little weaker than the median for masses close to 260 MeV (where the biggest excess is observed) and is a bit stronger than the median for higher masses around 340 MeV (where no events are observed in the relevant bin). The limit on the Higgs Portal scalar is world-leading among dedicated searches for the scalar. The competing limit from PS 191 that out performs this measurement is based on a reinterpretation of a separate search for heavy neutral leptons performed by authors outside of the collaboration. The limit on the heavy axion model probes an area of parameter space complimentary to prior searches for the particle. It limits nearly a decade of new parameter space in f_a, requiring (in combination with previous searches) $f_a \gtrsim 200$ TeV for $c_\mu = 0.01$ and $215 < m_a < 350$ MeV. The significant sensitivity of this search to gluonic axions is due to the octet enhancement of the $K \to a + \pi$ process in

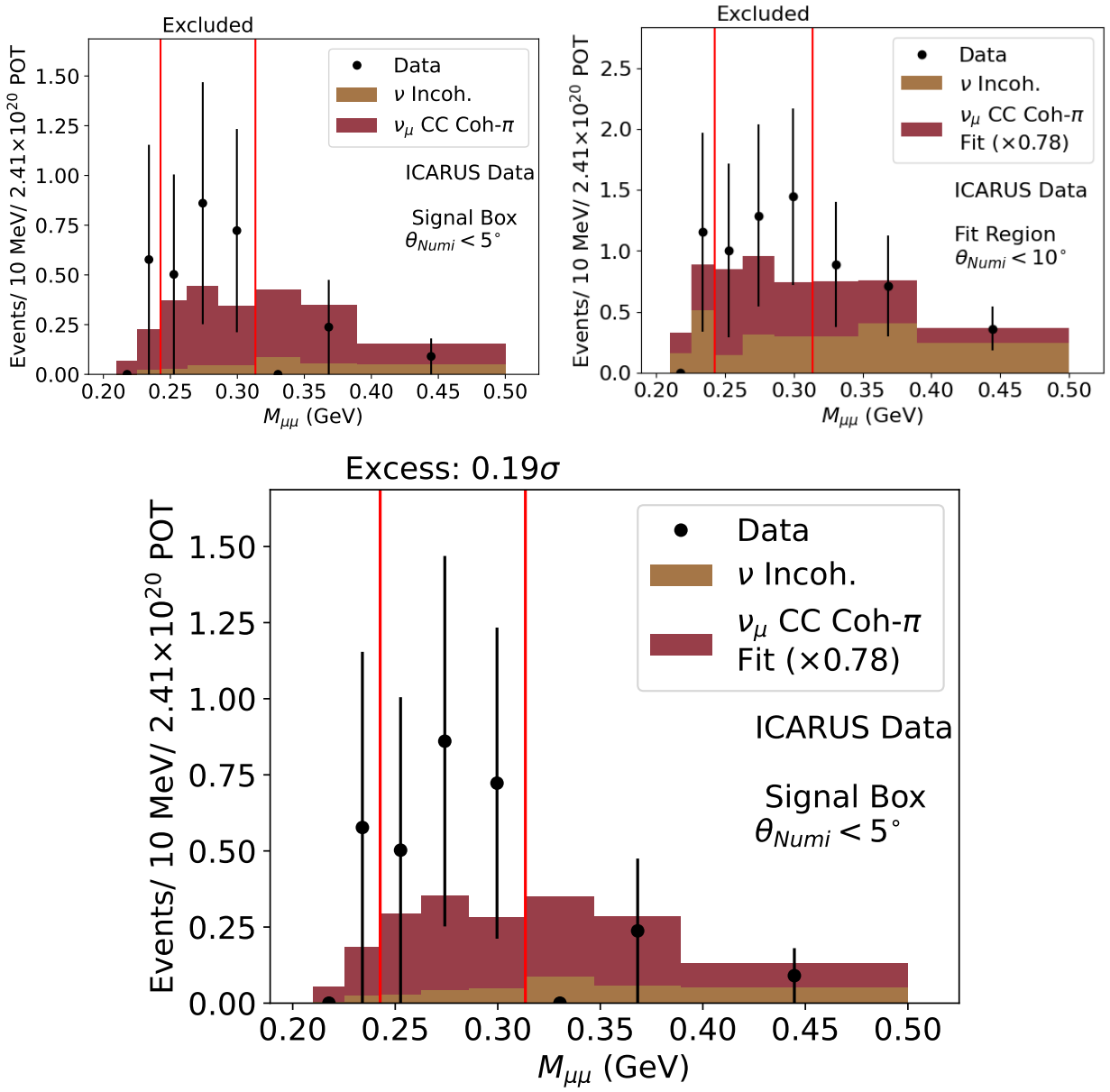

Figure 10.1: Reconstructed di-muon event spectra in the signal box region, as interpreted by the three-step signal identification procedure. Step 1 (top left): the region with the biggest initial bump above the nominal background prediction is excluded from the result. Step 2 (top right): going out to $\theta_{\mathrm{NuMI}} < 10°$, data in the "Fit Region" is used to obtain a scale factor on the ν_μCC-Coh-π component of the background. Step 3 (bottom): the fit background prediction is compared to the data in the signal box. The largest excess is identified, which has a 0.19σ significance.

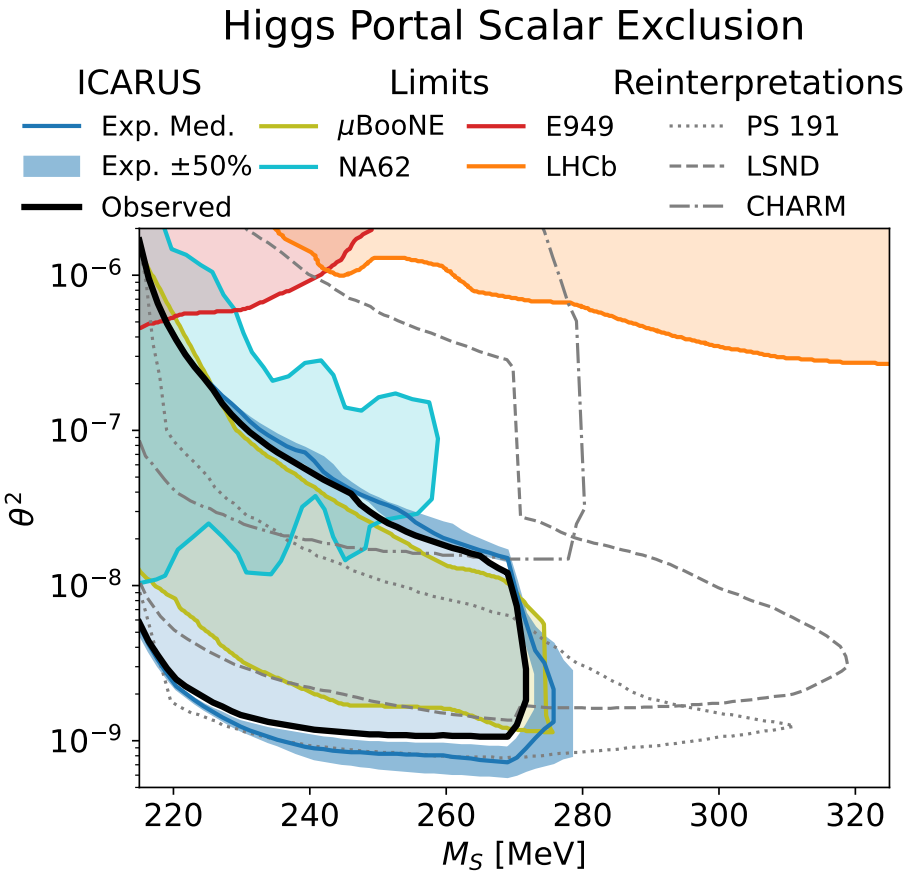

Figure 10.2: Limits from ICARUS on the Higgs Portal Scalar, applying the CLs method at the 90% confidence level. Shown compared to the median and ±50% expected limit. Shown alongside previous dedicated searches for scalar production in kaon decay (from NA62 [158] and E949 [157]), B-meson decay (from LHCb [159, 160]), and in a neutrino beam (from MicroBooNE [155]). Also shown are reinterpretations of other analyses from PS 191 [163], LSND [164], and CHARM [161].

the chiral Lagrangian, as was discussed in chapter 2.

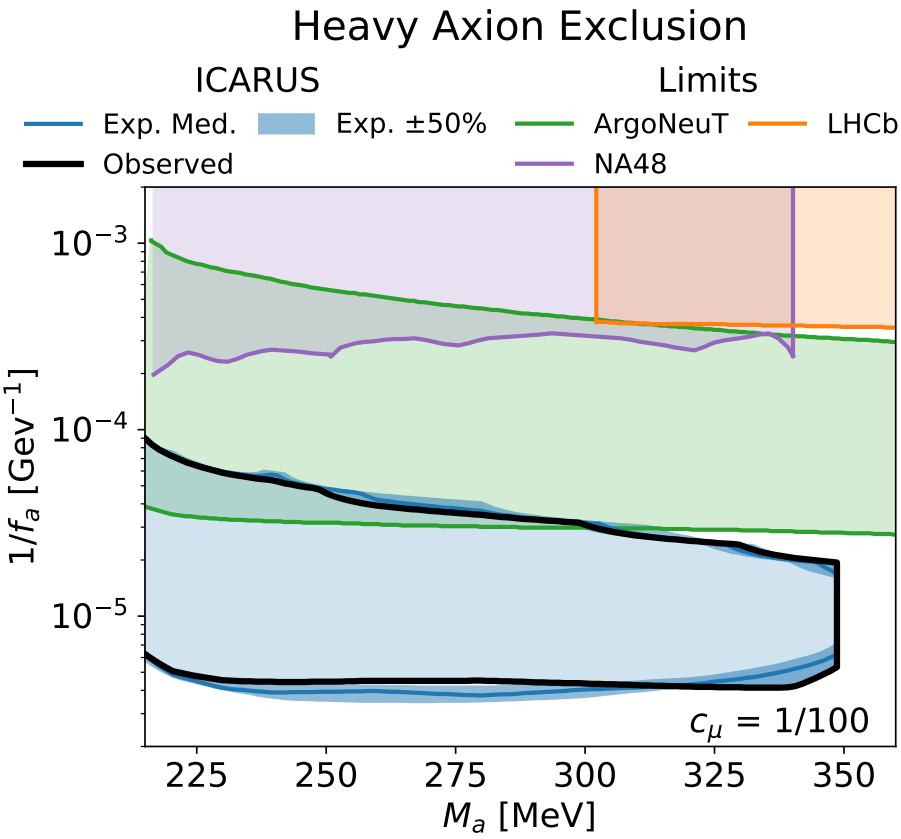

Figure 10.3: Limits from ICARUS on the heavy axion model (with $c_\mu = 1/100$), applying the CLs method at a 90% confidence level. Shown compared to the median and ±50% expected limit. Shown alongside previous results from ArgoNeuT [167], NA48 [166], and LHCb [159, 160].

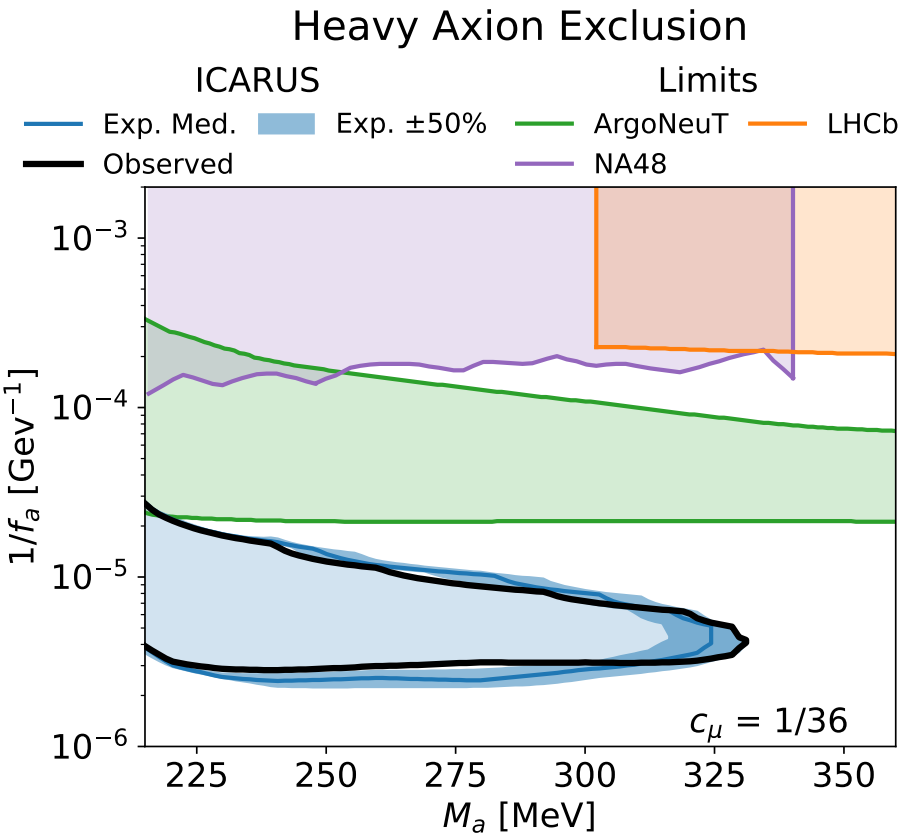

Figure 10.4: Limits from ICARUS on the heavy axion model (with $c_\mu = 1/36$), applying the CLs method at a 90% confidence level. Shown compared to the median and ±50% expected limit. Shown alongside previous results from ArgoNeuT [167], NA48 [166], and LHCb [159, 160].

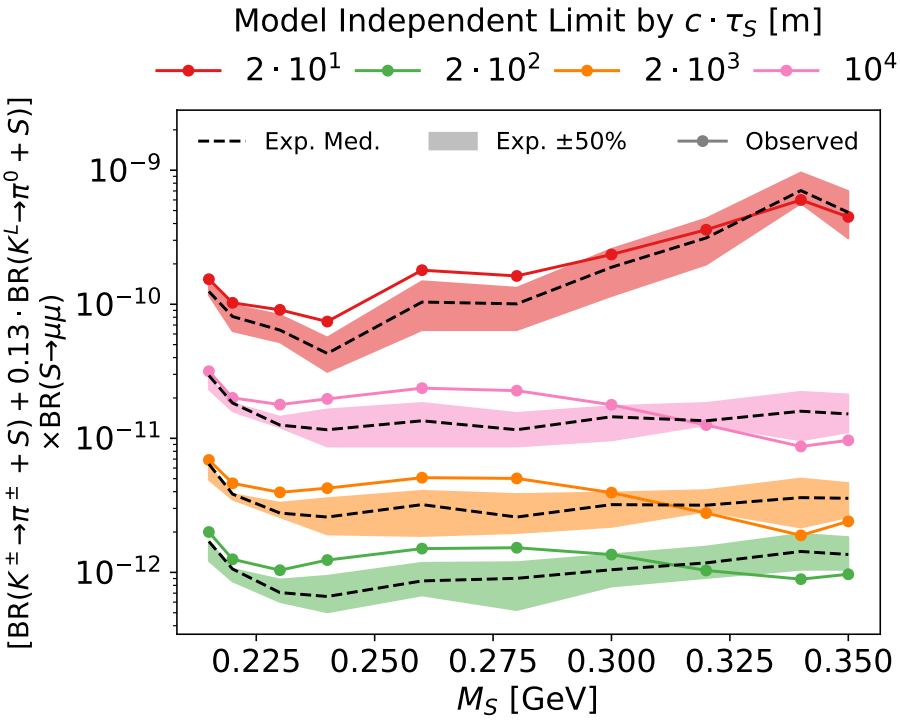

Figure 10.5: ICARUS limits on kaon-induced di-muon scalar resonances ($K \to \pi + S(\to \mu\mu)$), applying the CLs method at the 90% confidence level. Shown as a function of the scalar branching ratio and mass, for a few values of the decay length.

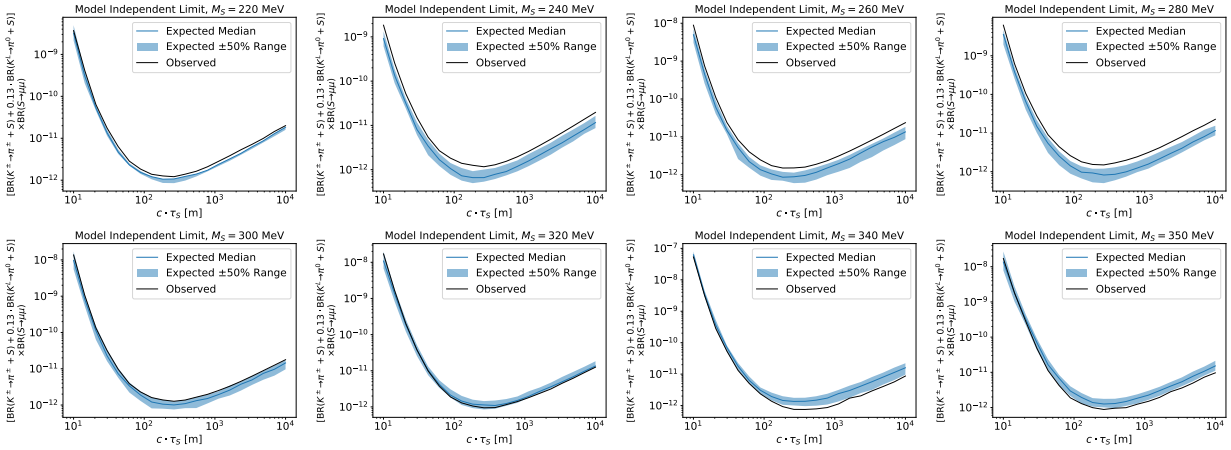

Figure 10.6: ICARUS limits on kaon-induced di-muon scalar resonances ($K \to \pi + S(\to \mu\mu)$), for a range of masses. Limits are computed with the CLs method at the 90% confidence level. Shown compared to the median and expected ±50% CLs exclusion sensitivity. The median and expected ±50% CLs exclusion sensitivity to kaon-induced di-muon scalar resonances ($K \to \pi + S(\to \mu\mu)$).

CHAPTER 11

CONCLUSION AND OUTLOOK

This thesis has presented a search for new physics through a long-lived di-muon resonance in the Neutrinos at the Main Injector (NuMI) beam with the ICARUS detector at Fermilab. No significant excess above background is observed, and we set world leading limits on two hidden sector models: the Higgs Portal scalar and a heavy axion model. We also compute the exclusion for the model independent process $K \to \pi + S(\to \mu\mu)$, for some particle S.

This search is enabled by the calibration of the ICARUS liquid argon time projection chamber (LArTPC) detector, which has also been presented. This calibration enables the application of ionization measurements in the ICARUS time projection chamber (TPC) for physics analysis. Together with the Short-Baseline Near Detector (SBND), ICARUS will search for neutrino oscillations to address the short-baseline anomalies in neutrino physics. The calibration has also demonstrated new techniques and phenomena important for the calibration of LArTPC detectors. First, the energy scale of cosmic muon depositions is impacted by ionization diffusion in the TPC. Second, simulated ionization signal shapes on the charge sensing wire planes can be tuned to data to improve the fidelity of the detector simulation. And finally, highly-ionizing energy depositions have an angular dependence in the amount of electron-ion recombination in liquid argon. These findings are all important for the calibration of future LArTPC detectors such as SBND and DUNE.

The di-muon LLP search is performed as a bump-hunt, which enables discrimination between a new physics signal and the smooth neutrino-induced background. The application of this technique can be useful for future new physics searches in neutrino experiments (such as DUNE) that have backgrounds from neutrino interactions. In addition, the observation in this thesis that the octet enhancement of kaon decays to axions significantly boosts the production rate of axions in neutrino experiments improves the outlook for future searches above the estimation of previous studies which only considered psuedoscalar meson mixing

as a production mechanism.

ICARUS continues to take physics data with the NuMI beam, and a search with the expanded dataset will enable further sensitivity to di-muon LLPs. In such a future search, new techniques to reduce the neutrino background will be critical. There are two promising avenues for such a reduction. First, improved charged pion rejection. Visually, many of the selected pions in the signal box region elastically scatter off argon nuclei before stopping. Identification of these elastic scatters by the automated reconstruction would enable rejecting these events as neutrino backgrounds. Second, neutrino rejection with PMT timing. Neutrinos, travelling at nearly the speed of light, arrive promptly in the detector compared to massive scalar particles, which typically have sub-luminal speeds. Precise event timing with scintillation light could thus be leveraged to reject neutrinos.

***

One might propose a goal for these future searches at experiments such as ICARUS, SBN, and DUNE: that they, taken together, are capable of excluding the hypothesis they test. That is, these searches are testing the possibility that outstanding puzzles in particle physics such as the nature of dark matter and the strong-CP problem are resolved by a hidden sector of new physics. If none are found after DUNE and SBN, can we conclude that hidden sectors indeed are not responsible for these puzzles?

Taking the Higgs Portal scalar as example, there is a relevant lower limit on the Standard Model mixing from the requirement that the dark matter particle thermalizes through coupling to the scalar in the early universe. This requires that $\theta_S^2 \gtrsim 2\times10^{-13}$. The world-leading limit presented here (combined with other previous null results) requires $\theta_S^2 \lesssim 1.5 \times 10^{-9}$ around $M_S \sim$250 MeV. There are thus many orders of magnitude left to probe in the model. The future ICARUS dataset, as well as the DUNE experiment, will probe further but will

not reach the lower bound. This is nothing to say of the many decades of possible masses for the scalar, as well as the variety of possible motivated hidden sectors to dark matter (vector, psuedo-scalar, and fermion, in addition to scalar). Experimental searches which probe this space will thus be a promising avenue of research for years to come, but the task of fully exploring the realm of hidden sectors is daunting. To complete the task, DUNE will not be enough. New experimental approaches, and the determination to perform them, will be required.

Are they worth it? The questions these searches seek to address are fundamental to the nature of matter and our reality. Even if each search is, to use a common metaphor, just one lamppost illuminating its own corner of the question, it does so towards a deeply important goal. But will any lamppost illuminate something new?

It is often remarked that particle physics has been very lucky with nature to make its many discoveries over the last century and a quarter. Taking neutrino oscillations as an example, the phenomenon was discovered due to a truly cosmic coincidence: that the density of the sun was matched to resonate with the solar neutrino mass splitting. This resonant enhancement was responsible for the significant deficit in neutrinos originally observed at the Homestake experiment. It required two values with no possible relation to each other, the neutrino masses and the density of the sun, to be precisely matched to each other. And the oscillation hypothesis was confirmed by Super-Kamiokande through a second cosmic coincidence: that the size of the earth is matched to the atmospheric oscillation length at atmospheric neutrino energies.

If particle physics is to resolve the puzzles that hidden sectors propose to solve, it seems like another stroke of luck is needed in the coming years. Hopefully ours has not run out.

APPENDIX A

THE DISTRIBUTION OF ENERGY LOSS SEEN BY A CHANNEL WITH A POSITION-DEPENDENT SENSITIVITY TO PARTICLE ENERGY

A.1 Derivation

Typically, the Landau and Landau-Vavilov distributions are derived by means of a Laplace transform leveraging the continuity property of the energy loss distribution [110]. Here we take an alternative approach, applying the convolution property (equation 4.1) by means of a Fourier transform. We also keep track of the channel ionization weight function as a function of the charged particle position ($w(x)$). We end at the same place, except for perturbations coming from the weight function. To start, we discretize $w(x)$ into weights w_i over infinitesimal steps dx_i, and build up the probability distribution over the full weight function by performing a product of convolutions:

$$p_w(E) = \int dT_1 \int dT_2 \cdots \int dT_n \frac{p_{dx_0}(\frac{E-T_n-\cdots-T_1}{w_0})}{w_0} \times \frac{p_{dx_1}(\frac{T_n-\cdots-T_1}{w_1})}{w_1} \times \cdots \times \frac{p_{dx_n}(\frac{T_n}{w_n})}{w_n} \,. \tag{A.1}$$

By use of a Fourier transform $\mathcal{F}$, we can turn this into a regular product:

$$p_w(E) = \underset{\tau \to E}{\mathcal{F}^{-1}} \prod_i \underset{T \to \tau}{\mathcal{F}} \frac{p_{dx_i}(T/w_i)}{w_i} \,.$$

Applying the scale property of a Fourier Transform:

$$p_w(E) = \underset{\tau \to E}{\mathcal{F}^{-1}} \prod_i \underset{T \to w_i\tau}{\mathcal{F}} p_{dx_i}(T) \,.$$

By taking the exponential of the log of the RHS, we can manipulate it into a sum:

$$p_w(E) = \underset{\tau\to E}{\mathcal{F}^{-1}} \exp\left[\sum_i \log \underset{T\to w_i\tau}{\mathcal{F}} p_{dx_i}(T)\right] .$$

Using the small$-\ell$ formula (4.2) for $p_{dx}(T)$, we can simplify its Fourier transform:

$$p_w(E) = \underset{\tau\to E}{\mathcal{F}^{-1}} \exp\left[\sum_i \log(1 - \sigma\rho dx_i + \rho dx_i \underset{T\to w_i\tau}{\mathcal{F}} \frac{d\sigma}{dT})\right] .$$

By applying $\log(1+\epsilon) \approx \epsilon$, we obtain:

$$p_w(E) = \underset{\tau\to E}{\mathcal{F}^{-1}} \exp\left[\sum_i -\sigma\rho dx_i + \rho dx_i \underset{T\to w_i\tau}{\mathcal{F}} \frac{d\sigma}{dT}\right] .$$

Which can be neatly turned into an integral:

$$p_w(E) = \underset{\tau\to E}{\mathcal{F}^{-1}} \exp\left[\int dx(-\rho\sigma + \rho \underset{T\to w(x)\tau}{\mathcal{F}} \frac{d\sigma}{dT})\right] .$$

Now we apply the definitions of σ and $\mathcal{F}$ to evaluate the integral. Noting $d\sigma/dT \neq 0$ only for $0 < T < T_{\max}$, we obtain

$$\begin{aligned} p_w(E) &= \underset{\tau\to E}{\mathcal{F}^{-1}} \exp\left[\rho \int dx \int_0^{T_{\max}} dT \frac{d\sigma}{dT}\left(e^{-2\pi i\tau w(x)T} - 1\right)\right] \\ &= \underset{\tau\to E}{\mathcal{F}^{-1}} \exp\left[\rho\frac{2\pi r_e^2 m_e}{\beta^2} \int dx \int_0^{T_{\max}} dT \frac{1-\beta^2 T/T_{\max}}{T^2}\left(e^{-2\pi i\tau w(x)T} - 1\right)\right] , \end{aligned}$$

where we have used the formula for the bare cross section (equation 4.3) in place of $d\sigma/dT$.

The integrand diverges as $1/T$ as $T \to 0$. This divergence appears because we have used the cross section of scattering on bare electrons instead of atomic electrons. At low

energy transfer the cross section is modified by atomic effects, which in particular cutoff the cross section near the excitation energy (above $T = 0$) to remove the divergence. We can remove the divergent behavior of the integrand by adding and subtracting the mean energy loss $\overline{E} = \int dx \int dT \rho \frac{d\sigma}{dT} T w(x)$. That subtracting the mean energy loss makes the integrand converge indicates that the shape of the distribution is not sensitive to atomic effects; these only act to change the mean. So once the impact of atomic effects on the mean energy loss is accounted for, it is safe to apply the bare cross section to find the shape of the distribution. Thus, for the purpose of this derivation, we take the mean energy loss as an external input (from Bethe-Bloch theory [112]) and find how the mean relates to the shape of the distribution. (There is also nothing new here coming from the weight function; this is precisely the same approximation that is made by Vavilov [110]). Applying this substitution, we get

$$p_w(E) = \underset{\tau \to E}{\mathcal{F}^{-1}} \exp \Bigg[-2\pi i \overline{E} \tau + \rho \frac{2\pi r_e^2 m_e}{\beta^2} \times \int dx \int_0^{T_{\max}} dT \frac{1 - \beta^2 T / T_{\max}}{T^2} \left(e^{-2\pi i \tau w(x) T} + 2\pi i \tau w(x) T - 1 \right) \Bigg] . \tag{A.2}$$

This integral converges to

$$p_w(E) = \underset{\tau \to E}{\mathcal{F}^{-1}} \exp \Bigg[-2\pi i \overline{E} \tau + \rho \frac{2\pi r_e^2 m_e}{\beta^2 T_{\max}} \int dx \Big(1 - e^{-2i\pi T_{\max} w(x) \tau} - 2\pi i \tau w(x) T_{\max} (1 + \beta^2) + (\beta^2 + 2i\pi T_{\max} w(x) \tau) \times (-\mathrm{Ei}[-2i\pi T_{\max} w(x) \tau] + \log[2i\pi T_{\max} w(x) \tau] + \gamma_{\mathrm{EM}}) \Big) \Bigg] ,$$

where γ_{EM} is the Euler constant and Ei is the exponential integral function, $\mathrm{Ei}(x) =$

$-\int_{-x}^{\infty} dt\ e^{-t}/t$. Next, we expand the inverse Fourier transform $\mathcal{F}^{-1}$:

$$p_w(E) = \int_{-\infty}^{\infty} d\tau\ \exp\Bigg[2\pi i E\tau - 2\pi i\overline{E}\tau + \rho\frac{2\pi r_e^2 m_e}{\beta^2 T_{\max}}\int dx \Big(1 - e^{-2i\pi T_{\max} w(x)\tau} - 2\pi i\tau w(x) T_{\max}(1+\beta^2) + (\beta^2 + 2i\pi T_{\max} w(x)\tau)\times (-\mathrm{Ei}[-2i\pi T_{\max} w(x)\tau] + \log[2i\pi T_{\max} w(x)\tau] + \gamma_{\mathrm{EM}}) \Big)\Bigg] .$$

To simplify these integrals, we can leverage the ζ quantify defined earlier (equation 4.4) and $z \equiv 2\pi\tau\zeta T_{\max}$:

$$p_w(E) = \frac{1}{2\pi\zeta T_{\max}}\int_{-\infty}^{\infty} dz\ \exp\Bigg[\frac{iz}{\zeta T_{\max}}(E-\overline{E}) + \int dx\ \zeta(1 - e^{-iw(x)z/\zeta}) - izw(x)(1+\beta^2) + (\zeta\beta^2 + iw(x)z)\times (-\mathrm{Ei}[-iw(x)z/\zeta] + \log[iw(x)z/\zeta] + \gamma_{\mathrm{EM}})\Bigg] . \tag{A.3}$$

This integral definition gives the general result of the probability distribution of energy loss observed by some channel with a position-dependent weight function $w(x)$. In the nominal case, we would replace $\int dx \to \not{p}$ for some channel pitch $\not{p}$ and would obtain the Landau-Vavilov distribution. From here, we will consider for which channel sensitivities the distribution is equal to the Landau distribution (in the thin film case) or the Landau-Vavilov distribution (in the general case). In section A.2 it is shown that for all channel sensitivities that satisfy the thin film approximation, the distribution is a Landau one. Finally, in section A.3 we find that only for specific channel sensitivities is the distribution equivalent to a Landau-Vavilov distribution in the general case.

A.2 The Landau Limit

To restrict to the Landau case, we take the thin-film approximation. In the usual derivation, one takes the limit that $\zeta \cdot \ell \ll 1$, where ℓ is the width of the step function. In our case, since we don't have a single such width, we have to be more careful about this approximation. In this case we can make a requirement on w – that the range of values where w is not $\ll 1$, r, has the property that $\zeta \cdot r \ll 1$. Then, inside the integrand of $\int dx$, we can take the limit that ζ is small. In this limit, $p_w(E)$ converges to

$$p_w(E) = \frac{1}{2\pi i \zeta T_{\max} \not{p}} \int_{-i\infty}^{i\infty} dz' \, \exp\left[z'\left(\lambda + \log|z'|\right)\right] , \tag{A.4}$$

where $z' = iz/\zeta T_{\max}$, $\not{p} \equiv \int w(x)dx$, and $\lambda = \frac{E-\overline{E}}{\zeta T_{\max}\not{p}} - \log\zeta\not{p} + \gamma_{\rm EM} - 1 - \beta^2 + \frac{\int dx \; w(x)\log[w(x)]}{\not{p}}$. This equation can be recognized as the Landau distribution for a parameter λ.

A.3 General / Landau-Vavilov Case

To understand the general case, we will examine the cumulants of the probability distribution. To do this, it is useful to go back to the definition in equation A.2, modified slightly so that we obtain the cumulant-generating function $K(\tau) = \log \mathrm{E}\left[e^{-i\tau E}\right]$:

$$K(\tau) = -i\overline{E}\tau + \zeta T_{\max} \int dx \int_0^{T_{\max}} dT \frac{1-\beta^2 T/T_{\max}}{T^2}\left(e^{-i\tau w(x) T} + i\tau w(x) T - 1\right) . \tag{A.5}$$

We expand the term in parentheses in a Taylor series:

$$K(\tau) = -i\overline{E}\tau + \zeta T_{\max} \int_0^{T_{\max}} dT \frac{1-\beta^2 T/T_{\max}}{T^2} \sum_{n=2}^{\infty} \frac{(-i\tau T)^n}{n!} \int dx \; w(x)^n \, .$$

Which can be simplified to

$$K(\tau) = -i\overline{E}\tau + \zeta T_{\max} \sum_{n=2}^{\infty} \frac{(-i\tau)^n}{n!} T_{\max}^{n-1} \left(\frac{1}{n-1} - \frac{\beta^2}{n} \right) \int dx \; w(x)^n \, .$$

From here, the nth cumulant $\kappa_n = i^n K^{(n)}(0)$ can be directly read off:

$$\begin{aligned} \kappa_1 &= \overline{E} \\ \kappa_n &= \zeta T_{\max}^n \left(\frac{1}{n-1} - \frac{\beta^2}{n} \right) \int dx \; w(x)^n \, . \end{aligned} \tag{A.6}$$

The cumulants of the Landau-Vavilov distribution are given for $w(x) = \Theta(x) - \Theta(x + \not{p})$ for some pitch $\not{p}$. Thus, the cumulants of the Landau-Vavilov distribution are

$$\begin{aligned} \kappa_1^{\mathrm{LV}} &= \overline{E} \\ \kappa_n^{\mathrm{LV}} &= \zeta \not{p} T_{\max}^n \left(\frac{1}{n-1} - \frac{\beta^2}{n} \right) \, . \end{aligned} \tag{A.7}$$

A necessary but not sufficient condition for two probability distributions to be equivalent is that they have the same cumulants. Allowing for the distributions to be different by location and scale parameters, the n-th cumulant must be equal up to a multiplicative (scale) factor c^n. Thus, we need $\kappa_n = \kappa_n^{\mathrm{LV}} c^n$ for a distribution (with cumulants κ) to be equivalent to the Landau-Vavilov distribution up to location and scale parameters. This puts a requirement on w that $\int dx \; w(x)^n = \not{p} c^{n-1}$ for all integers $n \geq 1$ for some constant c and the pitch $\not{p}$.

The cumulants being equivalent is not by itself a sufficient condition for the probability distributions to be the same. However, given this property on w we can simplify the

distribution further – starting from equation A.2:

$$p_w(E) = \underset{\tau\to E}{\mathcal{F}^{-1}} \exp\left[-2\pi i\overline{E}\tau + \rho\frac{2\pi r_e^2 m_e}{\beta^2}\int dx \int_0^{T_{\max}} dT \right.$$
$$\left. \frac{1-\beta^2 T/T_{\max}}{T^2}\left(e^{-2\pi i\tau w(x)T} + 2\pi i\tau w(x)T - 1\right)\right]$$
$$= \underset{\tau\to E}{\mathcal{F}^{-1}} \exp\left[-2\pi i\overline{E}\tau + \rho\frac{2\pi r_e^2 m_e}{\beta^2}\frac{\not{p}}{c}\int_0^{T_{\max}} dT \right.$$
$$\left. \frac{1-\beta^2 T/T_{\max}}{T^2}\left(e^{-2\pi ci\tau T} + 2\pi ci\tau T - 1\right)\right],$$

which integrates to:

$$p_w(E) = \underset{\tau\to E}{\mathcal{F}^{-1}} \exp\left[-2\pi i\overline{E}\tau + \rho\frac{2\pi r_e^2 m_e}{\beta^2 T_{\max}}\frac{\not{p}}{c}\left(1 - e^{-2i\pi T_{\max} c\tau} - 2\pi i\tau c T_{\max}(1+\beta^2) + \right.\right.$$
$$\left.\left. (\beta^2 + 2i\pi T_{\max} c\tau)(-\mathrm{Ei}[-2i\pi T_{\max} c\tau] + \log[2i\pi T_{\max} c\tau] + \gamma_{\mathrm{EM}})\right)\right].$$

Then, defining $\zeta' = \rho\frac{2\pi r_e^2 m_e}{T_{\max}\beta^2}\frac{\not{p}}{c}$ and $z' = 2\pi i\tau T_{\max} c$:

$$p_w(E) = \frac{1}{2\pi i T_{\max} c}\int_{-i\infty}^{i\infty} dz' \exp\left[\frac{z'}{T_{\max} c}(E-\overline{E}) + \zeta'(1-e^{-z'}) - z'\zeta'(1+\beta^2) + \right.$$
$$\left. \zeta'(\beta^2 + z')(-\mathrm{Ei}[-z'] + \log[z'] + \gamma_{\mathrm{EM}})\right],$$

which is the Landau-Vavilov distribution with a scale parameter c (this can be verified against [110] equation 8, with somewhat different notation). Thus, the probability distribution of energy loss recorded by a channel with a weight function $w(x)$ is equal to the Landau-Vavilov distribution precisely when

$$\int dx\ w(x)^n = \not{p} c^{n-1} \tag{A.8}$$

for all integers $n \geq 1$ for some $\not{p}, c$.

We can show further that this requirement means $w(x)$ is equal to some number of non-overlapping step functions multiplied by a scale factor c. First, define $\not{p}' = c\not{p}$ and $w'(x) = w(x)/c$. Then A.8 being satisfied means $\int dx\ w'(x)^n = \not{p}'$ for all $n \geq 1$. We show this means $w'(x)$ is equal to 1 or 0 for all x. Take n large enough that for $w' < 1$, $w'^n \approx 0$ and for $w' > 1$, $w'^n \approx \infty$. Then $w'(x)$ can't have some compact region where $w' > 1$, or else the integral would diverge. In this case, the integral breaks down to a sum of the compact regions where $w' = 1$: $\lim_{n\to\infty} \int dx\ w'(x)^n = \sum_{\text{region}-\text{i}} r_i = \not{p}'$, where r_i is the length of region i where $w' = 1$. Then, consider the integral $\int dx\ w'(x)$. This is equal to those same regions plus the integral of $w'(x)$ outside those regions: $\int dx\ w'(x) = \sum_{\text{region}-\text{i}} r_i + \int_{w'\neq 1} w'(x)$. Since $\sum_{\text{region}-\text{i}} r_i = \not{p}'$, we need $\int_{w'\neq 1} w'(x) = 0$. Since w' is positive for all x, this means w' must be equal to 0 wherever $w' \neq 1$. This means that w' should be given by the sum of some number of non-overlapping step functions at location x_i of length a_i: $w'(x) = \sum_i \Theta(x - x_i) - \Theta(x - x_i - a_i)$. Translating this back to w, this means w must be given by the sum of those step functions multiplied by some constant c where $0 \leq c \leq 1$.

Thus, when not considering the relativistic limit, the distribution of particle energy loss recorded by a channel with a weight function $w(x)$ is only equal to a Landau-Vavilov distribution (up to location and scale factors) when $w(x)$ is given by the sum of step functions multiplied by some overall constant. In general, the probability distribution will be different and is given by equation A.3 (equation 4.6 in the main text). The cumulants of this distribution are given by equation A.6.

APPENDIX B

RATIO OF LONG TO CHARGED KAON PARENTAGE OF SCALARS IN NUMI

The new physics models we consider here, including HPS and ALPs, involve particles that can be produced in both charged and long kaon decay. This creates a challenge for the model-independent interpretation of the result (section 2.3): how to record the sensitivity to different models with different ratios of charged to long kaon production? We demonstrate here that a suitable linear combination of the branching ratios describes our sensitivity.

First, there are no significant spectral differences between scalars produced in long and charged kaon decay. This is demonstrated in figure B.1. This figure neglects the component of kaon-decay-at-rest (KDAR) scalars, which are entirely from $K^{\pm}$. However, this analysis is not sensitive to the component of the flux.

Seeing no spectral differences, we verify that the relative rate of K^L:$K^{\pm}$ parentage is stable across different mass points. This is shown in figure B.2. The ratio of K^L:$K^{\pm}$ is stable at $0.13 : 1$. It starts to increase slightly at high mass, likely due to the approach towards the production mass threshold ($m_{K^{\pm}} - m_{\pi^{\pm}}$ is slightly smaller than $m_{K^L} - m_{\pi^0}$). However, the difference is not significant. Thus, the analysis is sensitive to the branching ratio combination $BR(K^{\pm} \to \pi^{\pm} + S) + 0.13 \times BR(K^L \to \pi^0 + S)$, independent of the scalar mass.

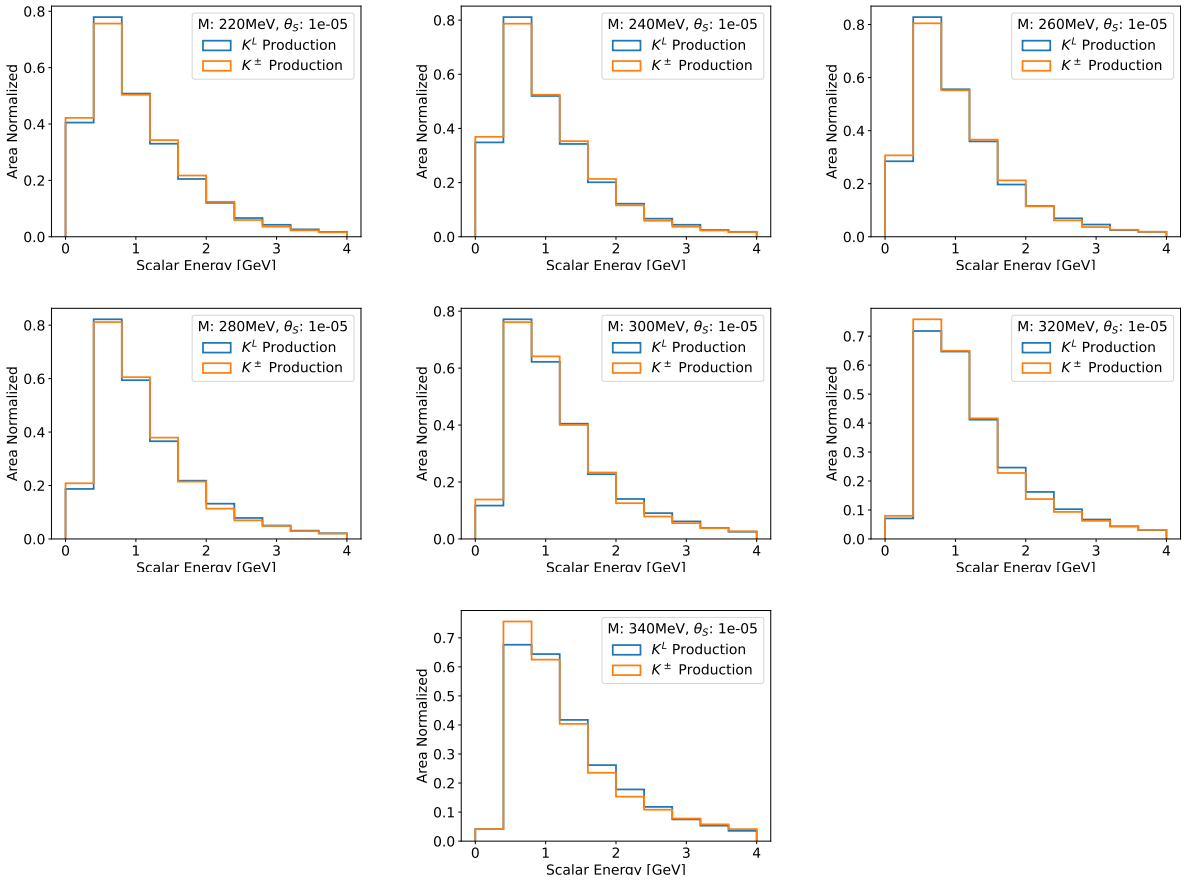

Figure B.1: Area normalized spectra of scalars produced in kaon decay at different HPS model points.

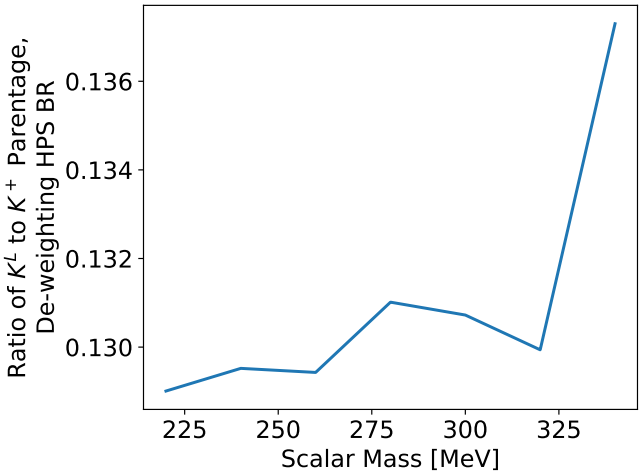

Figure B.2: Ratio of K^L to $K^\pm$ parentage of scalars by the scalar mass. Taken with the HPS model, where the relative branching ratio of $K^L \to S$ vs. $K^\pm \to S$ is divided out.

APPENDIX C

FIELD AND ELECTRONIC RESPONSE TRANSFORMATIONS IN SIGNAL SHAPE FIT

The single electron field response fit applies a set of non-linear transformations to the nominal Wire-Cell responses. The transformations depend on the time t and the location x along the direction perpendicular to the wire orientation ($\hat{w}$). The fit is done by splitting each field response into a left (denoted with a subscript ℓ) and right (denoted with a subscript r) side of a central time tick. The time tick is defined as the peak of the field response on the collection plane and the zero-cross point on the induction planes. Both the shape of the field response s and the time input to the field response t is transformed. All position dependence is encoded in an "offset parameter" o. The fit single electronics field response $s(x,t)$, in terms of the nominal WireCell single electronics field response $s^0(x,t)$, is defined below.

$$
\begin{aligned}
s(t,x) =& s_\ell(t'(t,x),x)\cdot(t'(t,x)<0) + s_r(t'(t,x),x)\cdot(t'(t,x)\geq 0)\\
s_{\ell,r}(t,x) =& a^0_{\ell,r}(x)s^s_{\ell,r}(t,x) + a^1_{\ell,r}(x)(s^s_{\ell,r}(t,x))^2\cdot\mathrm{sign}(s^s_{\ell,r}(t,x))\\
s^s_{\ell,r}(t,x) =& (s^0(t,x)+ds_{\ell,r}(t,x))\cdot\exp\left[(t>\boldsymbol{t^{\mathrm{start}}_{\ell,r}})\cdot\boldsymbol{e_{\ell,r}}|t|\right]\\
a^{0,1}_{\ell,r}(x) =& \boldsymbol{a0^{0,1}_{\ell,r}} + \boldsymbol{a1^{0,1}_{\ell,r}}\cdot o(x)\\
ds_\ell(t,x) =& 0\,,\quad ds_r(t,x)\frac{\boldsymbol{c^p_r}\cdot\exp[-|x|/\boldsymbol{\ell^p_r}]\cdot(|x|\leq 1.5\mathrm{mm})}{1+(|t|/\boldsymbol{\tau^p_r})\boldsymbol{a^p_r}}\cdot(|t|>\boldsymbol{t^{p-\mathrm{start}}_r})\\
t'(t,x) =& t'_\ell(t,x)\cdot(t<0) + t'_r(t,x)\cdot(t\geq 0) + \boldsymbol{c}\cdot o(x)\\
t'_{\ell,r}(t,x) =& t\cdot\left(s^0_{\ell,r}(x) + \frac{s^2_{\ell,r}(x)}{1+\left(t/\tau^2_{\ell,r}(x)\right)^2} + \frac{s^4_{\ell,r}(x)}{1+\left(t/\tau^4_{\ell,r}(x)\right)^4}\right)\\
s^{0,2,4}_{\ell,r}(x) =& \boldsymbol{s1^{0,2,4}_{\ell,r}}\cdot o(x) + \boldsymbol{s2^{0,2,4}_{\ell,r}}\cdot o(x)^2\\
\tau^{2,4}_{\ell,r}(x) =& \boldsymbol{\tau 1^{2,4}_{\ell,r}} + \boldsymbol{\tau 2^{2,4}_{\ell,r}}\cdot o(x)\\
o(x) =& 1-e^{-|x|/1.5\mathrm{mm}}\,.
\end{aligned}
\tag{C.1}
$$

The fit parameters in these equations are in bold. In these equation, there are 16 fit parameters on both sides of $t=0$ (ℓ,r): $t^{\mathrm{start}}_{\ell,r}$, $e_{\ell,r}$, $a0^0_{\ell,r}$, $a0^1_{\ell,r}$, $a1^0_{\ell,r}$, $a1^1_{\ell,r}$, $s1^0_{\ell,r}$, $s1^2_{\ell,r}$, $s1^4_{\ell,r}$, $s2^0_{\ell,r}$, $s2^2_{\ell,r}$, $s2^4_{\ell,r}$, $\tau 1^2_{\ell,r}$, $\tau 1^4_{\ell,r}$, $\tau 2^2_{\ell,r}$ and $\tau 2^4_{\ell,r}$. There are 5 parameters only on the right side of $t=0$: c^p_r, ℓ^p_r, τ^p_r, a^p_r, and $t^{p-start}_r$. Finally, there is the time shift parameter c. In total, there are 38 parameters in the field response fit.

The electronics response is also fit for. The nominal electronics response $e^0(\tau;t)$ is a Bessel shaping function with a nominal shaping time τ =1.3 µs. This nominal shape is convolved with the long RC-tail measured externally to the signal shape fit as described in section 5.2.2. To allow for further distortions, the response is convolved with an RC-RC tail

function with a time constant τ_{RCRC}. The full fit electronics response $e(t)$ is

$$\begin{aligned} e(t) &= (e^0(\boldsymbol{\tau}) \circledast \mathrm{RC}(\boldsymbol{A}, \boldsymbol{\tau}_{\mathrm{RC}}) \circledast \text{RC-RC}(\boldsymbol{\tau}_{\mathrm{RCRC}}))(t) \\ \mathrm{RC}(A, \tau; t) &= \delta(t) + Ae^{-t/\tau} \\ \text{RC-RC}(\tau; t) &= \left(\frac{t}{\tau} - 2\right) \frac{e^{-t/\tau}}{\tau}\,, \end{aligned} \tag{C.2}$$

where $\circledast$ denotes a convolution and δ is the dirac-delta function. The four fit parameters, τ, τ_{RC}, τ_{RCRC}, and A, are all in bold.

REFERENCES

[1] W. Pauli, *Dear radioactive ladies and gentlemen*, *Phys. Today* **31N9** (1978) 27.

[2] C.L. Cowan, F. Reines, F.B. Harrison, H.W. Kruse and A.D. McGuire, *Detection of the free neutrino: A Confirmation*, *Science* **124** (1956) 103.

[3] B. Pontecorvo, *Mesonium and anti-mesonium*, *Sov. Phys. JETP* **6** (1957) 429.

[4] B. Pontecorvo, *Inverse beta processes and nonconservation of lepton charge*, *Zh. Eksp. Teor. Fiz.* **34** (1957) 247.

[5] Z. Maki, M. Nakagawa and S. Sakata, *Remarks on the unified model of elementary particles*, *Prog. Theor. Phys.* **28** (1962) 870.

[6] B. Pontecorvo, *Neutrino Experiments and the Problem of Conservation of Leptonic Charge*, *Zh. Eksp. Teor. Fiz.* **53** (1967) 1717.

[7] R. Davis, *A review of the Homestake solar neutrino experiment*, *Prog. Part. Nucl. Phys.* **32** (1994) 13.

[8] SNO collaboration, *Direct evidence for neutrino flavor transformation from neutral current interactions in the Sudbury Neutrino Observatory*, *Phys. Rev. Lett.* **89** (2002) 011301 [nucl-ex/0204008].

[9] N. Jelley, A.B. McDonald and R.G.H. Robertson, *The Sudbury Neutrino Observatory*, *Ann. Rev. Nucl. Part. Sci.* **59** (2009) 431.

[10] Super-Kamiokande collaboration, *Evidence for oscillation of atmospheric neutrinos*, *Phys. Rev. Lett.* **81** (1998) 1562 [hep-ex/9807003].

[11] MINOS collaboration, *Observation of muon neutrino disappearance with the MINOS detectors and the NuMI neutrino beam*, *Phys. Rev. Lett.* **97** (2006) 191801 [hep-ex/0607088].

[12] T2K collaboration, *The T2K Experiment*, *Nucl. Instrum. Meth. A* **659** (2011) 106 [1106.1238].

[13] NOvA collaboration, *First measurement of muon-neutrino disappearance in NOvA*, *Phys. Rev. D* **93** (2016) 051104 [1601.05037].

[14] I. Esteban, M.C. Gonzalez-Garcia, M. Maltoni, T. Schwetz and A. Zhou, *The fate of hints: updated global analysis of three-flavor neutrino oscillations*, *JHEP* **09** (2020) 178 [2007.14792].

[15] R.N. Mohapatra et al., *Theory of neutrinos: A White paper*, *Rept. Prog. Phys.* **70** (2007) 1757 [hep-ph/0510213].

[16] T2K collaboration, *Measurements of neutrino oscillation parameters from the T2K experiment using* 3.6×10^{21} *protons on target*, *Eur. Phys. J. C* **83** (2023) 782 [2303.03222].

[17] NOvA collaboration, *Improved measurement of neutrino oscillation parameters by the NOvA experiment*, *Phys. Rev. D* **106** (2022) 032004 [2108.08219].

[18] DELPHI collaboration, *Measurement of the Mass and Width of the* Z^0 *Particle from Multi - Hadronic Final States Produced in* e^+e^- *Annihilations*, *Phys. Lett. B* **231** (1989) 539.

[19] ALEPH collaboration, *A Precise Determination of the Number of Families With Light Neutrinos and of the Z Boson Partial Widths*, *Phys. Lett. B* **235** (1990) 399.

[20] LSND collaboration, *Evidence for neutrino oscillations from the observation of* $\bar{\nu}_e$ *appearance in a* $\bar{\nu}_\mu$ *beam*, *Phys. Rev. D* **64** (2001) 112007 [hep-ex/0104049].

[21] MiniBooNE collaboration, *Significant Excess of ElectronLike Events in the MiniBooNE Short-Baseline Neutrino Experiment*, *Phys. Rev. Lett.* **121** (2018) 221801 [1805.12028].

[22] F. Kaether, W. Hampel, G. Heusser, J. Kiko and T. Kirsten, *Reanalysis of the GALLEX solar neutrino flux and source experiments*, *Phys. Lett. B* **685** (2010) 47 [1001.2731].

[23] J.N. Abdurashitov et al., *Measurement of the response of a Ga solar neutrino experiment to neutrinos from an Ar-37 source*, *Phys. Rev. C* **73** (2006) 045805 [nucl-ex/0512041].

[24] V.V. Barinov et al., *Search for electron-neutrino transitions to sterile states in the BEST experiment*, *Phys. Rev. C* **105** (2022) 065502 [2201.07364].

[25] G. Mention, M. Fechner, T. Lasserre, T.A. Mueller, D. Lhuillier, M. Cribier et al., *The Reactor Antineutrino Anomaly*, *Phys. Rev. D* **83** (2011) 073006 [1101.2755].

[26] PROSPECT collaboration, *Improved short-baseline neutrino oscillation search and energy spectrum measurement with the PROSPECT experiment at HFIR*, *Phys. Rev. D* **103** (2021) 032001 [2006.11210].

[27] STEREO collaboration, *STEREO neutrino spectrum of ^{235}U fission rejects sterile neutrino hypothesis*, *Nature* **613** (2023) 257 [2210.07664].

[28] MINOS+ collaboration, *Search for sterile neutrinos in MINOS and MINOS+ using a two-detector fit*, *Phys. Rev. Lett.* **122** (2019) 091803 [1710.06488].

[29] M. Dentler, A. Hernández-Cabezudo, J. Kopp, P.A.N. Machado, M. Maltoni, I. Martinez-Soler et al., *Updated Global Analysis of Neutrino Oscillations in the Presence of eV-Scale Sterile Neutrinos*, *JHEP* **08** (2018) 010 [1803.10661].

[30] Daya Bay collaboration, *Evolution of the Reactor Antineutrino Flux and Spectrum at Daya Bay*, *Phys. Rev. Lett.* **118** (2017) 251801 [1704.01082].

[31] C. Giunti, Y.F. Li, C.A. Ternes and Z. Xin, *Reactor antineutrino anomaly in light of recent flux model refinements*, *Phys. Lett. B* **829** (2022) 137054 [2110.06820].

[32] MicroBooNE collaboration, *Search for an Excess of Electron Neutrino Interactions in MicroBooNE Using Multiple Final-State Topologies*, *Phys. Rev. Lett.* **128** (2022) 241801 [2110.14054].

[33] C.A. Argüelles, I. Esteban, M. Hostert, K.J. Kelly, J. Kopp, P.A.N. Machado et al., *MicroBooNE and the νe Interpretation of the MiniBooNE Low-Energy Excess*, *Phys. Rev. Lett.* **128** (2022) 241802 [2111.10359].

[34] IceCube collaboration, *eV-Scale Sterile Neutrino Search Using Eight Years of Atmospheric Muon Neutrino Data from the IceCube Neutrino Observatory*, *Phys. Rev. Lett.* **125** (2020) 141801 [2005.12942].

[35] Hyper-Kamiokande Working Group collaboration, *T2HK: J-PARC upgrade plan for future and beyond T2K*, in *15th International Workshop on Neutrino Factories, Super Beams and Beta Beams*, 11, 2013 [1311.5287].

[36] DUNE collaboration, *Long-Baseline Neutrino Facility (LBNF) and Deep Underground Neutrino Experiment (DUNE): Conceptual Design Report, Volume 2: The Physics Program for DUNE at LBNF*, 1512.06148.

[37] MicroBooNE, LAr1-ND, ICARUS-WA104 collaboration, *A Proposal for a Three Detector Short-Baseline Neutrino Oscillation Program in the Fermilab Booster Neutrino Beam*, 1503.01520.

[38] P.A. Machado, O. Palamara and D.W. Schmitz, *The Short-Baseline Neutrino Program at Fermilab*, *Ann. Rev. Nucl. Part. Sci.* **69** (2019) 363 [1903.04608].

[39] P. Ballett, T. Boschi and S. Pascoli, *Heavy Neutral Leptons from low-scale seesaws at the DUNE Near Detector*, *JHEP* **03** (2020) 111 [1905.00284].

[40] N. Sabti, A. Magalich and A. Filimonova, *An Extended Analysis of Heavy Neutral Leptons during Big Bang Nucleosynthesis*, *JCAP* **11** (2020) 056 [2006.07387].

[41] C.A. Argüelles, N. Foppiani and M. Hostert, *Heavy neutral leptons below the kaon mass at hodoscopic neutrino detectors*, *Phys. Rev. D* **105** (2022) 095006 [2109.03831].

[42] R. Essig et al., *Working Group Report: New Light Weakly Coupled Particles*, in *Snowmass 2013: Snowmass on the Mississippi*, 10, 2013 [1311.0029].

[43] J. Alexander et al., *Dark Sectors 2016 Workshop: Community Report*, 8, 2016 [1608.08632].

[44] J. Beacham et al., *Physics Beyond Colliders at CERN: Beyond the Standard Model Working Group Report*, *J. Phys. G* **47** (2020) 010501 [1901.09966].

[45] J. Berger et al., *Snowmass 2021 White Paper: Cosmogenic Dark Matter and Exotic Particle Searches in Neutrino Experiments*, in *Snowmass 2021*, 7, 2022 [2207.02882].

[46] P. Ballett, S. Pascoli and M. Ross-Lonergan, *MeV-scale sterile neutrino decays at the Fermilab Short-Baseline Neutrino program*, *JHEP* **04** (2017) 102 [1610.08512].

[47] B. Batell, J. Berger and A. Ismail, *Probing the Higgs Portal at the Fermilab Short-Baseline Neutrino Experiments*, *Phys. Rev. D* **100** (2019) 115039 [1909.11670].

[48] R.T. Co, S. Kumar and Z. Liu, *Searches for heavy QCD axions via dimuon final states*, *JHEP* **02** (2023) 111 [2210.02462].

[49] B. Dutta, A. Karthikeyan and D. Kim, *Longer-Lived Mediators from Charged Mesons and Photons at Neutrino Experiments*, 2308.01491.

[50] K.J. Kelly, S. Kumar and Z. Liu, *Heavy axion opportunities at the DUNE near detector*, *Phys. Rev. D* **103** (2021) 095002 [2011.05995].

[51] J.M. Berryman, A. de Gouvea, P.J. Fox, B.J. Kayser, K.J. Kelly and J.L. Raaf, *Searches for Decays of New Particles in the DUNE Multi-Purpose Near Detector*, *JHEP* **02** (2020) 174 [1912.07622].

[52] Y. Ema, Z. Liu and R. Plestid, *Searching for axions with kaon decay at rest*, 2308.08589.

[53] E. Izaguirre, T. Lin and B. Shuve, *Searching for Axionlike Particles in Flavor-Changing Neutral Current Processes*, *Phys. Rev. Lett.* **118** (2017) 111802 [1611.09355].

[54] B. Batell, W. Huang and K.J. Kelly, *Keeping it simple: simplified frameworks for long-lived particles at neutrino facilities*, *JHEP* **08** (2023) 092 [2304.11189].

[55] G. Krnjaic, *Probing Light Thermal Dark-Matter With a Higgs Portal Mediator*, *Phys. Rev. D* **94** (2016) 073009 [1512.04119].

[56] B.W. Lee and S. Weinberg, *Cosmological lower bound on heavy-neutrino masses*, *Phys. Rev. Lett.* **39** (1977) 165.

[57] J.F. Gunion, H.E. Haber, G.L. Kane and S. Dawson, *The Higgs Hunter's Guide*, vol. 80 (2000).

[58] F. Bezrukov and D. Gorbunov, *Light inflaton Hunter's Guide*, *JHEP* **05** (2010) 010 [0912.0390].

[59] R.D. Peccei and H.R. Quinn, CP *conservation in the presence of pseudoparticles*, *Phys. Rev. Lett.* **38** (1977) 1440.

[60] S. Weinberg, *A new light boson?*, *Phys. Rev. Lett.* **40** (1978) 223.

[61] F. Wilczek, *Problem of strong p and t invariance in the presence of instantons*, *Phys. Rev. Lett.* **40** (1978) 279.

[62] R.D. Peccei and H.R. Quinn, *Constraints imposed by* CP *conservation in the presence of pseudoparticles*, *Phys. Rev. D* **16** (1977) 1791.

[63] B. Graner, Y. Chen, E.G. Lindahl and B.R. Heckel, *Reduced limit on the permanent electric dipole moment of* ^{199}Hg, *Phys. Rev. Lett.* **116** (2016) 161601.

[64] C. Abel et al., *Measurement of the Permanent Electric Dipole Moment of the Neutron*, *Phys. Rev. Lett.* **124** (2020) 081803 [2001.11966].

[65] G. 't Hooft, *Symmetry Breaking Through Bell-Jackiw Anomalies*, *Phys. Rev. Lett.* **37** (1976) 8.

[66] R. Holman, S.D.H. Hsu, T.W. Kephart, E.W. Kolb, R. Watkins and L.M. Widrow, *Solutions to the strong CP problem in a world with gravity*, *Phys. Lett. B* **282** (1992) 132 [hep-ph/9203206].

[67] S.M. Barr and D. Seckel, *Planck scale corrections to axion models*, *Phys. Rev. D* **46** (1992) 539.

[68] M. Kamionkowski and J. March-Russell, *Planck scale physics and the Peccei-Quinn mechanism*, *Phys. Lett. B* **282** (1992) 137 [hep-th/9202003].

[69] A. Hook, S. Kumar, Z. Liu and R. Sundrum, *High Quality QCD Axion and the LHC*, *Phys. Rev. Lett.* **124** (2020) 221801 [1911.12364].

[70] P. Coloma, J. Martín-Albo and S. Urrea, *Discovering long-lived particles at DUNE*, *Phys. Rev. D* **109** (2024) 035013 [2309.06492].

[71] FASER collaboration, *FASER's physics reach for long-lived particles*, *Phys. Rev. D* **99** (2019) 095011 [1811.12522].

[72] M. Bauer, M. Neubert, S. Renner, M. Schnubel and A. Thamm, *Consistent Treatment of Axions in the Weak Chiral Lagrangian*, *Phys. Rev. Lett.* **127** (2021) 081803 [2102.13112].

[73] W.A. Bardeen, S.H.H. Tye and J.A.M. Vermaseren, *Phenomenology of the New Light Higgs Boson Search*, *Phys. Lett. B* **76** (1978) 580.

[74] M. Bauer, M. Neubert, S. Renner, M. Schnubel and A. Thamm, *Flavor probes of axion-like particles*, *JHEP* **09** (2022) 056 [2110.10698].

[75] E. de Rafael, *Chiral Lagrangians and kaon CP violation*, in *Theoretical Advanced Study Institute in Elementary Particle Physics (TASI 94): CP Violation and the limits of the Standard Model*, 1, 1995 [hep-ph/9502254].

[76] V. Cirigliano, G. Ecker, H. Neufeld, A. Pich and J. Portoles, *Kaon Decays in the Standard Model*, *Rev. Mod. Phys.* **84** (2012) 399 [1107.6001].

[77] E. Izaguirre, T. Lin and B. Shuve, *Searching for axionlike particles in flavor-changing neutral current processes*, *Phys. Rev. Lett.* **118** (2017) 111802.

[78] D. Aloni, Y. Soreq and M. Williams, *Coupling QCD-Scale Axionlike Particles to Gluons*, *Phys. Rev. Lett.* **123** (2019) 031803 [1811.03474].

[79] ICARUS collaboration, *Design, construction and tests of the ICARUS T600 detector*, *Nucl. Instrum. Meth. A* **527** (2004) 329.

[80] ICARUS-T600 collaboration, *Overhaul and Installation of the ICARUS-T600 Liquid Argon TPC Electronics for the FNAL Short Baseline Neutrino Program*, *JINST* **16** (2021) P01037 [2010.02042].

[81] MiniBooNE collaboration, *The Neutrino Flux Prediction at MiniBooNE*, *Phys. Rev. D* **79** (2009) 072002 [0806.1449].

[82] P. Adamson et al., *The NuMI Neutrino Beam*, *Nucl. Instrum. Meth. A* **806** (2016) 279 [1507.06690].

[83] ICARUS collaboration, *ICARUS at the Fermilab Short-Baseline Neutrino program: initial operation*, *Eur. Phys. J. C* **83** (2023) 467 [2301.08634].

[84] MicroBooNE collaboration, *Design and Construction of the MicroBooNE Detector*, *JINST* **12** (2017) P02017 [1612.05824].

[85] ICARUS/NP01 collaboration, *New read-out electronics for ICARUS-T600 liquid Argon TPC. Description, simulation and tests of the new front-end and ADC system*, *JINST* **13** (2018) P12007 [1805.03931].

[86] MicroBooNE collaboration, *The Pandora multi-algorithm approach to automated pattern recognition of cosmic-ray muon and neutrino events in the MicroBooNE detector*, *Eur. Phys. J. C* **78** (2018) 82 [1708.03135].

[87] DUNE collaboration, *Reconstruction of interactions in the ProtoDUNE-SP detector with Pandora*, *Eur. Phys. J. C* **83** (2023) 618 [2206.14521].

[88] M. Bonesini et al., *An innovative technique for TPB deposition on convex window photomultiplier tubes*, *JINST* **13** (2018) P12020 [1807.07123].

[89] Double Chooz collaboration, *Double Chooz: A Search for the neutrino mixing angle theta(13)*, hep-ex/0606025.

[90] R. Ainsworth, P. Adamson, B.C. Brown, D. Capista, K. Hazelwood, I. Kourbanis et al., *High intensity operation using proton stacking in the Fermilab Recycler to deliver 700 kW of 120 GeV proton beam*, *Phys. Rev. Accel. Beams* **23** (2020) 121002.

[91] S. Agostinelli et al., *Geant4—a simulation toolkit*, *Nuclear Instruments and Methods in Physics Research Section A: Accelerators, Spectrometers, Detectors and Associated Equipment* **506** (2003) 250.

[92] L. Aliaga Soplin, *Neutrino flux prediction for the numi beamline*, .

[93] MINERνA Collaboration collaboration, *Neutrino flux predictions for the numi beam*, *Phys. Rev. D* **94** (2016) 092005.

[94] ICARUS collaboration, *DocDB: 27384 Prediction of NuMI electron and muon neutrino flux in ICARUS*, .

[95] P. Ballett, M. Hostert, S. Pascoli, Y.F. Perez-Gonzalez, Z. Tabrizi and R. Zukanovich Funchal, *Neutrino Trident Scattering at Near Detectors*, *JHEP* **01** (2019) 119 [1807.10973].

[96] A. Kayis-Topaksu et al., *Measurement of charm production in neutrino charged-current interactions*, *New J. Phys.* **13** (2011) 093002 [1107.0613].

[97] GENIE collaboration, *Recent highlights from GENIE v3*, *Eur. Phys. J. ST* **230** (2021) 4449 [2106.09381].

[98] D.I. Scully, *Neutrino induced coherent pion production.*, Ph.D. thesis, Warwick U., 2013.

[99] D. Rein and L.M. Sehgal, *Coherent pi0 Production in Neutrino Reactions*, *Nucl. Phys. B* **223** (1983) 29.

[100] C. Berger and L.M. Sehgal, *PCAC and coherent pion production by low energy neutrinos*, *Phys. Rev. D* **79** (2009) 053003 [0812.2653].

[101] ArgoNeuT collaboration, *First Measurement of Neutrino and Antineutrino Coherent Charged Pion Production on Argon*, *Phys. Rev. Lett.* **113** (2014) 261801 [1408.0598].

[102] MINERvA collaboration, *Neutrino-Induced Coherent $\pi+$ Production in C, CH, Fe, and Pb at $\langle E\nu\rangle\sim$6 GeV*, *Phys. Rev. Lett.* **131** (2023) 051801 [2210.01285].

[103] L. Alvarez-Ruso, L.S. Geng, S. Hirenzaki and M.J. Vicente Vacas, *Charged current neutrino induced coherent pion production*, *Phys. Rev. C* **75** (2007) 055501 [nucl-th/0701098].

[104] S.K. Singh, M. Sajjad Athar and S. Ahmad, *Nuclear effects in neutrino induced coherent pion production at K2K and MiniBooNE*, *Phys. Rev. Lett.* **96** (2006) 241801 [nucl-th/0601045].

[105] J.E. Amaro, E. Hernandez, J. Nieves and M. Valverde, *Theoretical study of neutrino-induced coherent pion production off nuclei at T2K and MiniBooNE energies*, *Phys. Rev. D* **79** (2009) 013002 [0811.1421].

[106] D. Heck, J. Knapp, J.N. Capdevielle, G. Schatz and T. Thouw, *CORSIKA: A Monte Carlo code to simulate extensive air showers*, .

[107] ArgoNeuT collaboration, *A Study of Electron Recombination Using Highly Ionizing Particles in the ArgoNeuT Liquid Argon TPC*, *JINST* **8** (2013) P08005 [1306.1712].

[108] MicroBooNE collaboration, *Ionization electron signal processing in single phase LArTPCs. Part I. Algorithm Description and quantitative evaluation with MicroBooNE simulation*, *JINST* **13** (2018) P07006 [1802.08709].

[109] R. Veenhof, *Garfield, recent developments*, *Nuclear Instruments and Methods in Physics Research Section A: Accelerators, Spectrometers, Detectors and Associated Equipment* **419** (1998) 726.

[110] P.V. Vavilov, *Ionization losses of high-energy heavy particles*, *Sov. Phys. JETP* **5** (1957) 749.

[111] L. Landau, *On the energy loss of fast particles by ionization*, *J. Phys. (USSR)* **8** (1944) 201.

[112] H. Bethe, *Zur Theorie des Durchgangs schneller Korpuskularstrahlen durch Materie*, *Annalen der Physik* **397** (1930) 325.

[113] G. Putnam and D.W. Schmitz, *Effect of diffusion on the peak value of energy loss observed in a LArTPC*, *JINST* **17** (2022) P10044 [2205.06745].

[114] P.A.Z. et. al. (Particle Data Group), *Review of Particle Physics*, *Progress of Theoretical and Experimental Physics* **2020** (2020) .

[115] K.S. Kolbig and B. Schorr, *Asymptotic expansions for the landau density and distribution functions*, *Comput. Phys. Commun.* **32** (1984) 121.

[116] Y. Li et al., *Measurement of Longitudinal Electron Diffusion in Liquid Argon*, *Nucl. Instrum. Meth. A* **816** (2016) 160 [1508.07059].

[117] DUNE collaboration, *First results on ProtoDUNE-SP liquid argon time projection chamber performance from a beam test at the CERN Neutrino Platform*, *JINST* **15** (2020) P12004 [2007.06722].

[118] LArIAT collaboration, *The Liquid Argon In A Testbeam (LArIAT) Experiment*, *JINST* **15** (2020) P04026 [1911.10379].

[119] ArgoNeuT collaboration, *Analysis of a Large Sample of Neutrino-Induced Muons with the ArgoNeuT Detector*, *JINST* **7** (2012) P10020 [1205.6702].

[120] MicroBooNE collaboration, *Calibration of the charge and energy loss per unit length of the MicroBooNE liquid argon time projection chamber using muons and protons*, *JINST* **15** (2020) P03022 [1907.11736].

[121] C. Anderson et al., *The ArgoNeuT Detector in the NuMI Low-Energy beam line at Fermilab*, *JINST* **7** (2012) P10019 [1205.6747].

[122] MicroBooNE collaboration, *Measurement of the longitudinal diffusion of ionization electrons in the MicroBooNE detector*, *JINST* **16** (2021) P09025 [2104.06551].

[123] V.M. Atrazhev and I.V. Timoshkin, *Transport of electrons in atomic liquids in high electric fields*, *IEEE Transactions on Dielectrics and Electrical Insulation* **5** (1998) 450.

[124] R. Sternheimer, M. Berger and S. Seltzer, *Density effect for the ionization loss of charged particles in various substances*, *Atomic Data and Nuclear Data Tables* **30** (1984) 261.

[125] D.E. Groom, N.V. Mokhov and S.I. Striganov, *Muon stopping power and range tables 10 mev–100 tev*, *Atomic Data and Nuclear Data Tables* **78** (2001) 183.

[126] A. Bettini et al., *A study of the factors affecting the electron lifetime in ultra-pure liquid argon*, *Nuclear Instruments and Methods in Physics Research Section A: Accelerators, Spectrometers, Detectors and Associated Equipment* **305** (1991) 177.

[127] R. Andrews, W. Jaskierny, H. Jostlein, C. Kendziora, S. Pordes and T. Tope, *A system to test the effects of materials on the electron drift lifetime in liquid argon and observations on the effect of water*, *Nucl. Instrum. Meth. A* **608** (2009) 251.

[128] M. Mooney, *The MicroBooNE Experiment and the Impact of Space Charge Effects*, in *Meeting of the APS Division of Particles and Fields*, 11, 2015 [1511.01563].

[129] MicroBooNE collaboration, *Measurement of space charge effects in the MicroBooNE LArTPC using cosmic muons*, *JINST* **15** (2020) P12037 [2008.09765].

[130] MicroBooNE collaboration, *Ionization electron signal processing in single phase LArTPCs. Part II. Data/simulation comparison and performance in MicroBooNE*, *JINST* **13** (2018) P07007 [1804.02583].

[131] MicroBooNE collaboration, *First Measurement of Inclusive Muon Neutrino Charged Current Differential Cross Sections on Argon at $E_\nu \sim 0.8$ GeV with the MicroBooNE Detector*, *Phys. Rev. Lett.* **123** (2019) 131801 [1905.09694].

[132] MicroBooNE collaboration, *First Measurement of Energy-Dependent Inclusive Muon Neutrino Charged-Current Cross Sections on Argon with the MicroBooNE Detector*, *Phys. Rev. Lett.* **128** (2022) 151801 [2110.14023].

[133] MicroBooNE collaboration, *Search for an Excess of Electron Neutrino Interactions in MicroBooNE Using Multiple Final-State Topologies*, *Phys. Rev. Lett.* **128** (2022) 241801 [2110.14054].

[134] ICARUS collaboration, *Muon momentum measurement in ICARUS-T600 LAr-TPC via multiple scattering in few-GeV range*, *JINST* **12** (2017) P04010 [1612.07715].

[135] A. Lister and M. Stancari, *Investigations on a fuzzy process: effect of diffusion on calibration and particle identification in Liquid Argon Time Projection Chambers*, *JINST* **17** (2022) P07016 [2201.09773].

[136] J. Thomas and D.A. Imel, *Recombination of electron-ion pairs in liquid argon and liquid xenon*, *Phys. Rev. A* **36** (1987) 614.

[137] J. Thomas, D.A. Imel and S. Biller, *Statistics of charge collection in liquid argon and liquid xenon*, *Phys. Rev. A* **38** (1988) 5793.

[138] ICARUS collaboration, *Study of electron recombination in liquid argon with the ICARUS TPC*, *Nucl. Instrum. Meth. A* **523** (2004) 275.

[139] G. Jaffé, *Zur theorie der ionisation in kolonnen*, *Annalen der Physik* **347** (1913) 303 .

[140] V. Cataudella, A. de Candia, G.D. Filippis, S. Catalanotti, M. Cadeddu, M. Lissia et al., *Directional modulation of electron-ion pairs recombination in liquid argon*, *JINST* **12** (2017) P12002.

[141] M. Cadeddu et al., *Directional dark matter detection sensitivity of a two-phase liquid argon detector*, *JCAP* **01** (2019) 014 [1704.03741].

[142] M. Wojcik and M. Tachiya, *Electron thermalization and electron–ion recombination in liquid argon*, *Chemical Physics Letters* **379** (2003) 20.

[143] U. Sowada, J.M. Warman and M.P. de Haas, *Hot-electron thermalization in solid and liquid argon, krypton, and xenon*, *Phys. Rev. B* **25** (1982) 3434.

[144] R. Brun and F. Rademakers, *Root - an object oriented data analysis framework*, in *AIHENP'96 Workshop, Lausane*, vol. 389, pp. 81–86, 1996.

[145] M. Strait, *Evaluation of the mean excitation energy of liquid argon*, 2212.06286.

[146] M. Miyajima, T. Takahashi, S. Konno, T. Hamada, S. Kubota, H. Shibamura et al., *Average energy expended per ion pair in liquid argon*, *Phys. Rev. A* **9** (1974) 1438.

[147] ArgoNeuT collaboration, *Demonstration of MeV-Scale Physics in Liquid Argon Time Projection Chambers Using ArgoNeuT*, *Phys. Rev. D* **99** (2019) 012002 [1810.06502].

[148] MicroBooNE collaboration, *Determination of muon momentum in the MicroBooNE LArTPC using an improved model of multiple Coulomb scattering*, *JINST* **12** (2017) P10010 [1703.06187].

[149] J. Calcutt, C. Thorpe, K. Mahn and L. Fields, *Geant4Reweight: a framework for evaluating and propagating hadronic interaction uncertainties in Geant4*, *JINST* **16** (2021) P08042 [2105.01744].

[150] G. Choudalakis, *On hypothesis testing, trials factor, hypertests and the BumpHunter*, in *PHYSTAT 2011*, 1, 2011 [1101.0390].

[151] ATLAS collaboration, *Search for new high-mass phenomena in the dilepton final state using 36 fb^{-1} of proton-proton collision data at $\sqrt{s}$ = 13 TeV with the ATLAS detector*, *Journal of High Energy Physics* (2017) .

[152] ATLAS collaboration, *Search for new resonances in mass distributions of jet pairs using 139 fb^{-1} of pp collisions at $\sqrt{s}$ = 13 tev with the ATLAS detector*, *Journal of High Energy Physics* (2020) .

[153] *Search for new particles in two-jet final states in 7 TeV proton-proton collisions with the ATLAS detector at the LHC*, *Physical Review Letters* (2010) .

[154] A.L. Read, *Modified frequentist analysis of search results (The CL(s) method)*, in *Workshop on Confidence Limits*, pp. 81–101, 8, 2000.

[155] MicroBooNE collaboration, *Search for long-lived heavy neutral leptons and Higgs portal scalars decaying in the MicroBooNE detector*, *Phys. Rev. D* **106** (2022) 092006 [2207.03840].

[156] L. Vaslin, S. Calvet, V. Barra and J. Donini, *pyBumpHunter: A model independent bump hunting tool in Python for High Energy Physics analyses*, *SciPost Phys. Codeb.* **2023** (2023) 15 [2208.14760].

[157] E949 collaboration, *Search for heavy neutrinos in $K^+ \to \mu^+ \nu_H$ decays*, *Phys. Rev. D* **91** (2015) 052001 [1411.3963].

[158] NA62 collaboration, *Measurement of the very rare $K^+ \to \pi^+ \nu\overline{\nu}$ decay*, *JHEP* **06** (2021) 093 [2103.15389].

[159] LHCb collaboration, *Search for hidden-sector bosons in $B^0 \to K^{*0} \mu^+ \mu^-$ decays*, *Phys. Rev. Lett.* **115** (2015) 161802 [1508.04094].

[160] LHCb collaboration, *Search for long-lived scalar particles in $B^+ \to K^+ \chi(\mu^+ \mu^-)$ decays*, *Phys. Rev. D* **95** (2017) 071101 [1612.07818].

[161] M.W. Winkler, *Decay and detection of a light scalar boson mixing with the Higgs boson*, *Phys. Rev. D* **99** (2019) 015018 [1809.01876].

[162] CHARM collaboration, *Search for Axion Like Particle Production in 400-GeV Proton - Copper Interactions*, *Phys. Lett. B* **157** (1985) 458.

[163] D. Gorbunov, I. Krasnov and S. Suvorov, *Constraints on light scalars from PS191 results*, *Phys. Lett. B* **820** (2021) 136524 [2105.11102].

[164] S. Foroughi-Abari and A. Ritz, *LSND Constraints on the Higgs Portal*, *Phys. Rev. D* **102** (2020) 035015 [2004.14515].

[165] LSND collaboration, *Search for pi0 —> nu(mu) anti-nu(mu) decay in LSND*, *Phys. Rev. Lett.* **92** (2004) 091801 [hep-ex/0310060].

[166] NA48/2 collaboration, *Searches for lepton number violation and resonances in $K^\pm \to \pi\mu\mu$ decays*, *Phys. Lett. B* **769** (2017) 67 [1612.04723].

[167] ArgoNeuT collaboration, *First Constraints on Heavy QCD Axions with a Liquid Argon Time Projection Chamber Using the ArgoNeuT Experiment*, *Phys. Rev. Lett.* **130** (2023) 221802 [2207.08448].